Part I. Polar-π Interactions in Aryl Alkyne Molecular Rotors

Part II. Electrostatic Modeling of Potassium Ion Channels

Dissertation

zur

Erlangung der naturwissenschaftlichen Doktorwürde
(Dr. sc. nat.)

vorgelegt der

Mathematisch-naturwissenschaftlichen Fakultät

der

Universität Zürich

von

Arif R. Karim

aus den USA

Promotionskomitee:

Prof. Dr. Jay S. Siegel (Vorsitz)

Prof Dr. Kim K. Baldridge

Prof. Nathan Luedtke

Zürich, 2007

Die vorliegende arbeit wurde von

Der Mathematisch-naturwissenschaftlichen Fakultät

der Universität Zürich im September 2007

als Dissertation angenommen

Promotionskomitee:

Prof. Dr. Jay S. Siegel,

Vorsitz

Prof. Dr. Kim K. Baldridge

Prof. Nathan Luedtke

Universität Zurich 2007

1 POLAR-π INTERACTIONS

1.1 Overview

Noncovalent interactions play a significant role in determining molecular organization, ranging from the complex three-dimensional folding of large proteins to the binding geometry in host:guest complexes. Further, many of the functional properties of molecules are a result of the molecular organization instilled by interactions of this type. Therefore, a fundamental understanding of noncovalent interactions is critical to identifying, predicting, and utilizing the relationship between structure and function.

Noncovalent interactions can be intermolecular or intramolecular, but are generally weaker than the covalent bonds commonly encountered in organic chemistry. Some examples of noncovalent interactions are ionic interactions, hydrogen bonding, dipole-dipole interactions, and dispersion forces.

Ionic interactions are purely electrostatic interactions between two oppostively charged species, and are governed by Coulomb's Law. In terms of atomic interactions, an ionic bond forms when the difference in electronegativity between the two atoms is large enough that one atom almost completely removes an electron from the other atom. However, there are no purely ionic bonds, as sharing of electrons always occurs to some extent. Ionic compounds generally have high melting and boiling points, due to the significant amount of energy required to overcome the interaction between the charged ions.

Whereas ionic bonding involves the electrostatic interaction between charged species, hydrogen bonding occurs between the partial positive charge of a hydrogen atom and a highly electronegative atom. Hydrogen bonding is one of the most common and energetically significant of the weak interactions. It most frequently occurs when a hydrogen atom is bound to a strongly electronegative atom and another

electronegative atom is present in the system. Hydrogen bonds consist of strong, single point interactions with well-defined geometries (Figure 1.1).[1] The magnitude of a hydrogen bond is determined by the electrostatic forces between the donor hydrogen atom and the electronegative acceptor.[2] Hydrogen bonding is responsible for the unique properties of water and also provides an intermolecular force that holds together adjacent base pair strands in the DNA double helix. This attractive force is commonly described with the notation X-H•••Y, where X and Y are the two electronegative atoms, both interacting with the electron deficient hydrogen atom. In comparison to hydrogen bonding, the other weak interactions are not nearly as well understood.

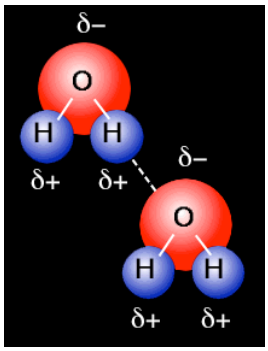

Figure 1.1 Hydrogen bonding between two water molecules.[2]

Dipole-dipole interactions occur between two molecules with permanent dipoles. They are similar to ionic interactions, but weaker in magnitude because only partial charges are involved. The critical difference between hydrogen bonding and dipole-dipole interactions is that, in hydrogen bonding, the hydrogen is partially transferred from one molecule to the other, in a manner similar to tautomerism.

Dispersion forces involve the interactions between transient dipoles. These interactions are generally weaker than dipole-dipole interactions or hydrogen bonding. Transient dipoles of this type can be induced by proximity to another dipole or can simply result from an instantaneous uneven distribution of electrons.

Dispersion forces become more significant in larger systems due to their increased polarizability. Dispersion is the only attractive force between the noble gases, and is the reason they can be obtained in the liquid form.

Our primary interest in this thesis is in noncovalent interactions in aromatic systems. Interactions in these systems can involve a wide array of functional groups, multiple points of contact, and play a significant role in determining molecular geometries.[2] Aromatic interactions consist of dipole-dipole interactions and dispersion effects. The interactions are primarily dependent on the size and charge distribution of the aromatic species involved.

In the case of benzene, the regions directly above and below the plane of the ring have high electron densities. In contrast, the periphery of the ring is electron deficient, due to the polarized C—H bonds. This environment fits the criteria described above for polar interactions, although the symmetry of benzene precludes the existence of a dipole. The herringbone structure of crystalline benzene, in which the electron deficient edge of one molecule is directed into the electron rich face of an adjacent one, provides evidence for the existence of this type of interaction in π systems (Figure 1.2).[3] The term used here to describe this intermolecular attraction is polar-π interaction. The stacking motif in crystalline benzene not only enables favorable electrostatic interactions, but also deters repulsive face-to-face and edge-to-edge interactions. Similar orientations of benzene have been observed in solution[4,5] as well as in the gas phase.[6-8]

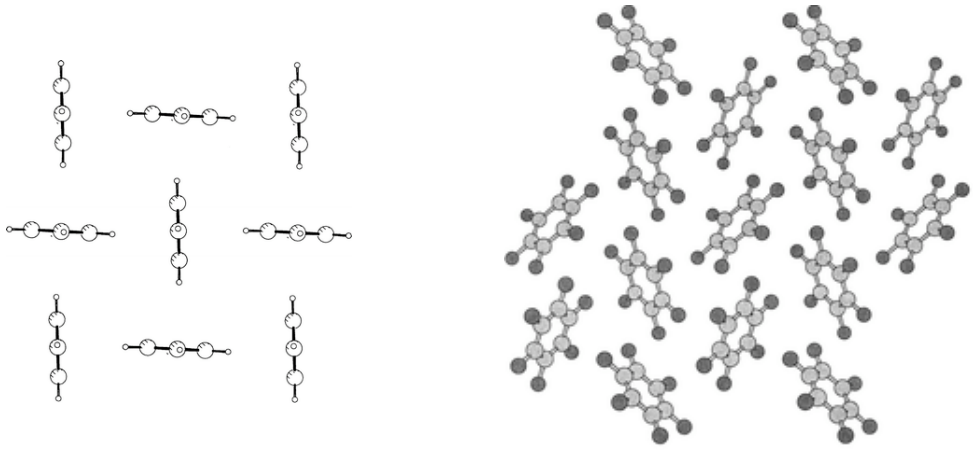

Figure 1.2 Packing diagrams from crystal structure of benzene found by neutron diffraction at -135 °C.[3]

In 1960, a 1:1 complex of benzene and hexafluorobenzene was reported.[9] When equal amounts of the two liquids were combined at room temperature, a complex was formed, and, although both are liquids at room temperature, the binary mixture is a solid. The interaction was originally attributed to charge-transfer, but no charge-transfer band was found in the UV spectrum. Neutron diffraction experiments showed the complex to consist of alternating layers of benzene and hexafluorobenzene (Figure 1.3).[9] X-ray structures of other binary mixtures of hexafluorobenzene and methylated benzenes showed similar interactions (Figure 1.4).[10]

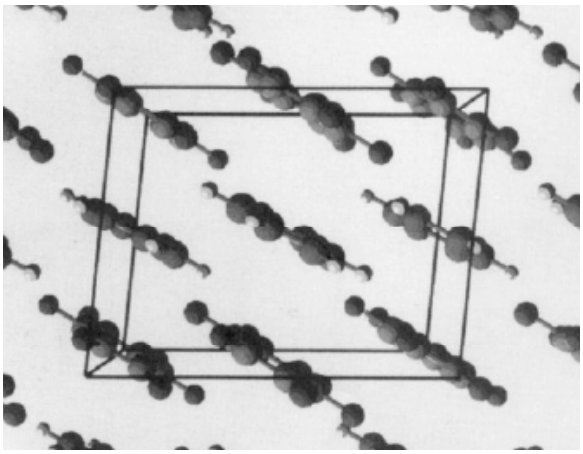

Figure 1.3 The structure of solid C_6H_6/C_6F_6, in its lowest temperature phase (T < 205 K) viewed along the *b* crystalline axis, as revealed by neutron and synchotron diffraction experiments.[9]

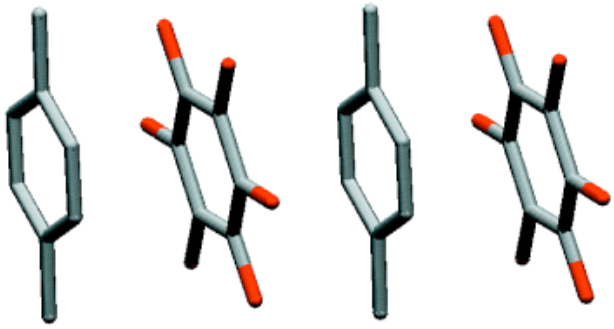

Figure 1.4 The structure of solid p-xylene/hexafluorobenzene, indicating face-to-face stacking.[10]

The formation of alternating stacks of benzene and hexafluorbenzene was rationalized in terms of the quadrupole moment of the two molecules. In the case of benzene, the quadrupole moment is large and negative (-29.0×10^{-40} C m^2). The quadrupole moment of hexafluorobenzene is large and positive due to the high electronegativity of fluorine (31.7×10^{-40} C m^2).[2] The observed alignment of benzene and hexafluorobenzene maximizes the interaction energy because a positive quadrupole moment is found parallel and adjacent to a negative quadrupole moment (Figure 1.5). This arrangement enabled favorable face-to-face stacking of the rings, and, in addition, the C—H bonds of benzene molecules are directed towards the C—F bonds of hexafluorobenzene molecules in the adjacent layers.

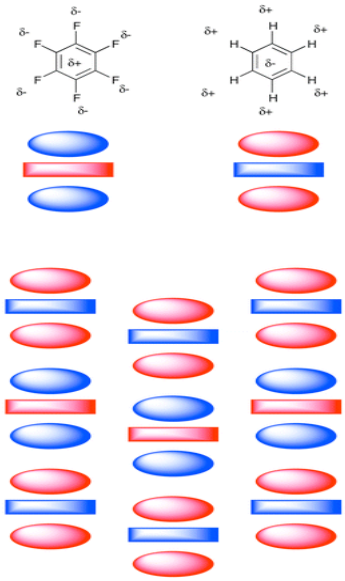

Figure 1.5 A schematic of the alignment of the quadrupole moments in the binary mixture of benzene and hexafluorobenzene.[2]

Polar-π interactions are manifested in the crystal structures of benzene and the binary mixture of benzene and hexafluorobenzene. In both cases, molecule orientations maximize favorable electrostatic interactions and minimize unfavorable ones, which is consistent with what was predicted.

1.2 Intramolecular Arene-Arene Interactions

1.2.1 1,8-Diarylnapthalenes

Cozzi and Siegel developed a model system for the study of the parallel stacking interaction between two benzenes using 1,8-diarylnapthalenes.[11-13] In this model, two arenes are held in close proximity in a stacked geometry.

The steric congestion in the diarylnapthalene system forces the two aryl groups to be parallel to each other, but perpendicular to the plane of the naphthalene (Figure 1.6). In this parallel stacked geometry, the coulombic term is presumed to be repulsive. Therefore, rotation of one of the phenyl groups through 180° must traverse a transition state where the repulsive interaction is eliminated. The activation energy

for this isomerization provides a measure of the difference between the "repulsive" ground state and the transition state. The strength of the polar aromatic interaction between the stacked rings can be determined if one assumes the polar interactions in the transition state are negligible and other transition state factors are constant. The substituent at the 4 position of one of the rings was varied and the dependence of the rotational barrier on the identity of this substituent was investigated.[12]

A)

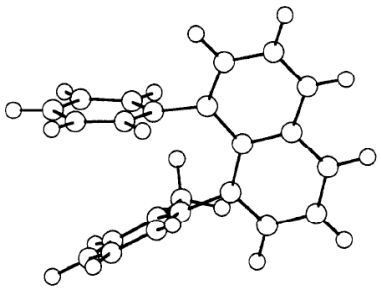

B)

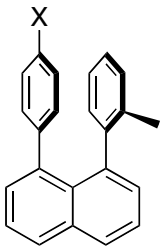

X	
OMe	**1a**
Me	**1b**
H	**1c**
Cl	**1d**
CO_2Me	**1e**
NO_2	**1f**

Figure 1.6 A) Molecular model, indicating the parallel arrangement of the two phenyl rings. B) A series of derivatives were prepared, with **X** varied from electron-donating to electron-withdrawing groups.

The ring that remains constant in this system is the tolyl group, which makes the regions of space above and below the naphthalene plane diastereotopic. This differentiation enables the use of variable temperature ^{1}H NMR spectroscopy to determine the barrier to rotation. At room temperature, compounds **1a-f** exhibit four distinct signals for the *p*-substituted ring. Upon warming, coalescence to two signals was observed, and the rotational barriers were determined by line shape analysis. The

barrier increases on passing from electron donating to electron withdrawing substituents, which can be rationalized by the existence of a through-space polar-π interaction between the two aryl groups.

Table 1.1 Rotational barriers for **1a-1f**

Compound	Substituent	$\Delta G^{\neq}$ (kcal/mol)
1a	OMe	13.9
1b	Me	14.4
1c	H	14.7
1d	Cl	15.5
1e	CO_2Me	16.9
1f	NO_2	17.3

The addition of an electron donating substituent causes the electrostatic repulsion of the parallel stacked geometry to increase relative to the unsubstituted compound. As a result, the ground state conformation is destabilized, which leads to a decrease in the actual rotational barrier. Conversely, the addition of an electron withdrawing substituent stabilizes the ground state conformation, causing the rotational barrier to increase relative to the unsubstituted compound. The stabilization in the case of an electron withdrawing group adjacent to the tolyl group is analogous to the favorable stacked geometry seen in the benzene-hexafluorobenzene complex. This arrangement places the opposing quadrupole moments in close proximity, and is therefore energetically favored.

An additional series of diarylnapthalenes was synthesized in order to elucidate the relative significance of polar-π vs. charge-transfer interactions.[13] A favorable charge transfer interaction would mean that adjacent electron-poor and electron-rich rings would prefer a stacked geometry; however, if a polar-π interaction were the dominant effect, the maximum repulsion in a stacked geometry would occur with two electron-rich rings and the maximum attraction would be observed with two electron-poor rings. To investigate both possibilities, a system was developed in which the

substituents were varied on both rings and the relative stabilities were determined based on the rate of aryl ring rotation (epimerization).

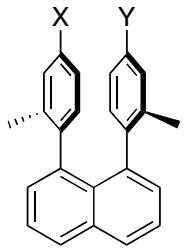

	X	Y
2a	OMe	OMe
2b	OMe	CO_2Me
2c	CO_2Me	CO_2Me
2d	OMe	NO_2
2e	NO_2	CO_2Me
2f	H	NO_2

The energies determined for these molecules are indicative of polar-π interactions as opposed to charge transfer interactions. If a charge transfer effect had been dominant, then **2d**, in which an electron rich ring is paired with an electron poor ring, would have had the highest barrier. However, instead a strong linear correlation between the electron withdrawing character of the substituents and the barrier to epimerization is observed. In addition, the rotational barrier of **2d** does not deviate significantly from the linear correlation, further supporting a polar-pi interaction as the dominant effect.

Table 1.2 Barriers to epimerization and Hammett parameters for **2a-2f**

	Substituents	Σσ	$\Delta G^{\neq}$ (syn-anti)	$\Delta G^{\neq}$ (anti-syn)
2a	OMe/OMe	-0.54	24.0	24.8
2b	OMe/CO_2Me	0.25	24.4	25.3
2c	CO_2Me/CO_2Me	1.04	24.8	25.5
2d	OMe/NO_2	0.51	24.7	25.6
2e	NO_2/CO_2Me	1.30	25.4	26.2
2f	H/ NO_2	0.78	24.9	25.8

The coulombic repulsion is minimized when both rings bear single electron poor substituents, which in turn stabilizes the ground state and leads to an increase in the barrier. In contrast, the repulsion is maximized when the two rings are electron rich, which destabilizes the ground state, leading to a decrease in the rotational

barrier. This work demonstrates that a polar-π effect is clearly dominant over any charge transfer interaction.

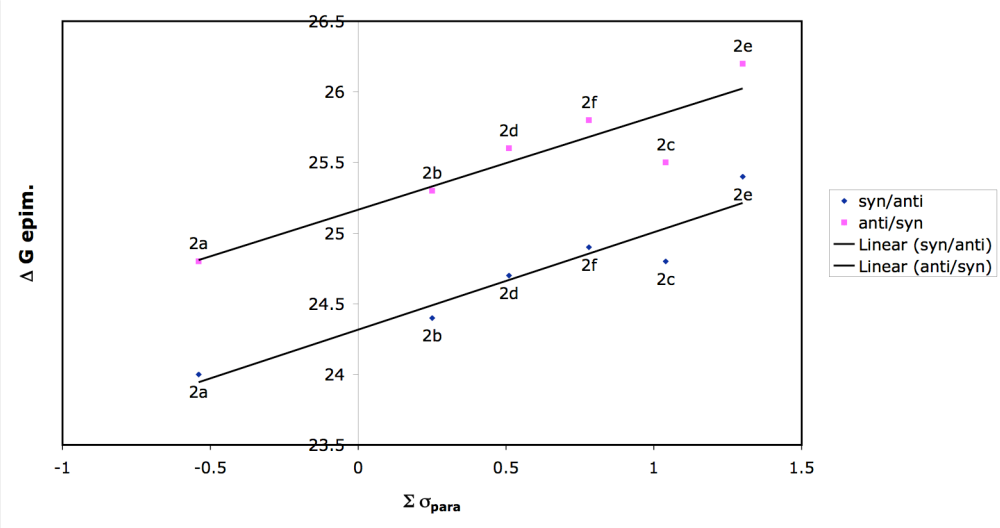

Figure 1.7 Plot of epimerization energies vs. Hammett parameter for **2a**-**2e**

Substitution by fluorine atoms on one of the arenes further tests the electrostatic model by reversing the charge distribution.[14] In **3a-d**, one ring remains unsubstituted while fluorine atoms are progressively added to the second ring. In **4a-d**, one ring is perfluorinated while the meta substituent of the other ring is varied. The meta position is used rather than the para in order to introduce the asymmetry required for NMR experiments.

	F position
3a	2
3b	2, 3
3c	2, 5
3d	2, 3, 4

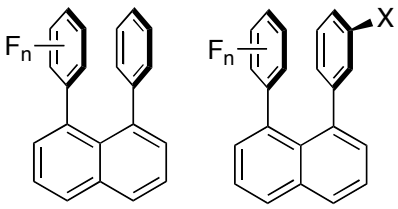

	X
4a	NO_2
4b	CO_2Me
4c	Me
4d	NH_2

For **3a-d**, each additional fluorine atom led to a linear barrier increase of approximately 0.5 kcal/mol, independent of the position. This observation was consistent with previous results, as removing electron density from one of the rings

led to stabilization of the ground state and an increase in the rotational barrier. **4a-d** were investigated to determine the impact of inverting the polarity. With one perfluorinated ring, the polar-π effect would lead to a favorable face-to-face interaction when the other ring contained an electron donating group, as seen in the benzene:hexafluorobenzene complex.

Table 1.3 Rotational barriers for fluorinated derivatives **3a-d** and **4a-c**

Compound	Substituent	Position	$\Delta G^{\neq}$ (kcal/mol)
3a	F	2	17.1
3b	F	2,3	17.6
3c	F	2,5	17.7
3d	F	2,3,4	18.1
4a	NO_2	3	19.5
4b	CO_2Me	3	19.8
4c	Me	3	20.2
4d	NH_2	3	-

There was not a drastic change in rotational barriers for **4a-c** (**4d** was not stable enough to measure), but there was a slight increase with increasing electron donating character. This result is consistent with a polar-π interaction acting as the dominant force in determining the rotational barrier.

1.2.2 Intramolecular Aromatic Interactions in Cyclophanes

In order to evaluate the contribution of non-covalent aromatic interactions, Gellman and coworkers investigated the conformation of 4.4.cyclophanes in solution and the solid state.[15] Their original interest was in studying the role of intramolecular aromatic interactions in determining the conformation of bridged aromatics **5** and **8**. However, they determined that cyclophanes would provide a more appropriate environment for studying such interactions because the degrees of freedom are more limited.

As was previously shown, ^{1}H NMR spectroscopy methods are effective for determining barriers to rotation. Cozzi and Siegel implemented this methodology in their investigation of aromatic interactions. ^{1}H NMR also serves as a sensitive tool for investigating arene-arene proximity because the close approach of aromatics can be detected due to the magnetic anisotropy created by the π electron systems. In order to evaluate the extent of arene-arene interactions, the ^{1}H NMR data for **5** was compared with data for the "monomer" reference systems **6** and **7**. In a similar fashion, **9** served as a reference compound for **8**.

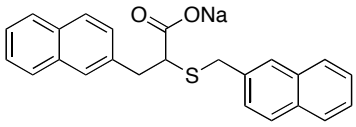

5

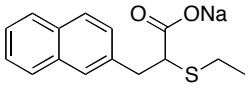

6

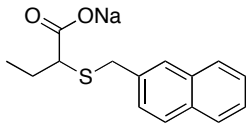

7

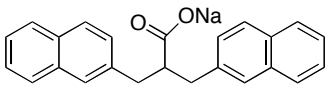

8

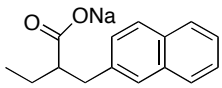

9

In **5**, there is a significant upfield shift of the aromatic protons relative to **6** and **7** in aqueous media. However, there is no such shift in **8** relative to **9**. These results suggest close intramolecular proximity in **5**, but not in **8**. This observation was explained by simple computational modeling, which demonstrated that a 3-atom linker is long enough to allow for face-to-face arene interactions, but not edge-to-face interactions. The slightly more flexible 4-atom linker, on the other hand, is long enough to allow both types of interactions.

Unfortunately, a more detailed conformational analysis of **5** and **8** was not possible because the interconversions were faster than the NMR timescale. To address this limitation, a series of cyclophanes, consisting of two aromatic units bridged by two 4-atom linking chains, was synthesized. Gellman and coworkers had previously synthesized several cyclophanes designed to promote face-to-face aromatic interactions by restricting the size of the linking chain,[16] but the goal with this series was to use flexible linkers so that the geometry of the molecules would be influenced by the intrinsic aromatic interactions. The various cyclophanes, **10**-**15**, consist of either naphthalenes or benzenes, connected between the meta or para positions, leading to a series of six compounds.

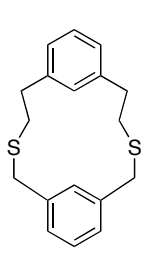

10

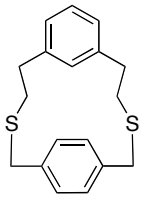

11

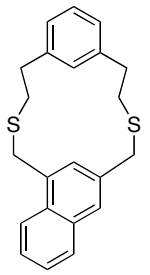

12

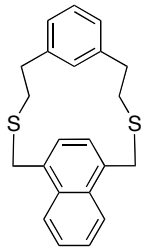

13

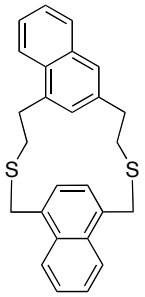

14

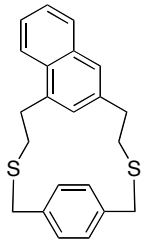

15

X-ray structures were determined for **10**-**14**. In the case of **10** and **12**, edge-to-face arrangements are present and the aryl-aryl angles are 62˚ and 69˚, respectively (Figure 1.8,1.9). In both cases, the ortho hydrogen between the linkers is directed towards the face of the opposing ring. In contrast to **10** and **12,** cyclophanes **11**,**13**,

and **14**, do not have this interaction. The crystal structure of **11** actually indicates a face-to-face interaction, with an angle of 3.6° between the two aromatic planes (Figure 1.10).

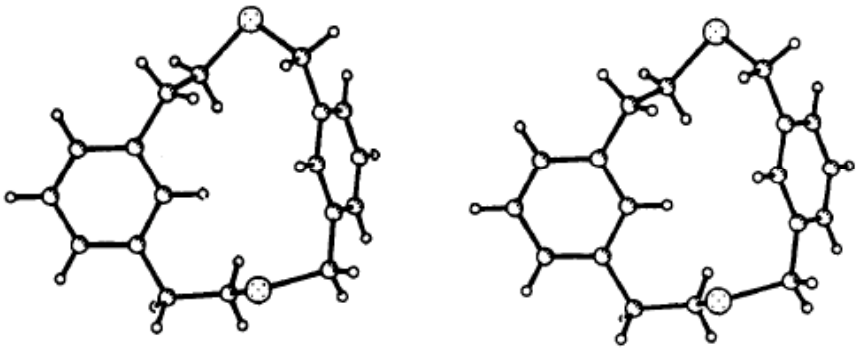

Figure 1.8 Crystal structure of cyclophane **10** (stereoview). The angle between the two aromatic planes is 62.3°

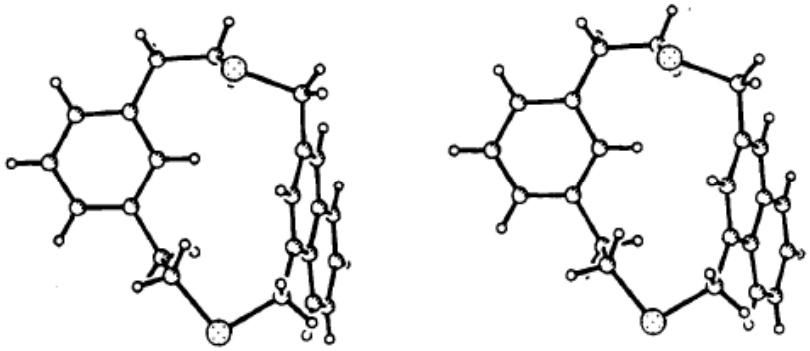

Figure 1.9 Crystal structure of cyclophane **12** (stereoview). The angle between the two aromatic planes is 68.9°

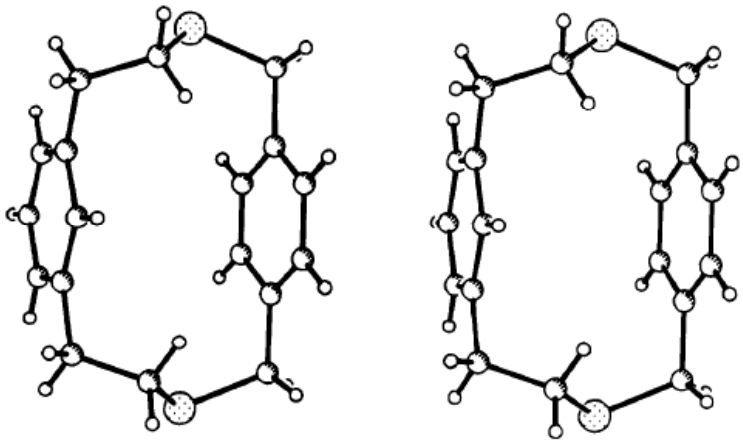

Figure 1.10 Crystal structure of cyclophane **11** (stereoview). The angle between the two aromatic planes is 3.6°

Solution phase NMR studies were conducted to determine the conformational preferences of cyclophanes **10-14**. The NMR data for the cyclophanes was compared with NMR data for reference compounds **16** and **17**. In the case of **11**-**13**, there is one set of sharp resonances at –78 °C. Investigation of the NMR data focused on the ortho proton between the linkers, as this is the one directed towards the face of the opposing ring in the crystal structures of **10** and **12**.

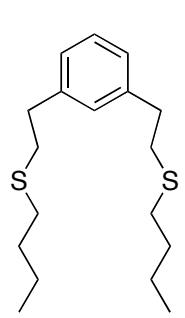

16

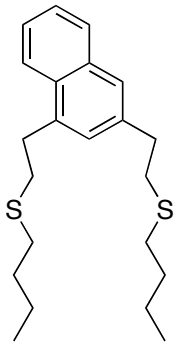

17

Relative to **16** and **17**, there is a dramatic Δδ for the meta, para cyclophanes and a less substantial change for the meta, meta compounds. The consistently large shift of 1.5 ppm for all of the meta, para cyclophanes suggests that these molecules have similar conformational preferences. In addition, this is the only proton in the NMR spectrum that is significantly upfield of the aromatic region.

The most logical explanation for the upfield shift of only one hydrogen is the population of an intramolecular edge-to-face conformer. If the upfield shift was instead a result of a face-to-face interaction, more than one proton would be shifted upfield. In the meta,meta compounds, the upfield shift is only 0.4-0.5 ppm, suggesting the edge-to-face conformer is populated to a lesser extent. NMR data collected at –78 °C for cyclophanes **11**-**13** demonstrated an increase in Δδ relative to the measurements at room temperature, suggesting an increase of the population of the edge-to-face conformer at lower temperatures.

Variable concentration studies were also conducted and confirmed that the interaction was indeed intramolecular. The results of the NMR studies on the cyclophanes can be extrapolated to serve as qualitative guidance for interpreting the NMR data of **5**. The relatively small Δδ of 0.3 ppm suggests that, in **5**, the edge to face conformation is not highly populated.

The floppy linkers in the cyclophanes permitted edge-to-face interactions in solution in some of the compounds, as evidenced by ^{1}H NMR data. However, the presence of such interactions in the crystal structure did not mandate their presence in solution. The compounds exhibiting edge-to-face interactions in the crystal (**10** and **12)** were actually shown to have a lower population of the edge-to-face conformation in solution than the cyclophane (**11)** that did not show this interaction in the crystal.

1.2.3 Intramolecular Hydrogen-Arene Interactions

In order to study intramolecular interactions between adjacent aryl groups, Pascal and coworkers investigated the degree of end-to-end twisting in a series of fused aromatics in which hydrogen atoms and arenes were in close proximity.[17] Initially, they synthesized **18** and **19**, and observed an end-to-end twist of 60.8° and 69.7°, respectively.[18] This result raised the question of a possible substituent effect that governed the extent of twisting of the two attached phenanthrene moieties.

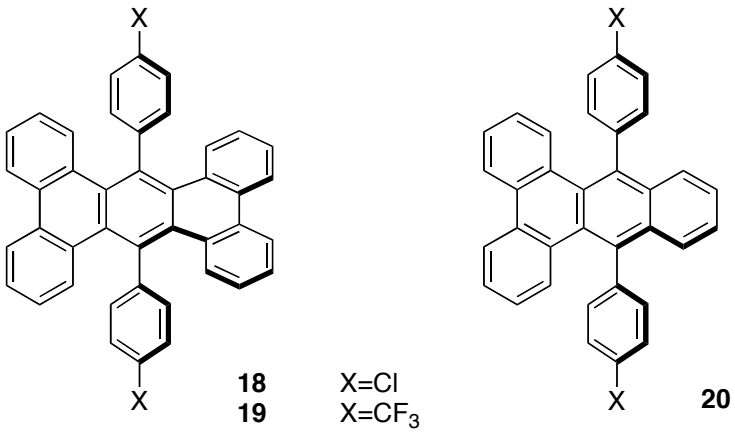

18 X=Cl
19 X=CF_3

20

Two possible modes of action were envisioned. The first was that twisting was determined exclusively by the repulsion of electron clouds, meaning electron donating groups would increase the repulsion and result in greater twisting, and electron withdrawing groups would reduce the repulsion and lead to less twisting. There is also the possibility that a favorable edge-to-face interaction determines the extent of twisting. In this case, the substituent effect discussed above would be reversed. Electron donating groups would make the edge-to-face interaction more favorable, thereby reducing the twisting in the molecule.

In order to investigate these possibilities, the more synthetically accessible **20** was prepared. Compound **20** was found to be a crystalline solid and its x-ray structure was determined (Figure 1.11).

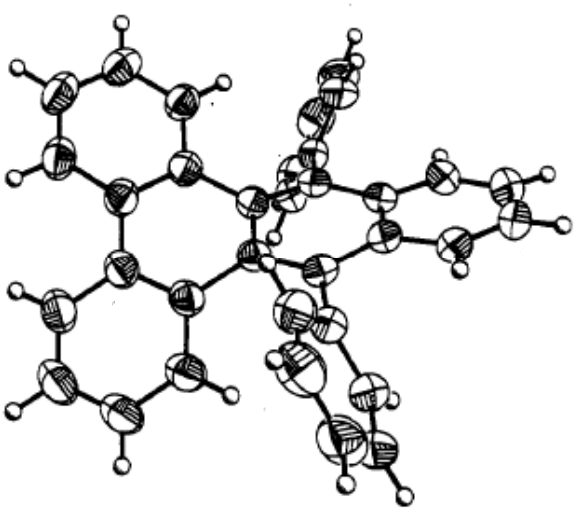

Figure 1.11 Crystal structure of **20**, with end-to-end twisting of 40.4°

The end-to-end twisting in **20** was found to be 40.4°. Basic molecular mechanics calculations [MM2(85)][19] predicted an end-to-end twist of 42.2° in the gas phase, providing relatively good agreement with the solid state value. A series of derivatives of **20** was synthesized to determine the significance of substituent effects.

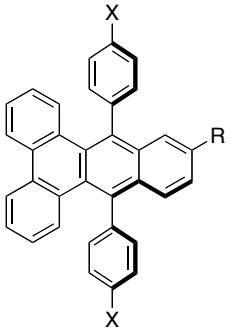

20	X=H, R=H
21	X=NO_2, R=H
22	X=OMe, R=H
23	X=SMe, R=H
24	X=Cl, R=H
25	X=Br, R=H
26	X=CF_3, R=H
27	X=CN, R=H
28	X=Me, R=H
29	X=NO_2, R=Me

Compared to the rest of the series, the crystal structure of **21** indicated an unusual bending of the phenanthrene core, whereas **22-28** were all structurally very similar to **20**. In order to investigate the unique crystal structure of **21** further, an extra methyl group was added in **29** to ensure different crystal packing. The crystal structure of **29** was then found to be similar to that of **22-28**, leading to the conclusion that the unique structure of **21** was the result of packing forces as opposed to an intramolecular interaction.

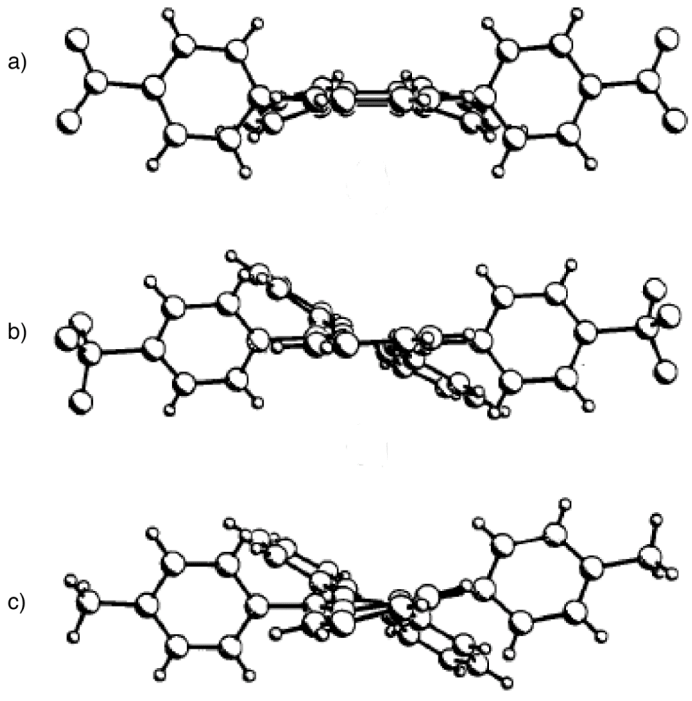

Figure 1.12 X-ray structures of **21**, **26**, and **28**. Views are looking down the long axis of the triphenylene core.

Across the series, the smallest end-to-end twist is seen in **26** (33.0˚), whereas the largest twist is 43.1˚, found in **28**. In **26** and **29**, there are two crystallographically independent molecules in the unit cell, which lead to two twisting values for each compound. The difference in the twists of the two independent molecules of **26** is 3.3˚. The difference in twisting in **29** is 7.0˚. These results suggest a significant role is played by crystal packing in determining the extent of twisting.

In the original compounds **18** and **19**, the difference in twisting between the two structures is 9˚. In light of the results for **26** and **29**, it is very possible that packing effects alone could account for this variation. There was no statistically significant correlation of the data with common Hammett parameters or with the estimated dipoles of the substituted phenyl groups. The mean twisting value for the series was 38.3˚. Four of the five compounds with twist angles less than this bear electron withdrawing substituents.

Pascal and coworkers concluded that packing forces were dominant over substituent effects in this series of compounds; but they tentatively concluded that electron withdrawing groups led to a smaller twist angle. They made no conclusion about the relative significance of electron repulsion as opposed to favorable edge-to-face interactions, as most of these observations are attributed to packing effects.

1.2.4 Aromatic Interactions in Proteins

The possibility of favorable interactions between aryl groups in close proximity has also been investigated in biomolecules. The work of Petsko and Burley focused on polar-π interactions between aromatic sidechains in proteins.[20,21] These sidechains, phenylalanine, tyrosine and tryptophan, are normally located in the hydrophobic core of the protein.

High resolution crystal structures of 33 proteins (< 2 Å) were examined to identify favorable edge-to-face polar-π interactions between aromatic sidechains. The crystal structures were searched for sidechains with a separation between ring centroids of less than 10 Å, using a polar coordinate system (Figure 1.13). This search led to 580 pairs of aromatic sidechains, 225 of which had centroid separations between 3.4 and 6.5 Å.

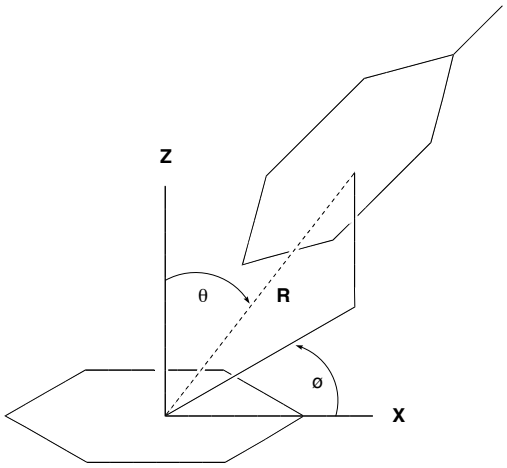

Figure 1.13 Coordinate axes for the reference aromatic sidechain, and the definition of the polar coordinate system (R,θ,ϕ)

A rigorous statistical analysis of the data showed that the frequency distribution differed significantly from a purely random distribution, indicating that aromatic sidechains preferentially form pairs with centroid-centroid distances between 3.4 and 6.5 Å. The non-bonded interaction energy for each of these pairs was determined by ab initio calculations, using a method formulated by Karlstrom and coworkers in similar work with dibenzene.[22] In practice, the calculation compares the difference between the interaction energy of the observed alignment with that of an identically positioned pair of alanine residues. From the 225 pairs, 84% were found to have favorable interaction energies, while the remaining 16% did not. The unfavorable energies may be attributed to poorly resolved portions of the crystal

structure or locally unfavorable side chain packing offset by favorable packing elsewhere. The histograms in figure 1.14 indicate the pertinent parameters for these interactions.

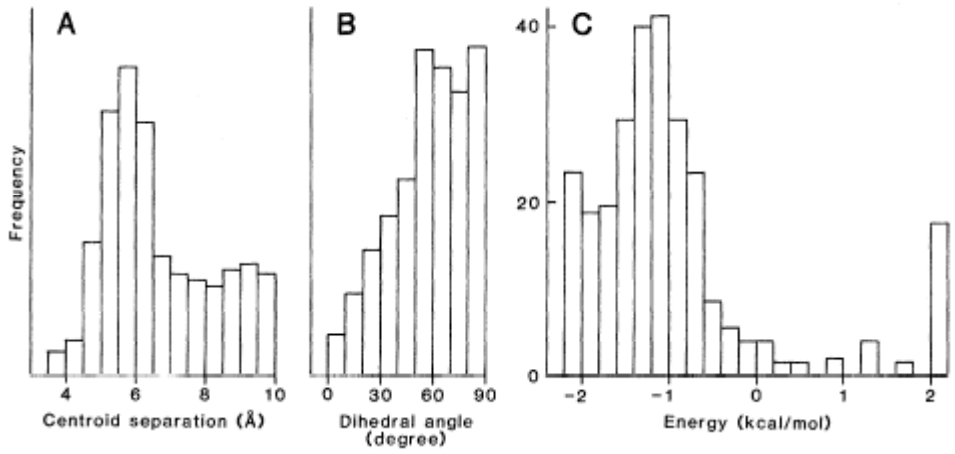

Figure 1.14 Histograms of (A) the centroid separation, (B) the dihedral angle between rings, and (C) the energy of interaction.[20]

The mean phenyl ring centroid separation was 5.05 angstoms and the mean dihedral angle was found to be 77°, which supports an edge-to-face interaction. The mean interaction energy was 1.28 kcal/mol. All of these values are in accordance with the values for crystalline benzene.

On average, there are 7 favorable edge-to-face aromatic-aromatic interactions per protein, and each interaction provides between 1 and 2 kcal/mol of stabilization relative to the alanine-alanine case, which leads to a substantial overall contribution in each protein. The naturally occurring edge-to-face interactions in the protein crystal structures led Petsko and Burley to conclude that these types of interactions are essential in proteins, and, although relatively small in magnitude, may collectively serve a critical role in protein folding and stabilization of tertiary structure.

1.3 Intermolecular Arene-Arene Interactions

1.3.1 Aromatic Interactions and Molecular Recognition

In light of the importance of intramolecular aromatic interactions, the role of these interactions in intermolecular molecular recognition processes was also investigated. There are examples of biological recognition processes with both face-to-face[20] and edge-to-face aromatic interactions.[23] The work of Hamilton and coworkers examined protein recognition of nucleotide bases and the role of aromatic interactions in such recognition processes.[24] In this study, artificial thymine receptors were designed based on a two-site binding strategy. The receptor is capable of both hydrogen bonding and π-π stacking. The goal of the work, starting from **30**, was to investigate the effect of modulating the electron density of the naphthalene ring by changing the substituents.

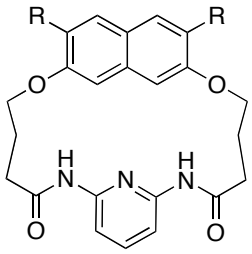

30 R=H

31 R=$CO_2(CH_2)_2CH_3$

32 R=$O(CH_2)_3CH_3$

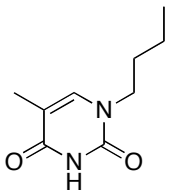

33

Whereas **31** contains electron withdrawing ester groups, **32** contains electron donating ether units. A strong complex is formed between **31** and **33** (K_s = 570 M^{-1}) in $CDCl_3$. The upfield shifts in the ^1H NMR of the thymine CH and CH_3 groups on thymine are consistent with a face-to-face stacking of the naphthalene ring and thymine in solution. The solid state structure was determined by X-ray crystallography, and displayed a face-to-face geometry (Figure 1.15).

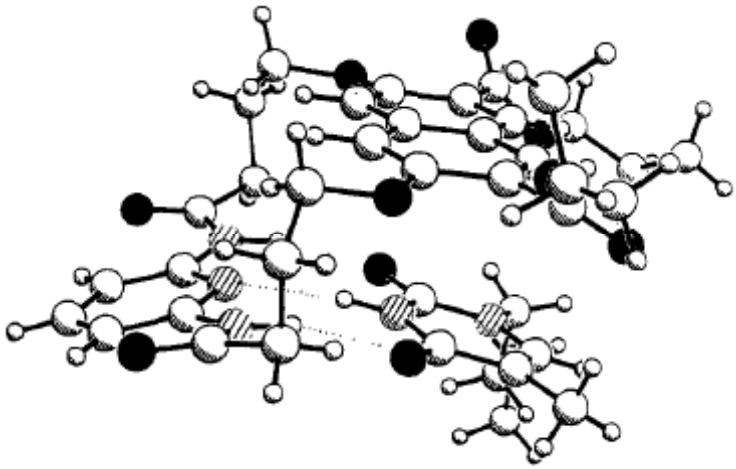

Figure 1.15 Crystal structure of **31**:**33** complex

The crystal structure shows a π-π stacking distance of 3.54 Å between the two rings. Hamilton and coworkers also conducted MNDO[25] calculations, which indicate a precise alignment of 5 pairs of oppositely charged atoms in the face-to-face arrangement. The complementary electrostatic interactions in the parallel stacked geometry provide the stabilizing force which leads to this arrangement of the complex.

A complex was also formed between **32** and **33**, but with weaker binding (138 M^{-1}). In this case, there are no upfield shifts of the thymine CH or CH_3 groups, which were previously observed in the face-to-face complex. However, an upfield shift of the naphthalene 1,8 hydrogens suggests that these protons are in closer proximity to the thymine than the other protons on the naphthalene ring. The crystal structure for this complex shows an angle of 77˚ between the planes of the naphthalene and thymine rings (Figure 1.16). The weaker binding compared to the **31:33** complex and the nearly perpendicular alignment of the rings are both consistent with an edge-to-face interaction in the **32:33** complex.

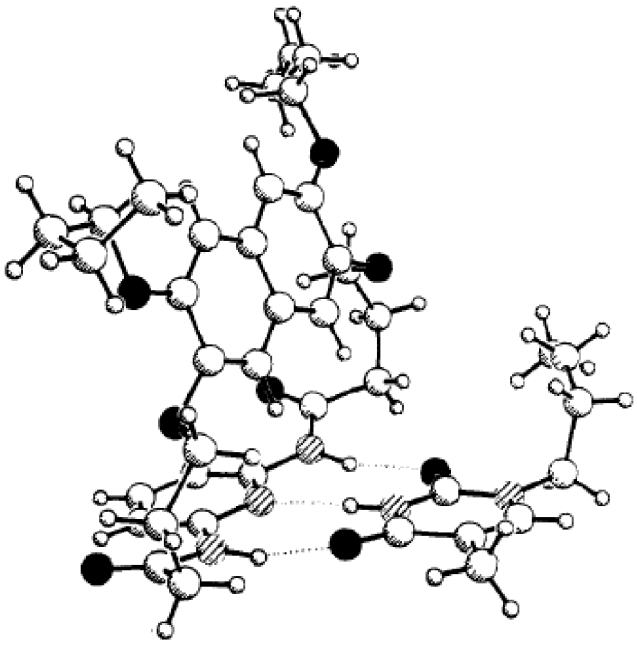

Figure 1.16 Crystal structure of **32**:**33** complex

The work of Hamilton and coworkers demonstrates the role of aromatic interactions in molecular recognition processes. Tuning of the electron density of the naphthalene ring at least partially determined the geometry of the complex by favoring either a face-to-face or edge-to-face interaction. However, one should also consider the geometric implications of changing the substituents on the host on the naphthalene, as the drastic geometry change may not only be a reflection of favorable electronic interactions.

1.3.2 Polar-π Interactions in Host:Guest Complexes

The ability to control molecular recognition processes between small molecules with polar-π interactions was transferred to the formation of host:guest complexes between small aromatic molecules and large cyclophanes. The work of Diederich involved the investigation of inclusion complexation of small aromatics by water soluble cyclophanes.[26] The guests consisted of 2,6-disubstituted napthalenes

and 1,4-disubstituted benzenes, with both electron withdrawing and donating groups. The primary attractive forces responsible for the binding are edge-to-face interactions and π-π stacking.

The goal of Diederich's work was to investigate the parameters affecting binding by ^{1}H NMR studies. The parameters investigated were 1) the electronic properties of the guest, 2) the polarity of the solvent and 3) the nature of the cyclophane host. The cyclophanes used for these studies consist of two sets of three rings connected by ether linkages of varying lengths. A total of five cyclophanes, **34**-**38**, were prepared for use in this study.

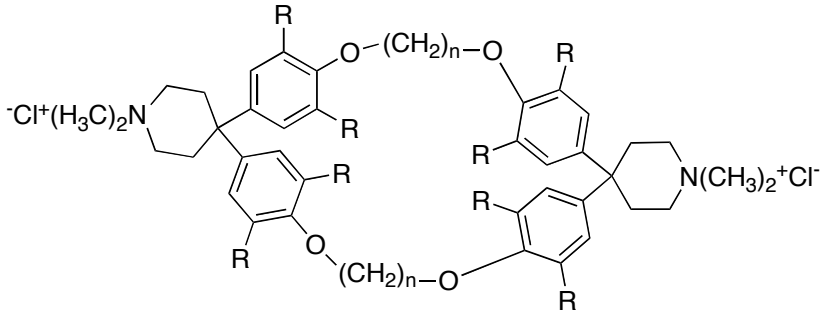

	n	R
34	3	H
35	3	OCH_3
36	4	H
37	4	CH_3
38	4	OCH_3

As seen in the crystal structure of **35**, the macrocycle adopts a rectangular geometry with the four electron rich aromatic rings as the walls. The guests are presumed to prefer the complexation geometry depicted in A over that of B (Figure 1.17), based on upfield shifts in ^{1}H NMR spectra consistent with these types of orientations.

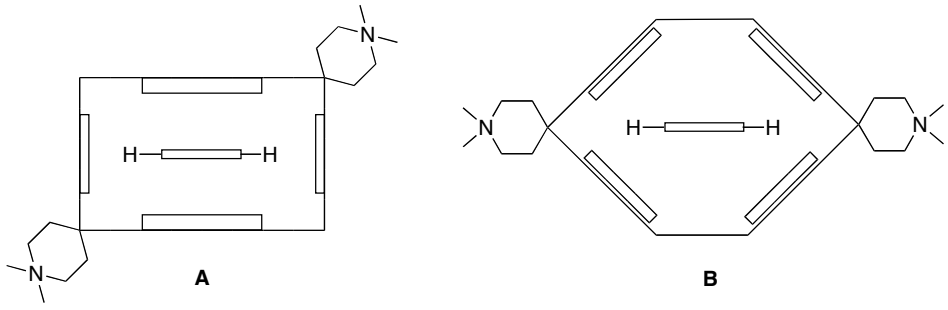

Figure 1.17 Possible guest orientations within the rectangular cyclophane cavity.

Diederich proposed that π-π stacking and edge-to-face interactions should become more energetically favorable with increasing electron affinity of the guest.[26] Based on previous examples, it is reasonable to anticipate that edge-to-face interactions should become more favorable with increasing polarization of the C—H bonds.

In addition to the properties of the guest molecules, the effects of slight variations in the host cyclophane were also investigated. It was determined that both methyl and methoxy substituents ortho to the ether bridges deepen the cyclophane cavity, with **38** slightly deeper than **37**, and **37** significantly deeper than **36**. Also, the torsional angles about the C-O bonds in **36** are close to 0°. Conversely, these angles approach 90° for **37** and **38**. The binding studies were done in a 60:40 mixture of D_2O and CD_3OD, in which aggregation of the macrocycles does not occur. The order of binding strength follows **37** > **38** > **36**, suggesting that cavity depth is not the only factor that determines binding strength. Diederich and coworkers proposed that hydrogen bonding with the methoxy group in **38** may lead to favorable solvation of the more polar portions of the cavity, which would then reduce the solvophobic driving forces for apolar binding. In comparison, **37** would have more apolar character, leading to stronger binding, which is the observed result.

If solvophobicity is the major driving force for complex formation, then the strength of complexation should decrease relative to the solubility of the guest. However, donor/acceptor arguments rather than solvophobicity rationalize the majority of the results when the guests are 2,6-disubstituted napthalenes. As the cyclophane is electron rich, one would anticipate the strongest binding with napthalenes bearing electron withdrawing groups. This is indeed the case, as guests

with two withdrawing groups bind more strongly than guests bearing two donating groups. Guests with one donor and one acceptor have binding constants between these two extremes. The largest binding energy difference between a donor/donor and acceptor/acceptor naphthalene is 1.6 kcal/mol. A Hammett plot indicates good correlation for guest binding with **37** (Figure 1.18).[26]

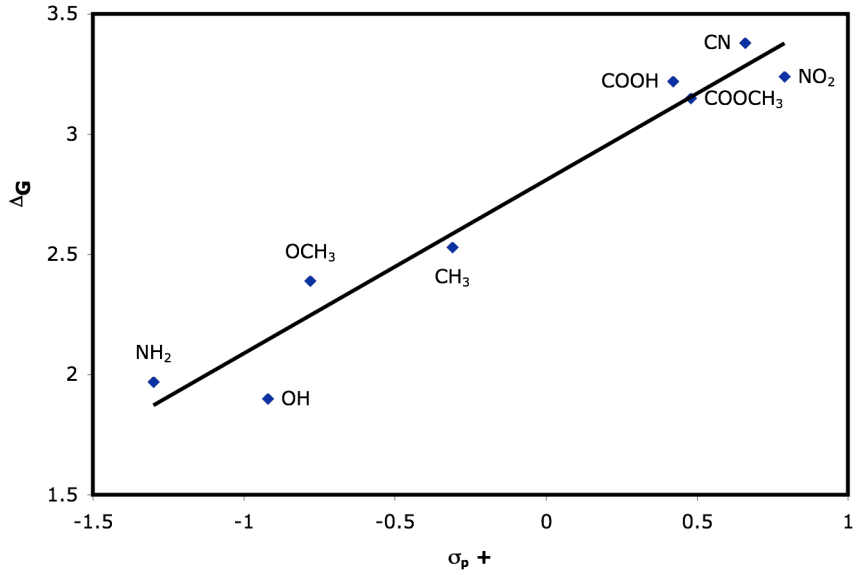

Figure 1.18 Linear free energy relationship correlating the free energy of complexation between **37** and donor-donor and acceptor-acceptor substituted napthalenes with the Hammett parameter of their substituents.[26]

In terms of binding energy as a function of guest solubility of the disubstituted napthalenes, there is not an obvious trend. Of the donor/acceptor guests, the best binder is also the most soluble. In contrast, the most soluble acceptor/acceptor is the poorest binder in that subclass.

Diederich predicted that solvation effects should increase with 1,4-disubstituted benzenes relative to the napthalenes because the smaller guests will not be able to reach as far out of the host cavity into solution. An initial binding comparison study of **35** and **38** demonstrated that both formed stable complexes with 1,4-disubstituted benzenes in D_2O; however the larger **38** formed more stable

complexes than **35**. There was no correlation between the magnitude of the association constant and the electronic character of the benzene substituents. When the trials were repeated with **34** as the host, the donor-acceptor trend was followed once again. Based on NMR analysis, the guests in **34** bind in the A fashion (Figure 1.17), whereas the guests in **35** and **38** bind as depicted in B.

The importance of donor/acceptor interactions increased for **35** and **38** with increasing CD_3OD added to D_2O. The binding by **36** and **37** of acceptor-acceptor guests became significantly better than the binding of donor-donor guests when more CD_3OD was added. The percentage of methanol added to water was varied across a fairly wide range, and this demonstrated a linear correlation of free energy of complexation and the solvent polarity term $E_T(30)$ (Figure 1.19).[27]

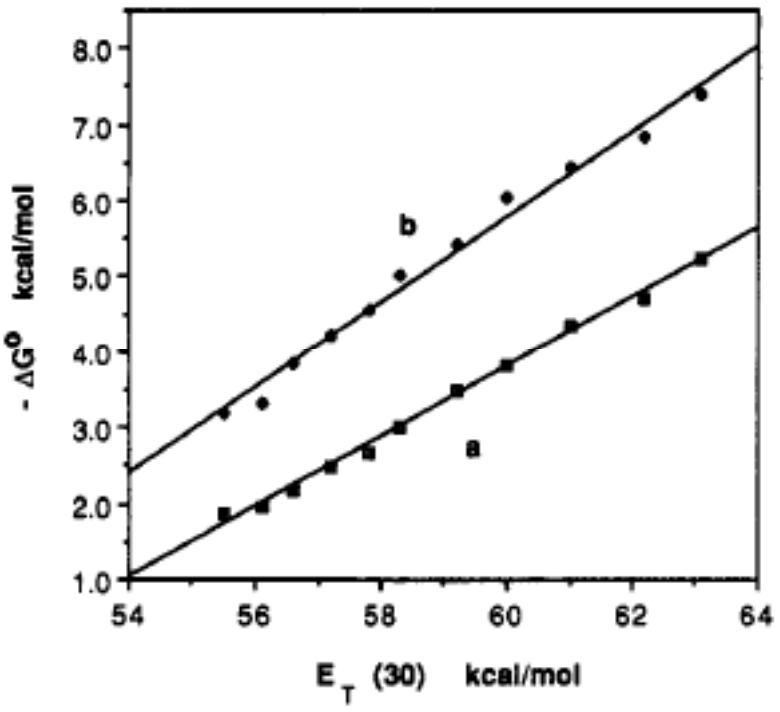

Figure 1.19 Linear free energy relationship between $E_T(30)$ and the free energies of complex formation with benzodinitrile (a) and 1,4-dimethoxy benzene (b). Curve b is displaced 2 kcal/mol for clarity.[26]

Diederich concluded that host:guest binding events are very complicated and a wide array of parameters must be considered. In his systems, binding was increased

with a deeper host cavity, provided that the substituents added to the host did not interfere with the apolar character of the binding pocket. The addition of methanol also increased the binding strength. Given the significant role of each of the various parameters, cavity size and depth, donor/acceptor interactions, and solvent polarity must all be considered. However, ultimately the authors conclude that the primary force for these molecular recognition processes is the electrostatic interactions between aromatic rings.[26]

1.4 Anion-π and Cation-π Interactions

1.4.1 2,6-Diarylbenzoic acids

In light of the previously demonstrated significance of through space interactions between arenes, Chen and Siegel investigated the ability of polar-π interactions to modulate the properties of a carboxylic acid.[28] A series of 2,6-diaryl benzoic acids was synthesized by the Hart reaction[29] with a CO_2 quench. The goal with this series of compounds was to maximize the polar-π effect by both symmetry and proximity. In addition, solvent interactions with the carboxyl group should be prevented by the steric bulk of the two flanking rings.

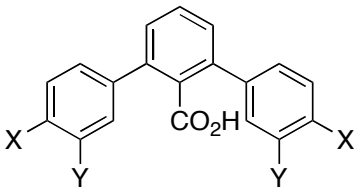

	X	Y
39	OMe	H
40	Me	H
41	H	H
42	F	H
43	Cl	H
44	Br	H
45	C(O)Me	H
46	H	OMe
47	H	C(O)Me

Once the series of meta and para substituted diaryl benzoic acids was prepared, the extent of the arene-acid interaction could be monitored by evaluating the pK_a values of the different acids. The goal was to determine the effects of electron withdrawing and donating groups on the measured value. The pK_a values were determined by titration using a potentiometric microtitration apparatus.[30]

Table 1.4 Hammett parameters and pK_a values for acids **39-47**

Compound	Substituent	σ	pK_a	K_b (M^{-1})
39	*p*-OMe	-0.28	6.61	830
40	*p*-Me	-0.14	6.50	
41	H	0.00	6.39	
42	*p*-F	0.15	6.14	
43	*p*-Cl	0.24	5.97	
44	*p*-Br	0.26	5.98	1560
45	*p*-C(O)Me	0.47	5.87	1930
46	*m*-OMe	0.10	6.61	
47	*m*-C(O)Me	0.36	5.87	

For the series of acids with para-substituted flanking groups, there was strong correlation between the pK_a and the Hammett parameter. The compounds with flanking rings bearing electron withdrawing groups were found to be more acidic than those bearing electron donating groups. A possible explanation for an interaction of this type could be conjugation. However, in this particular series, conjugation is conformationally prohibited, and the results are most consistent with a polar-π effect. In addition, the meta substituted and para substituted acids had the same pK_a values, which suggests a through space interaction. In the Hammett plot, the meta substituted compounds only fit to the line when plotted with the corresponding σ_{para} value.

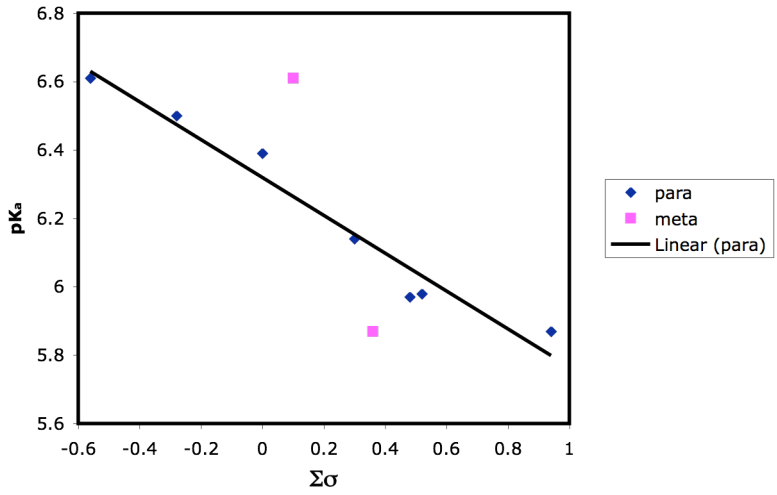

Figure 1.20 Plot of Σσ vs. pK_a for acids **39**-**47**

When there are withdrawing groups on the flanking rings, the acidity increases because the system is more capable of accommodating a negative charge. Conversely, when the flanking rings contain electron donating groups, there is not a favorable interaction to stabilize the anion.

Binding studies between acids **39**, **44**, and **45** with 9-ethyladenine were also conducted by Chen and Siegel. They found that binding constants increased with increasing electron withdrawing character of the substituents. In addition, the binding constant of **39** with 9-ethyladenine is three times larger than that of 2-aryl benzoic acid, even though their pK_a values are nearly equivalent. This result suggests that binding is determined by more than just hydrogen bonding. NMR analysis of the complexes shows a downfield shift of the 9-ethyladenine amino protons, consistent with participation in hydrogen bonding. In addition, the ortho aryl protons and H-2 and H-8 on the adenine are shifted downfield, indicating that the adenine is between and close to the flanking rings (Figure 1.21).

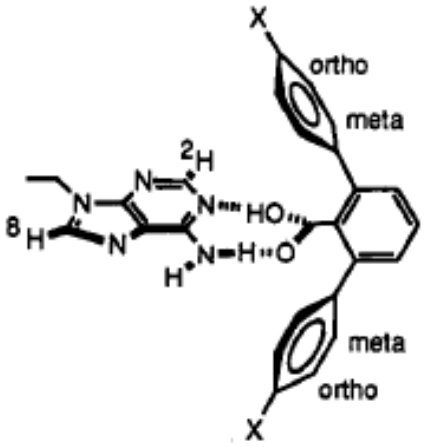

Figure 1.21 Proposed geometry of the complex between diarylbenzoic acid and 9-ethyladenine.[28]

The fact that the interaction energy varies with the substituent on the aryl group clearly points to an aryl-heterocycle interaction as the most reasonable explanation. Both studies done on this series of compounds demonstrate the significance of through space effects in molecular recognition. The changes in the acidity of the compounds provide a useful probe in understanding the extent of these anion-π interactions.

1.4.2 Terphenyl Pyridines

The work of Chen and Siegel demonstrated the ability of anion-π effects to modulate the properties of the carboxyl functional group. In related work, Woods and Siegel investigated the possibility of a similar cation-π behavior with the pyridyl functionality.[31] In this case, rather than stabilizing a negative charge, the ability of the system to accommodate a positive charge was examined. Once again, electron withdrawing or donating groups were used to modulate the electron density in the system. The substituents on the flanking rings were only introduced in the 4 position to avoid any steric effects. In addition, the connectivity of the pyridine to the

terphenyl core was varied, leading to a series of 12 terphenyl pyridines. The compounds were synthesized by the Hart reaction with an iodine quench. Subsequent boronic acid formation and Suzuki coupling[32] led to the desired products.

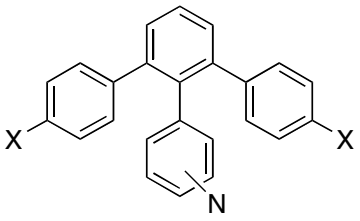

Pyridine Connectivity			
2'	3'	4'	X
48a	**49a**	**50a**	OMe
48b	**49b**	**50b**	Me
48c	**49c**	**50c**	H
48d	**49d**	**50d**	COMe

As a control experiment, the aryl groups were also replaced by alkyl groups or no substituent at all. The local steric bulk of an isopropyl group is approximately equal to that of an aryl substituent, providing a useful comparison to determine the extent of the cation-π effect.

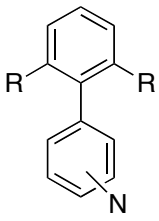

Pyridine Connectivity			
2'	3'	4'	R
51a	**52a**	**53a**	i-Pr
51b	**52b**	**53b**	Me
51c	**52c**	**53c**	H

The pK_a values of the various pyridines were determined by NMR titration.[33,34] Woods and Siegel report three major trends in the results. First, in moving from electron withdrawing groups to electron donating groups, the pK_a increases with good correlation to a linear Hammett relationship. In addition, the overall magnitude of the cation-π effect decreases going from the 2' to 3' to 4' pyridines. The change in substituents has a less profound effect on the pK_a in the 4' and 3' pyridines relative to the 2'. Further, the alkyl pK_a values are of similar order to the terphenyl pyridines. The results suggest that there is an interaction between the substituents and pyridine. It is reasonable that electron donating groups favor the formation of a positive charge

on pyridine. The fact that the magnitude of the effect decreases in going from 2' to 3' to 4' is also logical because the distance from the flanking groups is increased. However, as the arene interaction decreases, solvent interactions become more prevalent because the pyridine is less sterically protected. The 4' series is indeed more basic than either the 3' or 2', suggesting that solvent effects outweigh the cation-π interaction.

Table 1.5 pK_a values for terphenyl pyridines **48-53**

Substituent	2' series		3' series		4' series	
Aryl						
OMe	**48a**	3.10	**49a**	3.05	**50a**	3.47
Me	**48b**	3.03	**49b**	3.01	**50b**	3.42
H	**48c**	2.88	**49c**	2.94	**50c**	3.34
COMe	**48d**	2.30	**49d**	2.63	**50d**	3.07
Alkyl						
I-Pr	**51a**	2.90	**52a**	2.78	**53a**	3.18
Me	**51b**	3.03	**52b**	2.97	**53b**	3.29
H	**51c**	2.14	**52c**	2.94	**53c**	3.47

In the case of the 2' pyridines, only the two electron rich arenes, **48a** and **48b**, had a higher pK_a than the isopropyl derivative, suggesting that strong electron donation from the arene is required to provide greater stabilization than the alkyl groups. The energetic difference between **48a** and **51a** leads to an overall stabilization of 0.27 kcal/mol, which translates to about 0.14 kcal/mol per arene.

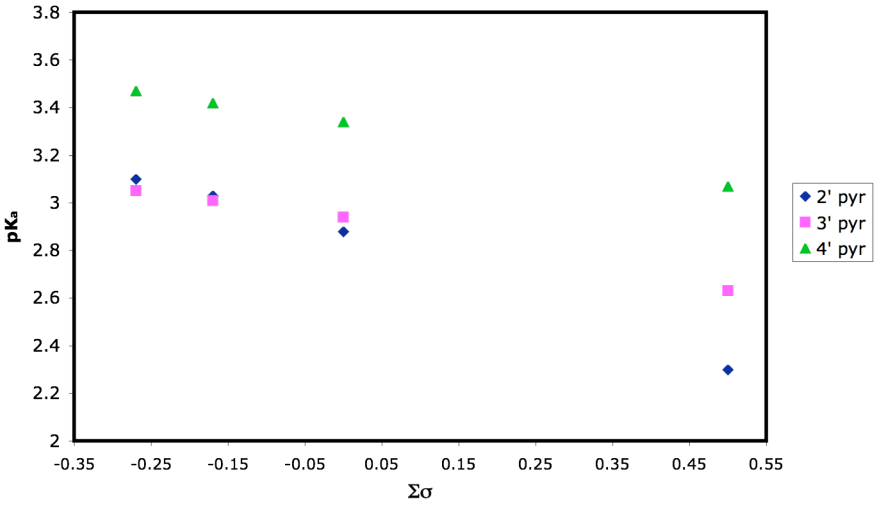

Figure 1.22 Plot of pK_a vs. Hammet parameter for terphenyl pyridines

The terphenyl core provided a useful framework to observe through space arene interactions and their influence on the properties of other adjacent functional groups. However, the magnitude of the cation-π effect in this system is slightly less than other reported values.[35] The relative importance of the solvent interactions makes the data somewhat difficult to interpret, but the cation-π effect seems to be quite small for this system.

1.5 Quantifying Polar-π Interactions

1.5.1 Double Mutant Cycle to Evaluate Polar-π Interactions

Whereas Siegel and coworkers were able to quantify cation-π and anion-π interactions by observing the pK_a value of the relevant acidic site, Hunter determined the magnitude of intermolecular edge-to-face polar-π interactions by observing a series of binding constants.[36] His unique approach to this problem was to utilize a chemical double-mutant cycle, a method adapted from a technique frequently used to quantify side-chain interactions in proteins.[37] The molecules of choice for this study

were hydrogen bonded molecular zipper complexes. The thermodynamic cycle used to quantify the interaction relied on the determination of free energies of association for four different complexes (Figure 1.23).[36]

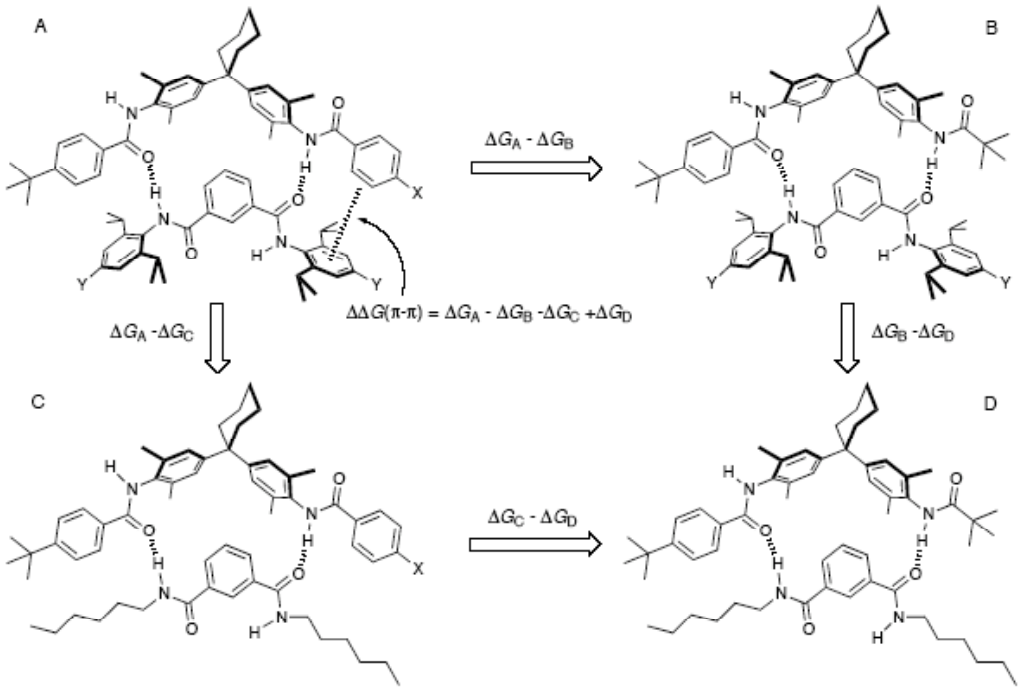

Figure 1.23 Double-mutant cycle for quantifying edge-to-face interactions.[36]

In the thermodynamic cycle, aromatic rings are converted to tert-butyl groups in order to remove the aromatic interaction of interest (A to B, Figure 1.24). However, when one performs this conversion, secondary interactions between the aromatic ring and the core of the complex are also lost. In addition, the change also affects the strength of the neighboring hydrogen bond. In order to account for this discrepancy, the same modification is carried out on C in order to account for the secondary interactions. As a result, by determining the binding constants and thus the free energy of association for all four complexes, the aromatic interaction of interest can be quantified. One may consider the step in the cycle from C to D as a correction

factor for the step from A to B. Hunter and coworkers used this method to perform a quantitative study of substituent effects. The relevant association constants were found by ^{1}H NMR titration.

One of the advantages of this particular method is that the two interacting groups are attached to a rigid framework, therefore a consistent interaction geometry is maintained. NOE and ROESY NMR experiments, as well as chemical shift changes upon complexation, suggest that all four complexes in each of the nine double mutant cycles adopt roughly the same conformation. For the three different substituents used in the cycle, the energetic values ranged from 1.2 kcal/mol repulsive to 4.6 kcal/mol attractive. One of the most interesting results is that when X is a dimethylamino group, varying the Y substituent does not have a significant influence on the energy. However, in the case where X = NO_2 or H, the attractive forces increase with increasing electron-donating character of Y.

Y	X = NO_2	X = H	X = NMe_2
NO_2	+1.2	-0.2	-1.4
H	-3.4	-1.4	-1.1
NMe_2	-4.6	-1.8	-0.9

The experimental results correlate well with Hammett substituent parameters. The exceptional fit of this equation suggests that these results can be extrapolated to determine the interaction energies between aryl groups with other substituents. The authors believe that their quantitative study provides critical information for understanding the role of aromatic interactions in molecular recognition events and will allow future work to take greater steps towards the goal of molecular design.

1.5.2 Quantifying Conformational Preference

Wilcox and coworkers investigated edge-to-face arene interactions in a model study for protein folding.[38] In this case, the interaction was quantified by observing conformational preference by NMR, as conformational isomerism was previously shown to be a sensitive probe for investigating weak molecular forces.[39] The series of esters prepared by Wilcox and coworkers, based on Tröger's base, possess two conformational states, one with an edge-to-face interaction (folded) and one without the interaction (unfolded).

Substituents on the flanking ester ring (b) were varied to observe the impact of substitution on conformational preference. Furthermore, a preliminary investigation, in which the aryl ester was replaced by a methyl ester, showed no conformational preference, indicating there were no significant long-range effects that may contribute to conformational preference and lead to false conclusions. In addition to the eight aryl esters, **54a-f** and **54i-k**, the cyclohexyl and tert-butyl esters, **54g** and **54h**, were also prepared.

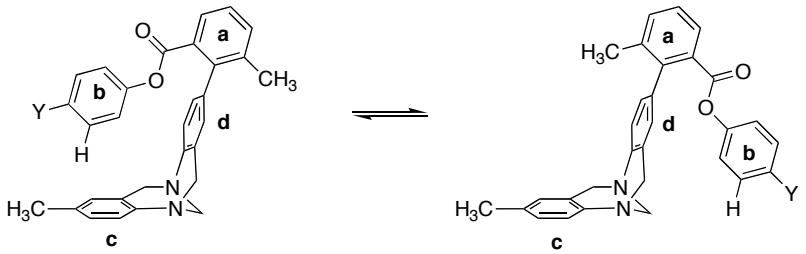

Entry	Y
54a	H
54b	CH3
54c	OCH3
54d	CN
54e	NO2
54f	I
54g	Cy-hex
54h	t-butyl
54i	m-CH3
54j	m-CN
54k	3,5-CH3

The rotational barrier for interconversion of the folded to unfolded conformers is 18 kcal/mol, making room temperature NMR measurements an effective tool in investigating conformational preference. As a result, direct NMR observation of the

populations of each state should demonstrate the significance of edge-to-face arene interactions. In addition, the folded and unfolded states are easily distinguishable, as the chemical shift of the hydrogen meta to the C-O bond is considerably upfield in the folded state, consistent with an edge-to-face geometry. X-ray structures also show the rings to be in close proximity, with an edge-to-face interaction (Figure 1.24). However, the crystal structures also indicate there may be steric interactions between the Y substituent and the methyl group on the c ring.

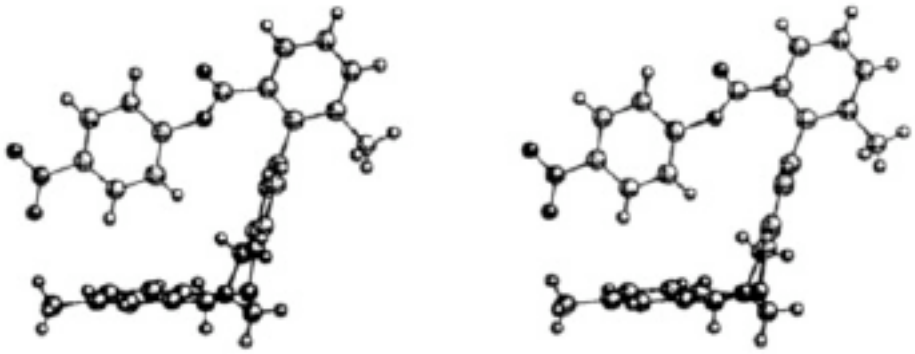

Figure 1.24 X-ray structure of **54e** (stereoview), indicating an edge-to-face interaction

NMR analysis of unsubstituted **54a** showed the folded conformer to be slightly favored over the unfolded in a ratio of 3:2, which corresponds to an energy difference of only 0.24 kcal/mol. The addition of a methyl group in **54b** led to a slight increase in the energy difference, However, preference for the folded conformer actually increased with electron-withdrawing groups. In addition, the cyclohexyl ester, **54g**, and the tert-butyl ester, **54h**, both have a stronger preference for the folded state than the phenyl ester does. A wide variety of solvents were also used for these studies, but the folded:unfolded ratio for the phenyl ester, **54a**, remained mostly unchanged.

Table 1.6 Barriers to Isomerization and Percent of folded isomer for **54**

Ester	% folded	ΔG	Ester	% folded	ΔG
54a	60	0.24	**54g**	65	0.37
54b	65	0.37	**54h**	80	0.82
54c	60	0.24	**54i**	50	0.00
54d	75	0.65	**54j**	60	0.24
54e	75	0.65	**54k**	35	0.37
54f	75	0.65			

The results did not appear to be consistent with the anticipated electrostatic trend for edge-to-face interactions. It was thus postulated that there may be ring stacking rather than an edge-to-face interaction in solution. If there was indeed an edge-to-face interaction, then adding a meta substituent would disfavor the folded conformer. The authors observed this result, and also found that adding a second meta substituent made the unfolded state even more favored.

The experiments conducted by Wilcox and coworkers demonstrated that a compound containing two easily discernible conformers does not have a significant preference for the conformer that permits edge-to-face arene interactions. Furthermore, the preference for the edge-to-face conformer is larger for tert-butyl and cyclohexyl substituents than for the simple phenyl substituent.

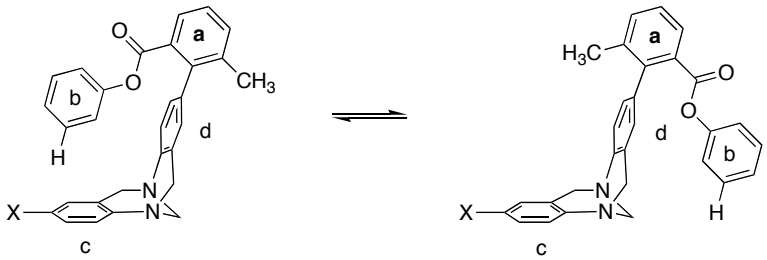

Figure 1.25 Investigating the effects of changing the bottom ring substituent on conformational preference

Wilcox and coworkers revisited this chemistry, this time modifying the substituents on the other ring (c) involved in the proposed edge-to-face interaction (Figure 1.25).[40] In addition to varying this substituent, folding energies were compared for phenyl, methyl, and isopropyl esters as the flanking groups.[41] With the methyl esters, there was little preference for either state, regardless of the substituent. The folding energy for the isopropyl esters were all found to be approximately 0.5 kcal/mol, whereas the energy for the phenyl esters were all near 0.3 kcal/mol. This observation shows that there is basically no significant substituent effect for any of these compounds. However, once again steric interactions between the X substituent and the b ring should be considered.

Table 1.7. Folding energies for the three esters as X substituent is varied

Entry	X	ΔG methyl ester	ΔG isopropyl ester	ΔG phenyl ester
1	**NO2**	0.11	0.51	0.21
2	**CN**	0.06	0.64	0.30
3	**I**	-0.06	0.46	0.23
4	**Br**	0.02	0.54	0.26
5	**CH_3**	-0.04	0.44	0.27
6	**OH**	-0.03	0.47	0.23
7	**NH_2**	-0.06	0.34	0.18

The authors next fluorinated the bottom ring to create a strongly electron deficient system. However, even under these conditions, there was no profound effect on the folding energy of either the isopropyl or phenyl ester. Although there were no dramatic substituent effects and the energetic contribution of the edge-to-face interactions was small in magnitude, one of the most noteworthy results is that the isopropyl ester had a stronger preference for the folded state than the phenyl ester, regardless of the substituent. In terms of through-space interactions between groups in close proximity, particularly with regard to protein folding, these results suggest that one should consider aryl-alkyl interactions as well as aryl-aryl interactions.

1.6 Conclusions

Aromatic interactions are present in a wide array of systems and their energetic contributions vary slightly between systems. The crystal packing of benzene provided a fundamental example of edge-to-face polar-π interactions and the stacking motif in benzene:hexafluorobenzene was at least partially determined by the preferential arrangement of quadrupole moments. Overall, attractive aromatic interactions are manifested in several systems, ranging from proteins to host:guest complexes. The interactions can be intermolecular or intramolecular, and often play a critical role in molecular recognition events.

Some of the work cited attempted only to demonstrate the presence of polar-π interactions, whereas others strived to quantify this interaction energy. The terphenyl systems used by Siegel and coworkers provided a constrained environment with the appropriate geometry to induce edge-to-face interactions, and determination of the pK_a values of the relevant sites shed light on the energetic significance of these interactions. The double mutant method developed by Hunter and coworkers provided a direct quantification of the edge-to-face interaction by taking advantage of a thermodynamic cycle. Wilcox and coworkers selected a two-state system in which the population of each state could be used to determine the polar-π interaction energy. The quantitative methods point to nearly the same result: edge-to-face polar-π interactions are worth at most 1-2 kcal/mol, close to the value calculated by Petsko and Burley for aromatic sidechains in proteins. Although a single interaction of this type is relatively insignificant, the collective contribution of several of these interactions in a single system may serve to stabilize a host:guest complex or define the three-dimensional structure of a protein.

REFERENCES:

1. Hobza P. ; Havlas, Z. *Chem. Rev*. **2000**, *100*, 4253.

2. Hunter, C.A.; Lawson, K.R.; Perkins, J.; Urch, C.J. *J. Chem. Soc., Perkin Trans. 2* **2001,** 651.

3. Cox, E.G.; Cruikshank, D.W.J.; Smith, J.C. *Proc. R. Soc. London* **1958,** *A247, 1.*

4. Lowden, L.J.; Chandler, D. *J. Chem. Phys.* **1974,** *61,* 5228.

5. Shi, X.; Bartell, L.S. *J. Phys. Chem.* **1988,** *92,* 5667.

6. Hobza, P.; Selze, H.L.; Schlag, E.W. *J. Am. Chem. Soc.* **1994,** *116, 3500.*

7. Janda, K.C.; Hemminger, J.C.; Winn, J.S.; Novick, S.E.; Harris, S.J.; Klemperer, W. *J. Chem. Phys.* **1975,** *63,* 1419.

8. Steed, J.M.; Dixon, T.A.; Klemperer, W. *J. Chem. Phys.* **1979,** *70,* 4940.

9. Patrick, C.R.; Prosser, G.S. *Nature* **1960,** 1021.

10. Dahl, T. *Acta Chem. Scan. Ser. A.* **1975,** *29,* 170.

11. Cozzi, F.; Siegel, J.S. *Pure & Appl. Chem.* **1995,** *67,* 683.

12. Cozzi, F.; Cinquini, M.; Annunziata, R.; Dwyer, T.; Siegel, J.S. *J. Am. Chem. Soc.* **1992,** *114,* 5729.

13. Cozzi, F.; Cinquini, M.; Annunziata, R.; Siegel, J.S. *J. Am. Chem. Soc*. **1993,** *115, 5330.*

14. Cozzi, F.; Ponzini, F.; Annunziata, R.; Cinquini, M.; Siegel, J.S. *Ang. Chem. Int. Ed. Engl.* **1995,** *34,* 1019.

15. Schladetzky, K.D.; Haque, T.S.; Gellman, S.H. *J. Org. Chem.* **1995,** *60,* 4108.

16. Newcomb, L.F.; Gellman, S.H. *J. Am. Chem. Soc*. **1994,** *116,* 4993.

17. L'Esperance, R.P.; Van Engen, D.; Dayal, R.; Pascal, R.A., Jr. *J. Org. Chem.* **1991,** *56,* 688.

18. Pascal, R.A., Jr.; McMillan, W.D.; Van Engen, D.; Eason, R.G. *J. Am. Chem. Soc*. **1987,** *109,* 4660.
19. Allinger, N.L. QCPE MM2(85) 1986.

20. Burley, S.K.; Petsko, G.A. *Science* **1985,** *229,* 23.

21. Burley, S.K.; Petsko, G.A. *J. Am. Chem. Soc*. **1986,** *108,* 7995.

22. Karlstroem, G.; Linse, P.; Wallqvist, A.; Jonsson, B. *J. Am. Chem. Soc.* **1983,** *105,* 3777.

23. Gould, R.O.; Gray, A.M.; Taylor, P.; Walkinshaw, M.D. *J. Am. Chem. Soc.* **1985,** *108,* 7995.

24. Muehldorf, A.V.; Van Engen, D.; Warner, J.C.; Hamilton, A.D. *J. Am. Chem. Soc.* **1988,** *110,* 6561.

25. Dewar, M.J.S.; Thiel, W. *J. Am. Chem. Soc.* **1977,** *99,* 4899.

26. Ferguson, S.B.; Sanford, E.M.; Seward, E.M.; Diederich, F. *J. Am. Chem. Soc.* **1991,** *113,* 5410.

27. Reichardt, C. *Solvents and Solvent Effects in Organic Chemistry,* 2nd ed.; VCH: Weinheim, 1988.

28. Chen, C.-T.; Siegel, J.S. *J. Am. Chem. Soc.* **1994,** *116,* 5959.

29. Du, C.-J.F.; Hart, H.; Ng, K.-K.D. *J. Org. Chem.* **1986,** *51,* 3162.

30. Simon, W.; Moerikofer, A.; Heilbronner, E. *Helv. Chim. Acta.* **1957,** *40,* 1918.

31. Woods, C.R. Ph.D. Thesis, University of California, San Diego, 1998.

32. Watanabe, T.; Miyaura, N.; Suzuki, A. *Synlett* **1992,** 207.

33. Perrin, C.L.; Fabian, M.A. *Analytical Chemistry* **1996,** *68,* 2127.

34. Perrin, C.L.; Fabian, M.A. *Analytical Chemistry* **1997,** *69,* 108.

35. Schneider, H.-J.; Schiestel, T.; Zimmermann, P. *J. Am. Chem. Soc.* **1992,** *114,* 7698.

36. Carver, F.J.; Hunter, C.A.; Seward, E.M. *Chem. Commun.* **1998,** 775.

37. Fersht, A.R.; Serrano, L. *Curr. Opin. Struct. Biol.* **1993,** *3,* 75.

38. Paliwal, S.; Geib, S.; Wilcox, C.S. *J. Am. Chem. Soc.* **1994,** *116,* 4497.

39. Eliel, E.L.; Allinger, N.L.; Angyal, S.J.; Morrison, G.A. *Conformational Analysis,* Interscience: New York, 1965.

40. Wilcox, C.S.; *Tetrahedon Lett.* **1985,** *53,* 98.

41. Kim, E.; Paliwal, S.; Wilcox, C.S. *J. Am. Chem. Soc.* **1998,** *120,* 11192.

2 MOLECULES IN MOTION

2.1 Overview

The primary focus of this chapter is the investigation of bond rotation in an array of molecules. Initially, classical examples in conformational analysis are discussed. Next, a series of more complicated systems are examined, in which the rotational barriers are tuned in various ways. The remaining examples follow the development of molecular machines that use controlled bond rotation, particularly in aryl alkynes. The field of molecular machines is still in its early stages, and consequently, the construction of useful molecular devices will require a strong foundation in the basic concepts of molecular motion.

2.1.1 Ethane Rotational Profile

The ethane molecule provides a classical case of bond rotation. The eclipsed conformation of ethane is 3 kcal/mol higher in energy than the staggered conformation.[1-3] The cause for this energy barrier can be rationalized in terms of hyperconjugation, as the staggered conformation provides a favorable interaction between the filled and empty orbitals (Figure 2.1).[4] Additionally, in this conformation, an unfavorable interaction between adjacent filled orbitals is avoided.

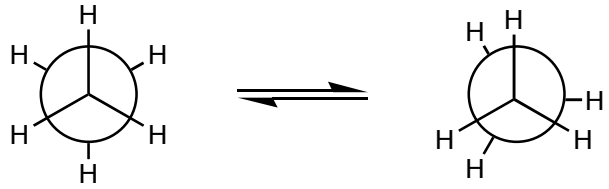

Figure 2.1 Newman projections of staggered and eclipsed conformations of ethane

2.1.2 Biphenyl Rotational Profile

Biphenyl, which has a rotational barrier of 2 kcal/mol,[5] is another fundamental example of conformational analysis. The molecule is planar in the crystalline state at room temperature, presumably due to packing effects as opposed to a geometric preference (Figure 2.2).[6] However, biphenyl is twisted in the gas phase, with a dihedral angle close to 45°.[7] This angle is a result of competition between the repulsion of the ortho hydrogens, which favors a perpendicular geometry, and the delocalization of π electrons, which is maximized in a planar structure.

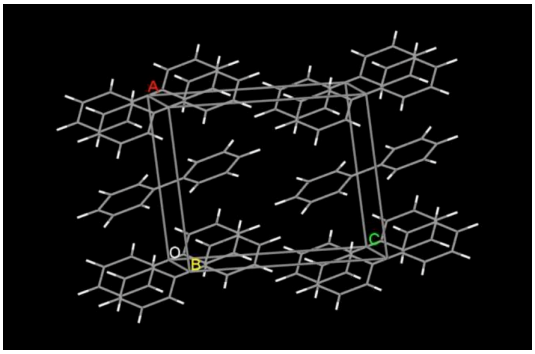

Figure 2.2 Crystal packing diagram of biphenyl.[6]

In calculations conducted by Grein, the optimized conformation of unsubstituted biphenyl has a dihedral angle of 46°.[8] This geometry is stabilized by 3 kcal/mol relative to the coplanar conformation and 1.5 kcal/mol relative to the perpendicular one. If one of the ortho hydrogens is replaced by a larger substituent, an increase in the dihedral angle relative to unsubstituted biphenyl is expected. If one ortho hydrogen on each ring is replaced by a larger substituent, a double minimum potential is anticipated, with syndiagonal and antidiagonal conformations (Figure 2.3). The antidiagonal geometry is lowest in energy because steric interactions are minimized and conjugation is partially maintained.

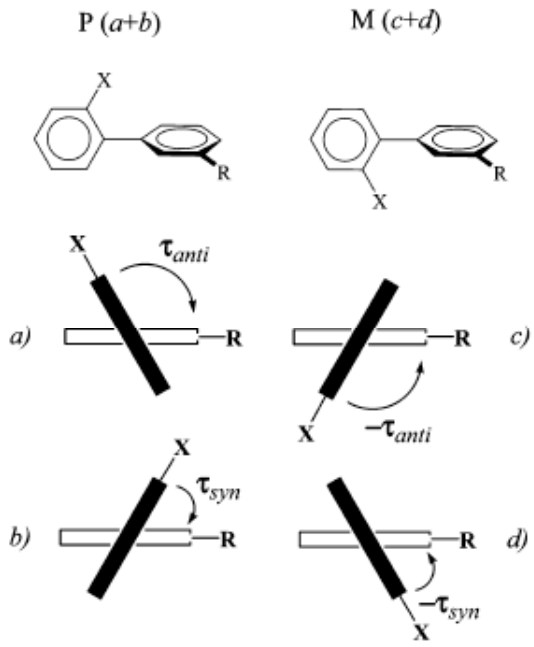

Figure 2.3 Syndiagonal and antidiagonal conformations of disubstituted biphenyls with both P and M helicity.

Several disubstituted biphenyls have been studied both experimentally and computationally. For example, according to the crystal structure, 2,2'-difluorobiphenyl has a dihedral angle of 57.6°.[9] This result is somewhat surprising because the angle is smaller than 90°, corresponding to a syndiagonal conformation. The value calculated by Grein (58°) is in close agreement with the crystal structure. This conformation is stabilized by 11 kcal/mol relative to the coplanar conformation with both fluorines on the same side. There is a significant decrease in the barrier when both fluorine substituents are in the meta position. In this case, the planar conformation is calculated to be only 2 kcal/mol higher in energy than the optimized geometry.

2.2 Rotation in Aryl Alkynes

2.2.1 Diphenylacetylene

In diphenylacetylene, also known as tolan, the space between adjacent rings is much larger than in biphenyl, and, as a result, interactions between substituents on the phenyl groups are considerably less significant. There are three primary possiblilities to consider in predicting the geometry of diphenylacetylene. First, the p orbitals of both phenyl rings could overlap with the same set of p orbitals in the alkyne, leading to a planar geometry. It is also possible that the molecule could act like two adjacent phenylacetylene units. In this case, the p orbitals of one phenyl ring would overlap with one set of p orbitals of the alkyne and the π system of the other ring interacts with the other p orbitals of the alkyne. This would favor a perpendicular geometry. A third possibility is that there is no strong preference for either geometry, leading to essentially free bond rotation.

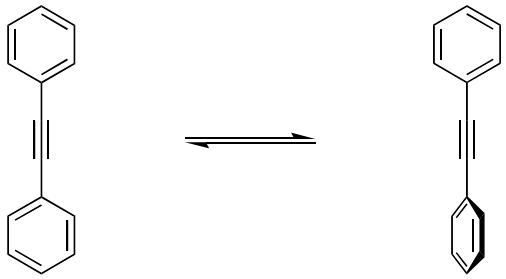

Figure 2.4 Rotational process in diphenylacetylene

Calculations using a wide range of methodologies were conducted by Liberles and Matlosz, who predicted barrier values between 0.4 and 0.7 kcal/mol, favoring the planar form.[10] This value is quite small, and can be interpreted as nearly free rotation. The crystal structure of tolan shows a planar structure with D_{2h} symmetry.[11] However, as in biphenyl, this may be the result of a packing effect rather than a reflection of the preferred geometry.

The absorbance spectra of diphenylacetylene were compared to the spectra of phenylacetylene as well as cis and trans-stilbene.[10] Tolan did not have absorbances in the same region as phenylacetylene, however there was significant peak overlap with the stilbenes. Tolan is therefore generally thought to be planar in solution because the UV spectrum more closely resembled stilbene rather than two independent phenylacetylene units. Subsequent calculations indicated a very small rotational barrier in tolan, only slightly favoring the planar species. The combination of the above results suggests there is basically free rotation in the molecule.

2.2.2 Sterically Congested Alkynes

Although tolan shows essentially no rotational barrier, the work of Toyota and coworkers looked to isolate rotational isomers of aryl alkynes by inducing steric interactions.[12-16] In their initial work, the rotational barriers of bis-triptycyl-ethynes were investigated. The threefold symmetry of triptycene makes this system similar to ethane, but more closely related to 2-butyne. Whereas the rotational barrier in ethane is 3 kcal/mol, the barrier in butyne is 0.01 kcal/mol.[17] The alkyne spacer increases the distance between the terminal methyls to 4 Å, effectively eliminating all steric interactions. Consequently, Toyota and coworkers determined that peri substituents would be necessary in order to induce a measurable barrier (Figure 2.5). Therefore, substituents were added in the 1 and 4 positions of each triptycene unit, leading to derivatives **1a-c** and **2a-d**.

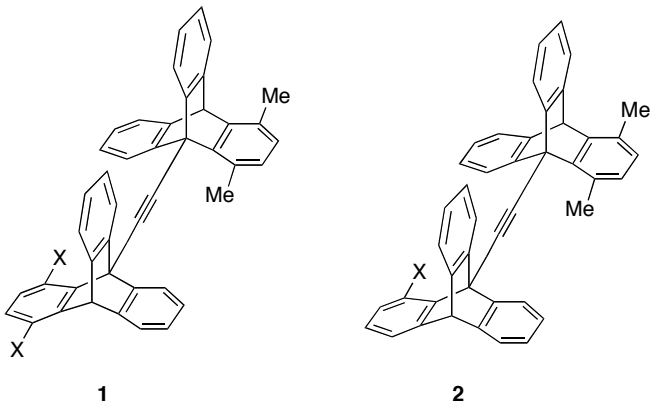

1 2

Figure 2.5 The introduction of peri substituents, indicated with X, were expected to lead to measurable rotational barriers for ditriptycyl ethynes.

Rotational barriers for a series of derivatives were measured using variable temperature NMR, and ranged from 9 to 17 kcal/mol, with good linear correlation between the barrier height and van der Waals radius of the substituent.[12]

Table 2.8 van der Waals radii and rotational barriers for **1a-c** and **2a-d**

Compound	X	Radius	Rotational Barrier
1a	H	1.20	10.1
1b	OMe	1.52	12.7
1c	Me	1.80	15.4
2a	F	1.47	11.6
2b	Cl	1.75	14.7
2c	Br	1.85	16.7
2d	I	1.98	17.3

In an effort to augment the barrier, the substituents were changed to different aryl and phenethynyl groups.[13] Whereas the barrier for a simple phenyl substituent was nearly equivalent to a methyl group at 15.7 kcal/mol, phenethynyl and napthethynyl substituents increased the barrier to 17.5 and 17.8 kcal/mol, respectively. A particularly noteworthy result is that when the X group was changed to mesityl, the barrier was found to be 18.8 kcal/mol. The authors state that the rigidity of the mesityl substituent relative to the ethynyl groups leads to the barrier

increase, suggesting that both steric bulk and flexibility must be considered when attempting to hinder rotation.

In the subsequent series, two terphenyl groups were connected by an ethyne linker.[14] In this case, tolyl groups were used as the flanking rings. Bromination produced **3**, the desired compound for variable temperature NMR spectroscopy.

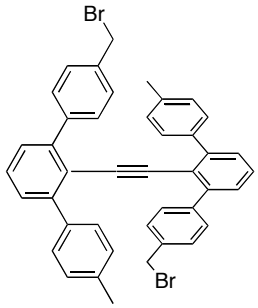

3

Unfortunately, it was not possible to determine the barrier for **3**. Throughout the investigated temperature range, the methylene group adjacent to bromine only showed a singlet, suggesting fast rotation about the triple bond and a barrier of less than 8 kcal/mol. This result is attributed to the flexibility of both the alkyne and the terphenyl system.

In ensuing work, the authors shifted to two anthracene moieties bridged by ethyne.[15] In this case, for the isopropylphenyl derivative, the rotational barrier was 12 kcal/mol. A DFT calculation for the parent compound without substituents gave a barrier of less than 1 kcal/mol. Therefore, the barrier can be appropriately attributed to the steric interactions between peri substituents (Figure 2.6).

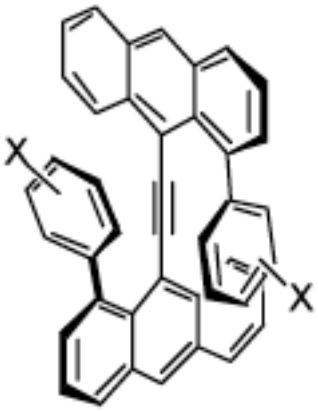

Figure 2.6 Steric interactions between peri substituents in dianthracenylethyne derivatives

In light of the significant barrier increase from phenyl to mesityl in the triptycene systems, mixed terphenyl **4** was prepared with one mesityl and one tolyl ring on each side of the alkyne.[16] Although the barrier was too low to be measured when all four rings were tolyl, in the case of **4**, a barrier of 12 kcal/mol was identified.

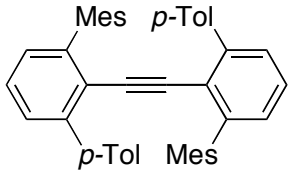

4

The work of Toyota and coworkers toward the isolation of rotational isomers of alkynes demonstrates the necessity of significant steric interactions in order to induce barriers to rotation observable by variable temperature NMR. In two cases, adding a mesityl substituent provided enough steric bulk to hinder rotation. In the most hindered systems, the maximum barrier was 18 kcal/mol.

2.2.3 A Molecular Turnstile

Moore and coworkers synthesized an alkyne-based rotary system, which they referred to as a molecular turnstile.[18] This molecule consists of a rigid macrocyclic framework containing an interior spindle with alkyne spacers. The size of the substituents attached to this spindle was varied and the barrier to rotation of the interior phenyl group was determined by variable temperature NMR. As the size of the substituents was increased, the barrier to rotation also increased due to steric interactions between these groups and the rigid framework. In the simplest case, **5**, where R is hydrogen, the barrier was too small to measure by NMR. In the case of **6**, the barrier was 13 kcal/mol and in **7**, the barrier was more than 20 kcal/mol.

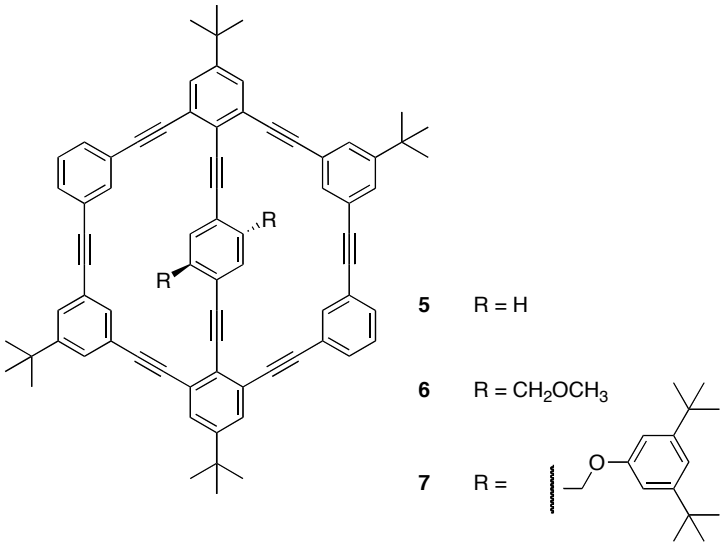

The authors demonstrated that the nearly free rotation of the spindle was dramatically hindered by the introduction of bulky substituents on the spindle, which led to significant steric interactions with the framework. Although there is no specific control of the rotation of the central spindle, this study lays the groundwork for the design of controllable molecular rotors.

2.2.4 Allosteric Binding in a Molecular Turnstile

In the turnstile synthesized by Shinkai and coworkers, the anion binding properties of the compound were investigated.[19] The authors observed that **8** was

capable of allosteric binding. When the first anion binds to the turnstile, the central spindle is forced to rotate, leaving the turnstile in an open state. This in turn elicits cooperative binding of another anion to the second binding site (Figure 2.7).

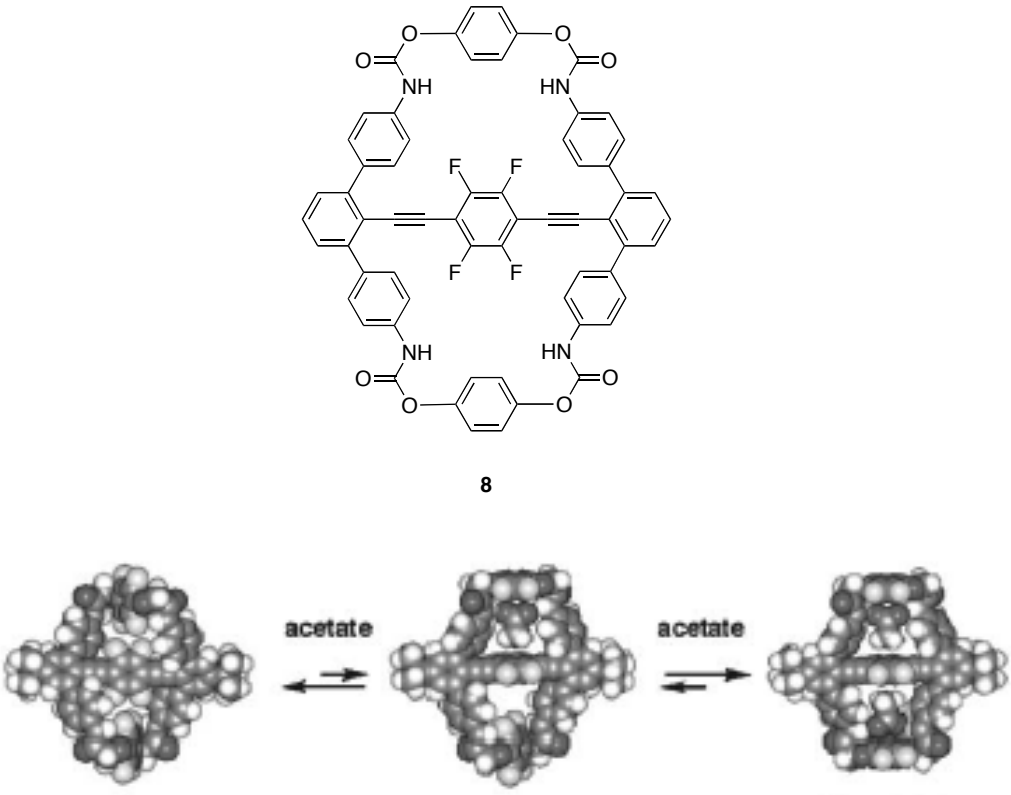

8

Figure 2.7 Proposed mechanism for allosteric binding of acetate ion by **8**

NMR titrations were performed on **8** in a mixture of deuterated THF and DMSO. Anions examined included bromide, acetate, hydrogensulfate, and dibenzylphosphide. NMR measurements in the presence of several of the anions showed the proton signal from the amide nitrogen and the fluorine signal both moved downfield with increasing anion concentration.

Job plots were conducted to observe complexation events and gave a maximum value at 0.33, corresponding to a 1:2 host:guest complex. Further, a Hill Plot demonstrated that binding took place cooperatively. Association constants could be estimated from a plot of the change in chemical shift versus the concentration of

guest anion, and these values correlated with the basicity of the guest anion. Most of the anions tested satisfied the condition of homotropic allosterism, in which the second association constant must be more than 0.25 times the first one ($K_2 > 0.25\ K_1$). Of the anions tested, chloride was a notable exception. The first binding constant was of the same order of magnitude as for other anions, however the significantly lower second association constant did not satisfy the requirements for allosteric binding, as it was less than 0.25 times the first one. The authors state that it may be the smaller size of the chloride ion that prevents allosteric binding, as the smaller anion is not large enough to rotate the spindle and open the second binding site. The radius of the chloride ion is reported to be 1.67 Å, whereas a bromide ion is 1.82 Å. Shinkai and coworkers conclude that they have prepared a new dynamic host capable of allosteric anion binding through the motion of a turnstile.

2.2.5 Molecular Compasses and Gyroscopes

Garcia-Garibay and coworkers worked towards the synthesis and arrangement of a series of alkyne rotors in a close-packed crystalline molecular assembly. Their intention was to control the rotary motion of this assembly using crystal engineering.[20] The rotary processes found in macroscopic machines, such as clocks and car engines, require sufficient free space within the high density apparatus, and a crystalline assembly requires a similar cavity. In a molecular rotor, the collective framework is referred to as a rotor, in which the stationary portion is called the stator and the spindle that turns is called the rotator (Figure 2.8). The synthetic targets of this project were aryl alkyne molecular rotors, which closely resemble the schematic. Dynamic properties of these rotors were observed by variable temperature solid-state NMR[21] and dielectric spectroscopy.[22]

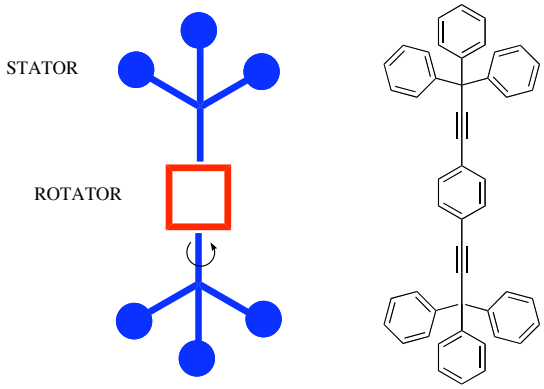

Figure 2.8 Schematic and chemical structure of a molecular rotor prepared by the Garcia-Garibay group. The stationary frame is referred to as the stator and the central component which spins is called the rotator.

In order to allocate enough free space for motion in the solid state assembly, the authors use crystal engineering to modify the packing density while still providing a durable crystal lattice.[23] The size of the stator is an important design component because it determines the density of the crystal packing. Larger stators generally reduce the crystal packing density and increase the cavity size by limiting interactions with adjacent molecules. As a result, increasing the stator size should reduce the barrier to rotation (Figure 2.9). However, the size of the stator as well as the nature of the crystal packing are both critical in determining the rotational barrier. For example, in rotors prepared by Garcia-Garibay, trityl and triptycyl stators were used. The trityl based rotor had a barrier of 12.8 kcal/mol in the solid state.[24] In comparison, the barrier in the triptycene based rotor was too high to be measured in the solid state, even though solution phase NMR spectroscopy shows free rotation of the central spindle.[25] The trityl stator creates more free space than the triptycyl stator for the central spindle, presumably due to less dense packing, which prevents interdigitation.

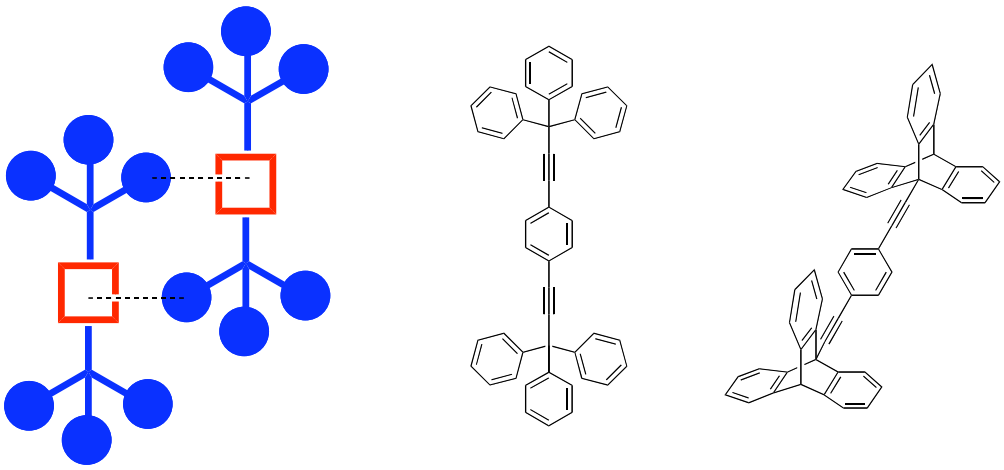

Figure 2.9 Interdigitation of adjacent rotors prevents free movement of the rotator. The rotational barrier in the solid state for the trityl rotor was 12.8 kcal mol, but the barrier was too high to be measured in the triptycenyl derivative.

The Garcia-Garibay group also synthesized molecular rotors containing dipolar rotator groups.[26] Whereas the rotator in the original system was a benzene ring, polarity is introduced by replacing one of the hydrogens on benzene with a fluorine atom, amino group, or nitro group, as seen in **9a-c**. The crystal structure and rotational barrier of **9a** is nearly identical to the parent compound. Dielectric spectroscopy measurements on the three-dimensional crystal lattice indicate rapid thermal motion of the rotors and no interaction between adjacent rotators. These results suggest that an oscillating electric field might be used to facilitate motion of the rotor in the crystal lattice.

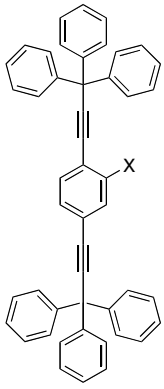

Compound	Substituent
9a	**F**
9b	**NH_2**
9c	**NO_2**

If several of these rotors are placed in proximity to each other in the solid state, it could be possible to construct a responsive crystalline molecular machine capable of correlated motion. The ability to design a molecular assembly that responds to a stimulus in order to carry out a specific function is a critical step towards the development of molecular machines.

2.3 Bond Rotation and Metal Compexation

2.3.1 A Molecular Brake

Kelly and coworkers reported the synthesis of what they referred to as a molecular brake, in which response to a chemical stimulus leads to hindered rotation of a previously free rotor.[27] In this case, the chemical stimulus is the addition of mercury cation, which causes the bipyridine moiety to lock into a single conformation (Figure 2.10). The goal was to demonstrate that this conformational change could stop rotation of the adjacent triptycene unit and that the change could be reversed by the removal of mercury.

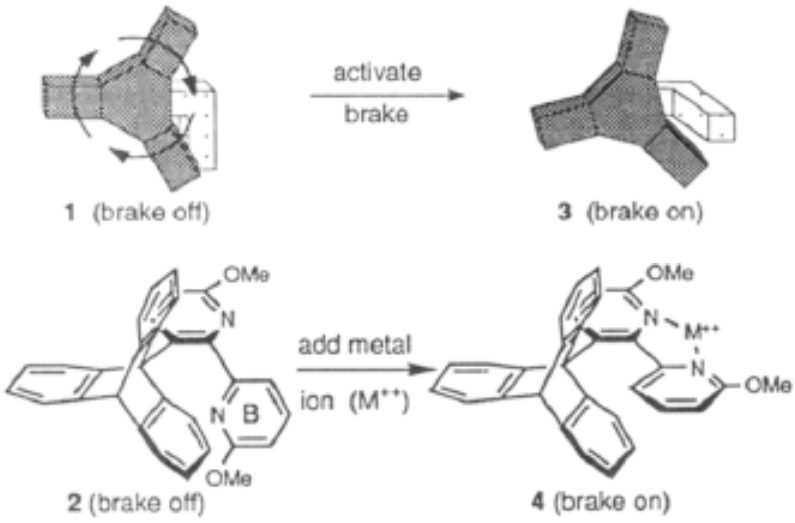

Figure 2.10 Activation and deactivation of Kelly's molecular brake with mercury cation.

The dynamic processes in the molecule were monitored by variable temperature NMR spectroscopy in the presence and absence of mercury cation. The measurements demonstrate that the system is effectively frozen in place at –30 °C in the presence of the metal, but there is still slow rotation in the absence of the metal. Addition of EDTA results in the removal of the mercury and rotation of the triptycene unit is no longer hindered, demonstrating that the change is reversible.

In their molecular brake, Kelly and coworkers demonstrate a response to a stimulus that leads to a change in the physical properties of the system. This is a significant proof of principle in terms of a reversible chemical stimulus leading to a change in the dynamics of a system.

2.3.2 Rotation in Metal-Arene Complexes

In a related system, Kilway and Siegel investigated rotational dynamics in metal-arene complexes.[28,29] In previous work by others, metal complexation with tricarbonyl chromium was shown to desymmetrize hexaethylbenzene by making the two faces of the π system nonequivalent, which made it possible to determine the rotational barrier of the ethyl groups.[30] It was not clear, however, if the metal was influencing the magnitude of the ethyl group barrier.

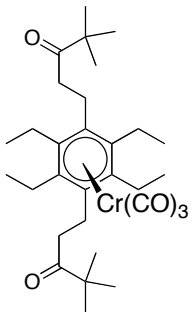

10

Kilway and Siegel synthesized a system in which the rotational barriers of the ethyl groups and the chromium tripod could be determined independently.[28] In **10**,

rotation of the tricarbonyl group makes the three C—O groups equivalent, but the ketone carbons remain nonequivalent. Ethyl group rotation is required to make these sites equivalent. At room temperature, the ^{13}C NMR shows one ketone signal and one C—O signal. Cooling the sample to –60 °C splits the ketone into two signals, while the tricarbonyl groups remain equivalent, indicating that ethyl group rotation has stopped. Decoalescence at -60 ˚C corresponds to a rotational barrier of 11.8 kcal/mol. Further cooling of the sample to -90 °C splits the carbonyl signal into two peaks with a 2:1 ratio, indicating that the tripod motion has stopped. The barrier for this process is found to be 9.5 kcal/mol. The ethyl group barrier was determined again in the uncomplexed arene to give a barrier of 11.3 kcal/mol.

From this work, Kilway and Siegel concluded that tri-carbonyl chromium does not significantly influence the measured barrier, and it provides a valid reference point for a rotational barrier determination. Additionally, they propose that the motion of the tripod may be gated by the proximal alkyl groups.

Kilway and Siegel studied the effect of metal complexation on the barrier to rotation of the ethyl groups in several related systems to further demonstrate the utility of this method, and indicate the small influence metal complexation has on the measured barrier.[31] In **11-13**, ethyl group barriers were determined in the free ligands and metal complexes. As expected, there was only a small perturbation of the barrier due to metal complexation. These results also point to the possibility of correlation between tripod and ethyl group rotation.

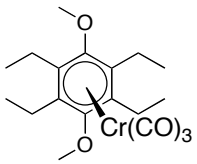

11

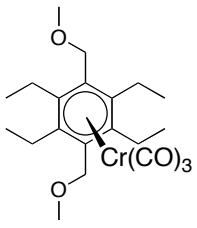

12

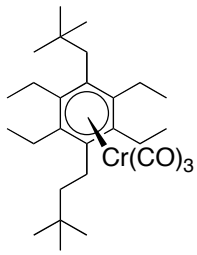

13

In order to investigate the prospect of correlated motion, the metal in **10** was changed from chromium to molybdenum to give **14**.[29] Comparing the crystal structures of the chromium and molybdenum complexes shows that the molybdenum-arene bond is 1.88 Å, which is 0.16 Å longer than the chromium-arene bond. Once again, the barriers were determined by variable temperature NMR. The barrier to ethyl group rotation in the molybdenum complex was 11.4 kcal/mol, nearly the same value found in the free ligand. The tripod rotational barrier was 6.7 kcal/mol, almost 3 kcal/mol less than the barrier for the chromium tripod.

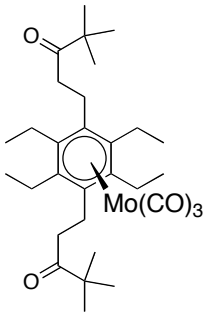

14

The barrier decrease from chromium to molybdenum suggests that the longer bond reduces steric interactions and therefore also reduces the rotational barrier. The significant barrier change relative to the chromium complex further supports the idea of correlation between the ethyl group and tripod motions.

2.4 Molecular Motors and Machines

2.4.1 Towards a Unidirectional Molecular Motor

Internal rotations are useful physical properties to study, however harnessing molecular motion is difficult to achieve. The ability to control molecular motion should enable the construction of useful molecular assemblies with practical functions. A significant advance in the design of molecular machines was reported by

Feringa and coworkers in 1999.[32] They prepared the first unidirectional molecular motor, using the photoisomerization of a double bond bridging two chiral elements (Figure 2.11).

The direction of movement is controlled by the wavelength of light used and the chirality of the molecule. The concerted action of two chiral elements in a single physical event leads to unique handedness of the molecule. In the two tetrahydrophenanthrenes, each one can have left-handed (M) or right-handed (P) helicity. Including the cis-trans isomerization of the double bond, the cycle contains four stereoisomers. Light is used to induce cis and trans isomerization whereas irreversible helicity inversion is caused thermally, without affecting the cis or trans configuration.

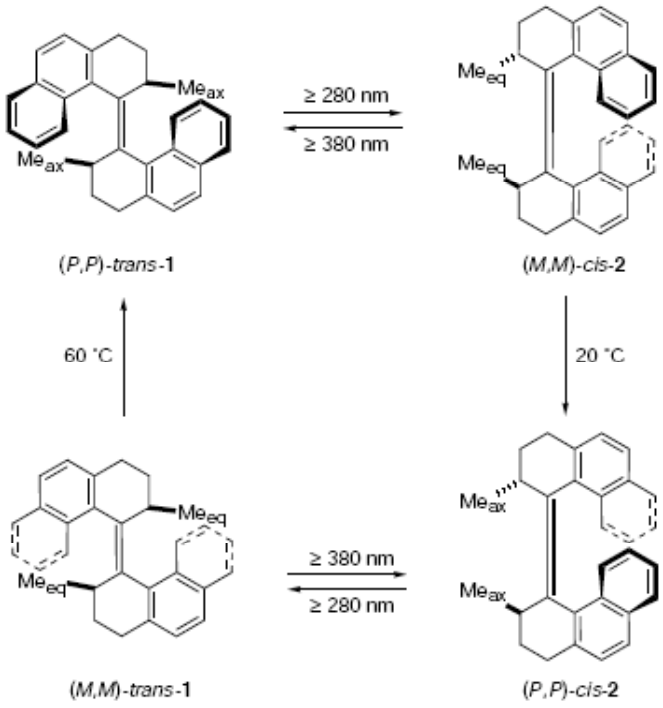

Figure 2.11 Rotary motion in Feringa's molecular motor

In the first step of the cycle, irradiation at 280 nm at 218 K converts the (P,P)-trans isomer to the (M,M)-cis isomer. The solution is then warmed to 293 K, at which

point there is irreversible conversion to the (P,P)-cis isomer. Subsequent irradiation at 280 nm produces the (M,M)-trans isomer. Further increasing the temperature to 333 K irreversibly converts back to the starting (P,P)-trans isomer. In the four step cycle, light and temperature are used to induce unidirectional motion. This motion is dictated by the stereogenic centers on each tetrahydrophenanthrene unit. In the first trans-cis isomerization, the axial methyl groups in the (P,P)-trans conformation are forced equatorial in the (M,M)-cis isomer. This strain is released in the next step, as the methyl groups are once again axial in the (P,P)-cis isomer. The subsequent light-driven isomerization again forces the methyl groups equatorial, and the following step returns them to their starting configuration, in which the methyl groups are axial.

In the second generation molecular motor synthesized by Feringa and coworkers, there are distinct upper and lower parts to the assembly, and only one stereogenic center.[33] However, one stereocenter is still enough to drive unidirectional motion. Additional modifications were made to reduce the barrier to the thermal isomerizations. In newly synthesized **15** and **16**, rotational barriers are reduced to 24.7 kcal/mol and 22.7 kcal/mol respectively, compared to the original barrier of 26.2 kcal/mol. In these systems, it should also be possible to attach one side to a surface in order to make a unidirectional molecular rotor.

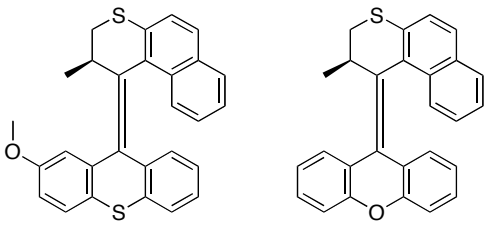

15 **16**

Related work by the Feringa group strived to control the rate of single bond rotation in a very similar system.[34] It was believed that isomerization of **17** to the trans isomer would reduce the rotational barrier by decreasing steric interactions. However,

results showed that the barrier is actually higher for the trans isomer. A plausible explanation is interaction between the ortho methyl groups and the adjacent ring methylenes, an interaction that is avoided in the cis conformation. The authors propose that the naphthalene unit easily bends away to enable passage of the rotor.

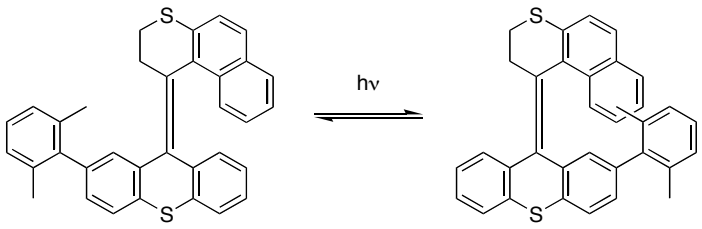

17

In summary, this work demonstrates the ability to induce light-driven, repetitive unidirectional motion. Chemical modifications led to changes in the rate of motion and slight modifications of the structure should allow it to be attached to surfaces or other molecules. Feringa and coworkers have demonstrated the ability to harness internal rotation and turn it into a potentially useful process.

2.4.2 Molecular Motion and Electronic Devices

In a related effort to harness molecular motion for practical applications, Mayor and coworkers synthesized macrocyclic aryl alkynes, **18** and **19**, with the goal of developing potential electronic devices.[35] The molecules prepared by the Mayor group contain three ethynyl-linked phenyl rings with protected terminal thiol groups at each end to eventually permit immobilization between gold contacts. A handle is connected to the ortho positions of the two terminal rings. Initially, two derivatives were investigated, one containing one nitro group on the central ring and the other containing two.

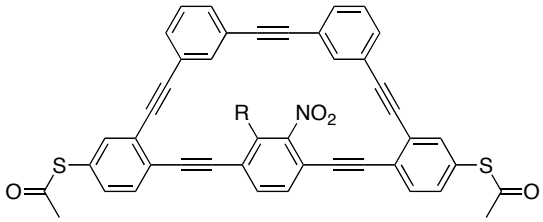

18 **R = H**

19 **R = NO_2**

The work of Mayor and coworkers is not the first example of using ethynyl linked phenyl rings to construct a molecular electronic device. Tour and coworkers previously prepared **20**, a bisphenethynyl compound with both a nitro and amino substituent on the central ring.[36] A self-assembled monolayer (SAM) of this compound was formed between gold electrodes. The authors observed negative differential resistance (NDR) behavior with **20**. NDR behavior means that, in a particular voltage range, current is a decreasing function of voltage. In a control experiment, a compound lacking substituents on the central ring was tested in the same manner, but, in this case, NDR behavior was not observed.

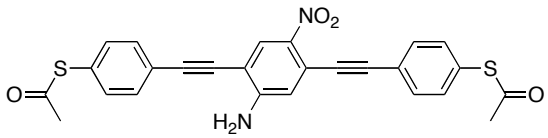

20

The authors rationalize the NDR behavior of **20** based on a two-step reduction process that modifies charge transport through the molecule. As the voltage increases, a one electron reduction takes place, which supplies a charge carrier for electron flow. A further increase in voltage results in a second reduction to the dianion, which blocks the current. The fact that NDR behavior was not observed in the absence of the nitro group indicates the importance of this functionality in facilitating the flow of current.

Computational investigations were conducted on these systems by Stokbro and coworkers to elucidate the basis of the NDR behavior.[37] Their work suggested that an intermolecular interaction between a nitro group and the phenyl ring of the neighboring molecule in the self-assembled monolayer is the cause for the NDR behavior. This assertion is further supported by the fact that the NDR was not observed in single molecule experiments.

Based on Tour's results, Mayor and coworkers decided to investigate a single macrocyclic structure containing both the central bis(phenylethynyl) core and the neighboring phenyl group. In this manner, the intermolecular interaction postulated by Stokbro and coworkers becomes an intramolecular interaction, and the conducting properties of the macrocycle can be investigated in single-molecule experiments.

Mayor and coworkers synthesized macrocycles **18** and **19** based on previously established acetylene scaffolding strategies. Whereas **18** has one nitro group in close proximity to an adjacent phenyl ring, there are two such interactions in the case of **18**. The authors point out that the "handle" bridging the two terminal rings consists of the poorly conjugated meta-diethynyl unit. Therefore, the current is still expected to travel predominantly through the central rod.

Mayor and coworkers attempted to grow crystals of *tert*-butyl protected dithiol **21** in order to determine the distance between the nitro group and the adjacent phenyl ring. In efforts to increase the solubility of the compounds, a sample was dissolved in toluene and gently heated, which caused the solution to change from yellow to orange. The suspected decomposition product was determined to be isatogen **22**, and single crystals were collected from the orange solution. A crystal structure was obtained, indicating that an intramolecular rearrangement took place to form the isatogen derivative (Scheme 2.1).

Scheme 2.1

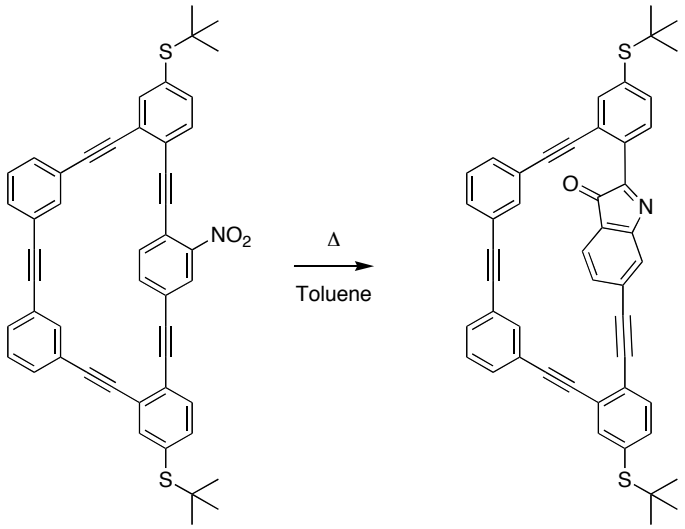

21 **22**

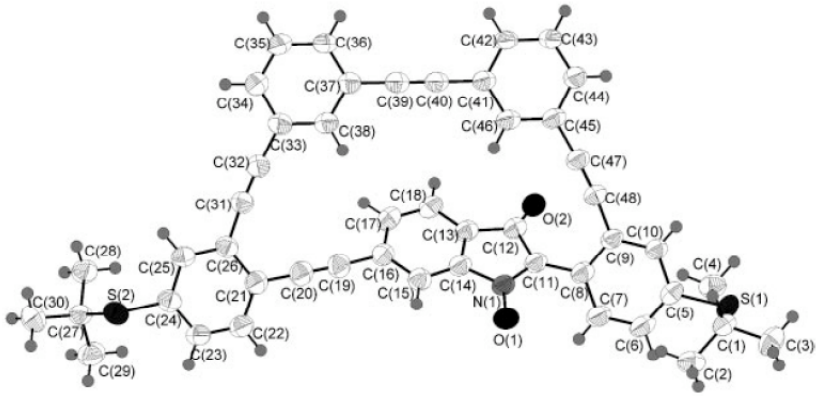

Figure 2.12 Crystal structure of rearrangement product **22**.

The authors state that the rearrangement indicates the delicate thermal stability of the macrocycle. Even without heating, the yellow solution of the original macrocycle turned orange within several weeks. Mayor and coworkers state that this rearrangement should also be considered as a means for tuning the electronic properties.

Mayor has demonstrated a successful synthesis of a prototype for a single molecule electronic device. Investigations of the conductance properties of this

molecule and related derivatives are ongoing. This work serves as another example of potential practical applications of aryl alkyne molecular rotors.

2.5 Conclusions

The initial determination of the rotational profiles of ethane and biphenyl provided the basis for conformational analysis of a wide array of complex molecules. As the example of tolan shows, rotational barriers in aryl alkynes are quite low. However, by varying certain parameters, the rotational barriers could be modulated in the congested aryl alkynes prepared by Toyota as well as the turnstile systems synthesized by Moore. The turnstile system of Shinkai and coworkers is structurally quite similar to the molecules synthesized by the Moore group; however, in Shinkai's system, the authors observed the response of the turnstile molecule to an external stimulus. The transition from the observation of physical properties to the investigation of response to a stimulus is a critical step towards the rational design of functional molecular devices. The final three examples all aim to take advantage of bond rotation in order to accomplish mechanical or electrical work. The work of Garcia-Garibay in pursuit of a responsive crystalline molecular assembly and the efforts by Feringa towards the design of a molecular motor both enter the realm of rational design. Finally, the work of Mayor is primarily interested in the conductance properties of aryl alkynes and the possibility of bond rotation inducing on-off switching.

The field of molecular machines is in its early stages, and efforts towards the rational design of functional molecular assemblies are critical to its development. However, this area of research must first rely on fundamental studies of simpler molecules before progressing towards the construction of complex assemblies. A

strong foundation in the factors influencing molecular motion is essential to realizing true molecular machines.

REFERENCES:

1. Smith, L.G. *J. Chem. Phys.* **1949,** *17,* 139.

2. Weiss, S.; Leroi, G.E. *J. Chem. Phys.* **1968,** *48,* 962.

3. Hirota, E.; Saito, S.; Endo, Y. *J. Chem. Phys.* **1979,** *71,* 1183.

4. Pophristic, V.; Goodman, L. *Nature* **2001,** *411,* 565.

5. Katon, J.E.; Lippincott, E.R. *Spectrochim. Acta.* **1959,** *19,* 627.

6. Charbonneau, G.-P.; Delugeard, Y. *Acta. Crystallogr. B* **1976,** *32,* 1420.

7. Almenningen, A.; Bastiansen, O.; Fernholt, L.; Cyvin, B.N.; Cyvin, S.J.; Samdal, S. *J. Mol. Struct. (THEOCHEM)* **1985,** *128, 59.*

8. Grein, F. *J. Phys. Chem. A* **2002,** *106, 3823.*

9. Aldridge, B.; DeLuca, G.; Edgar, M.; Emsley J.W.; Furby, M.I.C.; Webster, M. *Liquid Cryst.* **1998,** *24,* 569.

10. Liberles, A.; Matlosz B. *J. Org. Chem.* **1971,** *36,* 2610.

11. Robertson, J.M.; Woodward, I. *Proc. Roy. Soc., Ser. A,* **1938,** *164,* 436.

12. Toyota, S.; Yamamori, T.; Asakura, M.; Oki, M. *Bull. Chem. Soc. Jpn.* **2000,** *73,* 205.

13. Toyota, S.; Yamamori, T.; Makino, T.; Oki, M. *Bull. Chem. Soc. Jpn.* **2000,** *73, 2591.*

14. Toyota, S.; Yamamori, T.; Makino, T. *Tetrahedron* **2001,** *57,* 3521.

15. Toyota, S.; Iida, T.; Kunizane, C.; Tanifuji, N.; Yoshida, Y. *Org. Biomol. Chem.* **2003,** *1,* 2298.

16. Toyota, S.; Yanagihara, T.; Yoshida, Y.; Goichi, M. *Bull. Chem. Soc. Jpn.* **2005,** *78,* 1351.

17. Olson, W.B.; Papousek, D. *J. Mol. Spectrosc.* **1971,** *37,* 527.

18. Bedard, T.C.; Moore, J.S. *J. Am. Chem. Soc.* **1995,** *117,* 10662.

19. Hirata, O.; Takeuchi, M.; Shinkai, S. *Chem. Commun.* **2005,** 3805.

20. Khuong, T.-A.V.; Nunez, J.E.; Godinez, C.E.; Garcia-Garibay, M.A. *Acc. Chem. Res.* **2006,** *39,* 420.

21. Pines, A.; Gibby, M.G.; Waugh, J.S. *J. Chem. Phys.* **1973,** *59,* 569.

22. Clarke, L.I.; Horinek, D.; Kottas, G.S.; Varaska, N.; Magnera, T.F., Hinderer, T.P.; Horansky, R.D.; Michl, J.; Price, J.C. *Nanotechnology* **2002,** *13, 533.*

23. Dominguez, Z.; Dang, H.; Strouse, M.J.; Garcia-Garibay, M.A. *J. Am. Chem. Soc.* **2002,** *124,* 2398.

24. Dominguez, Z.; Dang, H.; Strouse, M.J.; Garcia-Garibay, M.A. *J. Am. Chem. Soc.* **2002,** *124,* 7719.

25. Godinez, C.E.; Zepeda, G.; Garcia-Garibay, M.A. *J. Am. Chem. Soc.* **2002,** *124,* 4701.

26. Dominguez, Z.; Khoung, T.-A.V.; Dang, H.; Sanrame, C.N.; Nunez, J.E.; Garcia-Garibay, M.A. *J. Am. Chem. Soc.* **2003,** *125,* 8827.

27. Kelly, T.R.; Bowyer, M.C.; Bhaskar, K.V.; Bebbington, D.; Garcia, A.; Lang, F.; Kim, M.H.; Jette, M.P. *J. Am. Chem. Soc.* **1994,** *116,* 3657.

28. Kilway, K.V.; Siegel, J.S. *J. Am. Chem Soc.* **1991,** *113,* 2332.

29. Kilway, K.V.; Siegel, J.S. *Organometallics* **1992,** *11,* 1426.

30. Iverson, D.J.; Hunter, G.; Blount, J.F.; Damewood, J.R., Jr.; Mislow, K. *J. Am. Chem. Soc.* **1981,** *103,* 6073.

31. Kilway, K.V.; Siegel, J.S. *J. Am. Chem. Soc.* **1992,** *114,* 255.

32. Koumura, N.; Zijlstra, R.W.J.; van Delden, R.A.; Harada, N.; Feringa, B.L. *Nature* **1999,** *401,* 152.

33. Koumura, N.; Geertsema, E.M.; Meetsma, A.; Feringa, B.L. *J. Am. Chem. Soc.* **2001,** *122,* 12005.

34. Schoevaars, A.M.; Kruizinga, W.; Zijlstra, R.W.J.; Veldman, N.; Spek, A.L.; Feringa, B.L. *J. Org. Chem.* **1997,** *62,* 4943.

35. Blaszczyk, A.; Chadim, M.; von Haenisch, C.; Mayor, M. *Eur. J. Org. Chem.* **2006,** 3809.

36. Chen, J.; Reed, M.A.; Rawlett, A.M.; Tour, J.M. *Science* **1999,** *286,* 1550.

37. Taylor, J.; Brandbyge, M..; Stokbro, K. *Phys Rev. B* **2003,** *68,* 121101.

3 POLAR-π INTERACTIONS IN ARYL ALKYNE MOLECULAR ROTORS

3.1 Project Design

3.1.1 Overview

In the first chapter, the significance of edge-to-face polar-π interactions in a wide range of systems was discussed. Attractive forces of this type were identified in small molecules, host:guest complexes, and large proteins. In general, the energetic contribution of each polar-π interaction was found to be less than 2 kcal/mol by experimental and computational methods. Although the amount of energy for an individual interaction is relatively small, a survey of protein crystal structures by Burley showed an average of seven edge-to-face interactions in each protein.[1] Consequently, the collective contribution of several favorable polar-π interactions in a single protein, could provide significant stabilization of a particular geometry.

In addition to the computational analysis by Burley, other methods for quantifying polar-π interactions were also discussed in the first chapter. The torsion balances synthesized by Wilcox and coworkers were intended to model protein folding by permitting conformational isomerism between a "folded" state, in which there is an edge-to-face interaction between two aryl groups, and an "unfolded" state, in which the rings are remote.[2,3] The substituent (Y) was varied and NMR spectroscopy was used to determine the population of each state (Figure 3.1). However, the experimental results indicated almost no additional preference for the "folded" state relative to the unsubstituted (Y=H) parent compound.

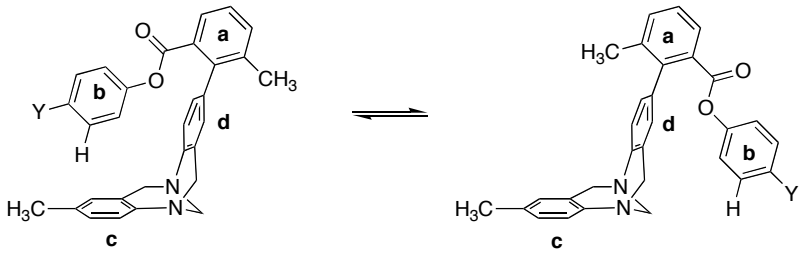

Figure 3.1 Torsion balances prepared by Wilcox and coworkers. The ratio of conformers was determined by NMR spectroscopy.

The unsubstituted system has an inherent barrier of 18 kcal/mol, and, in light of the small energetic contribution of an edge-to-face interaction, it may be difficult to appropriately assign a small variation in the relative populations to the interaction of interest.[2] The ability to assign the observed trend to the interaction of interest and eliminate other variables is critical to the accurate evaluation of edge-to-face polar-π interactions. An appropriate system for probing weak interactions must have a high signal-to-noise ratio and remove as many outside variables as possible.

The meta terphenyl carboxylic acids used by Siegel and coworkers to quantify anion-π interactions eliminated two important variables.[4] In the terphenyl core, the flanking rings are orthogonal to the central ring, preventing conjugation, and, consequently, allowing the observation of a through space interaction (Figure 3.2). In addition, the steric bulk of the flanking rings prevents solvent interactions with the central carboxyl group. In this work, the pK_a of the acid was monitored as a function of the substituent on the flanking ring. A Hammett plot showed good correlation between the pK_a and the Hammett parameter for the para-substituted compounds. The meta-substituted compounds only correlated when they were plotted using the para Hammett parameter, further supporting the through space nature of the interaction. The terphenyl core provided an ideal geometry for observing this type of interaction because of the close proximity of the flanking rings to the functional group of interest.

In addition, this system effectively eliminated solvent effects and conjugation, which allowed the observed trend to be appropriately attributed to polar-π interactions.

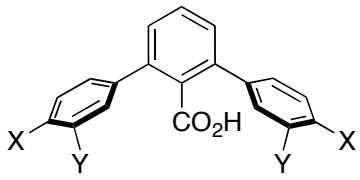

Figure 3.2 Siegel and coworkers used *m*-terphenyl acids to observe anion-π interactions by monitoring the pK_a of the carboxylic acid.

The second chapter began with a brief overview of bond rotation in simple molecules before moving to a discussion of efforts towards controlling bond rotation. The primary focus of the chapter was bond rotation in aryl alkynes, beginning with the simple example of tolan. Experimental and computational methods have shown the barrier in tolan to be quite low, on the order of 0.5 kcal/mol.[5,6] In order to dramatically increase the barrier in aryl alkynes, steric interactions had to be introduced, as seen in the work of Toyota and Moore.[7-12] Whereas significant steric interactions resulted in a drastic barrier increase, we postulated that a very subtle perturbation could also lead to an observable barrier increase in tolan derivatives.

3.1.2 Experimental Design

The inherently low barrier in tolan suggests that a weak attractive force, such as an edge-to-face polar-π interaction, could significantly modulate the rotational barrier. A properly designed derivative, in which interactions of this type are possible, could provide an appropriate environment to quantify polar-π interactions. As previously discussed, the terphenyl core provides a rigid geometry suitable for studying edge-to-face interactions. We postulated that a combination of tolan and the meta terphenyl ring system would provide an appropriate environment to study these interactions (Figure 3.3).

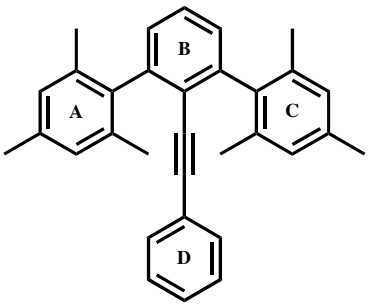

Figure 3.3 The initial series of terphenyl alkynes, with ring labeling scheme.

The terphenyl core places the two flanking rings, A and C, in close proximity to the D ring. The ortho methyl groups force rings A and C orthogonal to the plane of ring B. When the B and D rings are coplanar, an intramolecular edge-to-face interaction between the ortho hydrogens on the D ring and rings A and C is possible (Figure 3.4). Conversely, when rings B and D are perpendicular to each other, there is no possibility for such an interaction. Therefore, the rotational barrier should be almost entirely determined by the magnitude of edge-to-face polar-π interactions between ring D and the flanking rings.

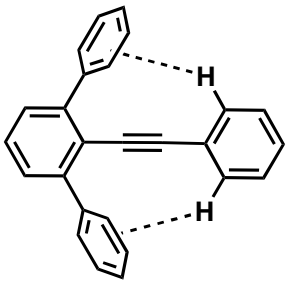

Figure 3.4 Proposed edge-to-face polar-π interactions in terphenyl alkynes.

In the work of Wilcox, NMR spectroscopy was used to determine the relative populations of two conformers, and these populations were used to evaluate the significance of polar-π interactions. In the case of the terphenyl alkynes, the goal was to determine the rotational barriers, rather than relative populations, by VT NMR

spectroscopy. The magnitude of the rotational barrier should be a measure of the significance of the edge-to-face interaction and the energetic contribution of the interaction can be extrapolated by comparison to the known barrier of tolan. Due to their shape, these molecules will be referred to as umbrella structures.

An appropriate symmetry environment is required in order to use VT NMR spectroscopy to measure the rotational barrier. The two initial synthetic targets were simple phenyl umbrella **1** and pyridyl umbrella **2a**. Whereas **1** possesses C_{2v} symmetry, in the absence of rotation about the triple bond, the pyridyl nitrogen in **2a** makes the molecule asymmetric and provides the appropriate environment for evaluating the rotational barrier by VT NMR spectroscopy (Figure 3.5).

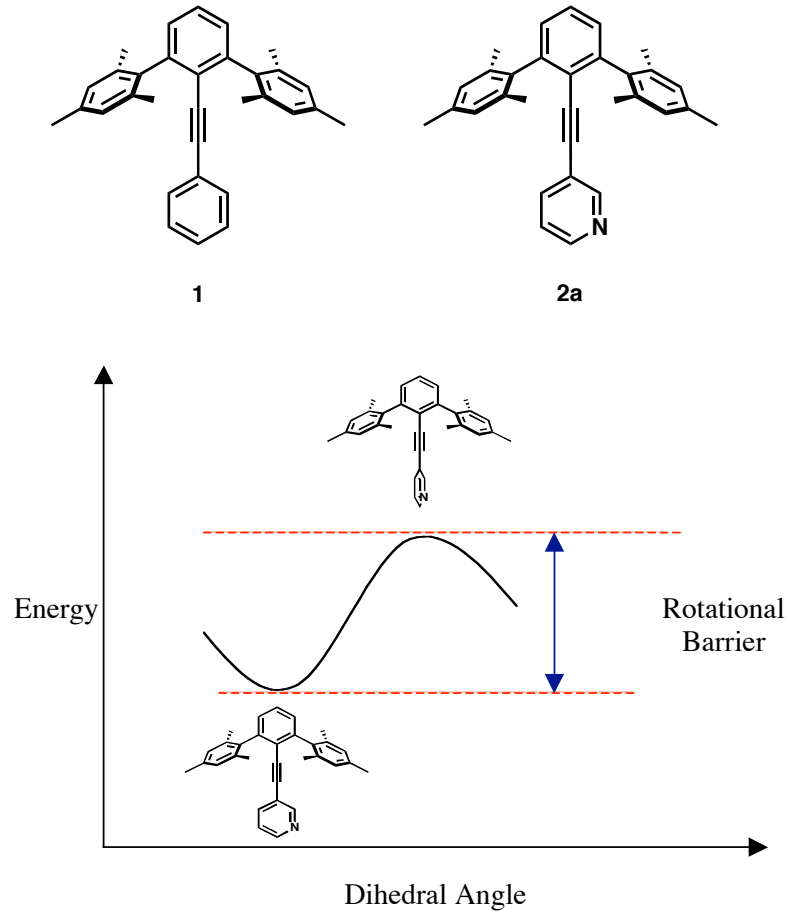

Figure 3.5 Proposed rotational profile of **2a**. The pyridyl nitrogen should provide the proper symmetry environment to determine the rotational barrier by variable temperature NMR.

3.2 Umbrella Structures

3.2.1 Calculations on Phenyl Umbrellas

Prior to beginning with synthesis, a series of calculations was conducted to determine the rotational barriers of the molecules of interest. The optimized geometry and rotational barriers were calculated for **1** as well as the parent tolan **3.** In the case of **1,** the coplanar conformation is 1.6 kcal/mol more stable than the perpendicular arrangement. Hessian calculations confirmed that the coplanar geometry was a minimum and the perpendicular geometry is a transition state. For comparison, the rotational barrier in tolan **3** was found to be 0.5 kcal/mol by the same method. This calculated value is consistent with experimentally determined values for the rotational barrier.[5,6] The only difference between the two structures is the flanking groups in **1**, and, consequently, the additional energy can be attributed to interaction between the D ring and the flanking rings. By extrapolation, and based on the assumption that the interaction energies are additive and linear, the 1.1 kcal/mol energy difference corresponds to 0.55 kcal/mol for each edge-to-face polar π interaction.

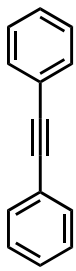

3

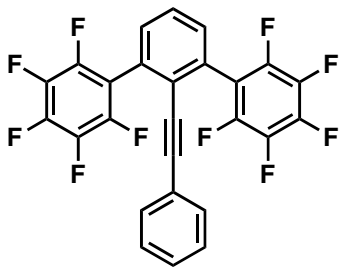

4

The rotational barrier was also calculated for **4**, in which the flanking mesityl groups were replaced by perflourobenzenes in order to reverse the charge distribution on the flanking rings. In this case, the rotational barrier was 0.2 kcal/mol, slightly favoring the coplanar conformation. However, this value is less than the barrier measured for tolan itself, a result that can be rationalized by a repulsive edge-to-face

interaction between the electron deficient flanking groups and the hydrogen atoms on the central ring. Once again, assuming the interactions are additive and linear, each interaction destabilizes the coplanar conformation by 0.15 kcal/mol, however this effect is not significant enough to make the perpendicular geometry the favored conformation.

Table 3.1 Rotational Barriers in Phenyl Umbrellas

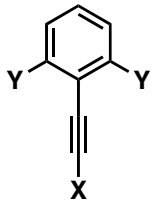

Entry	X	Y	Method / Basis Set	Barrier
1	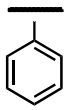	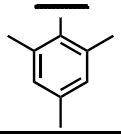	**RHF/ 6-31G(d,p)** **B3LYP / 6-31G(d,p)**	**1.70** **1.60**
3	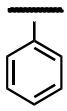	**H**	**RHF/ 6-31G(d,p)** **B3LYP / 6-31G(d,p)** **MP2 / 6-31G(d,p)**	**0.43** **0.92** **0.50**
4	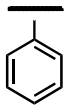	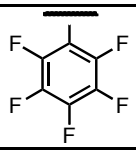	**RHF/ 6-31G(d,p)** **B3LYP / 6-31G(d,p)**	**0.2** **0.8**

3.2.2 Calculations on Pyrimidyl Umbrellas

In the series of phenyl umbrellas, reversal of the charge distribution on the flanking rings led to repulsion in the ground state and a significant decrease in the rotational barrier. We postulated that introducing electron density in the ortho positions of the D ring, as in **5**, would also destabilize the ground state by causing repulsive interactions with the electron-rich flanking rings.

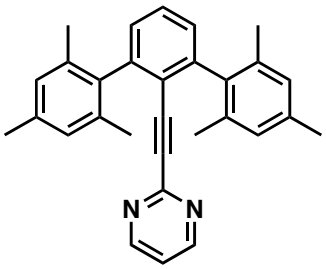

5

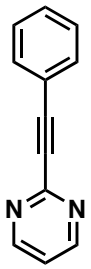

6

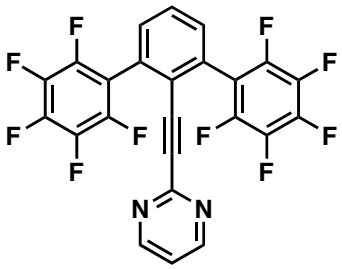

7

In the case of **5**, the rotational barrier was calculated to be 0.2 kcal/mol. The pyrimidyl umbrella does not have hydrogens in the proper positions to interact with the flanking rings; however, the electron density of the nitrogen lone pairs is in the same location. The rotational barrier of the parent 2-phenylethynylpyrimidine **6** was calculated to be 0.7 kcal/mol, nearly the same as tolan. Once again, there is a slight destabilization of the coplanar geometry of **5** as a result of electrostatic interactions between the nitrogen lone pairs and the electron rich flanking rings. In this case, based on the assumption of linearity, each repulsive interaction is worth 0.25 kcal/mol.

We postulated that reversing the charge distribution on the flanking rings by replacing the mesityl groups with perfluorobenzenes would actually stabilize the ground state in the pyrimidyl umbrella. The rotational barrier of **7** was 1.5 kcal/mol, which is consistent with a favorable interaction between the nitrogen lone pairs and the electron poor flanking rings. As there are two interactions, each one stabilizes the ground state by 0.4 kcal/mol by comparison to **6**.

Table 3.2 Rotational Barriers in Pyrimidyl Umbrellas

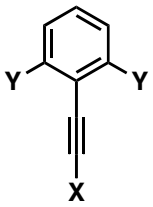

Entry	X	Y	Method / Basis Set	Barrier
5	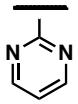	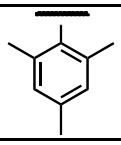	**RHF/ 6-31G(d,p)** **B3LYP / 6-31G(d,p)**	**0.23** **0.22**
6	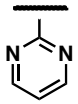	**H**	**RHF/ 6-31G(d,p)** **B3LYP / 6-31G(d,p)** **MP2 / 6-31G(d,p)**	**1.06** **1.33** **0.71**
7	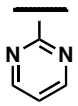	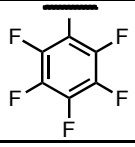	**RHF/ 6-31G(d,p)** **B3LYP / 6-31G(d,p)**	**1.50** **1.60**

In the calculations discussed above, a variety of weak intramolecular interactions were observed computationally; however, no single interaction appears to contribute more than 0.5 kcal/mol. Furthermore, the determined rotational barriers for these compounds are all less that 2 kcal/mol. Although these values were determined in the gas phase, we believed that variable temperature NMR measurements would most likely not be sensitive enough to evaluate the rotational barriers in solution. Nevertheless, we moved forward with the synthesis of **1** to observe its solid state structure, particularly the edge-to-face distances.

3.2.3 Umbrella Retrosynthesis

In the retrosynthesis of **1**, the two obvious disconnections are the aryl-aryl single bonds and the alkyne-aryl linkage. There are two basic possibilities to consider,

and in both cases, the product can be prepared in two steps starting from 1,2,3-tri-substituted benzene. The final product could be derived from a meta terphenyl ring system, which can be prepared from dichloroiodoobenzene using the Hart Reaction.[13] An alternative approach would be to obtain the product from dihalotolan, using a palladium-catalyzed cross-coupling reaction.[14] The dihalotolan could be prepared using a selective Sonogashira reaction between phenylacetylene and a 1,2,3-trihalobenzene.[15] The common trihalobenzene starting material for both routes can be prepared in high yield starting from 2,6,dibromoaniline. Both synthetic routes were pursued, however it was determined that the second method provided a more efficient synthesis of **1**.

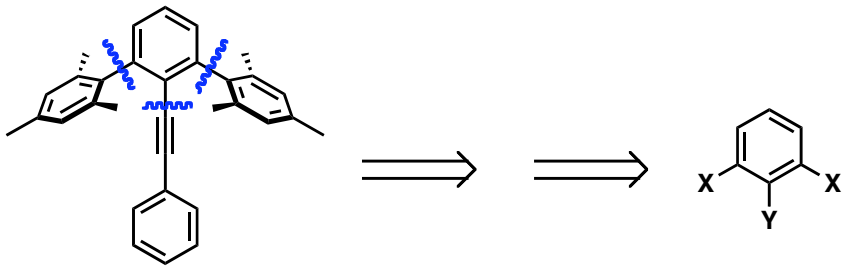

1

Figure 3.6 Proposed disconnections for retrosynthesis of **1**

3.2.4 Synthesis of Phenyl Umbrella

Starting from the commercially available aniline **8**, Sandmeyer reaction[16] with a potassium iodide quench afforded the desired trihalide **9** (Scheme 3.1). Selective Sonogashira coupling[15] with phenylacetylene yielded dibromoalkyne **10** and subsequent Negishi coupling[17] with the zincate of 2-bromomesitylene gave **1**.

Scheme 3.1

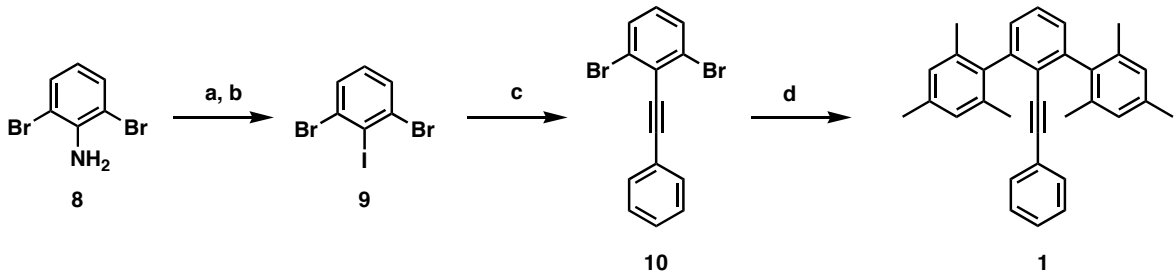

a. $NaNO_2$, HCl b. KI, H_2O, 83% c. Phenylacetylene, $Pd(PPh_3)_2Cl_2$, CuI, TEA, 65%
d. ArZnCl, $Pd(PPh_3)_4$, THF, 68%

3.2.5 Synthesis of Pyridyl Umbrellas

The 3-pyridyl umbrella **2a** was originally a desired target molecule for VT NMR spectroscopy. However, the calculated barriers were quite low, suggesting that such a measurement would not prove useful. Nevertheless, **2a** was synthesized in order to determine its solid state structure relative to phenyl umbrella **1**, with the assumption that the structures would be quite similar. In contrast to **2a**, we postulated that **2b** would have a different solid state structure than **1** due to repulsion between the electron donating flanking rings and the nitrogen lone pair electrons. This repulsion was observed in calculations on C_{2v} symmetric pyrimidyl umbrella **5**, and was therefore expected it to also be present in the asymmetric 2-pyridyl derivative. Consequently, both **2a** and **2b** were prepared (Scheme 3.2).

A nearly identical synthetic procedure was followed for the preparation of the pyridyl derivatives. In this case, commercially available 3- and 2-ethynylpyridine were used in place of phenylacetylene in the Sonogashira reaction to give **11a** and **11b**, respectively. Subsequent Negishi coupling gave pyridyl umbrellas **2a** and **2b**.

Scheme 3.2

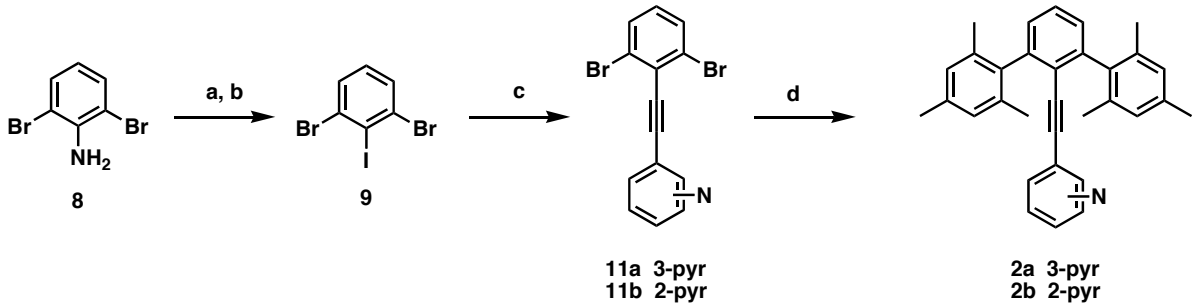

a. $NaNO_2$, HCl b. KI, H_2O, 83% c. Ethynylpyridine, $Pd(PPh_3)_2Cl_2$, CuI, TEA, 56%(11a),65%(11b)
d. ArZnCl, $Pd(PPh_3)_4$, THF, 24%(2a), 13%(2b)

3.2.6 Synthesis of Pyrimidyl Umbrellas

The pyrimidyl derivative was synthesized in order to determine the effect of introducing two nitrogens in close proximity to the electron rich flanking rings and to compare the solid state structure with the calculated structure. A few modifications were necessary for the preparation of the pyrimidyl analog, primarily because 2-ethynylpyrimidine was not commercially available. In the synthesis of **5**, a selective Sonogashira coupling of trihalide **9** and trimethylsilylacetylene followed by deprotection under basic conditions provided free alkyne **12b** (Scheme 3.3). Commercially available 2-chloropyrimidine was converted to 2-iodopyrimidine by treatment with hydriodic acid at 0 ˚C. Without purification of the pyrimidine, the Sonogashira reaction with **12b** afforded pyrimidyl alkyne **13**. Subsequent Negishi coupling yielded **5**.

Scheme 3.3

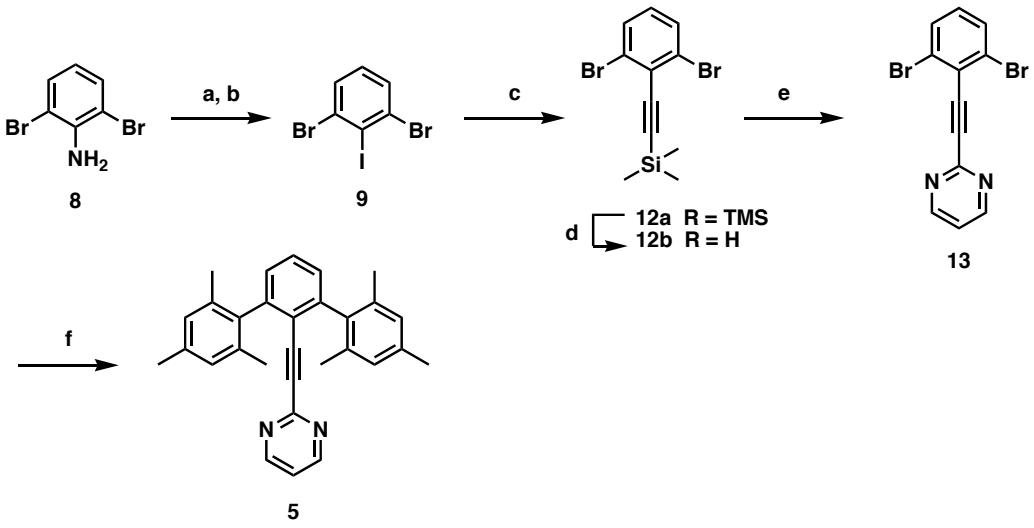

a. $NaNO_2$, HCl b. KI, H_2O, 83% c. $Pd(PPh_3)_2Cl_2$, CuI, TEA, 76% d. K_2CO_3, MeOH, 64%
e. 2-iodopyrimidine, $Pd(PPh_3)_4$, TEA, 61% f. ArZnCl, $Pd(PPh_3)_4$, THF, 23%

3.2.7 Crystal Structure Properties

Crystal structures were obtained for all of the umbrella molecules and their basic geometric features were investigated, particularly the torsion angle between the central rings (Figure 3.7) and the shortest edge-to-face distance (Figure 3.8). The angle between the flanking rings and the triple bond angles (Figure 3.9) were also determined.

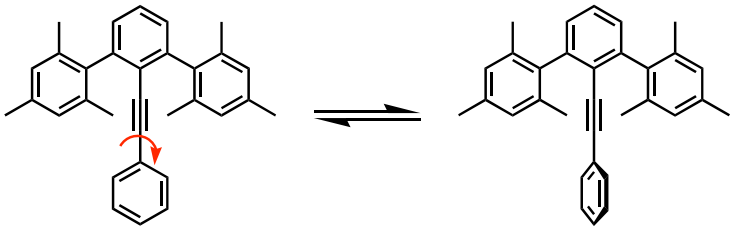

Figure 3.7 The torsion angle for the central ring was determined in the crystal structure of each umbrella structure.

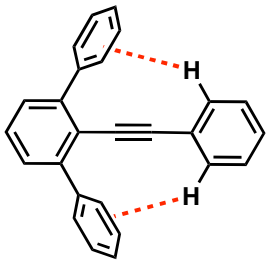

Figure 3.8 In each structure, the distance from the ortho hydrogens to the centroid of the nearest flanking ring was determined.

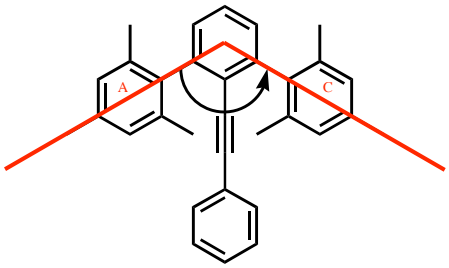

A)

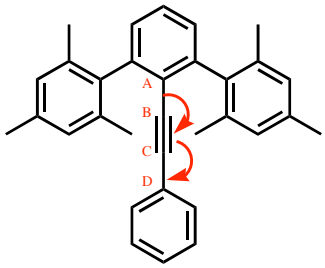

B)

Figure 3.9 A) The angle between flanking rings **B)** The two triple bond angles ∠ABC and ∠BCD

3.2.8 Crystal Structure of Phenyl Umbrella

Slow evaporation of a methylene chloride solution of **1** yielded crystals suitable for X-ray diffraction. The structure shows a shortest edge-to-face distance of 3.39 Å and the torsion angle between the B and D rings is 34.32°. The triple bond angles are both 173.17° and the angle between the flanking rings is 68.80°. The short edge-to-face distance could potentially allow polar-π interactions.

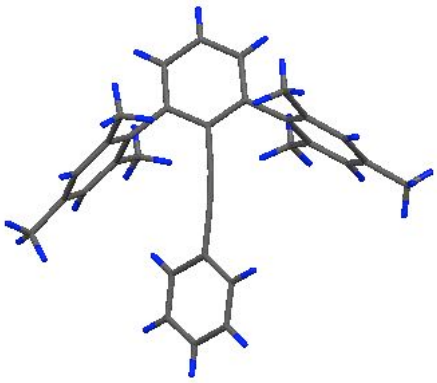

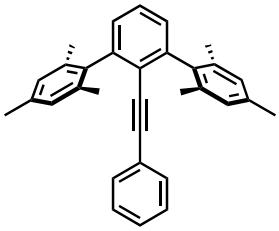

1

Figure 3.10 X-ray structure of **1**

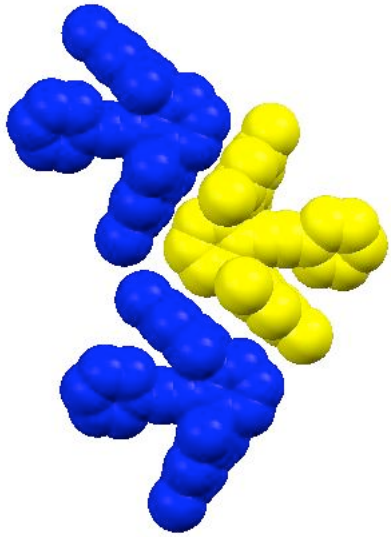

Figure 3.11 Crystal packing viewed along the a axis. The molecules stack in a head-to-tail fashion.

Viewing along the crystallographic a axis reveals that the molecules stack in a head-to-tail fashion (Figure 3.11). However, in the layers immediately above and below, the molecules are stacked directly on top of each other (Figure 3.12).

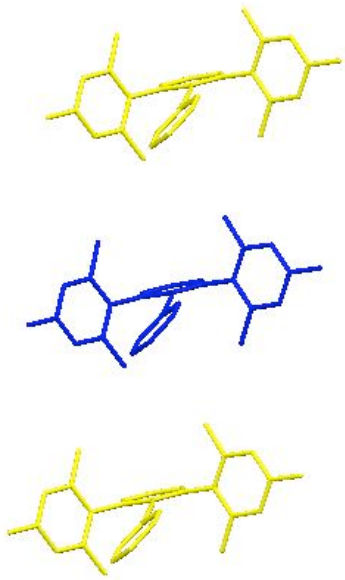

Figure 3.12 Each molecule shown in figure 3.11 also has a molecule stacked directly on top of it.

3.2.9 Crystal Structure of Pyridyl Umbrellas

Crystals of **2a** suitable for x-ray diffraction were obtained by slow evaporation of a methylene chloride solution of the compound. The crystal structure indicates a shortest edge-to-face distance of 4.21 Å and the torsion angle between the central rings is dramatically reduced to 23.29°. The triple bond angles are 176.86° and 177.67° and the angle between the flanking rings is 60.81°.

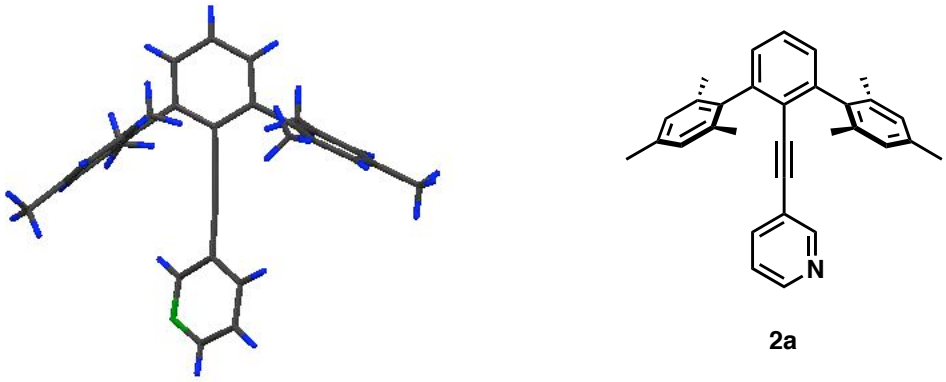

Figure 3.13 X-ray structure of **2a**

In the case of **2a**, the crystal packing shows two alternating arrangements of molecules. In both arrangements, the molecules are stacked directly on top of each other, but the two rows of molecules are nearly perpendicular (Figure 3.14).

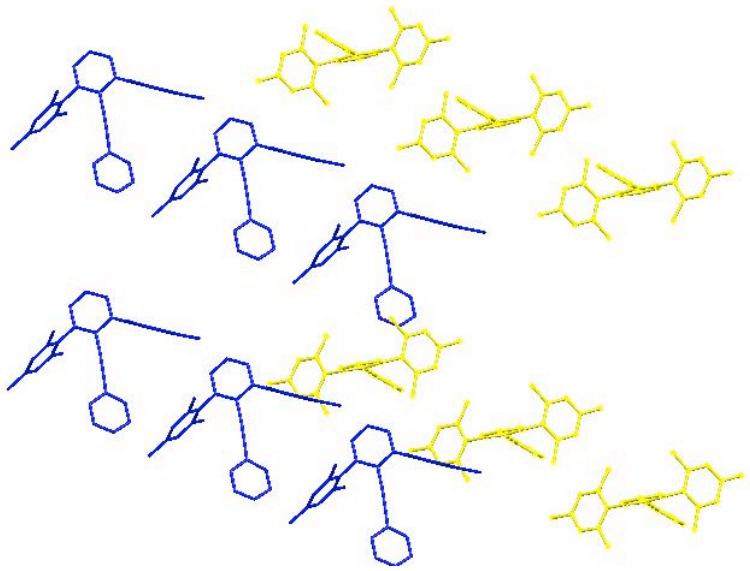

Figure 3.14 Packing diagram of **2a**, in which molecules are aligned in two alternating patterns

A crystal structure of **2b** was obtained, indicating an edge-to-face distance of 3.35 Å. The torsion angle between the central rings is 33.96°. The triple bond angles are 174.12° and 171.03° and the angle between the flanking rings is 72.54°. The increase in this angle relative to **1** is consistent with a repulsive interaction between the lone pair on the nitrogen and the electron rich flanking rings. The angle between the flanking rings is also significantly larger than in **2a**.

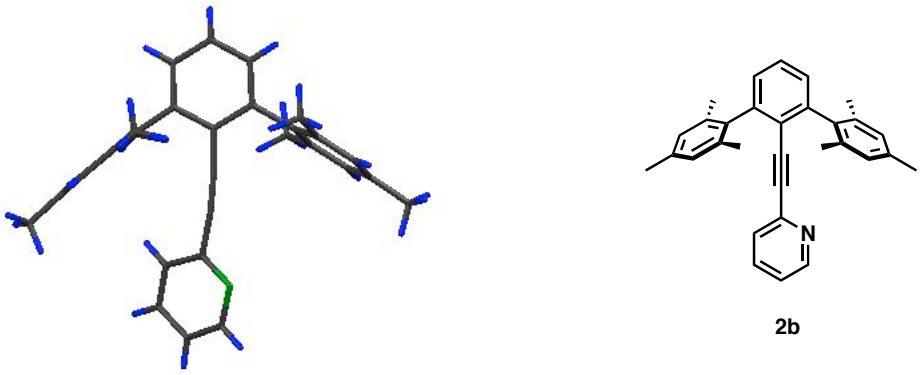

Figure 3.15 X-ray structure of **2b**

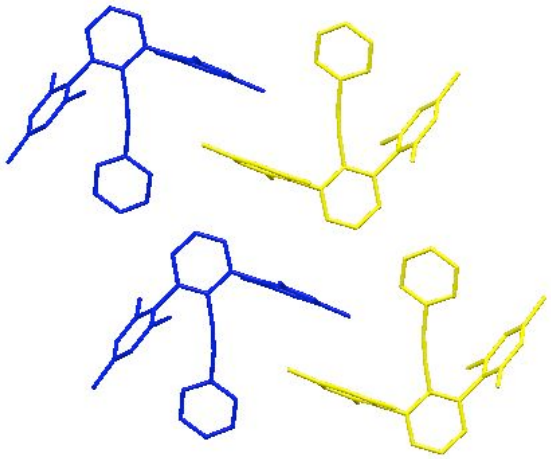

Figure 3.16 The packing diagram of **2b**, showing interdigitation of adjacent molecules

The crystal packing of **2b** indicates the same arrangement as in **1**. However, in addition to the head-to-tail packing, there is also interdigitation of adjacent molecules (Figure 3.16). The D ring appears to be twisting to avoid the nearest flanking ring of the neighboring molecule.

3.2.10 Crystal Structure of Pyrimidyl Umbrella

A crystal structure of **5** was obtained by slow evaporation of a methylene chloride solution of the compound. There is no edge to face contact in this case because there are no hydrogens in the appropriate positions. The torsion angle

between the central rings is 47.36° and the angle between the flanking rings is 77.32°. The presence of a second nitrogen in close proximity to the flanking rings further increases this angle relative to **2b**. The triple bond angles in this case are 180.00° and 177.03°. The packing diagram of **5** shows the molecules are stacked head to tail, but the A and C rings are interdigitated with each other (Figure 3.18).

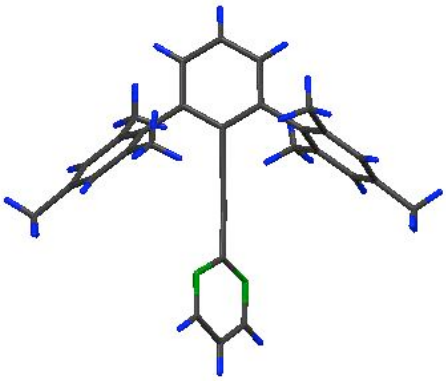

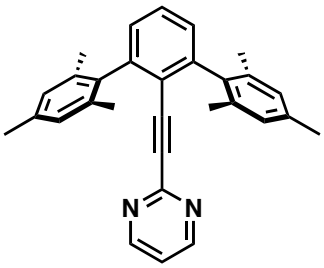

5

Figure 3.17 X-ray structure of **5**

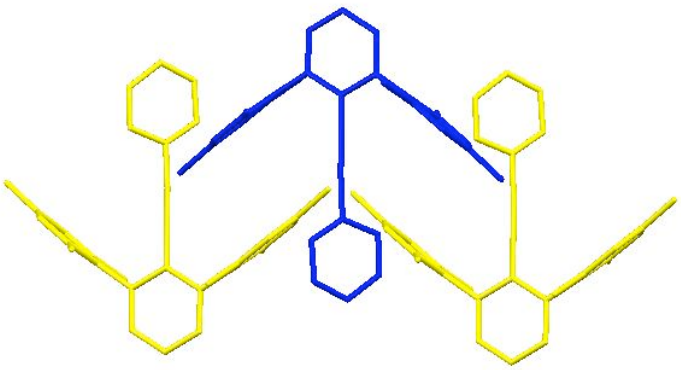

Figure 3.18 Packing diagram of **5**. The molecules are aligned in a head-to-tail fashion and there is significant interdigitation.

For comparison, structural information for all the compounds is summarized in Table 3.3. The results show the increase in the angle between flanking rings going from **1** to **2b** to **5**. The edge-to-face distance is slightly shorter in **2b** than **1**, and both of these distances are significantly shorter than the edge-to-face distance in **2a**. The torsion angle in **5** is much higher than in the other three derivatives.

Table 3.3 Structural Parameters from Crystal Structures of Umbrella Molecules

Compound	Angle between Central rings	Angle between Flanking Rings	Triple Bond Angles	Triple Bond Length	Edge to face Distance
1	34.32	68.80	173.17 173.17	1.203	3.389
2a	23.29	60.81	176.86 177.67	1.201	4.208
2b	33.96	72.54	174.12 171.03	1.203	3.353
5	47.36	77.32	180.00 177.03	1.199	---

3.3 Sandwich Structures

The umbrella molecules contain two potential sites for edge-to-face interactions and the crystal structures indicated an appropriate geometry for these interactions to occur. However, the calculated rotational barriers were quite low, suggesting that VT NMR could not be used to measure the barriers. We postulated that converting from an umbrella structure to a sandwich structure, in which there are four potential sites for interaction rather than two, would sufficiently increase the rotational barrier such that it could be evaluated experimentally (Figure 3.19). Based on our previous assumption of additivity, the rotational barrier should increase by 1-2 kcal/mol due to the two additional edge-to-face interactions as well as the barrier increase going from tolan to "ditolan".

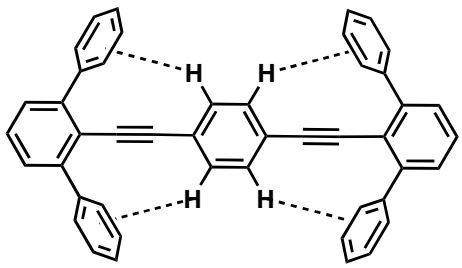

Figure 3.19 Potential edge-to-face interactions in sandwich structure

3.3.1 Rotational Barriers in Phenyl Sandwich

As before, the rotational barrier of phenyl sandwich **14a** was calculated prior to starting the synthesis. The coplanar conformation was stabilized by 3.5 kcal/mol relative to the twisted one. Hessian calculations showed the coplanar conformation was a minimum and the twisted conformation was a transition state. For comparison, the rotational barrier was also determined for "ditolan" **15**, which gave a value of 1.2 kcal/mol. Once again, the energy of a single polar-π interaction was extrapolated from this calculation. Each interaction was found to be worth 0.55 kcal/mol, almost exactly the same value found in phenyl sandwich **1**. The fact that the barrier increase from **15** to **14a** is exactly twice the energy increase going from tolan to **1** makes a strong case for the linear additivity of these interactions.

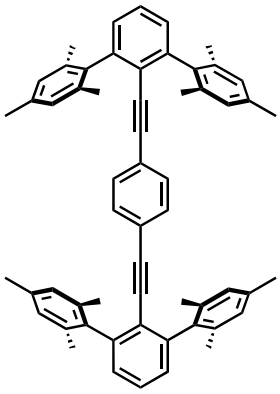

14a

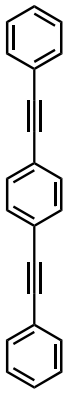

15

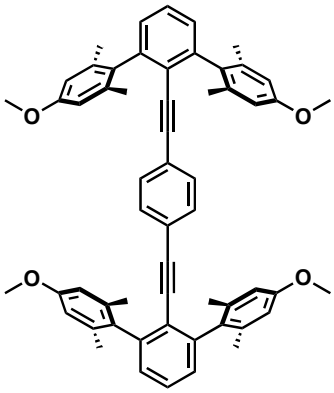

14b

A calculated barrier of 3.5 kcal/mol again suggests that VT NMR spectroscopy will not be a good method for evaluating the rotational barrier, but further supports the small energetic contribution of edge-to-face interactions. Nevertheless, the intention was to go forward with the synthesis of **14b** in order to determine the solid state properties of the molecule. It was believed that **14b** would provide the opportunity for further structural elaboration via deprotection of the methoxy ethers. One could imagine, for example, alkylating the free phenols and tethering the end groups. However, for the sake of consistency in the calculations, the

barrier to rotation was determined for **14a**. The synthesis of pyridyl sandwich **16** was also undertaken to provide an appropriate candidate for VT NMR spectroscopy, in the event that such measurements prove useful.

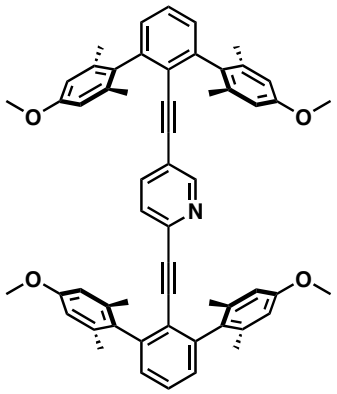

16

3.3.2 Sandwich Retrosynthesis

The retrosynthesis of the phenyl sandwich essentially involves the same disconnections as that of the phenyl umbrella. In this case, two unique aryl-alkyne bonds must be broken as well as a total of four aryl-aryl bonds. In the previous synthesis of **1**, the tolan unit was constructed first and the flanking groups were added afterwards. Once again, this general route was pursued, which leads to two basic possibilities. First, the final product could come from a fourfold addition of flanking rings to a tetrahalo "ditolan" core. Alternatively, the product could be formed by the addition of two equivalents of a terphenyl terminal alkyne to a 1,4-substituted benzene (Figure 3.20). In the synthesis of pyrimidyl umbrella **5**, Sonogashira reaction between trihalide **9** and trimethylsilyl acetylene produced dibromoalkyne **12a**. This molecule could serve as a precursor for the synthesis of a terphenyl terminal alkyne and subsequent addition of benzene would yield the desired product.

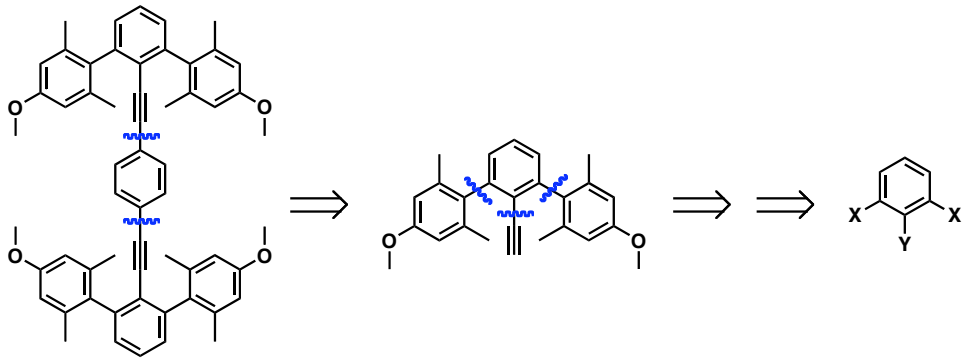

14b

Figure 3.20 Retrosynthesis of **14b** with proposed disconnections

3.3.3 Synthesis of Phenyl Sandwich

As with the previous series, the simple phenyl derivative was synthesized first. Starting from trihalide **9**, selective Sonogashira coupling produced **12a**. Subsequent Negishi coupling with the protected alkyne and the zincate of bromomanisyl gave **17a**. Deprotection under basic conditions yielded desired terphenyl terminal alkyne **17b**. Sonogashira reaction with 1,4-diiodobenzene gave **14b** in moderate yield.

Scheme 3.4

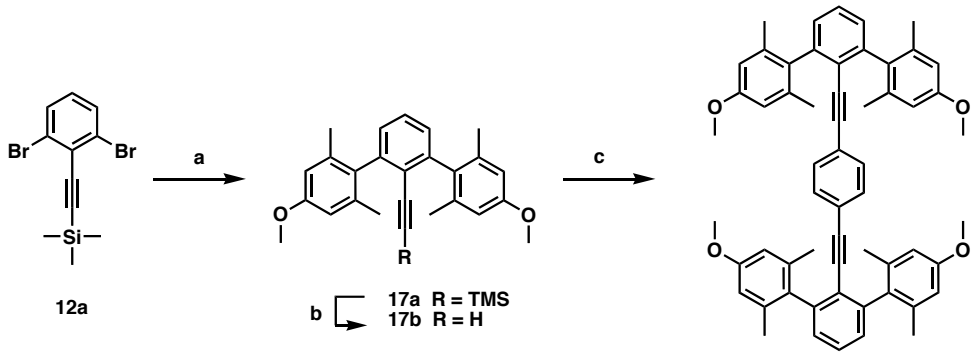

12a

14b

a. ArZnCl, $Pd(PPh_3)_4$, THF, 65% b. K_2CO_3, MeOH, 92% c. Diiodobenzene, $Pd(PPh_3)_4$, CuI, TEA, 38%

3.3.4 Synthesis of Biphenyl Sandwich

Following the synthesis of **17b**, the diarylalkyne was used to produce several related compounds. Sonogashira reaction with 4,4'-diiodobiphenyl also gave the desired sandwich structure **18** (Scheme 3.5).

Scheme 3.5

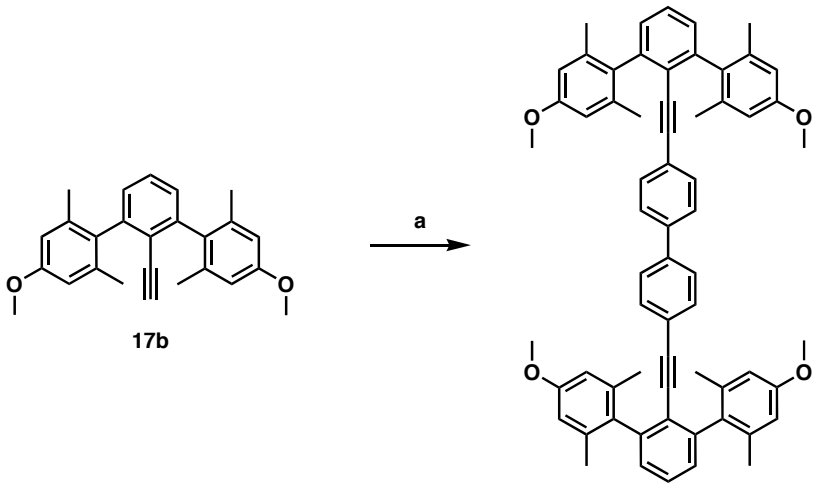

a. 4,4'-Diiodobiphenyl, $Pd(PPh_3)_4$, CuI, TEA, 34%

3.3.5 Synthesis of Pyridyl Sandwich

A similar synthetic method was used for the preparation of the asymmetric pyridyl derivative needed for variable temperature NMR studies. In this case, the reaction was initially attempted on commercially available 2,5-dibromopyridine. However, only single addition at the 2 position took place. To circumvent this problem, lithiation followed by iodine quench of 2,5-dibromopyridine produced 2-bromo-5-iodopyridine quantitatively. The Sonogashira reaction between diaryl alkyne **17b** and the dihalopyridine yielded **16** (Scheme 3.6).

Scheme 3.6

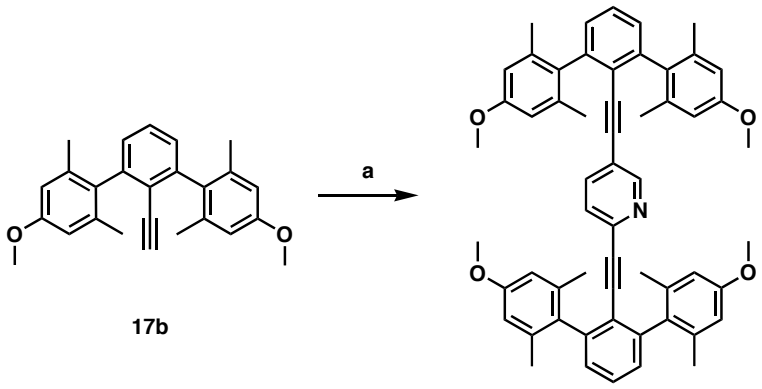

17b

16

a. 2-Bromo-5-iodopyridine, $Pd(PPh_3)_4$, CuI, TEA, 38%

3.3.6 Crystal Structure Properties

Crystal structures were obtained for the series of sandwich molecules, and, as before, the basic geometric properties of the structures were studied. The same geometric parameters defined in section 3.2.7 were investigated for this series of compounds.

3.3.7 Crystal Structure of Phenyl Sandwich

In the crystal structure of **14**, the three central rings are nearly coplanar with an end-to-end torsion angle of only 7.57° (Figure 3.21). The shortest edge-to-face distance is 3.22 Å, slightly closer than the distances in the umbrella structure. The angle between flanking rings is 73.39° and the triple bond angles are 174.17° and 174.57°, causing some twisting in the molecule along the central axis. In the packing diagram, the molecules are staggered, and the flanking rings of adjacent molecules are interdigitated (Figure 3.22).

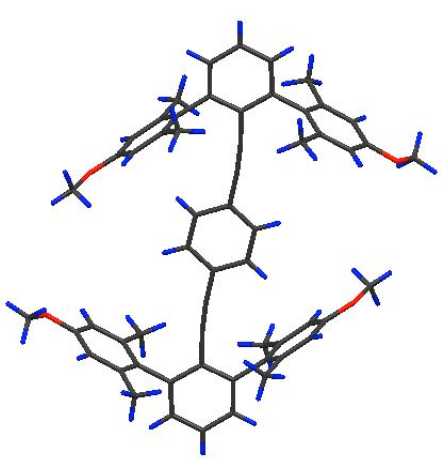

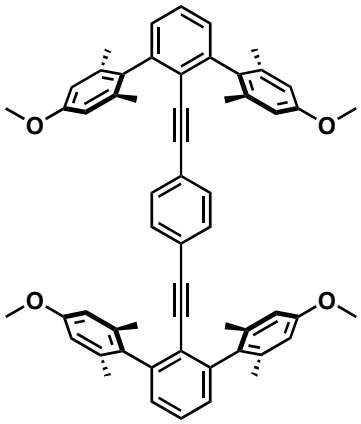

14

Figure 3.21 X-ray structure of **14**

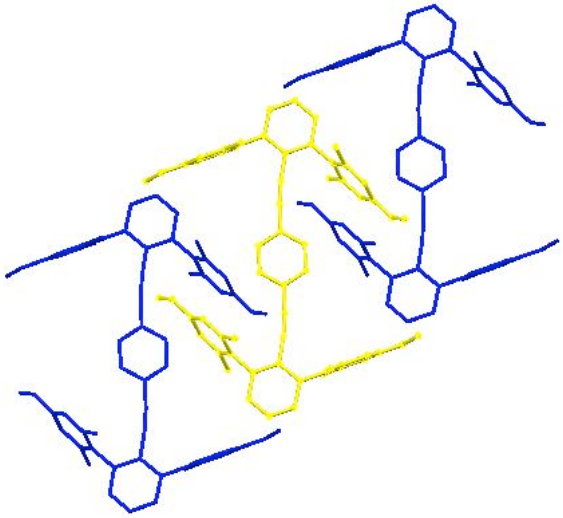

Figure 3.22 Crystal packing diagram of **14**. The adjacent molecules are interdigitated with each other.

3.3.8 Crystal Structure of Biphenyl Sandwich

The crystal structures of **14** and **18** are quite similar as the central rings in both structures are nearly coplanar. The angle between the biphenyl rings is 14.23°. The angles between each of the biphenyl rings and each of the central rings are 10.87° and 15.02°. The angle between the flanking rings is 68.57° and the triple bond angles are 171.17° and 174.58°. The overall end-to-end twisting between the top and bottom rings is 0.81° indicating that the two terphenyl ends are almost completely coplanar.

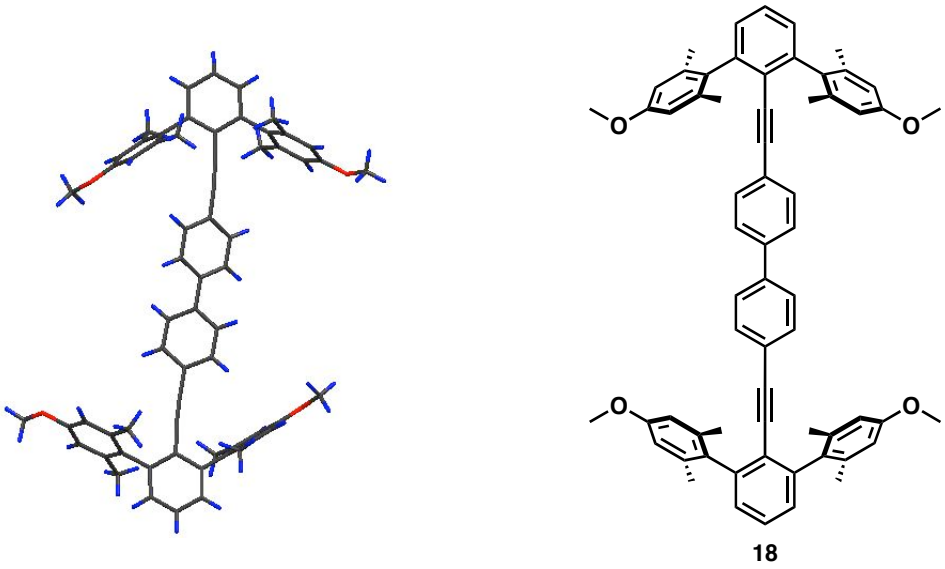

18

Figure 3.23 X-ray structure of **18**

3.3.9 Crystal Structure of Pyridyl Sandwich

The crystal structure of **16** also shows the central rings to be nearly coplanar. In this case, the angle between rings is 6.70° and the shortest edge-to-face distance is 3.25 Å. The angle between the flanking rings is 63.96° and the triple bond angles are 173.99° and 174.47°. In the crystal packing diagram, the terphenyl subunits of adjacent molecules are arranged head-to-tail (Figure 3.25). In addition, there is also interdigitation of neighboring molecules (Figure 3.26).

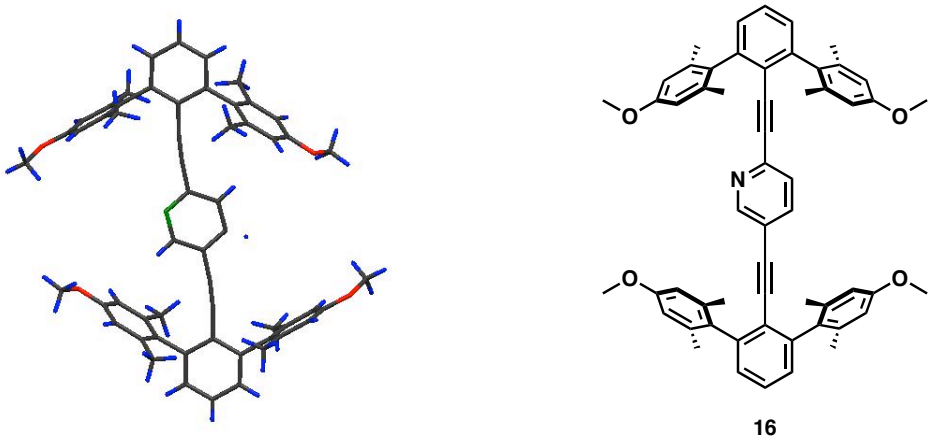

16

Figure 3.24 X-ray structure of **16**

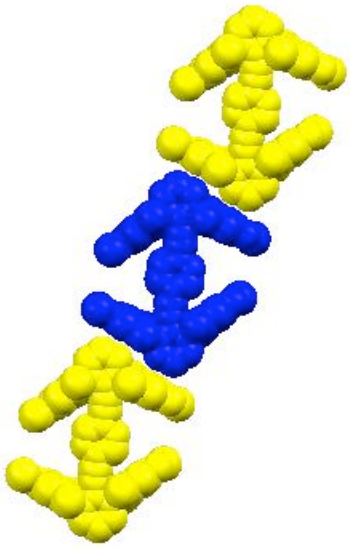

Figure 3.25 The terphenyl subunits in **16** are arranged in a head-to-tail fashion.

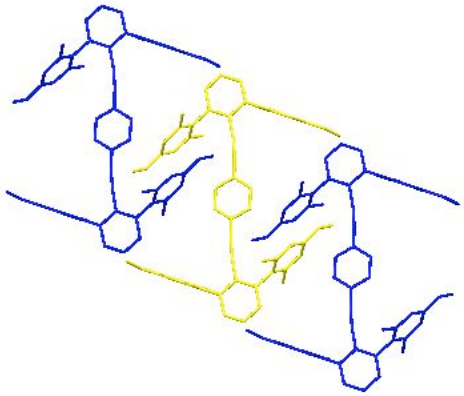

Figure 3.26 Crystal packing diagram of **16**, indicating close contacts between adjacent molecules.

3.3.10 Synthesis of Terphenyl Alkyne Dimer

The crystal structures of the sandwich compounds indicated near coplanarity of the central rings as well as significant interdigitation of adjacent molecules. In light of the planar structures, we considered the structural requirements necessary to induce end-to-end twisting in these molecules. It was postulated that directly coupling terphenyl alkyne **17b** to itself would result in a highly twisted molecule, similar to the

systems of Toyota and coworkers. Oxidative alkyne coupling conditions were used to yield **19** in high yield.

Scheme 3.7

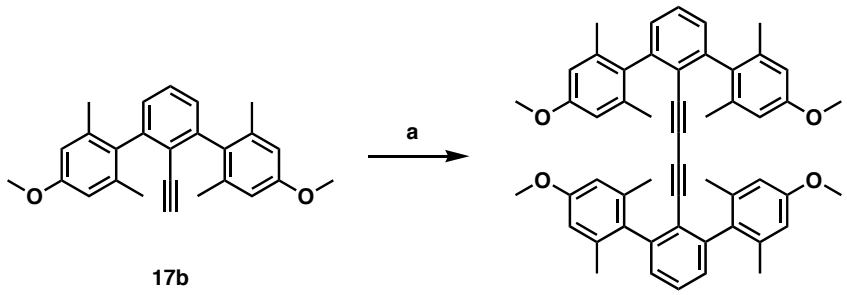

a. $Cu(OAc)_2 \cdot H_2O$, EtOH, 80%

3.3.11 Crystal Structure of Terphenyl Alkyne Dimer

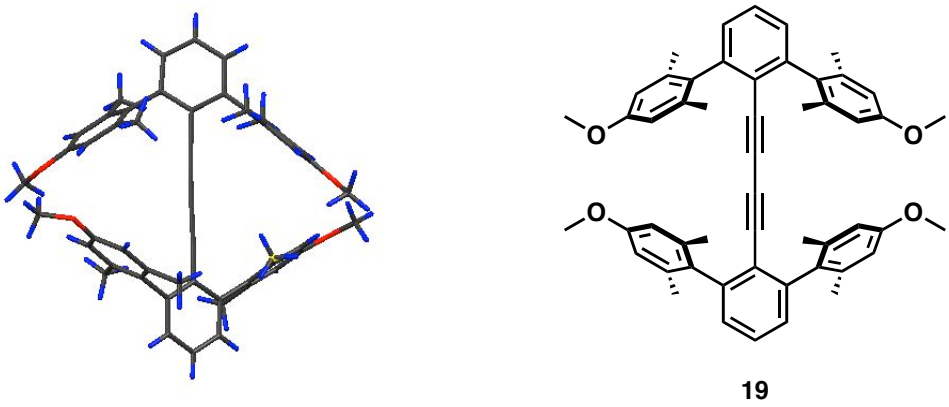

Figure 3.27 X-ray structure of **19**

From the crystal structure, it became apparent that steric interactions between the flanking groups could induce significant twisting of the molecule (Figure 3.27). The end-to-end twisting was found to be 38.60°. The crystal packing shows two orientations of the molecule, which are nearly perpendicular to each other.

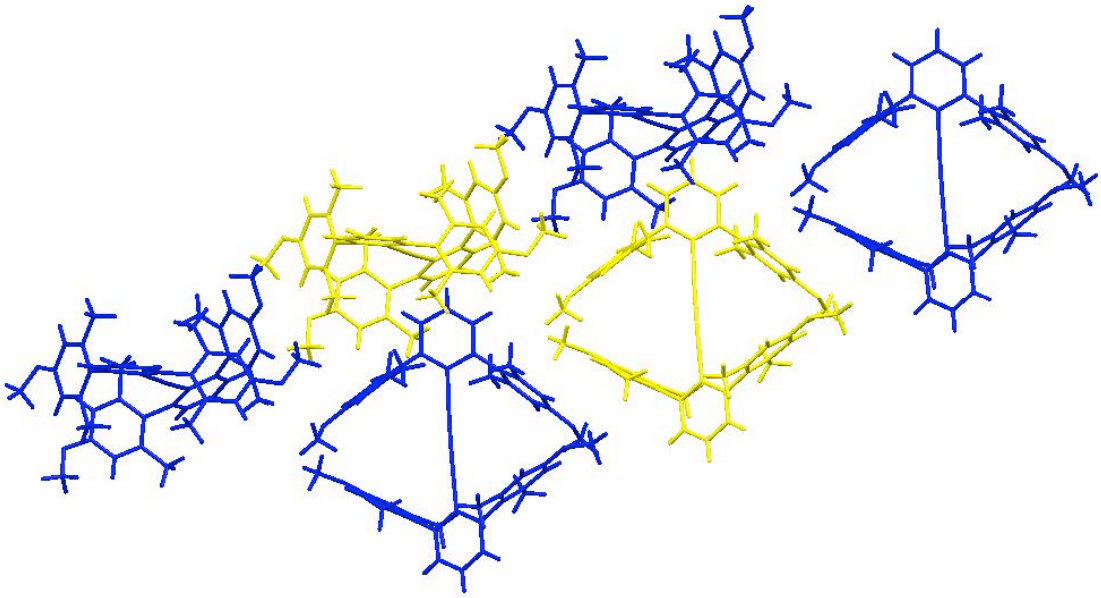

Figure 3.28 Packing diagram for **19**, indicating two orientations of the molecules. The two arrangements are nearly perpendicular to each other.

3.3.12 Calculations on Twisted Sandwich Structures

In the case of **19**, steric interactions between opposing flanking rings caused end-to-end twisting in the molecule. In contrast, the crystal structure of **14** showed near planarity across the central rings and the rotational barrier was calculated to be 3.5 kcal/mol. We postulated that inducing steric interactions by modifying the structure of **14** could also lead to significant end-to-end twisting. Calculations were conducted to determine the effect of end-to-end twisting on the rotational barrier of the central phenyl ring. In the previous calculation on **14**, the molecule went from one conformation with C_{2v} symmetry to another with the same symmetry. The terphenyl end groups were held coplanar to each other as the energetic cost of rotating the central ring 90° was determined. In a subsequent calculation, the molecule began in a conformation with C_{2v} symmetry, in which the terphenyl end groups were held orthogonal to each other and the central phenyl ring was aligned with one set of end groups. In this calculation, the cost of turning the central ring 45° was calculated

(Figure 3.29). The final conformation, with the central ring turned 45°, has D_2 symmetry. In this case, the barrier decreased significantly to 0.2 kcal/mol, nearly 1 kcal/mol less than the barrier in the parent "ditolan" **15**.

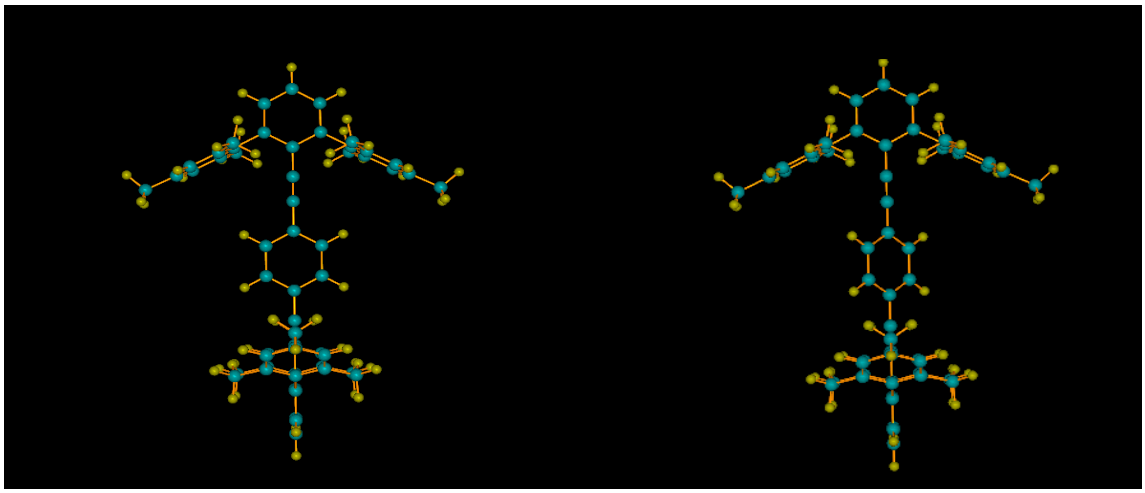

Figure 3.29 Rotational process in twisted phenyl sandwich, in which central ring is turned 45°. The first conformation has C_{2v} symmetry and the second one has D_2 symmetry.

In the coplanar conformation of **14**, rotating the central spindle 90° breaks conjugation between the three central rings and also reduces the favorable polar-π interactions between the middle ring and all four flanking groups. As a result of the loss of these interactions, there is an energy cost of 3.5 kcal/mol associated with turning the ring. Conversely, when the two terphenyl units are held orthogonal to each other, there is essentially no net energy cost associated with turning the central ring. In this higher order symmetry, the energy lost from the interactions due to turning away from one terphenyl unit is replaced by favorable interactions with the opposing terphenyl group.

Table 3.4 Rotational Barriers in Phenyl Sandwiches

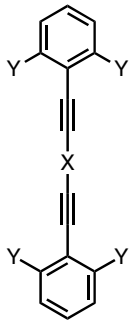

Compound	X	Y	Method / Basis Set	Barrier
15	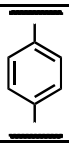	H	**RHF/ 6-31G(d,p)** **MP2 / 6-31G(d,p)**	**1.2** **1.2**
14a	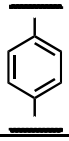	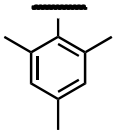	**RHF/ 6-31G(d,p)**	**3.5**
14a*	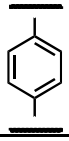	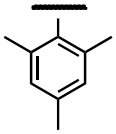	**RHF/ 6-31G(d,p)**	**0.2**

*** Flanking rings held orthogonal to each other**

Based on this series of calculations, we postulated that a molecule in which the flanking groups are held orthogonal to each other would have essentially no rotational barrier. In the previous chapter, the discussion focused on aryl alkynes and the potential use of these molecules in the construction of molecular machines. A critical distinction was made between observing the arbitrary motion of a molecule and actually controlling the bond rotation. In order to qualify as a machine, the molecule would have to respond to an external stimulus and then carry out a specific function. In the case of the phenyl sandwich, the intent is not to create a controllable machine, but rather a free molecular rotor. In future work, however, it may be possible to create a controllable rotor using the pyridyl sandwich, in which the dipole

could be addressed by an external stimulus. As previously discussed, similar dipolar rotors were synthesized and investigated by Garcia-Garibay and coworkers.[18]

The crystal structure of terphenyl alkyne dimer **19** showed significant end-to-end twisting due to steric interactions between the opposing flanking groups. It was postulated that similar interactions could be induced in the phenyl sandwich by extending the flanking groups, resulting in twisting of the molecule. Consequently, with the intent of producing a free rotor, the flanking groups were extended in order to cause steric repulsion and prevent the molecule from attaining a coplanar conformation.

3.4 Extended Phenyl Sandwich

In the extended sandwich, the goal was to introduce steric interactions between the opposing end groups in order to force the molecule into a nonplanar geometry. Each flanking group was extended by one phenyl ring, and, as a result, a few modifications to the original synthesis of **14** were necessary.

3.4.1 Synthesis of Extended Sandwich

The synthesis of the extended sandwich structure required additional steps to prepare the larger flanking groups (Scheme 3.8). Deprotection of **20** followed by triflation provided **22**, which was then used to prepare the extended flanking group. Selective Negishi coupling to give **23** proceeded in moderate yield. A subsequent Negishi coupling with protected alkyne **12a**, followed by deprotection gave desired terminal alkyne building block **25b**. Sonogashira coupling with diiodobenzene afforded **26** (Scheme 3.9).

Scheme 3.8

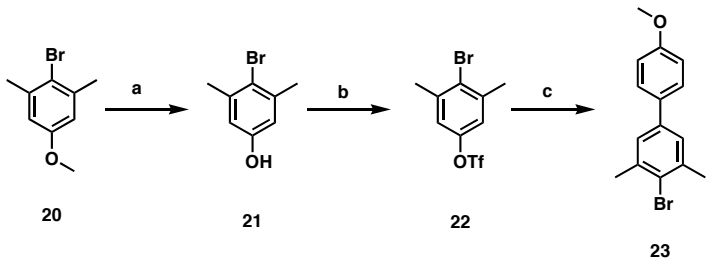

a. BBr_3, CH_2Cl_2, 94% b. $(CF_3SO_2)_2O$, CH_2Cl_2, TEA, 79% c. ArZnCl, $Pd(PPh_3)_4$, THF, 45%

Scheme 3.9

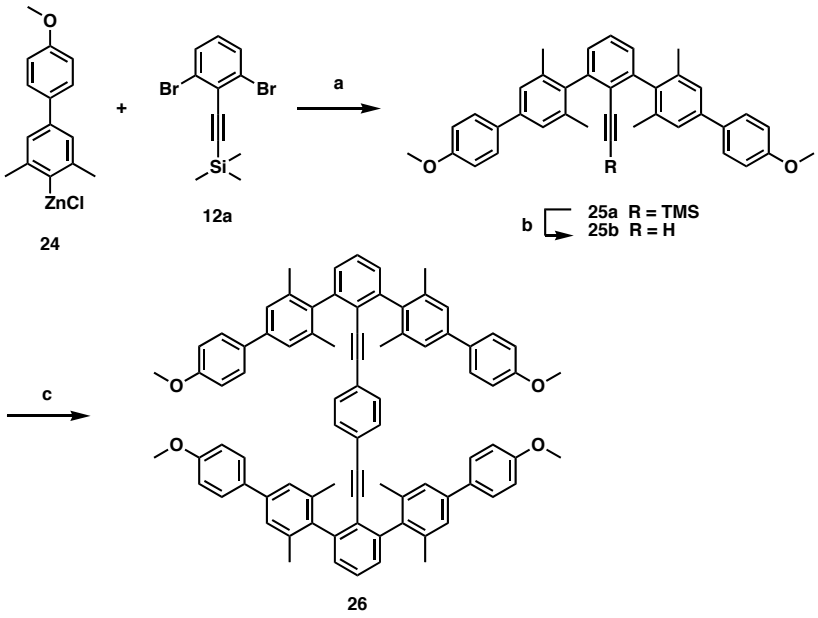

a. $Pd(PPh_3)_4$, THF, 30% b. K_2CO_3, MeOH, 92% c. Diiodobenzene, $Pd(PPh_3)_4$, CuI, TEA, 42%

3.4.2 Synthesis of Extended Alkyne Dimer

Following the successful dimer formation with terminal alkyne **17b** to form **19**, we postulated that an even more twisted structure could be obtained by dimerizing extended alkyne **25b**. Oxidative copper (II) conditions were also used in this case to yield **27**.

Scheme 3.10

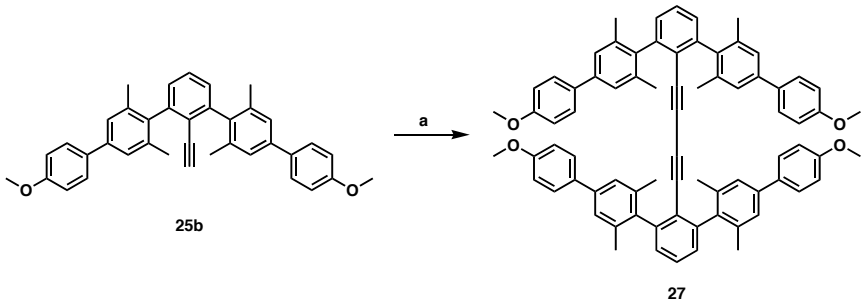

a. $Cu(OAc)_2 \cdot H_2O$, EtOH, 42%

3.4.3 Crystal Structure of Extended Phenyl Sandwich

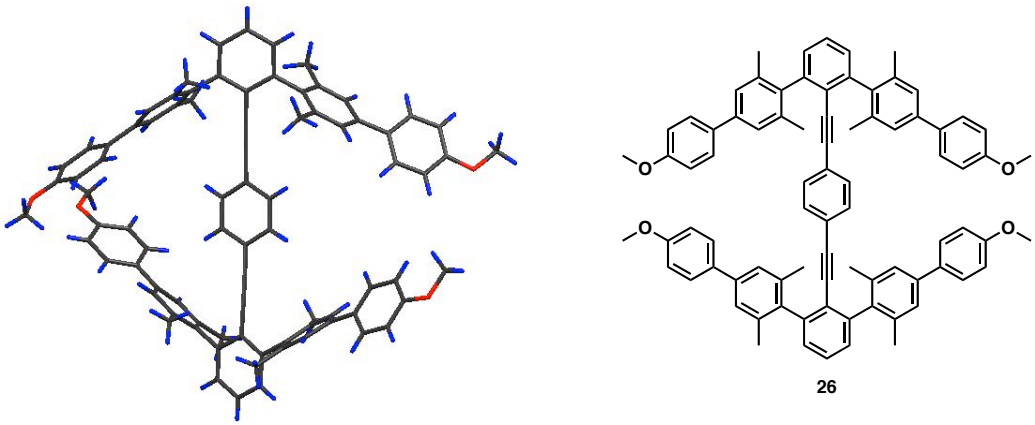

Figure 3.30 X-ray structure of **26**

Crystals of **26** were obtained by slow evaporation of a methylene chloride solution of the compound. The crystal structure of **26** differs significantly from the structure of **14**. In this case, the angle between the top and central rings increases to 33.57°. The angle between the central ring and the bottom ring is only 10.06°, but this results in an overall end-to-end twisting of more than 43°. The angle between the flanking rings is 73.39° and the triple bond angles are 178.26° and 177.57°. The closest edge-to-face contact is 4.27 Å. The space filling diagram more clearly demonstrates the extent of twisting in this molecule (Figure 3.31). The crystal packing

shows two orientations of the molecule, and can best be described as a head-to-tail arrangement (Figure 3.32).

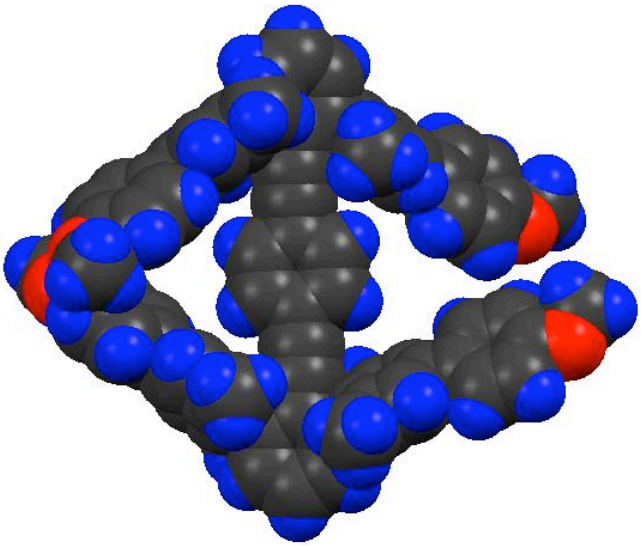

Figure 3.31 Space filling diagram of **26**

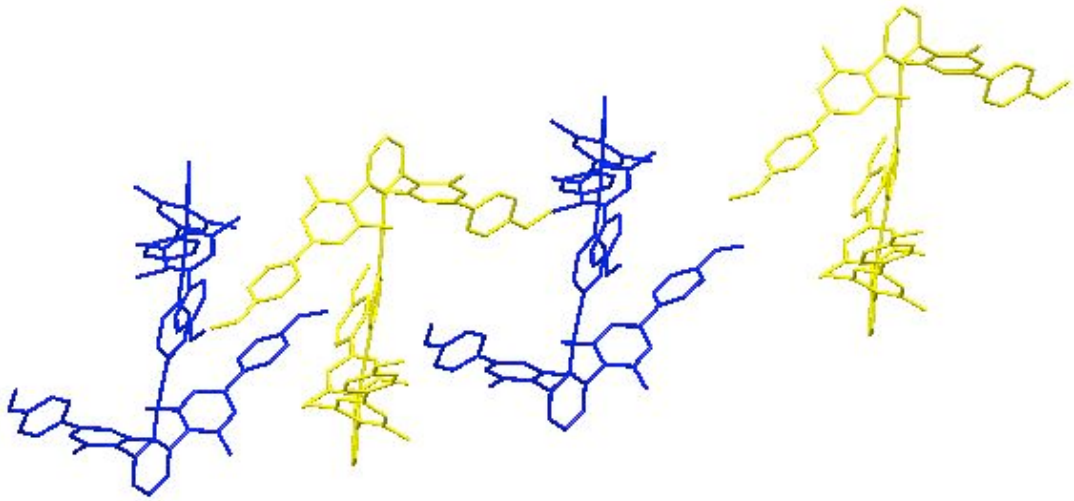

Figure 3.32 Crystal packing diagram of **26**. Adjacent molecules are oriented head-to-tail and this alternating pattern continues through the crystal lattice.

3.4.4 Crystal Structure of Extended Alkyne Dimer

The crystal structure of **27** shows a twist angle of 51.0° between the two central rings, an increase of 8° compared to **26**. The extent of twisting is seen more

clearly in the space filling diagram (Figure 3.34). The crystal packing diagram shows the molecules are arranged in rows in the lattice (Figure 3.35).

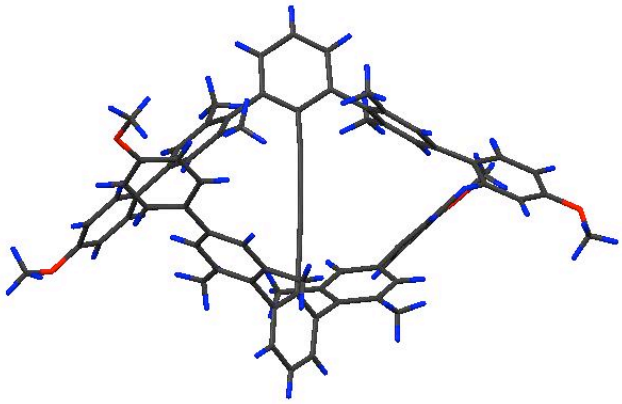

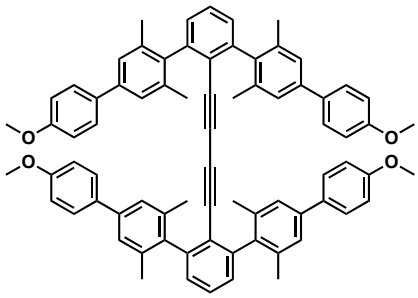

27

Figure 3.33 X-ray structure of **27**

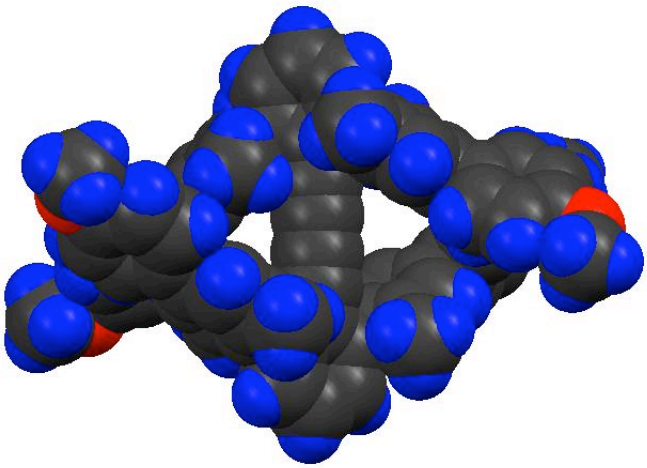

Figure 3.34 Space filling diagram of **27**

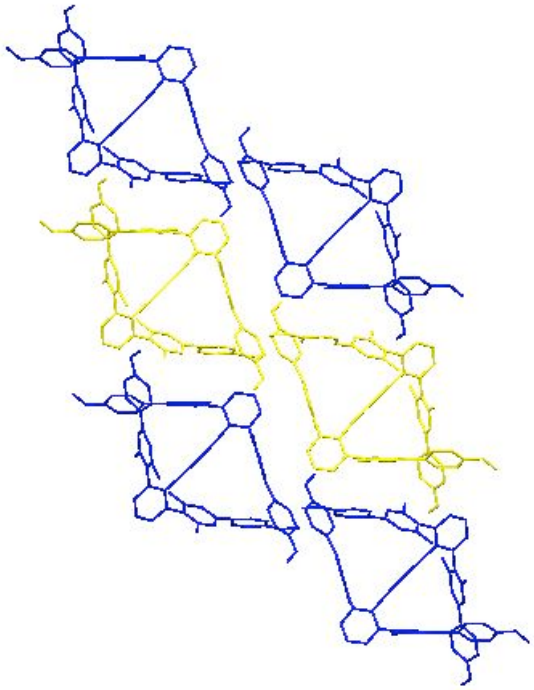

Figure 3.35 The crystal packing diagram of **27** shows the molecules are aligned in offset rows.

3.5 Cyclophanes

The synthesis of extended sandwich **26** and dimer **27** showed the extent to which steric interactions can influence the solid state conformation of these molecules. Whereas steric bulk induced nonplanarity, it was postulated that tethering the opposing end groups together in the phenyl sandwich would result in a highly planar structure. By constraining the flanking groups in this manner, it may become possible to further induce edge-to-face polar-π interactions with the central ring by pinching the flanking groups together.

When the basic molecular architecture was changed from the umbrella structure to the sandwich structure, the flanking group was changed from mesityl to manisyl. The intention was to later remove the methyl group to give the free phenol, which

would enable further structural elaboration. In particular, one could imagine forming an analogous sandwich structure, then alkylating the phenols and tethering the adjacent flanking groups together in order to form a cyclophane. The proposed structure for cyclophane **28** is shown in the retrosynthesis (Figure 3.36). The synthesis of the alkyne dimers relied on oxidative alkyne coupling, and the same methodology was proposed for macrocycle formation. It should be possible to form cyclophane **28** from the corresponding tetryne, which could be synthesized by fourfold alkylation of a tetrol sandwich. The preparation of the tetrol sandwich basically involves the same synthetic steps as the synthesis of the simple phenyl sandwich; however at some point, the flanking group ether linkages must be cleaved to yield the free phenols.

3.5.1 Retrosynthesis of Cyclophane 28

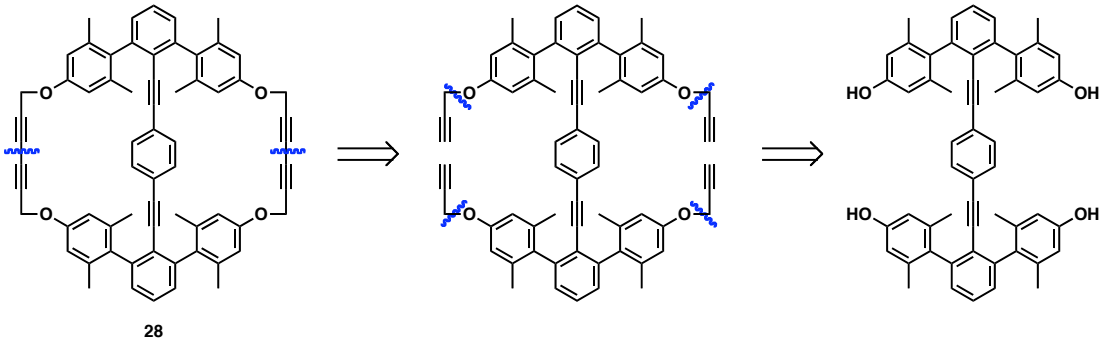

Figure 3.36 Retrosynthesis of **28**, indicating proposed disconnections

The original intention was to get to the tetrol sandwich via methyl group removal from phenyl sandwich **14**. Another alternative would be to start with a more labile protecting group to avoid the harsh conditions required for methoxy group deprotection, particularly in the presence of the sensitive alkyne moiety. Although it is certainly preferable to avoid protecting group chemistry, it was necessary to consider this route as a viable, albeit longer alternative synthetic pathway. It was

determined that the strongly acidic conditions required to remove the methoxy group were not compatible with the alkyne functionality, and, as a result, it became necessary to use a more labile protecting group in the early steps of the cyclophane synthesis.

3.5.2 Cyclophane Synthesis

Starting from phenol **21**, tert-butyldimethylsilyl chloride was used as a protecting group. Negishi coupling of this compound with protected alkyne **12a** proceeded in moderate yield. Deprotection under basic conditions gave **32** and Sonogashira coupling with commercially available diiodobenzene produced tetrol **33**. It was initially believed that one could selectively deprotect the alkyne while leaving the phenols protected. However, since the Sonogashira reaction with the free diol worked well, the alternative route was not investigated further. The alkylation of the tetrol with propargyl bromide to give **32** did not proceed in very high yield. However, the subsequent ring closure to yield **28** was successful (Scheme 3.11).

Scheme 3.11

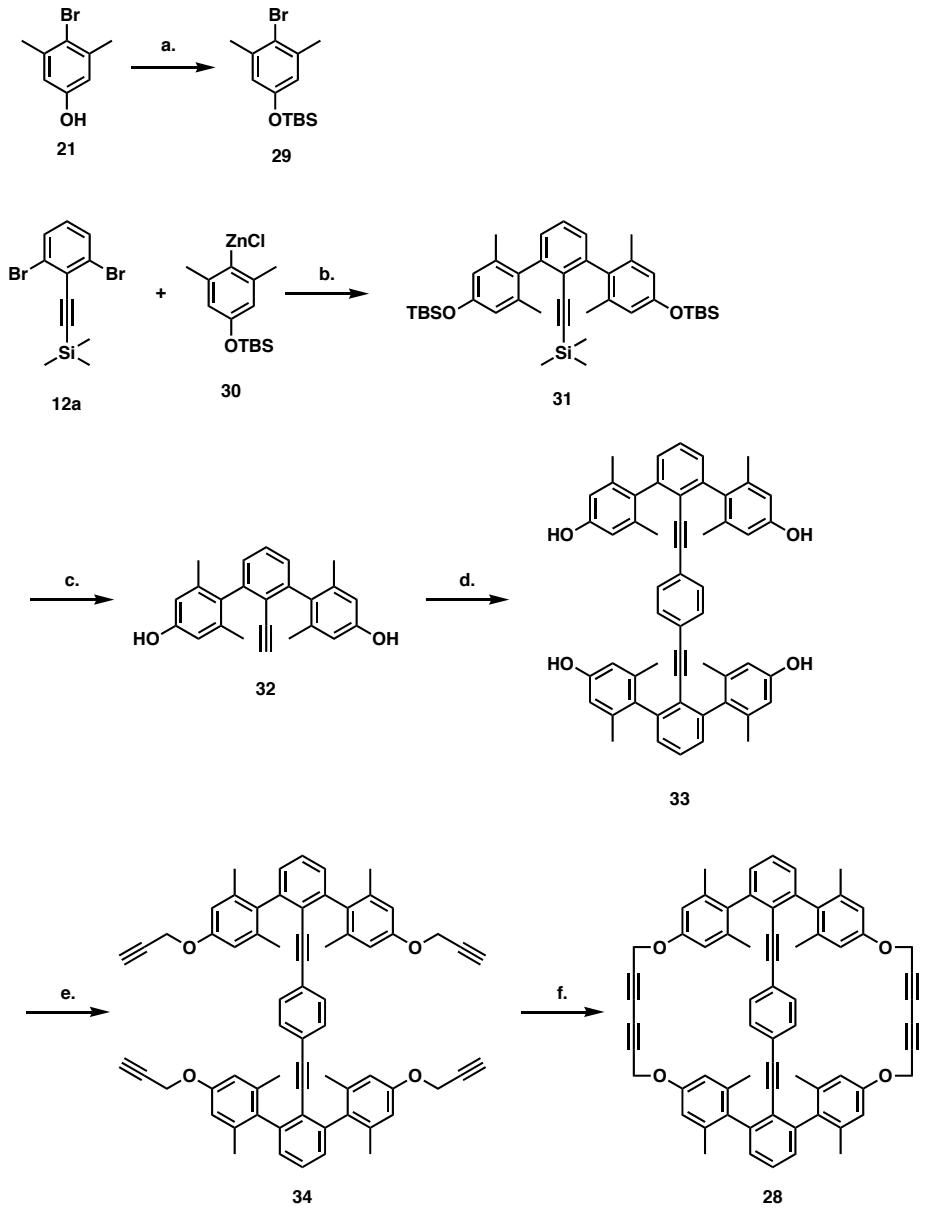

a. TBDMSCl, CH_2Cl_2, TEA, 84% b. $Pd(PPh_3)_4$, THF, 30% c. K_2CO_3, MeOH, THF, 81%

d. $Pd(PPh_3)_4$, CuI, TEA, 41% e. Propargyl Bromide, DMF, Cs_2CO_3, 18% f. $Cu(OAc)_2 \cdot H_2O$, EtOH, 40%

3.5.3 Crystal Structure of Cyclophane

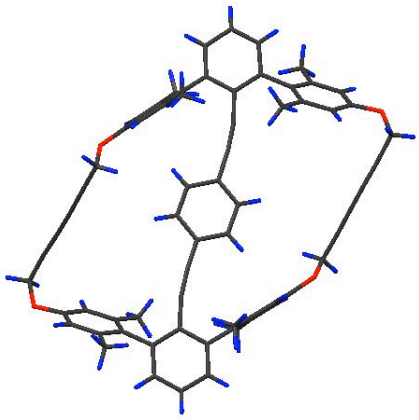

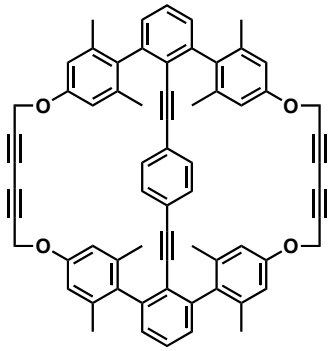

28

Figure 3.37 X-ray structure of **28**

The crystal structure of **28** indicates an almost completely coplanar structure, with a torsion angle of 3.33°. There is significant distortion on the long axis with triple bond angles of 169.46° and 173.54°. The shortest edge-to-face contact is 2.40 Å, nearly an angstrom shorter than any of the edge-to-face distances in the other compounds. In addition, the angle between the flanking rings is dramatically reduced to 50.43° compared to 68° for the simple phenyl sandwich. The space filling diagram further indicates the extent of distortion in the molecule and the close edge-to-face contacts. The packing diagram shows two orientations of the molecule. Between two molecules arranged coplanar to each other is another molecule twisted nearly 90° relative to its two neighbors.

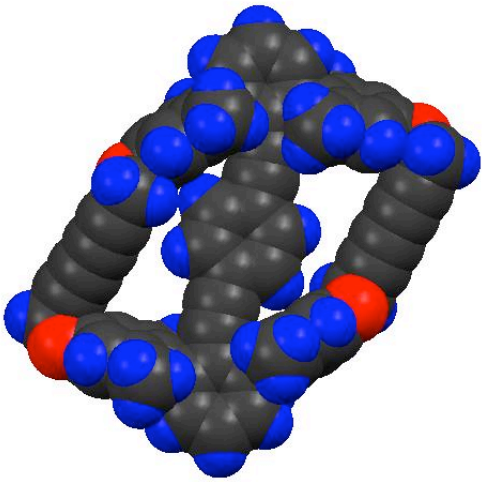

Figure 3.38 Space filling diagram of **28**

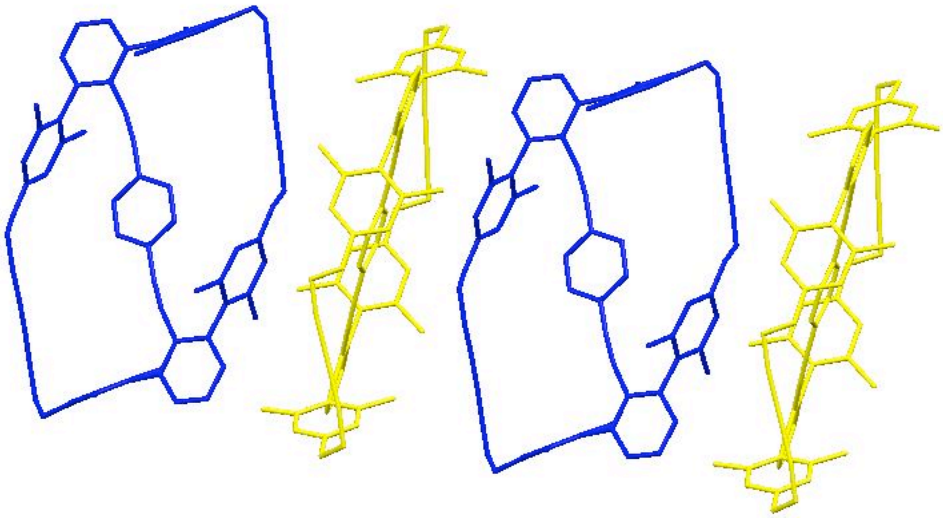

Figure 3.39 Crystal packing diagram of **28**, in which alternating molecules are perpendicular to each other.

3.6 Physical Properties

The physical properties of a representative group of the compounds were investigated. Studies included photophysical and solid state NMR measurements. The goal of the photophysical measurements was to compare the spectra with those of the parent 1,4-bisphenethynylbenzene **15** to determine the effect of maintaining coplanarity across the core. Solid state NMR measurements were conducted in order

to determine the rotational barrier of the central spindle in the solid as a function of flanking group bulk.

3.6.1 Photophysics

The absorbance and emission spectra were measured for a select group of the compounds that were synthesized. The compounds measured were the simple phenyl umbrella, **1**, phenyl sandwich **14**, extended sandwich **26**, and cyclophane **28** and the results were compared with the values for the parent "ditolan" **15**.

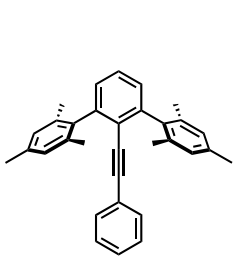

1

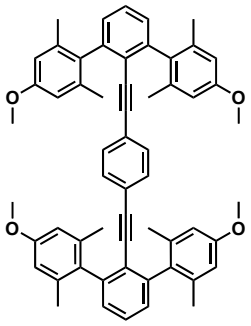

14

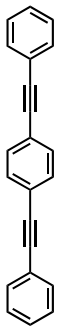

15

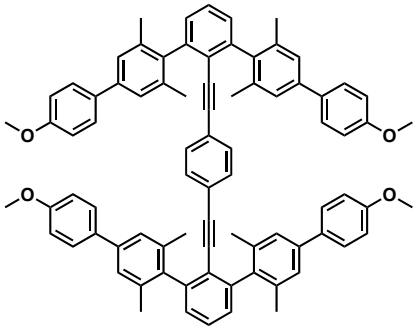

26

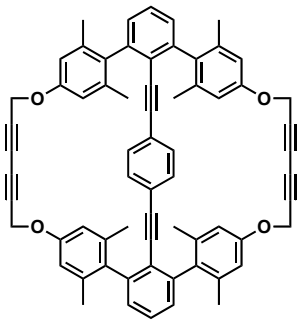

28

The absorbance spectra for all four compounds are fairly similar in shape. The sandwich structures are all red-shifted relative to the simple phenyl umbrella; however, the double peak pattern is seen in all four compounds. The extended sandwich spectrum also contains a large peak near 275 nm. It is possible that this peak can be attributed to the extended biphenyl arms in the compound.

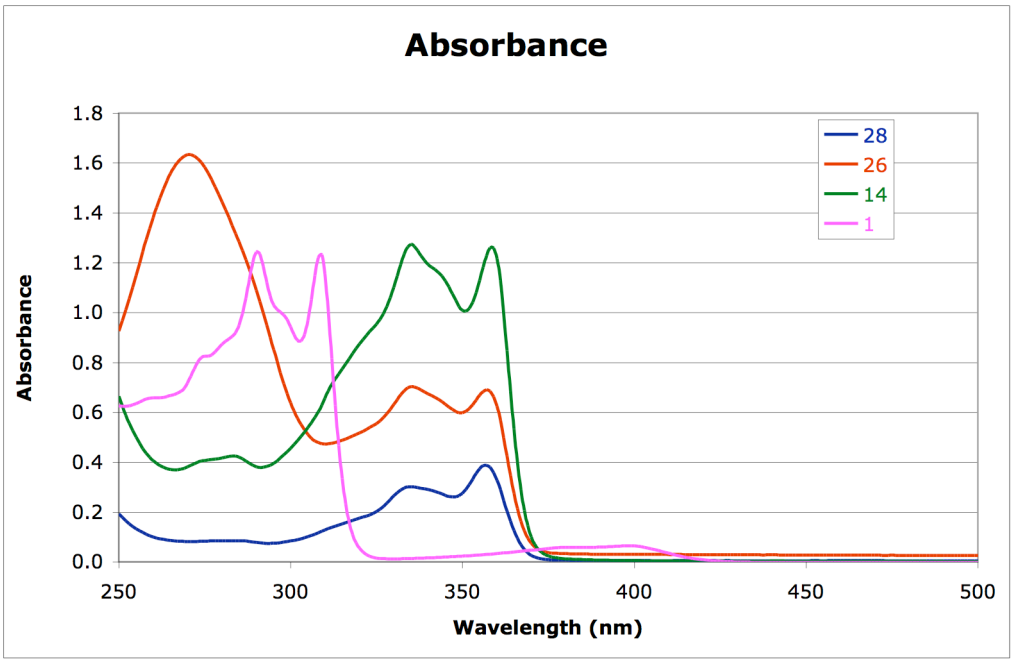

The emission spectra, lifetimes, and quantum yields were measured for **14, 26,** and **28**, using 9,10-diphenylanthracene as the quantum yield standard. The emission spectra were measured at 355 nm, and are very similar in shape for all three compounds. Across the series, there is a slight variation in quantum yield and lifetime, with the highest quantum yield and longest lifetime found for **26**. The quantum yields and lifetimes of **14** and **28** are nearly identical. In the case of **26**, coplanarity of the three central rings is not possible due to the bulky flanking groups. Conversely, the crystal structures of **14** and **28** show the three central rings to be in the same plane. In the case of **28**, the opposing flanking groups are tethered together to ensure coplanarity. For comparison, the quantum yield of the parent 1,4-bisphenethynylbenzene **15** is 0.90 and the lifetime is 0.64 nanoseconds.[19] All of the compounds, including the parent, exhibit high quantum yields and short lifetimes.

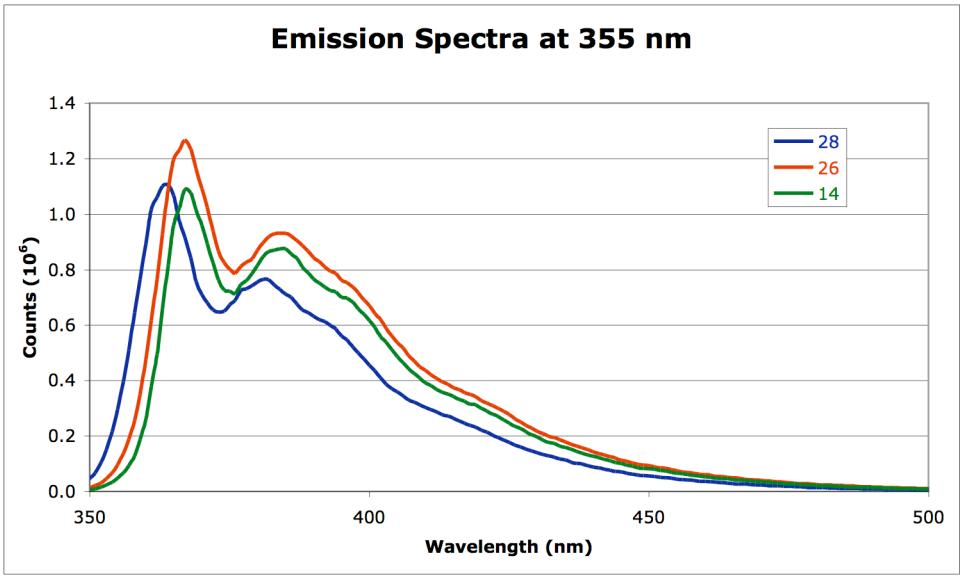

Table 3.5 Quantum Yields and Lifetimes in CH_2Cl_2

Compound	Φ	τ
15	0.90	0.64
14	0.75	0.75
26	0.86	0.94
28	0.70	0.76

3.6.2 Solid State NMR

In light of the work of Garcia-Garibay and coworkers on crystalline rotors,[20] the solid state properties of the sandwich compounds were considered. As seen previously, they prepared a series of aryl alkyne molecular rotors with the goal of designing crystalline molecular machines. Solid state rotational barriers were determined for these compounds using CPMAS NMR methods. We postulated that the same method could be used in this case to determine the rotational barriers in the solid phase.

Solid state measurements were conducted on both **14** and **26**. In the work of Garcia-Garibay, it was determined that interdigitation of adjacent molecules was the primary cause for a rotational barrier. Therefore, it was postulated that **26**, with larger

flanking groups would not have the problem of interdigitation, potentially leading to a free molecular rotor in the solid state. However, rotational barriers could not be determined in either case. Even upon heating, rotation of the central spindle was not observed, suggesting that the barriers are relatively high. Based on the number of carbon signals shown in each spectra, it was determined by symmetry that the central phenyl ring was not in motion in either molecule. The previously mentioned crystalline rotors synthesized by Garcia-Garibay and coworkers have triptycyl and trityl stators that take up space around the perimeter of each molecule, but also above and below the plane of each molecule. It is possible that in the case of **14** and **25**, this space above and below the plane of the molecule is not sufficient enough to permit free rotation. A free rotor sequestered from its surroundings is an attractive synthetic target, with potential applications in the field of molecular machines. However, solid state NMR measurements suggest that the extended sandwich is not a good prototype for the design of a free crystalline rotor.

3.7 Catenanes

Whereas the cyclophane architecture ensures that the opposing end groups are held coplanar to each other, the previously reported extended sandwich shows end-to-end twisting of nearly 45˚. However, there may still be the possibility for the end groups to pass over each other. To address this issue and ensure that a nearly orthogonal geometry is maintained, we postulated that the end-to-end twisting could be made permanent by constructing a bridged catenane, in which the interlocking rings greatly inhibit conformational flexibility.

The term catenane comes from the latin word *catena*, which means chain.[21] There are numerous recent examples of metal-templated catenane syntheses; however

the use of metal templates in catenane synthesis is relatively new.[22] The first catenane prepared using a metal templating approach was reported in 1983.[23] Prior to this time, covalent templates were used to form interlocking rings, and, even earlier, statistical threading alone was used for the formation of such structures. [24-26]

One relatively recent example showing the use of covalent templates for catenane formation is the work of Godt and coworkers, in which a carbonate template was used to orient the two halves of the molecule for catenane closure.[27] The core was then oxidatively removed to furnish the desired catenane (Scheme 3.12).

Scheme 3.12

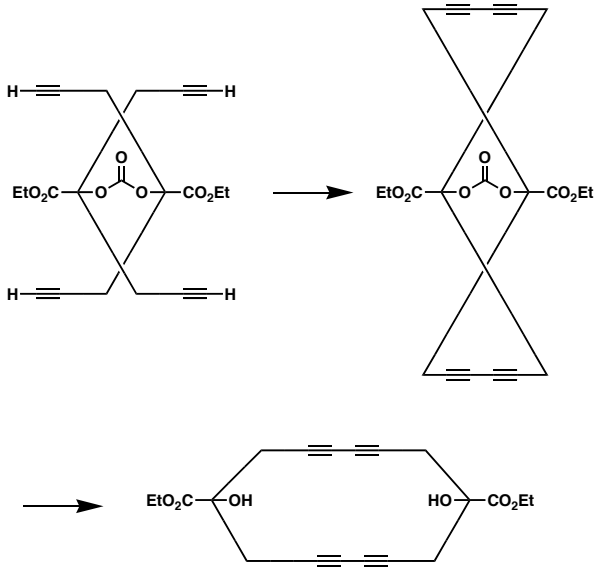

Recent work by our group involved the preparation of a series of metal-templated terpyridine catenanes (Figure 3.40).[28] Although a metal template is used to hold the two subunits in close proximity, the general structure of this precatenane is of particular interest because the core diaryl terpyridine structure is very similar to that of extended sandwich **26**. In the case of the terpyridine catenanes, the terminal phenols were alkylated with floppy linkers containing terminal alkynes. Following the

alkylation of the core diaryl terpyridine, ring closure was achieved by oxidative alkyne coupling.

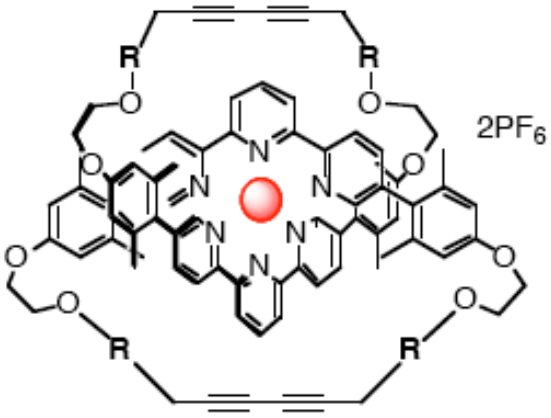

Figure 3.40 General structure of polypyridine metal-templated catenanes previously prepared by this group.

3.7.1 Catenane Retrosynthesis

It should be possible to build a system analogous to the above metal-templated catenanes using a derivative of extended sandwich **26**. In the extended sandwich, the central phenyl spindle could serve as a covalent template in place of the metal ion, as it holds the opposing pentaphenyl units in close proximity. The structure of the target molecule is shown in the retrosynthesis (Figure 3.41). The desired product could be formed from the analogous tetryne using oxidative alkyne coupling, and the tetryne intermediate would be prepared by alkylation of the extended tetrol. Using the methodology developed in the cyclophane synthesis, the formation of the extended tetrol should be possible.

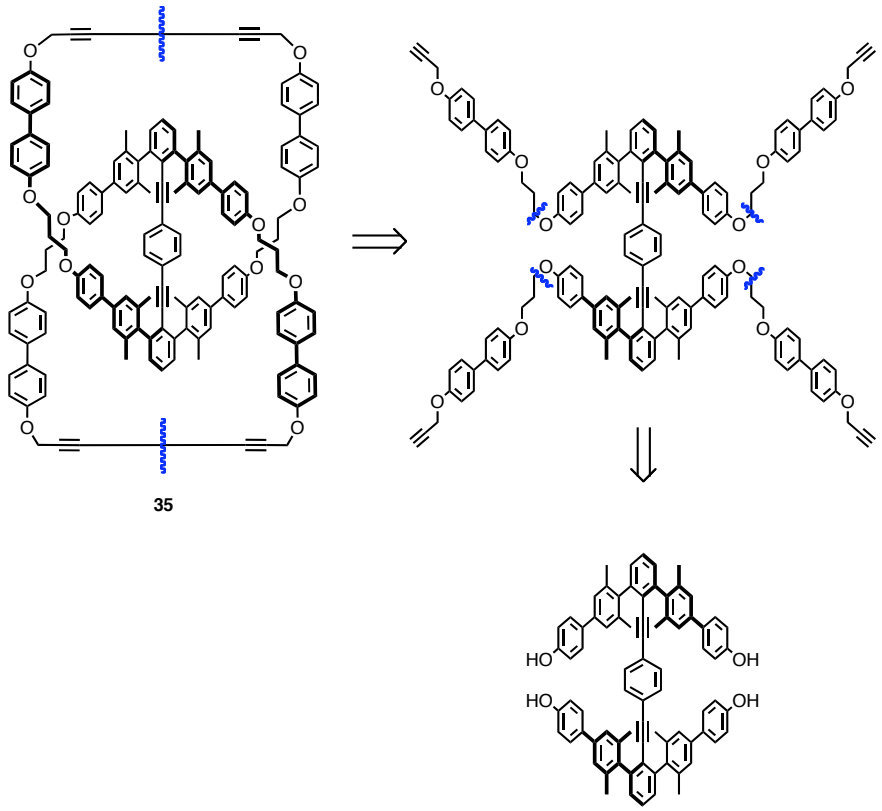

Figure 3.41 Retrosynthesis of catenane **35**, indicating proposed disconnections

3.7.2 Catenane Synthesis

The initial steps in the synthesis of catenane **35** proceeded forward with a few minor modifications relative to the previous syntheses. One significant variation was the use of the Hart Reaction. The Hart reaction provides a robust one-pot procedure for the preparation of terphenyl systems.[13] This method was applied to the preparation of extended iodide **38**. Reaction of Grignard reagent **36**, formed from previously reported **23,** with 2,6-dichloroiodobenzene, followed by iodine quench, yielded **38** in moderate yield. Subsequent deprotection with boron tribromide afforded iododiol **39**. Sonogashira reaction with the diol and trimethylsilyl acetylene gave **40a**. The silyl group was removed under basic conditions to yield **40b**.

Scheme 3.13

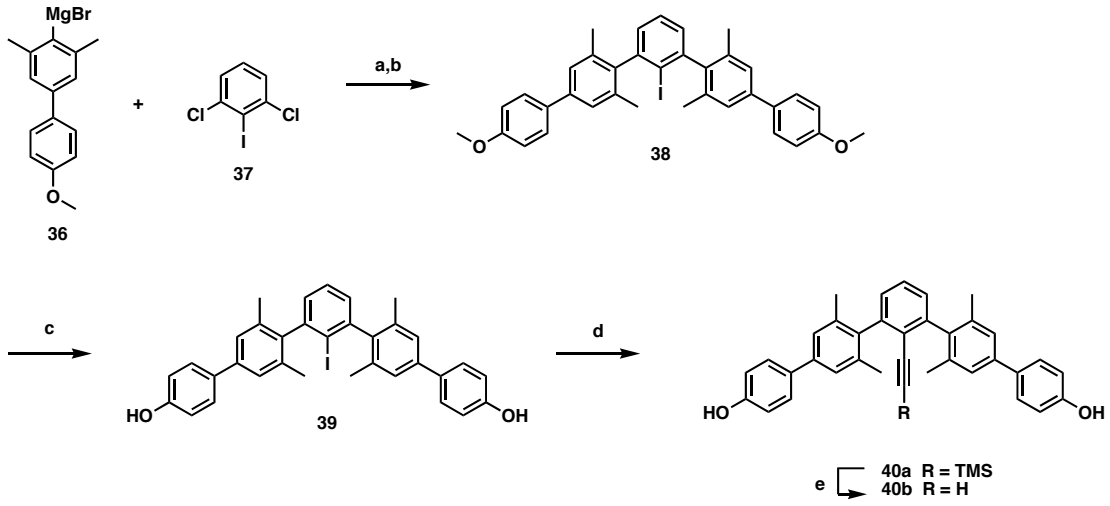

a. THF, reflux b. I_2, THF, 54% c. BBr_3, CH_2Cl_2, 95%
d. TMS Acetylene, $Pd(PPh_3)_4$, CuI, TEA, DMF, 27% e. K_2CO_3, MeOH, THF, 76%

Following the previously established method for preparing the sandwich compounds, **41** was synthesized in high yield (Scheme 3.14). As previously mentioned, 4,4'-dihydroxybiphenyl derivatives were already used by our group as linkers to close the series of terpyridine catenanes. In the case of the current target molecule, a very similar linker was synthesized (Scheme 3.15). Using sodium hydride in THF, **42** was alkylated twice to give desired linker **44**.

Scheme 3.14

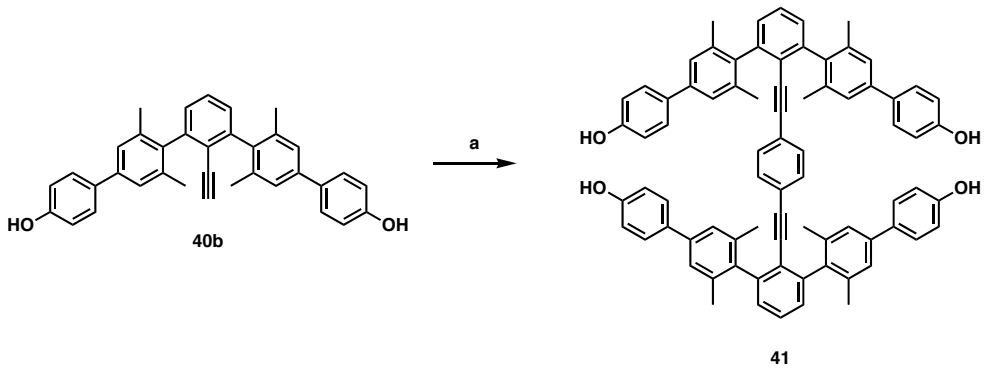

a. Diiodobenzene, $Pd(PPh_3)_4$, CuI, TEA, DMF, 60%

Scheme 3.15

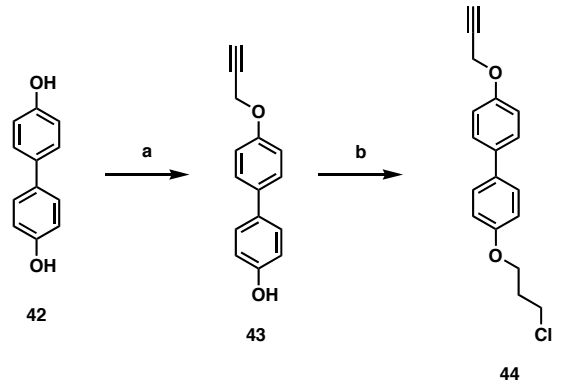

a. NaH,THF, Propargyl Bromide, 61% b. NaH, THF, Bromochloropropane, 90%

Crystals of **41** suitable for x-ray diffraction were obtained by slow evaporation of an acetone solution of the tetrol. The end-to-end twisting is this molecule is 42˚ and the structure is nearly identical to the methoxy analog. The oxygen-oxygen distances are 5.6 and 7.8 Å.

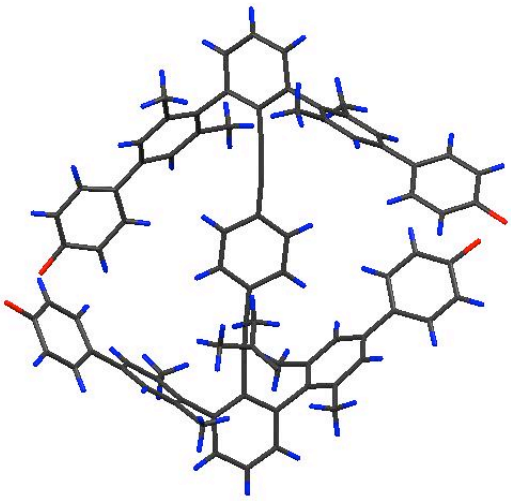

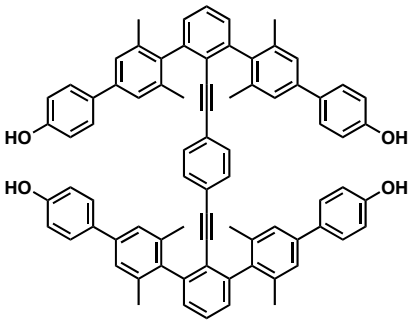

41

Figure 3.42 X-ray structure of tetrol **41**

Tetrol **41** was then alkylated with linker **44** in moderate yield to provide tetryne **45**. Basic molecular modeling indicated that the floppy arms of **45** were of sufficient length to close over the top to form the catenane. However, there is still the

possibility of competitive macrocycle or "dumbbell" formation. Macrocycle formation would occur if both "arms" from one side of the phenyl bridge formed bonds with both "arms" from the other side. If the bonds formed between diagonally opposite linkers, the molecule would still give a macrocycle. Dumbbell formation would occur if the two ring closures occurred between "arms" on the same side of the phenyl bridge, giving two macrocycles attached by the bridge. Following the preparation of the tetryne, oxidative alkyne coupling under high dilution conditions using copper acetate monohydrate was attempted in order to form catenane **35**.

Scheme 3.16

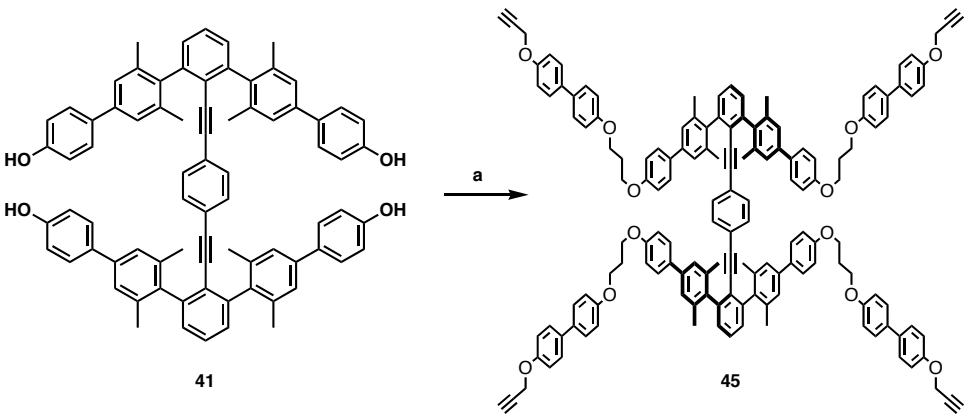

a. Cs_2CO_3, DMF, 44, 27%

Scheme 3.17

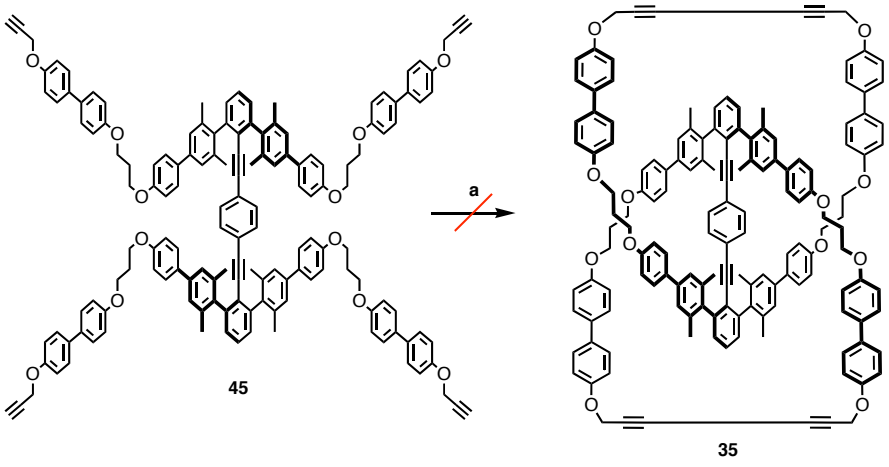

a. $Cu(OAc)_2 \cdot H_2O$, EtOH

Initial closure attempts with **45** were unsuccessful and only starting material was recovered from the oxidative alkyne coupling. Although molecular modeling indicated that the linkers were of sufficient length to form the desired catenane, we decided to repeat the synthesis with a significantly longer linker. It is not necessarily the case that the linker length is the reason the reaction failed; however the linker length is a parameter that can be easily modified.

There are two possibilities for extending the 4,4'-dihydroxy-based linkers, increasing the length of the chloroalkyl chain or the alkynyl chain. It was decided, as before, to first propargylate diol **42**, and then prepare multiple derivatives of varying alkane chain length. Increasing the chain length by one carbon corresponds to extending the overall reach of the linkers by two carbons because the two linkers must come together to form the catenane. The synthetic modification for the second attempt at catenane formation involved a 3-carbon increase in chain length.

Starting from the mono-propargylated compound, alkylation with bromochlorohexane afforded **46**. Subsequent attachment of **46** to the tetrol yielded catenane precursor **47**. Once again, catenane closure was attempted using oxidative alkyne coupling, however no product formation was detected and only a small amount of starting material was recovered. There is no obvious reason for the reaction to fail. It may be the case that the terminal alkynes are never in close enough proximity to react. However, simple molecular modeling suggests that the linkers are of sufficient length to enable catenane formation. The prior success of oxidative alkyne coupling in this work and the work of others makes the failure of this reaction particularly surprising.

Scheme 3.18

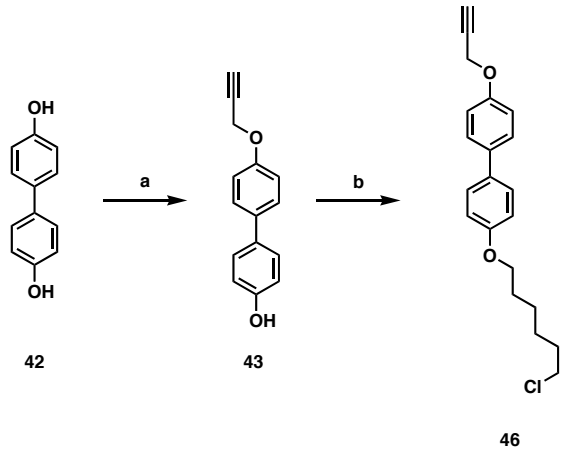

42 43 46

a. NaH,THF, Propargyl Bromide, 61% b. NaH, THF, Bromochlorohexane, 47%

Scheme 3.19

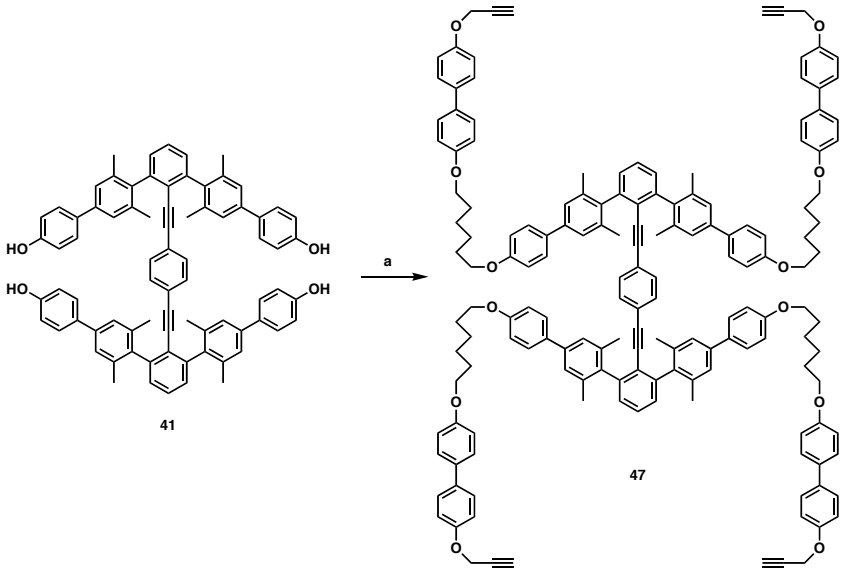

41 47

a. Cs_2CO_3, DMF, 46, 21%

Scheme 3.20

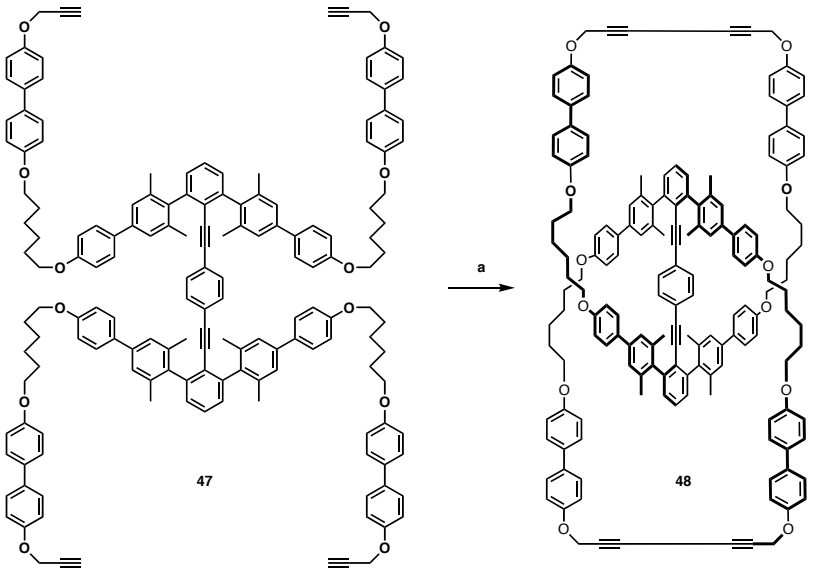

a. $Cu(OAc)_2 \cdot H_2O$, EtOH

3.8 Conclusions

The initial goal of this work was to quantify edge-to-face polar-π interactions and the terphenyl scaffold provided an appropriate geometry to study this type of interaction. It was predicted that the rotation barrier of an aryl alkyne could be used to extrapolate the energy associated with a polar-π interaction by comparison with the known barrier of tolan. Crystal structures of these molecules showed the edge-face distance to be close enough for such an interaction to occur. Subsequent calculations determined this type of polar-π interaction to be worth 0.5-0.6 kcal/mol. The overall rotational barrier in the molecule was calculated to be near 2 kcal/mol, a value too low to be measured by VT NMR spectroscopy.

It was next postulated that a molecule containing two terphenyl units, and therefore four polar-π interactions, might have a barrier significant enough to be measured by NMR. Calculations showed the barrier to be twice as large as the barrier

for the simple terphenyl system. An analog of appropriate symmetry was prepared, however, the barrier could not be measured by NMR spectroscopy.

In light of the work of Toyota and coworkers, the possibility of making a twisted structure containing two terphenyl units was considered. Following the successful synthesis of the desired molecule, the crystal structure showed dramatic end-to-end twisting in the molecule. However, this compound lacked the central spindle critical to the observation of polar-π interactions.

It was believed that extending the flanking groups of the original double terphenyl molecule would induce twisting even after the introduction of a central spindle unit. In addition, calculations showed that, in a double terphenyl molecule with an end-to-end twist of 90°, the central spindle would have almost no rotational barrier. The extended sandwich compound was successfully synthesized and the crystal structure showed an end-to-end twist of 40°. Solid state NMR measurements were conducted to determine the rotational barrier for the spindle in the solid. However, motion of the central spindle could not be detected, even upon heating, indicating there is a significant barrier to rotation.

Whereas extending the flanking rings caused significant twisting in the molecule, it was postulated that tethering the ends together could impose planarity and induce more dramatic edge-to-face interactions. To this end, a cyclophane was synthesized, with the end groups tethered by oxidative alkyne coupling. The crystal structure showed a much shorter edge-to-face distance than previous derivatives as well as significant distortion of the central triple bonds.

Appropriate synthetic modifications were made in order to prepare highly twisted as well as rigid planar derivatives of the original terphenyl sandwich structure. However, although the crystal structure of the extended sandwich indicates a twisted

structure, the flanking groups may have the ability to pass over each other. Therefore, a twisted structure is not necessarily maintained in solution. It was proposed that a concatenated structure would prevent this from occurring. Further, the structure would likely be more twisted and the central spindle would be completely sequestered from its surroundings. Therefore, efforts towards this synthetic target were undertaken. At present, the preparation of two precatenane structures has been successfully achieved.

The calculated values for the polar-π effect differ slightly from previously reported values; the values calculated in these systems are 0.5 kcal/mol whereas the interaction energy was previously found to be worth1-2 kcal/mol. Solid state structures demonstrated the close proximity of the terphenyl ring face with the hydrogen of the central ring. Particularly noteworthy is the cyclophane, in which the edge-face distance was nearly one angstrom shorter than in any of the other systems. It is possible that in this case the interaction energy is closer to the previously reported values. Unfortunately, solution phase variable temperature NMR spectroscopy was not a sensitive enough method to determine any of the values experimentally, and it may be possible that there is another more suitable method for measurements in this range. Additional work towards geometrically interesting structures yielded highly twisted molecules. It was postulated that this twisted structure could be modified to form a bridged catenane, with the intent of constructing a frictionless molecular rotor; however, this synthetic target remains elusive and efforts are ongoing.

REFERENCES:

1. Burley, S.K.; Petsko, G.A. *J. Am. Chem. Soc.* **1986,** *108,* 7995.

2. Wilcox, C.S.; *Tetrahedon Lett.* **1985,** *53,* 98.

3. Paliwal, S.; Geib, S.; Wilcox, C.S. *J. Am. Chem. Soc.* **1994,** *116,* 4497.

4. Chen, C.-T.; Siegel, J.S. *J. Am. Chem. Soc.* **1994,** *116,* 5959.

5. Robertson, J.M.; Woodward, I. *Proc. Roy. Soc., Ser. A,* **1938,** *164,* 436.

6. Liberles, A.; Matlosz B. *J. Org. Chem.* **1971,** *36,* 2710.

7. Toyota, S.; Yamamori, T.; Asakura, M.; Oki, M. *Bull. Chem. Soc. Jpn.* **2000,** *73,* 205.

8. Toyota, S.; Yamamori, T.; Makino, T.; Oki, M. *Bull. Chem. Soc. Jpn.* **2000,** *73,* 2591.

9. Toyota, S.; Yamamori, T.; Makino, T. *Tetrahedron* **2001,** *57,* 3521.

10. Toyota, S.; Iida, T.; Kunizane, C.; Tanifuji, N.; Yoshida, Y. *Org. Biomol. Chem.* **2003,** *1,* 2298.

11. Toyota, S.; Yanagihara, T.; Yoshida, Y.; Goichi, M. *Bull. Chem. Soc. Jpn.* **2005,** *78,* 1351.

12. Bedard, T.C.; Moore, J.S. *J. Am. Chem. Soc.* **1995,** *117,* 10662.

13. Du, C.-J.F.; Hart, H.; Ng, K.-K.D. *J. Org. Chem.* **1986,** *51,* 3162.

14. *Metal-Catalyzed Cross-Coupling Reactions, 2nd ed.* (Eds.: A. de Meijere, F. Diederich), Wiley-VCH, Weinheim, 2004

15. Sonogashira, K.; Tohda, Y.; Hagihara, N. *Tet. Lett.* **1975,** 4467.

16. Sandmeyer, T. *Ber. Dtsch. Chem. Ges.* **1884,** *17,* 1633.

17. Negishi, E.-I. *Acc. Chem. Res.* **1982,** *15,* 340.

18. Dominguez, Z.; Khoung, T.-A.V.; Dang, H.; Sanrame, C.N.; Nunez, J.E.; Garcia-Garibay, M.A. *J. Am. Chem. Soc.* **2003,** *125,* 8827.

19. Beeby, A.; Findlay, K.; Low, P.J.; Marder, T.B. *J. Am. Chem. Soc.* **2002,** *124,* 8280.

20. Khuong, T.-A.V.; Nuñez, J.E.; Godinez, C.E.; Garcia-Garibay, M.A. *Acc. Chem. Res.* **2006,** *39.*

21. "catenane." *Merriam-Webster Online Dictionary*, **2007**. http://www.merriam-webster.com (12 Jul. 2007).

22. C. Dietrich-Buchecker, G. Rapenne, and J. P. Sauvage, *Coord. Chem. Rev.*, **1999**, *186*, 167-176.

23. C. O. Dietrich-Buchecker, J. P. Sauvage, and J. P. Kintzinger, *Tetrahedron Lett.*, **1983**, *24*, 5095-5098.

24. Wasserman, E. *Scient. Am.,* **1962,** *207,* 94.

25. Schill, G.; Lüttringhaus *Angew. Chem., Int. Ed.,* **1964,** *3,* 546.

26. Schill, G. *Chem. Ber.,* **1965,** *98,* 2906.

27. Godt, A. *Eur. J. Org. Chem.* **2004,** *8,* 1639.

28. Loren, J.C.; Gantzel, P.; Linden, A.; Siegel, J.S. *Org. Biomol. Chem.* **2005,** *3,* 3105.

3.9 Experimental

Materials and Methods

^{1}H NMR and ^{13}C NMR were recorded on Bruker 300, 400, 500, and 600 MHz spectrometers and were referenced to residual solvent peak: chloroform (^{1}H NMR: 7.26 ppm; ^{13}C NMR: 77.00 ppm) or acetone (^{1}H NMR: 2.05 ppm; ^{13}C NMR: 29.84 ppm). All experiments were carried out under normal atmosphere in reagent grade solvents unless otherwise noted. Commercial chemicals were used as supplied by Alrich or Acros Chemical Co. Column chromatography was performed on silica gel (230-425 mesh). Melting points are uncorrected and were recorded on a Mel-Temp Laboratory Device.

All spectra were recorded in spectroscopic grade dichloromethane and are uncorrected. UV-Vis absorption spectra were recorded on Perkin-Elmer UV-Vis Lambda 19 spectrometer at concentrations of 10^{-5-} M. Emission measurements were made using an Edinburgh FLSP920 combined steady state, fluorescence and phosphorescence spectrometer. Emission and excitation spectra were collected using the Xe900 450W steady state xenon lamp.

1-(2,6-di(2,4,6-trimethylphenyl)-2-phenylethyne (1)

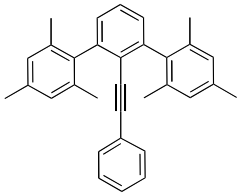

To an anhydrous solution of 2-bromomesitylene (700 mg, 3.6 mmol) in THF at -78 °C was slowly added n-butyllithium (1.05 equiv of 2.4 M hexane) by syringe. To this mixture was added a solution of anhydrous zinc chloride (485 mg, 3.6 mmol) in THF via cannula. The cold bath was removed after the addition was complete. Upon warming to room temperature, this solution was transferred via cannula to an anhydrous solution of **5** (300 mg, 0.9 mmol) and palladium tetrakis(triphenylphosphine) (103 mg, 0.09 mmol) in THF. This flask was equipped with a condenser and the reaction mixture was heated to reflux. Stirring was continued at this temperature for 16 h. The solvent was evaporated under reduced pressure and methylene chloride was added to the mixture. The contents of the flask were transferred to a separatory funnel and the organic phase was washed once with an aqueous saturated EDTA solution and twice with water, then dried over magnesium sulfate. Solvent was removed under reduced pressure. The crude product was purified by column chromatography (hexanes on silica) to give 250 mg (68%) of a yellow solid: mp = 168-170 °C; ^{1}H NMR (600 MHz, $CDCl_3$) δ 7.41 (t, *J* = 8 Hz, 1H), 7.16 (d, *J* = 8 Hz, 2H), 7.05 (m, 3H), 6.94 (s, 4H), 6.64 (d, *J* = 8 Hz, 2H), 2.38 (s, 6H), 2.06(s, 12H); ^{13}C NMR (150 MHz, $CDCl_3$) δ 144.48, 138.21, 136.70, 136.31, 131.54, 128.42, 128.08, 128.07, 127.96, 127.76, 123.90, 123.51, 94.47, 87.49, 21.33, 20.55; MS (EI) 414.1

2-(2,6-di(2,4,6-trimethylphenyl)phenyl)-1-(pyridin-3-yl)ethyne (2a)

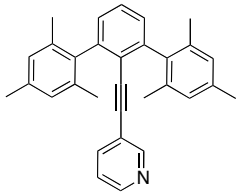

To an anhydrous solution of 2-bromomesitylene (955 mg, 4.8 mmol) in THF at -78 °C was slowly added n-butyllithium (1.05 equiv of 2.4 M hexane) by syringe. To this was added a solution of anhydrous zinc chloride (650 mg, 4.8 mmol) in THF via cannula. The cold bath was removed after the addition was complete. Upon warming to room temperature, this solution was transferred via cannula to an anhydrous solution of **11a** (400 mg, 1.2 mmol) and palladium tetrakis(triphenylphosphine) (140 mg, 0.12 mmol) in THF. This flask was equipped with a condenser and the reaction mixture was heated to reflux. Stirring was continued at this temperature for 16 h. The solvent was evaporated under reduced pressure and methylene chloride was added to the mixture. The contents of the flask were transferred to a separatory funnel and the organic phase was washed once with a saturated EDTA solution and twice with water, then dried over magnesium sulfate. Solvent was removed under reduced pressure. The crude product was purified by column chromatography (methylene chloride on silica) to yield 120 mg (24%) of a white solid: mp = 306-308 °C; ^{1}H NMR (600 MHz, $CDCl_3$) δ 8.34 (m, 1H), 7.84 (m, 1H), 7.49 (t, *J* = 7 Hz, 1H), 7.21 (d, *J* = 7 Hz, 2H), 7.06 (m, 1H), 6.98 (s, 4H), 6.95 (d, *J* = 8 Hz, 1H) 2.45 (s, 6H), 2.10 (s, 12H); ^{13}C NMR (150 MHz, $CDCl_3$) δ 151.94, 147.63, 144.54, 138.02, 137.69, 136.77, 136.02, 128.88, 128.07, 127.98, 127.82, 122.57, 90.72, 90.63, 21.16, 20.39; MS (Hi-res EI) found: 415.229086 calcd: 415.23000

2-(2,6-di(2,4,6-trimethylphenyl)phenyl)-1-(pyridin-2-yl)ethyne (2b)

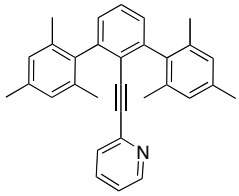

To an anhydrous solution of 2-bromomesitylene (1.4 g, 7.1 mmol) in THF at -78 °C was slowly added n-butyllithium (1.05 equiv of 2.4 M hexane) by syringe. To this was added a solution of anhydrous zinc chloride (970 mg, 7.1 mmol) in THF via cannula. The cold bath was removed after the addition was complete. Upon warming to room temperature, this solution was transferred via cannula to an anhydrous solution of **11b** (600 mg, 1.8 mmol) and palladium tetrakis(triphenylphosphine) (205 mg, 0.18 mmol) in THF. This flask was equipped with a condenser and the reaction mixture was heated to reflux. Stirring was continued at this temperature for 16 h. The solvent was evaporated under reduced pressure and methylene chloride was added to the mixture. The contents of the flask were transferred to a separatory funnel and the organic phase was washed once with a saturated EDTA solution and twice with water, then dried over magnesium sulfate. Solvent was removed under reduced pressure. The crude product was purified by column chromatography (2:1 hexanes: methylene chloride on alumina) to give 100 mg (13%) of a white solid: mp = 193-195 °C; ^{1}H NMR (600 MHz, $CDCl_3$) δ 8.40 (d, *J* = 3 Hz, 1H), 7.49 (t, *J*= 8 Hz, 1H), 7.37 (ddd, *J1* = *J2* = 1 Hz, *J3* = 5 Hz, 1H), 7.18 (d, *J* = 8 Hz, 2H), 7.01 (ddd, *J1* = *J2* =1 Hz, *J3*= 5 Hz, 1H), 6.97 (s, 4H), 6.42 (d, *J* = 8 Hz, 1H), 2.37 (s, 6H), 2.11 (s, 12H); ^{13}C NMR (150 MHz, $CDCl_3$) δ 149.38, 144.91, 143.72, 137.67, 136.61, 135.93, 135.52, 129.04, 128.14, 128.11, 127.91, 122.20, 121.92, 93.47, 87.82, 21.09, 20.33; MS (EI) 415.1

2-(2,6-di(2,4,6-trimethylphenyl))-1-(pyrimidin-2-yl)ethyne (5)

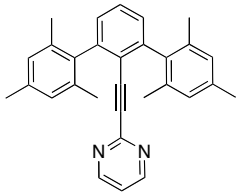

To an anhydrous solution of 2-bromomesitylene (870 mg, 4.4 mmol) in THF at -78 °C was slowly added n-butyllithium (1.05 equiv of 2.4 M hexane) by syringe. To this was added a solution of anhydrous zinc chloride (600 mg, 4.4 mmol) in THF via cannula. The cold bath was removed after the addition was complete. Upon warming to room temperature, this solution was transferred via cannula to an anhydrous solution of **13** (370 mg, 1.1 mmol) and palladium tetrakis(triphenylphosphine) (126 mg, 0.11 mmol) in THF. This flask was equipped with a condenser and the reaction mixture was heated to reflux. Stirring was continued at this temperature for 16 h. The solvent was evaporated under reduced pressure and methylene chloride was added to the mixture. The contents of the flask were transferred to a separatory funnel and the organic phase was washed once with a saturated EDTA solution and twice with water, then dried over magnesium sulfate. Solvent was removed under reduced pressure. The crude product was purified by column chromatography (methylene chloride on silica) to give 105 mg (23%) of a white solid: mp = 204-206 °C; ^{1}H NMR (600 MHz, $CDCl_3$) δ 8.51 (d, *J* = 5 Hz, 2H), 7.49 (t, *J* = 8 Hz, 1H), 7.18 (d, *J* = 8 Hz, 2H), 7.00 (t, *J* = 5 Hz, 1 H), 6.92 (s, 4H), 2.31 (s, 6H), 2.10 (s, 12H); ^{13}C NMR (100 MHz, $CDCl_3$) δ 156.79, 153.04, 145.17, 137.21, 136.53, 135.76, 129.32, 128.30, 127.92, 121.52, 119.00, 92.10, 85.20, 21.07, 20.37 ; MS: EI: 416.2

2,6-Dibromoiodobenzene (9)

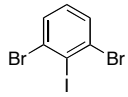

To a solution of 2,6-dibromoaniline (10.0 g, 40 mmol) in concentrated HCl (40 mL) at 0 °C was added dropwise an aqueous solution of sodium nitrite (3.0 g, 44 mmol) over 45 min. Stirring was continued for an additional 30 min. The resulting solution was added dropwise over 30 min to a vigorously stirred aqueous solution of potassium iodide (66.4 g, 0.4 mol) at 0 °C. Stirring was continued for an additional 3 h and the crude product was collected by filtration. The solid was then dissolved in methylene chloride and the solution was transferred to a separatory funnel. The organic phase was washed twice with a 10% aqueous sodium bisulfite solution and once with water, then dried over magnesium sulfate. Solvent was evaporated under reduced pressure. The product was dry loaded onto silica and passed through a silica plug with hexanes to yield 12.0 g (83%) of a white solid: mp = 98-99 °C; ^{1}H NMR (600 MHz, $CDCl_3$) δ 7.55 (d, *J* = 8 Hz, 2H), 7.06 (t, *J*=8 Hz, 1H); ^{13}C NMR (150 MHz, $CDCl_3$) δ 131.27, 131.04, 130.30, 109.36; MS: GC/MS: 360:362:364 (1:2:1)

1-(2,6-dibromophenyl)-2-phenylethyne (10)

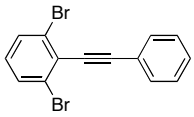

A solution of **9** (1.0 g, 2.8 mmol), phenylacetylene (560 mg, 5.5 mmol), and trans-dichlorobis(triphenylphosphine)palladium(II) (96 mg, 0.14 mmol) in triethylamine (10 mL) was heated in a sealed flask to 75 °C and stirred at this temperature for 18 h. The reaction mixture was allowed to cool to room temperature, then diluted with methylene chloride. The mixture was transferred to a separatory

funnel, washed twice with water, and dried over magnesium sulfate. Solvent was evaporated under reduced pressure. The crude product was purified by column chromatography (hexanes on silica) to yield 600 mg (65%) of a white solid: mp = 85-87 °C; ^{1}H NMR (600 MHz, $CDCl_3$) δ 7.64 (d, *J* = 8 Hz, 1H), 7.56 (d, *J* = 8 Hz, 2H), 7.38 (m, 3H), 7.03 (t, *J* = 8 Hz, 1H); ^{13}C NMR (150 MHz, $CDCl_3$) δ 131.83, 131.36, 129.65, 127.46, 127.39, 127.24, 127.09, 121.40, 95.41, 94.68; MS: GC/MS: 334:336:338 (1:2:1)

2-(2,6-dibromophenyl)-1-(pyridin-3-yl)ethyne (11a)

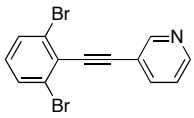

A solution of **9** (500 mg, 1.4 mmol), 3-ethynylpyridine (280 mg, 2.8 mmol), copper iodide (5 mg, 0.07 mmol), and trans-dichlorobis(triphenylphosphine)palladium(II) (48mg, 0.07 mmol) in triethylamine (10 mL) was heated in a sealed flask to 75 °C and stirred at this temperature for 18 h. The reaction mixture was allowed to cool to room temperature, then diluted with methylene chloride. The mixture was transferred to a separatory funnel, washed twice with water, then dried over magnesium sulfate. Solvent was evaporated under reduced pressure. The crude product was purified by column chromatography (5:1 hexanes: ethyl acetate on silica) to yield 260 mg (56%) of a white solid: mp = 81-83 °C; ^{1}H NMR (300 MHz, $CDCl_3$) δ 8.85(s, 1H), 8.61 (d, *J* = 5 Hz, 1H), 7.93 (dd, *J* = 2 Hz, 6 Hz, 1H), 7.60 (d, *J* = 8 Hz, 2H), 7.36 (dd, *J* = 5 Hz, 7 Hz, 1H), 7.09 (t, *J* = 8 Hz, 1H); ^{13}C NMR (150 MHz, $CDCl_3$) δ 154.23, 150.67, 140.84, 133.93, 131.29, 129.34, 129.10, 124.63, 117.35, 94.36, 88.18; MS: GC/MS: 335:337:339 (1:2:1)

2-(2,6-dibromophenyl)-1-(pyridin-2-yl)ethyne (11b)

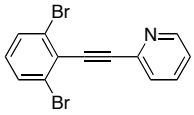

A solution of **9** (1.0 g, 2.8 mmol), 2-ethynylpyridine (850 mg, 8.4 mmol), copper iodide (26 mg, 0.14 mmol), and trans-dichlorobis(triphenylphosphine)palladium(II) (72 mg, 0.28 mmol) in triethylamine (20 mL) was heated in a sealed flask to 75 °C and stirred at this temperature for 18 h. The reaction mixture was allowed to cool to room temperature, then diluted with methylene chloride. The mixture was transferred to a separatory funnel, washed twice with water, then dried over magnesium sulfate. Solvent was evaporated under reduced pressure. The crude product was purified by column chromatography (methylene chloride on silica) to yield 600 mg (65%) of a green liquid: ^{1}H NMR (600 MHz, $CDCl_3$) δ 8.69 (dd, *J*=1,5 Hz, 1H), 7.74 (dt, *J*=2,5 Hz, 1H), 7.64 (m, 1H) 7.60 (d, *J* = 7 Hz, 2H), 7.29 (m, 1H), 7.07 (t, *J* = 7 Hz, 1H); ^{13}C NMR (150 MHz, $CDCl_3$) δ 150.21, 142.80, 136.00, 131.24, 130.23, 127.72, 126.70, 126.30, 123.22, 96.97, 86.62; MS: GC/MS: 335:337:339 (1:2:1)

2-(2,6-dibromophenyl)-1-(trimethylsilyl)ethyne (12a)

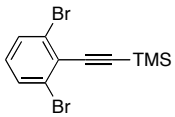

A solution of **9** (2.0 g, 5.5 mmol), (trimethysilyl)acetylene (1.6 g, 16.5 mmol), copper iodide (0.28 mmol 52 mg), and palladium tetrakis(triphenylphosphine) (320 mg, 0.55 mmol) in triethylamine (20 mL) was heated in a sealed flask to 75 °C and stirred at this temperature for 18 h. The reaction mixture was allowed to cool to room

temperature, then diluted with methylene chloride. The mixture was transferred to a separatory funnel, washed twice with water, then dried over magnesium sulfate. Solvent was evaporated under reduced pressure. The crude product was purified by column chromatography (hexanes on silica) to yield 1.4 g (76%) of a yellow liquid: ^{1}H NMR (300 MHz, $CDCl_3$) δ 7.52 (d, J = 8 Hz, 2H), 7.00 (t, J = 8 Hz, 1H), 0.30 (s, 9 H); ^{13}C NMR (150 MHz, $CDCl_3$) δ 131.38, 130.50, 127.25, 126.77, 105.55, 101.95, 0.00; MS: GC/MS: 330:332:334 (1:2:1)

2,6-Dibromoethynylbenzene (12b)

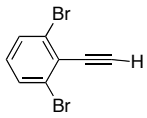

To a solution of **12a** (1.3 g, 3.9 mmol) in methanol was added potassium carbonate (2.7 g, 19 mmol) and the mixture was stirred at room temperature for 16 h. Methylene chloride was added to the reaction mixture, which was then transferred to a separatory funnel. The organic phase was washed twice with water, then dried over magnesium sulfate. Solvent was evaporated under reduced pressure to yield 650 mg (64%) of a white solid: mp = 93-95 °C; ^{1}H NMR (600 MHz, $CDCl_3$) δ 7.55 (d, J = 8 Hz, 2H), 7.04 (t, J = 8 Hz, 1H), 3.69 (s, 1H); ^{13}C NMR (150 MHz, $CDCl_3$) δ 131.32, 130.23, 126.74, 126.04, 86.64, 80.84; MS: GC/MS: 258:260:262 (1:2:1)

2-(2,6-dibromophenyl)-1-(pyrimidin-2-yl)ethyne (13)

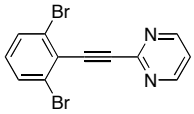

A solution of **12b** (650 mg, 2.5 mmol), 2-iodopyrimidine (770 mg, 3.8 mmol), copper iodide (24 mg, 0.13 mmol), and palladium tetrakis(triphenylphosphine) (144

mg, 0.13 mmol) in triethylamine (20 mL) was heated in a sealed flask to 75 °C and stirred at this temperature for 18 h. The reaction mixture was allowed to cool to room temperature, then diluted with methylene chloride. The mixture was transferred to a separatory funnel, washed twice with water, then dried over magnesium sulfate. Solvent was evaporated under reduced pressure. The crude product was purified by column chromatography (methylene chloride on silica) to yield 515 mg (61%) of a tan solid: mp = 153-155 °C; ^{1}H NMR (300 MHz, $CDCl_3$) δ 8.83 (d, *J* = 7 Hz, 2H), 7.64 (d, *J* = 8 Hz, 2H), 7.28 (t, *J* = 7 Hz, 1H), 7.11 (t, *J* = 8 Hz, 1H); ^{13}C NMR (75 MHz, $CDCl_3$) δ 159.37, 153.49, 131.86, 131.39, 127.72, 126.12, 120.55, 96.43, 85.91; MS: GC/MS: 336:338:340

1,4-di(2,6-di(4-methoxy-2,6-dimethylphenyl)phenylethynyl)benzene (14b)

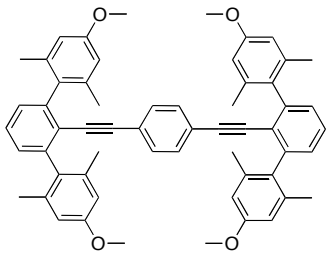

A solution of 1,4-diiodobenzene (54 mg, 0.16 mmol), **17b** (150 mg 0.4 mmol), copper iodide (3 mg, 0.02 mmol), and trans-dichlorobis(triphenylphosphine)palladium(II) (11 mg, 0.02 mmol) in triethylamine was heated to 75 °C and stirred at this temperature for 18 h. The reaction mixture was

allowed to cool to room temperature, then diluted with methylene chloride. The mixture was transferred to a separatory funnel, washed twice with water, then dried over magnesium sulfate. Solvent was evaporated under reduced pressure. The crude product was purified by column chromatography (2:1 hexanes: methylene chloride) to yield 50 mg (38%) of a white solid: mp = 304-306 °C; ^{1}H NMR (300 MHz, $CDCl_3$) δ 7.44 (t, *J* = 8 Hz, 2H), 7.17 (d, *J* = 8 Hz, 4H) 6.68 (s, 8H), 6.43 (s, 4H), 3.87 (s, 12H), 2.05 (s, 24H); ^{13}C NMR (125 MHz, $CDCl_3$) δ 158.70, 144.22, 137.79, 133.68, 131.05, 128.49, 124.04, 122.97, 112.58, 112.54, 94.41, 89.13, 55.41, 20.87; MS: MALDI: 814.3

2,5-di(2,6-di(4-methoxy-2,6-dimethylphenyl)phenylethynyl)pyridine (16)

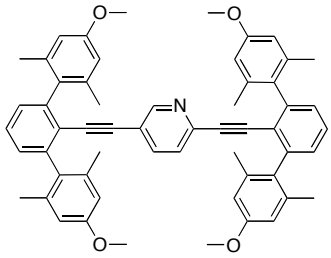

A solution of 2-bromo-5-iodopyridine (30 mg, 0.11 mmol), **17b** (80 mg, 0.22 mmol), palladium tetrakis(triphenylphosphine) (12 mg, 0.011 mmol), and copper iodide (2 mg, 0.011 mmol) in triethylamine (5 mL) was heated to 80°C and stirred at this temperature for 36 h. The reaction mixture was allowed to cool to room temperature, methylene chloride was added, and the mixture was transferred to a separatory funnel. The organic phase was washed twice with water, then dried over magnesium sulfate. Solvent was removed under reduced pressure. The crude product was purified by column chromatography (6:1 methylene chloride: hexanes on silica) to yield 34 mg (38%) of a white solid. mp = 310-312°C; ^{1}H NMR (300 MHz, $CDCl_3$) δ 7.69 (dd, *J* = 1, 2 Hz, 1H), 7.47 (t, *J* = 7 Hz, 1H), 7.46 (t, *J* = 7 Hz, 1H), 7.16 (d, *J* =

7 Hz, 2H), 7.15 (d, *J* = 7 Hz, 2H), 6.70 (dd, *J* = 2, 8 Hz, 1H), 6.65 (s, 4H), 6.64 (s, 4H), 6.29 (dd, *J* = 1, 8 Hz), 3.84 (s, 6H), 3.82 (s, 6H), 2.07 (s, 12H), 2.04 (s, 12H); ^{13}C NMR (150 MHz, $CDCl_3$) δ 159.09, 159.02, 145.22, 144.79, 138.24, 137.97, 133.59, 129.67, 129.39, 129.06, 128.88, 127.55, 123.69, 123.29, 119.47, 113.07, 112.89, 55.67, 55.63, 21.21, 21.17 ; MS: MALDI: 816.4

2-(2,6-di(4-methoxy-2,6-dimethylphenyl)phenyl)-1-(trimethylsilyl)ethyne (17a)

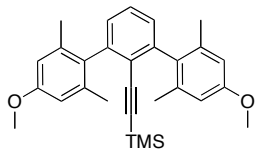

To an anhydrous solution of **20** (970 mg, 4.5 mmol) in THF at -78°C was slowly added n-butyllithium (1.05 equiv of 2.4 M hexane) by syringe. To this was added a solution of anhydrous zinc chloride (614 mg, 4.5 mmol) in THF via cannula. The cold bath was removed after the addition was complete. Upon warming to room temperature, this solution was transferred via cannula to an anhydrous solution of **12a** (500 mg, 1.5 mmol) and palladium tetrakis(triphenylphosphine) (173 mg, 0.15 mmol) in THF. This flask was equipped with a condenser and the reaction mixture was heated to reflux. Stirring was continued at this temperature for 16 h. The solvent was evaporated under reduced pressure and methylene chloride was added to the mixture. The contents of the flask were transferred to a separatory funnel and the organic phase was washed once with a saturated EDTA solution and twice with water, then dried over magnesium sulfate. Solvent was removed under reduced pressure. The crude product was purified by column chromatography (6:1 hexanes:methylene chloride on silica) to give 430 mg (65%) of a yellow oil : ^{1}H NMR (300 MHz, $CDCl_3$) δ 7.39 (t, *J* = 8 Hz, 1H), 7.12 (d, *J* = 8 Hz, 2H), 6.65 (s, 4H), 3.83 (s, 6H), 2.05 (s, 12H), -0.20 (s,

9H); ^{13}C NMR (150 MHz, $CDCl_3$) δ 159.01, 144.97, 137.91, 134.08, 128.71, 124.61, 113.18, 112.91, 102.89, 99.89, 55.73, 21.66, 0.00; MS: EI: 442.2

2,6-di(4-methoxy-2,6-dimethyl)ethynylbenzene (17b)

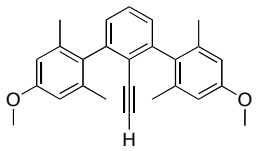

To a solution of **17a** (400 mg, 0.91 mmol) in methanol / THF was added potassium carbonate (625 mg, 4.5 mmol) and the mixture was stirred at room temperature for 16 h. Methylene chloride was added to the reaction mixture, which was then transferred to a separatory funnel. The organic phase was washed twice with water, then dried over magnesium sulfate. Solvent was evaporated under reduced pressure to yield 310 mg (92%) of a white solid: mp = 152-154°C; ^{1}H NMR (300 MHz, $CDCl_3$) δ 7.46 (t, *J* = 8 Hz, 1H), 7.13 (d, *J* = 8 Hz, 2H), 6.68 (s, 4H), 3.83 (s, 6H), 2.05 (s, 12H); ^{13}C NMR (150 MHz, $CDCl_3$) δ 158.98, 144.05, 136.54, 133.17, 130.75, 128.08, 125.43, 114.10, 94.50, 88.67, 55.34, 20.55; MS: EI: 370.2

4,4'-di(2,6-di(4-methoxy-2,6-dimethylphenyl)phenylethynyl)biphenyl (18)

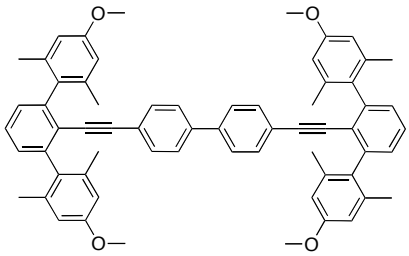

A solution of 4,4'-diiodobiphenyl (44 mg, 0.11 mmol), **17b** (100 mg, 0.27 mmol), copper iodide (2 mg 0.01 mmol), and trans-dichlorobis(triphenylphosphine)palladium(II) (8 mg, 0.01 mmol) in triethylamine was heated to 75°C and stirred at this temperature for 18 h. The reaction mixture was

allowed to cool to room temperature, then diluted with methylene chloride. The mixture was transferred to a separatory funnel, washed twice with water, then dried over magnesium sulfate. Solvent was evaporated under reduced pressure. The crude product was purified by column chromatography (2:1 hexanes: methylene chloride on silica) to yield 30 mg (34%) of a white solid: mp = 284-286 °C; ^{1}H NMR (300 MHz, $CDCl_3$) δ 7.44 (t, *J* = 8 Hz, 2H), 7.23 (d, *J* = 8 Hz, 4 H), 7.15 (d, *J* = 8 Hz, 4H), 6.75 (d, *J* = 8 Hz, 4H), 6.64 (s, 8H), 3.83 (s, 6H), 2.07 (s, 12H); ^{13}C NMR (100 MHz, $CDCl_3$) δ 158.49, 143.99, 139.53, 137.65, 133.58, 131.77, 128.27, 126.36, 123.93, 122.74, 112.38, 55.24, 20.70 ; MS: MALDI: 890.3

1,4-di(2,6-di(4-methoxy-2,6-dimethylphenyl)phenyl)buta-1,3-diyne (19)

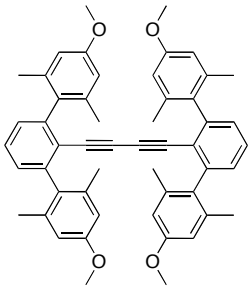

A solution of **17b** (100 mg, 0.27 mmol) and copper acetate monohydrate (540 mg, 2.7 mmol) in ethanol (10 mL) was heated to reflux. The reaction mixture was stirred at this temperature for 48 h, then allowed to cool and diluted with methylene chloride. The mixture was transferred into a separatory funnel and washed twice with water, then dried over magnesium sulfate. Solvent was evaporated under reduced pressure. The product was purified by column chromatography (2:1 methylene chloride: hexanes) to yield 80 mg (80%) of a white solid. mp = 255-257 °C; ^{1}H NMR (300 MHz, $CDCl_3$) δ 7.37 (t, *J* = 8 Hz, 2H), 7.08 (d, *J* = 8 Hz, 4H), 6.63 (s, 8H), 3.85 (s, 12H), 2.01 (s, 24H); ^{13}C NMR (75 MHz, $CDCl_3$) δ 158.34, 144.93, 137.17, 132.56, 128.33, 122.97, 112.35, 112.32, 79.80, 78.50, 54.92, 20.35; MS (EI) 738.4

4-methoxy-2,6-(dimethyl)bromobenzene (20)

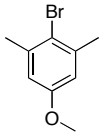

To a solution of 3,5-dimethylanisole in acetonitrile was added dropwise over 1 h a solution of N-bromosuccinimide in acetonitrile. Stirring was continued for 2 h after the addition was complete. Water was added to the reaction mixture, which was then transferred to a separatory funnel. Hexanes was added and the phases were separated. The organic phase was washed twice with water, then dried over magnesium sulfate. Solvent was evaporated under reduced pressure to yield a clear liquid. Spectral data matches literature values: ^{1}H NMR (300 MHz, $CDCl_3$) 6.63 (s, 2H), 3.74 (s, 3H), 2.36 (s, 6H); MS: GC/MS: 214:216 (1:1)

4-hydroxy-2,6-dimethylbromobenzene (21)

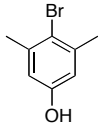

To a solution of **20** (5.0 g, 23.3 mmol) in methylene chloride at –78 °C was slowly added boron tribromide (4.4 mL, 46.6 mmol) by syringe. The reaction mixture was stirred for 16 h. Water was very slowly added to the reaction mixture at 0 °C and the contents were transferred to a separatory funnel. The organic phase was washed twice with water, then dried over magnesium sulfate. Solvent was evaporated under reduced pressure to yield 4.4 g (94%) of a white solid. mp = 112-114 °C; ^{1}H NMR (300 MHz, $CDCl_3$) δ 8.29 (s, 1H), 6.65 (s, 2H), 2.32 (s, 6H); ^{13}C NMR (75 MHz, $CDCl_3$) δ 156.96, 139.51, 116.88, 116.25, 23.72; MS: GC/MS: 201:203 (1:1)

4-Bromo-3,5-dimethylphenyltrifluoromethanesulfonate (22)

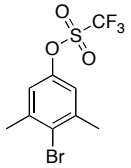

To a solution of **21** (2.6 g, 12.9 mmol) and pyridine (5 mL) in methylene chloride at –78°C was slowly added triflic anhydride (7.3 g, 25.8 mmol) by syringe. The reaction mixture was stirred for 18 h, then water was added. The solution was transferred to a separatory funnel, methylene chloride was added, and the phases were separated. The organic phase was washed twice with water, then dried over magnesium sulfate. Solvent was evaporated under reduced pressure and the product was purified by column chromatography (hexanes on silica) to yield 3.4 g (79%) of a clear liquid. ^{1}H NMR (300 MHz, $CDCl_3$) δ 7.01 (s, 2H), 2.46 (s, 6H); ^{13}C NMR (75 MHz, $CDCl_3$) δ 147.61, 140.72, 126.87, 124.98 (q, $J_{C\text{-}F}$ = 318 Hz, 1C); MS: GC/MS: 332:334 (1:1)

4-(4-methoxyphenyl)-2,6-dimethylbromobenzene (23)

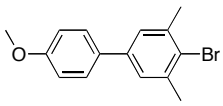

To an anhydrous solution of 4-bromoanisole (1.0 g, 5.3 mmol) in THF at -78 °C was slowly added n-butyllithium (1.05 equiv of 2.4 M hexane) by syringe. To this was added a solution of anhydrous zinc chloride (730 mg, 5.3 mmol) in THF via cannula. The cold bath was removed after the addition was complete. Upon warming to room temperature, this solution was transferred via cannula to an anhydrous solution of **22** (1.6 g, 4.9 mmol) and palladium tetrakis(triphenylphosphine) (283 mg, 0.49 mmol) in THF. This flask was equipped with a condenser and the reaction mixture was heated to reflux. Stirring was continued at this temperature for 18 h. The

solvent was evaporated under reduced pressure and methylene chloride was added to the mixture. The contents of the flask were transferred to a separatory funnel and the organic phase was washed once with a saturated EDTA solution and twice with water, then dried over magnesium sulfate. Solvent was removed under reduced pressure. The crude product was purified by column chromatography (10:1 hexanes: methylene chloride) to give 700 mg (45%) of a white solid. mp = 103-105 °C; ^{1}H NMR (300 MHz, $CDCl_3$) δ 7.51 (d, *J* = 8 Hz, 2H), 7.26 (s, 2H), 6.99 (d, *J* = 8 Hz, 2H), 3.86 (s, 3H), 2.48 (s, 6H); ^{13}C NMR (75 MHz, $CDCl_3$) δ 159.17, 139.24, 138.37, 132.75, 127.90, 126.44, 125.92, 114.13, 55.24, 23.88; MS: GC/MS: 290:292 (1:1)

2-(2,6-di[(4-methoxyphenyl)-2,6-dimethylphenyl]phenyl)-1-(trimethylsilyl)ethyne (25a)

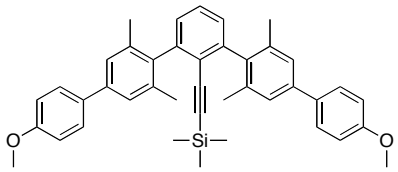

To an anhydrous solution of **23** (620 mg, 2.1 mmol) in THF at -78 °C was slowly added n-butyllithium (1.05 equivalents of a 2.4 molar solution in hexane) by syringe. To this was added a solution of anhydrous zinc chloride (290 mg, 2.1 mmol) in THF via cannula. The cold bath was removed after the addition was complete. Upon warming to room temperature, this solution was transferred via cannula to an anhydrous solution of **12a** (300 mg, 0.9 mmol) and palladium tetrakis(triphenylphosphine) (104 mg, 0.09 mmol) in THF. This flask was equipped with a condenser and the reaction mixture was heated to reflux. Stirring was continued at this temperature for 36 h. The solvent was evaporated under reduced

pressure and methylene chloride was added to the mixture. The contents of the flask were transferred to a separatory funnel and the organic phase was washed once with a saturated EDTA solution and twice with water, then dried over magnesium sulfate. Solvent was removed under reduced pressure. The crude product was purified by column chromatography (2:1 hexanes: methylene chloride) to give 230 mg (30%) of a white solid. mp: 170-172 °C; ^{1}H NMR (300 MHz, $CDCl_3$) δ 7.55 (d, *J* = 8 Hz, 4H), 7.45 (t, *J* = 7 Hz, 1H), 7.27 (s, 4H), 7.18 (d, *J* = 7 Hz, 2H), 6.98 (d, 4H, *J* = 8 Hz, 4H), 3.84 (s, 6H), 2.11 (s, 12H), -0.27 (s, 9H); ^{13}C NMR (75 MHz, $CDCl_3$) δ 159.61, 145.15, 140.23, 139.90, 137.02, 134.78, 128.72, 128.41, 126.42, 126.10, 123.83, 114.75, 102.73, 100.54, 55.94, 21.38, 0.00; MS: EI: 594.2

2,6-di[(4-methoxyphenyl)-2,6-dimethylphenyl]ethynylbenzene (25b)

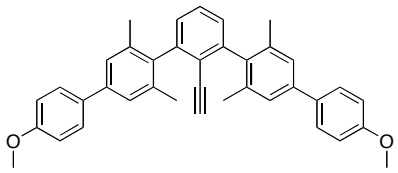

To a solution of **25a** (220 mg, 0.37 mmol) in methanol / THF was added potassium carbonate (255 mg, 1.85 mmol) and the mixture was stirred at room temperature for 18 h. Methylene chloride was added to the reaction mixture, which was then transferred to a separatory funnel. The organic phase was washed twice with water, then dried over magnesium sulfate. Solvent was evaporated under reduced pressure to yield 310 mg (92%) of a white solid: mp = 229-231 °C; ^{1}H NMR (300 MHz, $CDCl_3$) δ 7.63 (d, *J* = 7 Hz, 4H), 7.52 (t, *J* = 7 Hz, 1H), 7.36 (s, 4H), 7.23 (d, *J* = 7 Hz, 2H), 7.01 (d, *J* = 7 Hz, 4H), 3.84 (s, 6H), 2.18 (s, 12H), 2.66 (s, 1H); ^{13}C NMR (75 MHz, $CDCl_3$) 158.96, 144.81, 139.47, 139.01, 136.27, 133.65, 130.15, 128.81, 127.97, 125.39, 121.76, 114.03, 82.10, 80.13, 55.23, 20.45; MS: EI: 522.1

1,4-di(2,6-di[4-(4-methoxyphenyl)-2,6-dimethylphenyl]phenylethynyl)benzene (26)

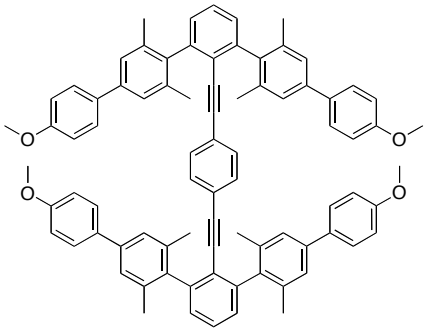

A solution of 1,4-diiodobenzene (13 mg, 0.076 mmol), **25b** (40 mg 0.038 mmol), copper iodide (1 mg, 0.007 mmol), and palladium tetrakis(triphenylphosphine) (4 mg, 0.007 mmol) in triethylamine was heated to 75 °C and stirred at this temperature for 18 h. The reaction mixture was allowed to cool to room temperature, then diluted with methylene chloride. The mixture was transferred to a separatory funnel, washed twice with water, then dried over magnesium sulfate. Solvent was evaporated under reduced pressure. The crude product was purified by column chromatography (1:1 hexanes:methylene chloride) to yield 17 mg (42%) of a white solid: mp = 292-294 °C; ^{1}H NMR (300 MHz, $CDCl_3$) δ 7.52 (d, *J* = 7Hz, 8H), 7.46 (t, *J* = 8 Hz, 2H), 7.27 (s, 8H), 7.21 (d, *J* = 8 Hz, 4H), 6.97 (d, *J* = 7 Hz, 8H), 6.32 (s, 4H), 3.87 (s, 12H), 2.10 (s, 24H); ^{13}C NMR (75 MHz, $CDCl_3$) δ 158.99, 144.05, 139.62, 139.18, 136.54, 133.94, 130.75, 128.45, 128.08, 127.86, 125.43, 122.88, 122.60, 114.10, 94.50, 88.67, 55.34, 20.55; MS: MALDI: 1118.4

1,4-di(2,6-di[4-(4-methoxyphenyl)-2,6-dimethylphenyl]phenyl)buta-1,3-diyne (27)

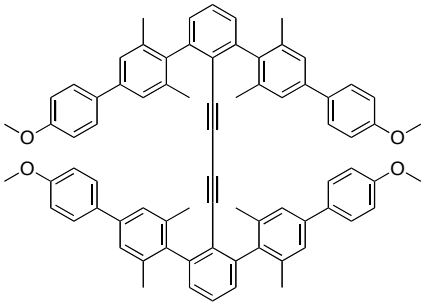

A solution of **25b** (170 mg, 0.33 mmol) and copper acetate monohydrate (650 mg, 3.3 mmol) in ethanol (10 mL) was heated to reflux. The reaction mixture was stirred at this temperature for 36 hours, then allowed to cool and diluted with methylene chloride. The mixture was transferred into a separatory funnel and washed twice with water, then dried over magnesium sulfate. Solvent was evaporated under reduced pressure. The product was purified by column chromatography (2:1 methylene chloride: hexanes) to yield 70 mg (42%) of a white solid. mp = 246-248 °C; ^{1}H NMR (300 MHz, $CDCl_3$) δ 7.50 (d, *J* = 7 Hz, 8H), 7.39 (t, *J* = 7 Hz, 2H), 7.10 (d, *J* = 7 Hz, 4H), 7.08 (s, 8H), 7.01 (d, *J* = 7 Hz, 8H), 3.89 (s, 12H), 1.96 (s, 24H); ^{13}C NMR (75 MHz, $CDCl_3$) δ 158.91, 145.06, 139.30, 138.22, 136.08, 133.82, 128.48, 128.09, 127.88, 125.23, 121.95, 113.94, 79.07, 78.45, 55.27, 20.21; MS: MALDI: 1043.4

Alkyne Cyclophane (28)

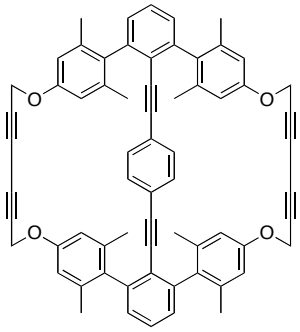

To a solution of **34** (15 mg, 0.016 mmol) in ethanol (15 mL) was added copper (II) acetate monohydrate (65 mg, 0.33 mmol). The reaction mixture was heated to 80 °C and stirred at this temperate for 36 h. After cooling to room temperature, methylene chloride was added and the mixture was transferred to a separatory funnel. The organic phase was washed twice with water, then dried over magnesium sulfate. Solvent was removed under reduced pressure. The crude product was purified by column chromatography (1:1 hexanes: methylene chloride on silica) to yield 6 mg (40%) of a white solid. m.p. > 350 °C ; ^{1}H NMR (600 MHz, $CDCl_3$) δ 7.44 (t, *J* = 8 Hz, 2H), 7.18 (d, *J* = 8 Hz, 4H), 6.72 (s, 8H), 6.43 (s, 4H), 4.82 (s, 8H), 2.01 (s, 24H); ^{13}C NMR (150 MHz, $CDCl_3$) δ 156.82, 144.06, 138.04, 135.05, 131.10, 128.58, 127.99, 124.11, 122.76, 114.27, 94.57, 88.16, 75.51, 70.78, 57.20, 20.84; MS: MALDI: 906.3

(4-Bromo-3,5-dimethylphenoxy)(*tert*-butyl)dimethylsilane (29)

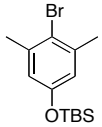

To a solution of **21** (2.0 g, 9.9 mmol) in methylene chloride (25 mL) was added triethylamine (1.5 mL, 10.9 mmol) and *tert*-butylchlorodimethylsilane (1.6 g, 10.4 mmol). The reaction mixture was stirred at room temperature for 16 h. Water

was added and the mixture was transferred into a separatory funnel. The organic phase was washed twice with water, then dried over magnesium sulfate. Solvent was evaporated under reduced pressure to yield 1.85 g (84%) of a clear liquid. ^{1}H NMR (300 MHz, $CDCl_3$) δ 6.57 (s, 2H), 2.35 (s, 6H), 0.97 (s, 9H), 0.18 (s, 6H); ^{13}C NMR (150 MHz, $CDCl_3$) δ 154.06, 138.90, 119.82, 118.88, 25.58, 23.77, 18.08, -4.15; MS: GC/MS: 314:316 (1:1)

2-[(2,6-di(4-*tert*butyldimethylsilyloxy-2,6-dimethylphenyl)phenyl]-1-(trimethylsilyl)ethyne (31)

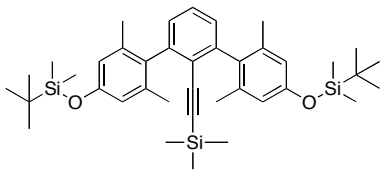

To an anhydrous solution of **29** (830 mg, 2.6 mmol) in THF at -78 °C was slowly added n-butyllithium (1.05 equiv of 2.4 M hexane) by syringe. To this was added a solution of anhydrous zinc chloride (360 mg, 2.6 mmol) in THF via cannula. The cold bath was removed after the addition was complete. Upon warming to room temperature, this solution was transferred via cannula to an anhydrous solution of **12a** (350 mg, 1.1 mmol) and palladium tetrakis(triphenylphosphine) (60 mg, 0.11 mmol) in THF. This flask was equipped with a condenser and the reaction mixture was heated to reflux. Stirring was continued at this temperature for 16 h. The solvent was evaporated under reduced pressure and methylene chloride was added to the mixture. The contents of the flask were transferred to a separatory funnel and the organic phase was washed once with a saturated EDTA solution and twice with water, then dried over magnesium sulfate. Solvent was removed under reduced pressure. The crude product was purified by column chromatography (10:1 hexanes: methylene chloride)

to give 200 mg (30%) of a clear film: ^{1}H NMR (300 MHz, $CDCl_3$) δ 7.39 (t, *J* = 8 Hz, 1H), 7.13 (d, *J* = 8 Hz, 2H), 6.60 (s, 4H), 2.01 (s, 12H), 1.05 (s, 18H), -0.15 (s, 9H); ^{13}C NMR (75 MHz, $CDCl_3$) δ 154.79, 145.04, 137.65, 134.52, 129.01, 128.60, 124.35, 118.84, 102.90, 99.51, 26.26, 20.88, 18.71, 0.00, -3.86; MS: EI: 643.4

2,6-di(4-hydroxy-2,6-dimethylphenyl)ethynylbenzene (32)

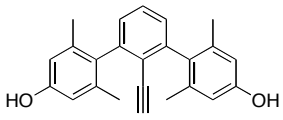

To a solution of **31** (300 mg, 0.47 mmol) in methanol / THF was added potassium carbonate (650 mg, 4.7 mmol) and the mixture was stirred at room temperature for 16 h. Methylene chloride was added to the reaction mixture, which was then transferred to a separatory funnel. The organic phase was washed twice with water, then dried over magnesium sulfate. Solvent was evaporated under reduced pressure to yield 130 mg (81%) of a white solid. mp = 256-258 °C; ^{1}H NMR (300 MHz, Acetone) δ 8.06 (s, 2H), 7.51 (t, *J* = 8 Hz, 1H), 7.11 (d, *J* = 8 Hz, 2H), 6.60 (s, 4H), 3.03 (s, 1H), 1.96 (s, 12H); ^{13}C NMR (75 MHz, Acetone) δ 157.03, 145.86, 137.57, 132.98, 129.45, 129.20, 123.84, 114.69, 83.00, 81.41, 20.52; MS: EI: 342.1

1,4-di[2,6-di(4-hydroxy-2,6-dimethylphenyl)phenylethynyl]benzene (33)

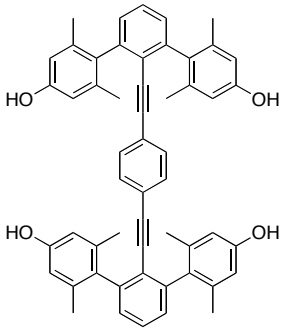

A solution of 1,4-diiodobenzene (96 mg, 0.29 mmol), **32** (200 mg 0.58 mmol), copper iodide (6 mg, 0.029 mmol), and palladium tetrakis(triphenylphosphine) (34 mg, 0.029 mmol) in triethylamine was heated to 80 °C and stirred at this temperature for 18 h. The reaction mixture was allowed to cool to room temperature, then diluted with ethyl acetate. The mixture was transferred to a separatory funnel, washed twice with water, then dried over magnesium sulfate. Solvent was evaporated under reduced pressure. The crude product was purified by column chromatography (2:1 hexane:ethyl acetate on silica) to yield 90 mg (41%) of a white solid: mp > 350 °C; ^{1}H NMR (300 MHz, acetone) δ 8.11 (s, 4H), 7.53 (t, *J* = 8 Hz, 2H), 7.18 (d, *J* = 8 Hz, 4H), 6.69 (s, 8H), 6.49 (s, 4H), 2.82 (s, 24H) ^{13}C NMR (100 MHz, acetone) δ 157.04, 144.84, 137.42, 132.19, 129.81, 129.27, 123.89, 123.29, 114.73, 114.68, 93.71, 90.69, 21.14; MS: MALDI: 758.7

1,4-di[2,6-di(2,6-dimethyl-4-(prop-2-ynoxy)phenyl)phenylethynyl]benzene (34)

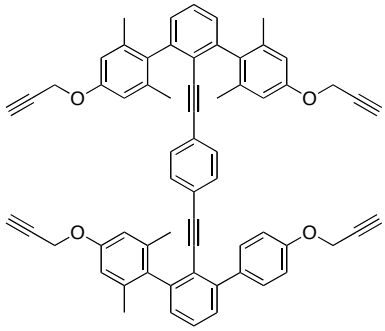

To a solution of **33** (90 mg, 0.12 mmol) and cesium carbonate (390 mg, 1.2 mmol) in N,N-dimethylformamide was added propargyl bromide (113 mg of a 80% solution in toluene). The reaction mixture was heated to 50 °C and stirred at this temperature for 20 h. Methylene chloride was added and the mixture was transferred to a separatory funnel. The organic phase was washed twice with water, then dried over magnesium sulfate. Solvent was evaporated under reduced pressure. The product was purified by column chromatography (2:1 hexanes: methylene chloride on silica) to yield 20 mg (18%) of a white solid: mp > 350 °C; ^{1}H NMR (600 MHz, $CDCl_3$) δ 7.42 (t, *J* = 8, 2H), 7.15 (d, *J* = 8, 4H), 6.73 (s, 8H), 6.40 (s, 4H), 4.74 (d, *J* = 2, 8H), 2.51(t, *J* = 2, 4H), 2.01 (s, 24H); ^{13}C NMR (150 MHz, $CDCl_3$) δ 156.58, 144.03, 137.89, 134.46, 131.09, 128.57, 128.41, 123.84, 122.87, 113.49, 94.51, 88.94, 79.17, 75.53, 55.88, 20.89; MS: MALDI: 910.4

2,6-dichloroiodobenzene (37)

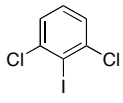

To a solution of 2,6-dichloroaniline (10.0 g, 62 mmol) in concentrated HCl (40 mL) at 0°C was added drop wise an aqueous solution of sodium nitrite (4.7 g, 68 mmol) over 45 min. Stirring was continued for an additional 30 min. The resulting

solution was added drop wise over 30 min to a vigorously stirred aqueous solution of potassium iodide (100.0 g, 0.62 mol) at 0 °C. Stirring was continued for an additional 3 h and the crude product was collected by filtration. The solid was then dissolved in methylene chloride and the solution was transferred to a separatory funnel. The organic phase was washed twice with a 10% aqueous sodium bisulfite solution and once with water, then dried over magnesium sulfate. Solvent was evaporated under reduced pressure. The product was dry loaded onto silica and passed through a silica plug with hexanes to yield 13.0 g (77%) of a white solid. mp = 63-65 °C; ^{1}H NMR (300 MHz, $CDCl_3$) δ 7.32 (d, *J* = 8 Hz, 2H), 7.20 (t, *J* = 8 Hz, 1H); ^{13}C NMR (75 MHz, $CDCl_3$) δ 140.63, 129.61, 127.24, 103.79; MS: GC/MS: 272:274:276 (9:6:1)

2,6-di[4-(4-methoxyphenyl)-2,6-dimethylphenyl]iodobenzene (38)

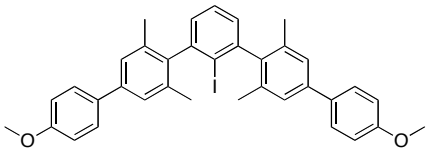

To predried magnesium (520 mg, 22 mmol) was added dropwise a solution of **23** (6.3 g, 22 mmol) in tetrahydrofuran over 45 min. The reaction mixture was heated to reflux and stirred at this temperature for 3 h. To this mixture was added dropwise a solution of **37** (1.5 g, 5.4 mmol) in tetrahydrofuran over 1 h. Stirring was continued at reflux for 16 hours. The reaction mixture was then cooled to 0 °C, and iodine (7.0 g, 28 mmol) was added all at once. Stirring was continued for 3 h, then aqueous thiosulfate solution was added to the reaction mixture. The mixture was transferred to a separatory funnel and the organic phase was washed twice with water, then dried over magnesium sulfate. Solvent was evaporated under reduced pressure. The crude product was purified by column chromatography (2:1 hexanes: methylene chloride on silica) to yield 1.8 g (54%) of a white solid. mp = 244-246 °C; ^{1}H NMR (300 MHz,

$CDCl_3$) δ 7.62 (d, *J* = 8 Hz, 4H), 7.52 (t, *J* = 8 Hz, 1H), 7.35 (s, 4H), 7.16 (d, *J* = 7 Hz, 2H), 7.00 (d, *J* = 8 Hz, 4H), 3.88 (s, 6H), 2.16 (s, 12H) ^{13}C NMR (75 MHz, $CDCl_3$) δ 158.94, 146.97, 143.15, 139.85, 135.86, 133.45, 128.89, 128.01, 127.73, 125.56, 113.97, 113.92, 55.24, 20.46; MS: MALDI: 624.3

2,6-di[4-(4-hydroxyphenyl)-2,6-dimethylphenyl]iodobenzene (39)

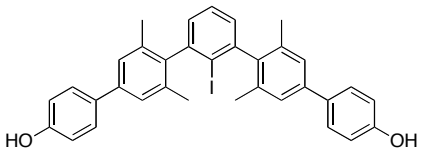

To a solution of **38** (1.5 g, 2.4 mmol) in dry methylene chloride at -78 °C was slowly added boron tribromide (9.6 mL of a 1.0 M solution in methylene chloride). The reaction mixture was stirred for 18 h. The flask was then placed in an ice bath and water was slowly added. Methylene chloride was added and the mixture was transferred to a separatory funnel. The organic phase was washed twice with water, then dried over magnesium sulfate. Solvent was removed under reduced pressure to yield 1.35 g (95%) of a white solid. mp = 222-224 °C; ^1H NMR (300 MHz, $CDCl_3$) δ 8.40 (s, 2H), 7.64 (t, *J* = 8 Hz, 1H), 7.58 (d, *J* = 7 Hz, 4H), 7.39 (s, 4H), 7.21 (d, *J* = 8 Hz, 2H), 6.95 (d, *J* = 7 Hz, 4H); ^{13}C NMR (100 MHz, Acetone) δ 158.07, 148.20, 144.09, 141.13, 136.90, 133.17, 130.26, 128.93, 128.90, 126.28, 116.64, 107.72, 20.85; MS: EI: 596.0

2-(2,6-di[4-(4-hydroxyphenyl)-2,6-dimethylphenyl]phenyl)-1-(trimethylsilyl)ethyne (40a)

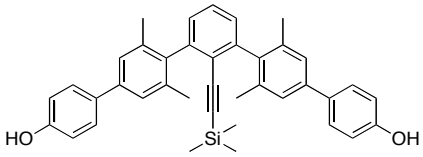

A solution of **39** (800 mg, 1.3 mmol), trimethylsilylacetylene (400 mg 4.0 mmol), copper iodide (12 mg, 0.06 mmol), and palladium tetrakis(triphenylphosphine) (77 mg, 0.06 mmol) in triethylamine and N,N-dimethylformamide was heated to 90 °C and stirred at this temperature for 36 h. The reaction mixture was allowed to cool to room temperature, then diluted with ether. The mixture was transferred to a separatory funnel, washed twice with water, then dried over magnesium sulfate. Solvent was evaporated under reduced pressure. The crude product was purified by column chromatography (60:1 methylene chloride: ethyl acetate on silica) to yield 200 mg (27%) of a yellow oil. ^{1}H NMR (400 MHz, acetone) δ 8.36 (s, 2H), 7.58 (t, *J* = 8 Hz, 1H), 7.54 (d, *J* = 7 Hz, 4H), 7.35 (s, 4H), 7.25 (d, *J* = 8 Hz, 2H), 6.94 (d, *J* = 7 Hz, 4H), 2.13 (s, 12H), -0.25 (s, 9H); ^{13}C NMR (150 MHz, acetone) δ 145.55, 140.72, 139.86, 136.92, 133.43, 129.70, 128.79, 128.77, 125.97, 123.81, 116.47, 116.41, 103.48, 100.13, 20.74, -0.44; MS: EI: 566.2

2,6-di-[4-(4-hydroxyphenyl)-2,6-dimethylphenyl]ethynylbenzene (40b)

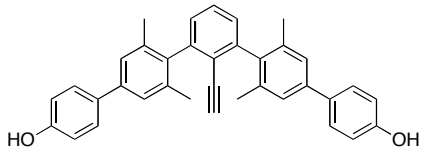

To a solution of **40a** (200 mg, 0.35 mmol) in tetrahydrofuran and methanol was added potassium carbonate (250 mg, 1.8 mmol). The reaction mixture was stirred at room temperature for 18 h. Water and methylene chloride were added and the

mixture was transferred to a separatory funnel. The organic phase was washed twice with water, then dried over magnesium sulfate. Solvent was evaporated under reduced pressure to yield 130 mg (76%) of a white solid. mp = 233-235 ˚C ; ^{1}H NMR (300 MHz, $CDCl_3$) δ 8.41 (s, 2H), 7.62 (t, *J* = 8 Hz, 1H), 7.57 (d, *J* = 7 Hz, 4H), 7.37 (s, 4H), 7.24 (d, *J* = 8 Hz, 2H), 6.94 (d, *J* = 7 Hz, 4H), 3.10 (s, 1H), 2.13 (s, 12H); ^{13}C NMR (150 MHz, acetone) δ 157.90, 145.81, 140.59,139.84, 136.90, 133.14, 130.00, 128.97, 128.73, 125.96, 116.50, 116.41, 83.80, 81.19, 20.73; MS: EI: 494.1

1,4-di-[2,6-di[4-(4-hydroxyphenyl)-2,6-dimethylphenyl]phenylethynyl]benzene (41)

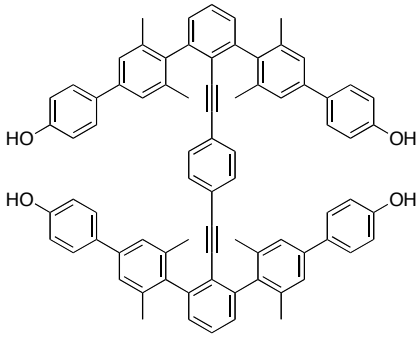

A solution of **40b** (86 mg, 0.17 mmol), diiodobenzene (28 mg 0.09 mmol), copper iodide (2 mg, 0.085 mmol), and palladium tetrakis(triphenylphosphine) (10 mg, 0.085 mmol) in triethylamine and N,N-dimethylformamide was heated to 90 °C and stirred at this temperature for 36 h. The reaction mixture was allowed to cool to room temperature, then diluted with methylene chloride. The mixture was transferred to a separatory funnel, and the organic phase was washed twice with water, then dried over magnesium sulfate. Solvent was evaporated under reduced pressure. The crude product was purified by column chromatography (1:1 hexanes: ethyl acetate on silica) to yield 55 mg (60%) of an off-white solid. mp = 301-303 °C; ^{1}H NMR (400 MHz, acetone) δ 7.61 (t, *J* = 8 Hz, 2H), 7.50 (d, *J* = 7 Hz, 8H), 7.32 (s, 8H), 7.28 (d, *J* = 8

Hz, 4H), 6.98 (d, *J* = 7 Hz, 8H), 6.36 (s, 4H), 2.10 (s, 24 H) ^{13}C NMR (100 MHz, acetone) δ 157.49, 144.78, 140.45, 139.39, 136.70, 132.91, 131.20, 129.43, 128.47, 128.37, 125.60, 123.21, 123.16, 116.18, 94.57, 89.72, 20.37; MS: MALDI: 1063.5

4'-hydroxy-4-(prop-2-ynoxy)biphenyl (43)

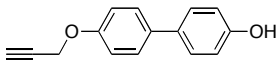

To a solution of 4,4'-dihydroxybiphenyl (3.5 g, 19 mmol) in N,N-dimethylformamide was added sodium hydride (820 mg, 19 mmol, 60% in mineral oil). The suspension was stirred for 30 min, at which point propargyl bromide (2.2 g, 19 mmol) was added. The reaction mixture was heated to 80˚C and stirred at this temperature for 24 h. The mixture was allowed to cool to room temperature, water was added, and the crude product was collected by filtration. The crude product was purified by column chromatography (methylene chloride on silica) to yield 2.6 g (61%) of a white solid. Spectral data matches literature values: ^{1}H NMR (300 MHz) δ 7.47 (d, *J* = 8 Hz, 2H), 7.43 (d, *J* = 8 Hz, 2H), 7.03 (d, *J* = 8 Hz, 2H), 6.88 (d, *J* = 8 Hz, 2H), 4.73 (d, *J* = 2 Hz, 2H), 2.54 (t, *J* = 2 Hz, 1H); MS: GC/MS: 224

4-(3-chloropropanoxy)-4'-(prop-2-ynoxy)biphenyl (44)

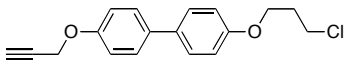

To a solution of **43 (**2.2 g, 10 mmol) in tetrahydrofuran was added sodium hydride (660 mg, 15 mmol, 60% in mineral oil). The suspension was stirred for 30 min, at which point 1-bromo-3-chloropropane (280 mg, 18 mmol) was added. The reaction mixture was heated to reflux and stirred at this temperature for 48 h. Solvent was removed under reduced pressure and recrystallization of the crude product in cyclohexane yielded 2.7 g (90%) of a white crystalline solid. mp = 144-146 ˚C; ^{1}H

NMR (300 MHz) δ 7.50 (d, *J* = 7 Hz, 2H), 7.49 (d, *J* = 7 Hz, 2H), 7.05 (d, *J* = 7 Hz, 2H), 6.98 (d, *J* = 7 Hz, 2H), 4.73 (d, *J* = 2 Hz, 2H), 4.17 (t, *J* = 6 Hz, 2H), 3.78 (t, *J* = 6 Hz, 2H), 2.54 (d, *J* = 2 Hz, 1H), 2.29 (m, 2H); ^{13}C NMR (100 MHz) δ 157.93, 156.68, 134.36, 133.56, 127.83, 127.76, 115.19, 114.80, 78.61, 75.53, 64.38, 55.91, 41.53, 32.31; MS: GC/MS: 300, 302 (3:1)

Extended tetrayne (45)

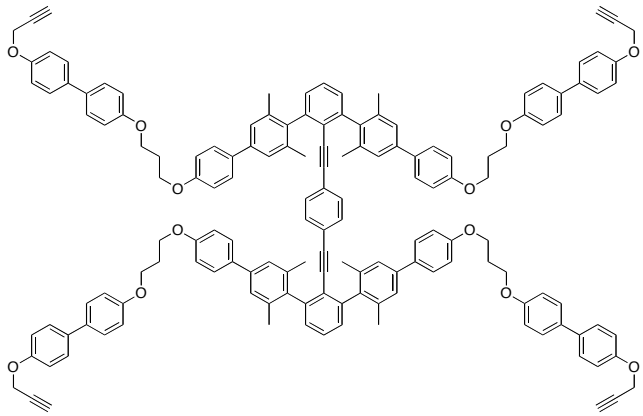

To a solution of **41** (55 mg, 0.05 mmol) in N,N-dimethylformamide was added cesium carbonate (340 mg, 1.0 mmol). The reaction mixture was stirred for 30 minutes, then **44** (250 mg, 0.8 mmol) was added. The reaction mixture was heated to reflux and stirred at this temperature for 36 h. Water was added and the mixture was transferred to a separatory funnel. Methylene chloride and 2 N hydrochloric acid were added to the funnel. The organic phase was washed twice with water, then dried over magnesium sulfate. Solvent was evaporated under reduced pressure. The crude product was purified by column chromatography (8:1 methylene chloride : hexane) to yield 30 mg (27%) of a white solid. mp > 350 °C; ^{1}H NMR (600 MHz, acetone) δ 7.59 (t, 2H, *J* = 8 Hz), 7.57 (d, 8H, *J* = 7 Hz), 7.53 (d, 8H, *J* = 7 Hz), 7.51 (d, 8H, *J* = 7 Hz), 7.32 (s, 8H), 7.27 (d, 4H, *J* = 8 Hz), 7.08 (d, 8H, *J* = 7 Hz), 7.05 (d, 8H, *J* = 7 Hz), 7.01 (d, 8H, *J* = 7 Hz), 6.31 (s, 4H), 4.80 (d, 8H, *J* = 2 Hz), 4.30 (m, 16H), 3.08

(t, 4H, *J* = 2 Hz), 2.32 (quin., 8 H, *J* = 7 Hz), 2.07 (s, 24 H); ^{13}C NMR (150 MHz, Acetone) δ 159.51, 159.20, 157.79, 145.10, 140.56, 140.00, 137.18, 134.82, 134.48, 133.92, 131.58, 128.84, 128.79, 128.40, 128.29, 126.13, 116.06, 115.77, 115.74, 115.70, 94.97, 90.09, 79.85, 77.00, 65.37, 65.34, 56.35, 54.97, 20.77; MS: MALDI: 2118.91

4'-(6-chlorohexanox-1-yl)-4-(prop-2-ynoxy)biphenyl (46)

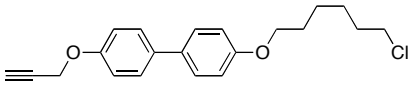

To a solution of **43** (1.6 g, 7 mmol) in tetrahydrofuran was added sodium hydride (530 mg, 12 mmol, 60% in mineral oil). The suspension was stirred for 30 min, at which point 1-bromo-6-chlorohexane (2.8 g, 14 mmol) was added. The reaction mixture was heated to reflux and stirred at this temperature for 38 h. Solvent was removed under reduced pressure and methylene chloride was added to the crude product. The mixture was transferred to a separatory funnel and the organic phase was washed twice with water. The aqueous phase was acidified and extracted with methylene chloride. The combined organic phases were dried over magnesium sulfate. Solvent was removed under reduced pressure and the crude product was purified by column chromatography (4:1 hexanes : diethyl ether) to yield 1.1 g (47%) of an off-white solid. mp = 161-163 ˚C ; ^{1}H NMR (400 MHz, $CDCl_3$) δ 7.50 (d, *J* = 7 Hz, 2H), 7.47 (d, *J* = 7 Hz, 2H), 7.05 (d, *J* = 7 Hz, 2H), 6.96 (d, *J* = 7 Hz, 2H), 4.73(d, *J* = 2 Hz, 2H), 4.01 (t, *J* = 8 Hz, 2H), 3.58 (t, *J* = 8 Hz, 2H), 2.54 (t, *J* = 2 Hz, 1H), 1.84 (m, 4H), 1.51 (m, 4H); ^{13}C NMR (100 MHz, $CDCl_3$) δ 158.28, 156.62, 134.46, 133.18, 127.77, 127.72, 115.17, 114.76, 78.62, 75.52, 67.82, 55.91, 45.00, 32.53, 32.44, 29.15, 26.66, 25.44; MS: CI: 342.2

Hexyl extended tetryne (47)

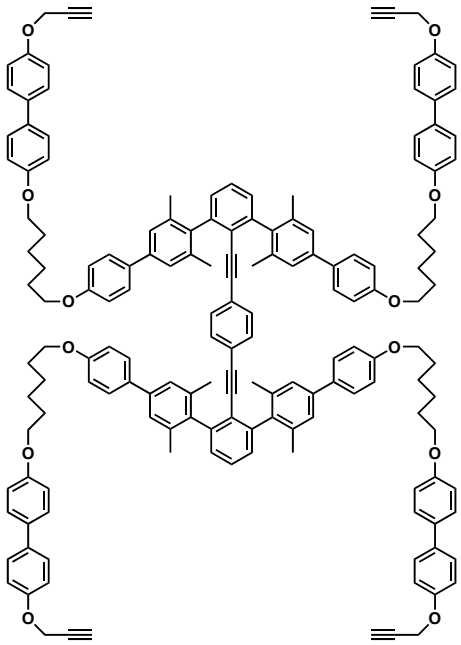

To a solution of **41** (50 mg, 0.047 mmol) in N,N-dimethylformamide was added cesium carbonate (310 mg, 0.94 mmol). The reaction mixture was stirred for 30 minutes, then **46** was added. The reaction mixture was heated to reflux and stirred at this temperature for 36 h. Water was added and the mixture was transferred to a separatory funnel. Methylene chloride and 2 N hydrochloric acid were added to the funnel. The organic phase was washed twice with water, then dried over magnesium sulfate. Solvent was evaporated under reduced pressure. The crude product was purified by column chromatography (4:1 methylene chloride : hexane) to yield 22 mg (21%) of a white solid. mp > 350 °C; ^{1}H NMR (600 MHz, $CDCl_3$) 7.54 (t, *J* = 8 Hz, 2H), 7.51 (d, *J* = 7 Hz, 8H), 7.48 (d, *J* = 7 Hz, 8H), 7.46 (d, *J* = 7 Hz, 4H), 7.25 (s, 8H), 7.21 (d, *J* = 8 Hz, 8H), 7.03 (d, *J* = 7 Hz, 8H), 6.98 (d, *J* = 7 Hz, 8H), 6.95 (d, *J* = 7 Hz, 8H), 6.31 (s, 4H), 4.73 (d, *J* = 2 Hz, 8H), 4.16 (t, *J* = 7 Hz, 8H), 4.01 (t, *J* = 7

Hz, 8H), 2.54 (t, J = 2 Hz, 4H), 2.09 (s, 24 H), 1.85 (m, 16H), 1.59 (m, 16H); ^{13}C NMR (150 MHz, $CDCl_3$) δ 158.73, 158.53, 156.80, 144.28, 139.86, 139.36, 136.74, 134.65, 133.99, 133.34, 130.95, 128.28, 128.06, 128.04, 125.62, 123.12, 122.80, 118.14, 117.23, 115.36, 114.97, 114.90, 94.74, 88.89, 78.83, 75.75, 68.11, 56.08, 28.86, 28.77, 26.17, 26.00, 20.78; MS: MALDI: 2288.2

Table 3.6 *Crystallographic Data for* **1**

Crystallised from	CH_2Cl_2
Empirical formula	$C_{32}H_{30}$
Formula weight [g mol^{-1}]	414.59
Crystal colour, habit	yellow, prism
Crystal dimensions [mm]	0.12 × 0.27 × 0.30
Temperature [K]	160 (1)
Crystal system	triclinic
Space group	$P\bar{1}$ (#2)
Z	2
Reflections for cell determination	4275
2θ range for cell determination [°]	4 – 50
Unit cell parameters a [Å]	8.4200(4)
b [Å]	10.4450(4)
c [Å]	15.4972(7)
α [°]	81.045(3)
β [°]	74.819(3)
γ [°]	68.224(3)
V [Å^3]	1218.90(10)
F(000)	444
D_x [g cm^{-3}]	1.130
μ(Mo $K\alpha$) [mm^{-1}]	0.0634
Scan type	ω
$2\theta_{(max)}$ [°]	50
Total reflections measured	17941
Symmetry independent reflections	4301
R_{int}	0.059
Reflections with $I > 2\sigma(I)$	3093
Reflections used in refinement	4298
Parameters refined	296
Final $R(F)$ [$I>2\sigma(I)$ reflections]	0.0530
$wR(F^2)$ (all data)	0.1430
Weights: $w = [\sigma^2(F_o^2) + (0.0552P)^2 + 0.3424P]^{-1}$ where $P = (F_o^2 + 2F_c^2)/3$	
Goodness of fit	1.067
Secondary extinction coefficient	0.033(5)
Final Δ_{max}/σ	0.001
$\Delta\rho$ (max; min) [e Å^{-3}]	0.23; -0.18
$\sigma(d_{(C-C)})$ [Å]	0.003

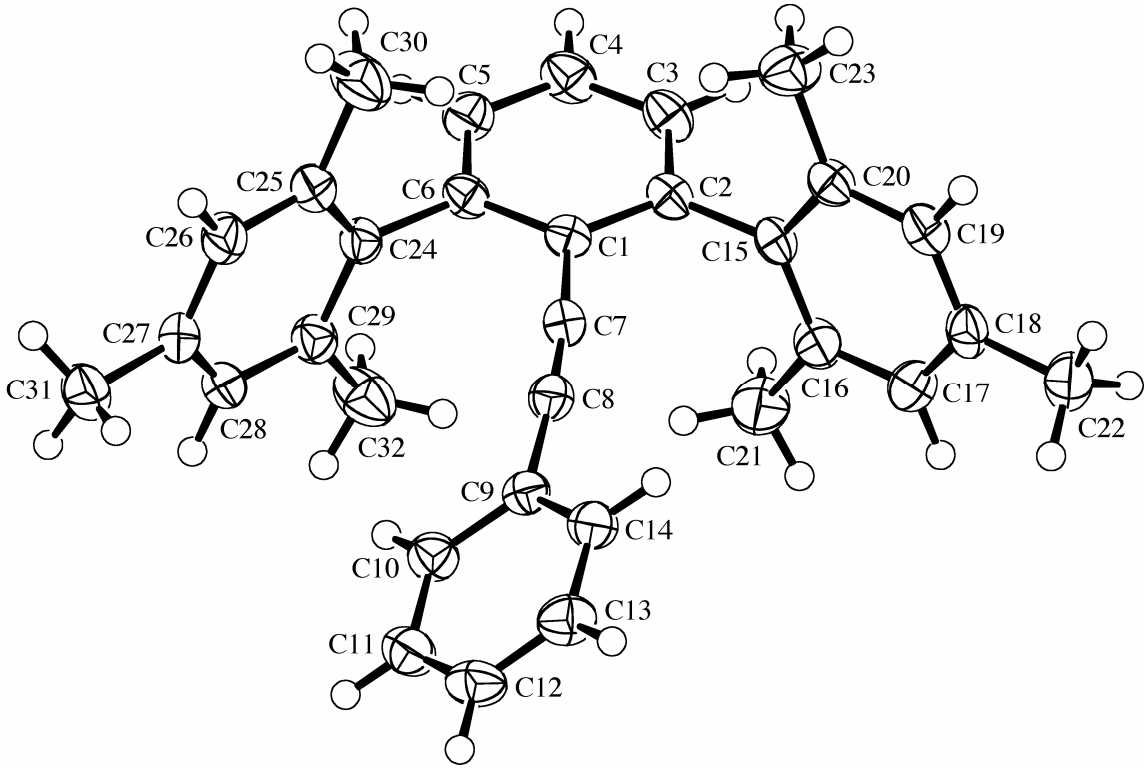
C30
C4
C5
C3
C23
C25
C6
C2
C20
C26
C24
C1
C15
C19
C27
C29
C7
C18
C31
C8
C16
C17
C28
C32
C21
C22
C9
C14
C10
C13
C11
C12

Table 3.7 *Crystallographic Data for* **2b**

Crystallised from	CH_2Cl_2 / EtOH
Empirical formula	$C_{31}H_{29}N$
Formula weight [g mol^{-1}]	415.58
Crystal colour, habit	colourless, prism
Crystal dimensions [mm]	0.20 × 0.20 × 0.25
Temperature [K]	160(1)
Crystal system	triclinic
Space group	$P\bar{1}$ (#2)
Z	2
Reflections for cell determination	6886
2θ range for cell determination [°]	4 – 60
Unit cell parameters a [Å]	8.3091(2)
b [Å]	10.5240(2)
c [Å]	15.4592(3)
α [°]	80.8186(9)
β [°]	74.994(1)
γ [°]	67.878(1)
V [Å^3]	1206.70(4)
$F(000)$	444
D_x [g cm^{-3}]	1.144
μ(Mo $K\alpha$) [mm^{-1}]	0.0653
Scan type	ϕ and ω
$2\theta_{(max)}$ [°]	60
Total reflections measured	30830
Symmetry independent reflections	7037
R_{int}	0.046
Reflections with $I > 2\sigma(I)$	4918
Reflections used in refinement	7032
Parameters refined	296
Final $R(F)$ [$I > 2\sigma(I)$ reflections]	0.0558
$wR(F^2)$ (all data)	0.1591
Weights: $w = [\sigma^2(F_o^2) + (0.0734P)^2 + 0.1784P]^{-1}$ where $P = (F_o^2 + 2F_c^2)/3$	
Goodness of fit	1.054
Secondary extinction coefficient	0.027(7)
Final Δ_{max}/σ	0.001
$\Delta\rho$ (max; min) [e Å^{-3}]	0.27; -0.27
$\sigma(d_{(C-C)})$ [Å]	0.002

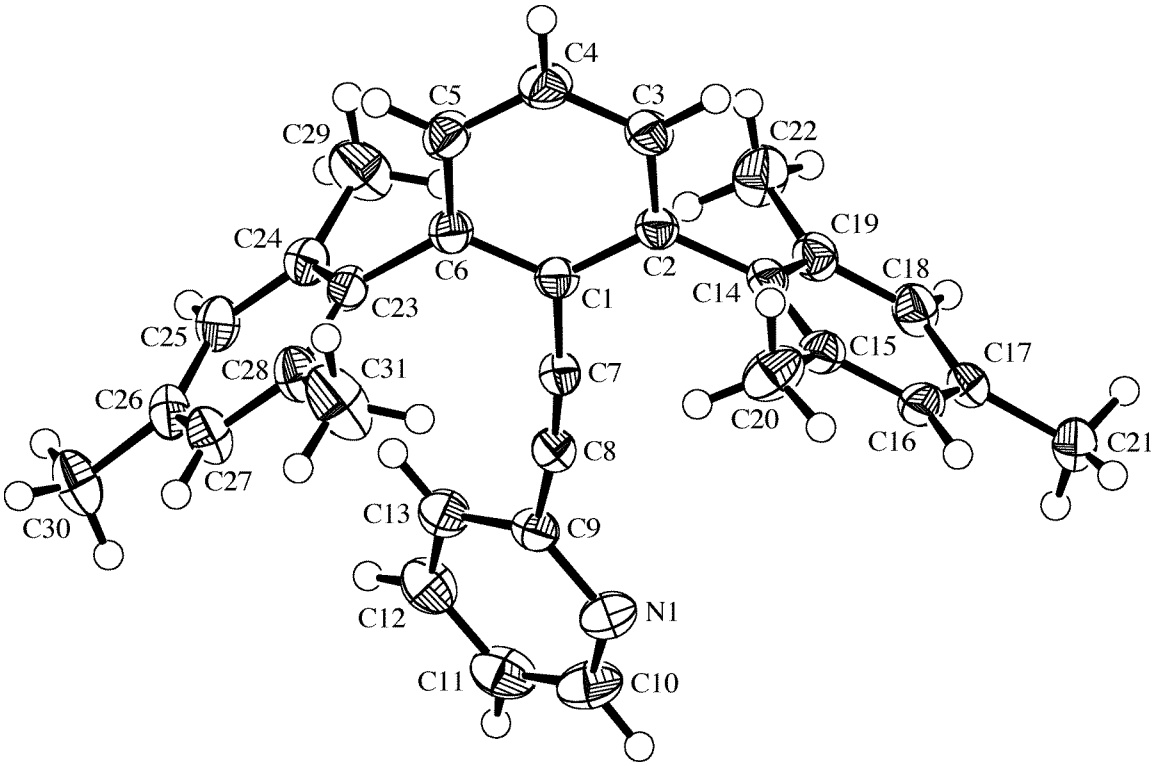
C4
C5
C3
C29
C22
C24
C6
C2
C19
C18
C23
C1
C14
C25
C28
C31
C7
C15
C17
C26
C20
C16
C21
C27
C8
C30
C13
C9
C12
N1
C11
C10

Table 3.8 *Crystallographic Data for* **2a**

Crystallised from	CH_2Cl_2 / MeOH
Empirical formula	$C_{31}H_{29}N$
Formula weight [g mol^{-1}]	415.58
Crystal colour, habit	colourless, prism
Crystal dimensions [mm]	0.12 × 0.25 × 0.27
Temperature [K]	160 (1)
Crystal system	triclinic
Space group	$P\bar{1}$ (#2)
Z	4
Reflections for cell determination	8433
2θ range for cell determination [°]	4 – 50
Unit cell parameters a [Å]	10.1034(4)
b [Å]	14.8715(6)
c [Å]	17.8686(7)
α [°]	74.014(3)
β [°]	75.146(2)
γ [°]	78.920(2)
V [Å^3]	2473.3(2)
$F(000)$	888
D_x [g cm^{-3}]	1.116
μ(Mo $K\alpha$) [mm^{-1}]	0.0637
Scan type	ω
$2\theta_{(max)}$ [°]	50
Total reflections measured	32418
Symmetry independent reflections	8627
R_{int}	0.055
Reflections with $I > 2\sigma(I)$	6228
Reflections used in refinement	8625
Parameters refined	590
Final $R(F)$ [$I>2\sigma(I)$ reflections]	0.0546
$wR(F^2)$ (all data)	0.1458
Weights: $w = [\sigma^2(F_o^2) + (0.0574P)^2 + 0.7937P]^{-1}$ where $P = (F_o^2 + 2F_c^2)/3$	
Goodness of fit	1.055
Secondary extinction coefficient	0.017(2)
Final Δ_{max}/σ	0.001
$\Delta\rho$ (max; min) [e Å^{-3}]	0.19; -0.16
$\sigma(d_{(C-C)})$ [Å]	0.003

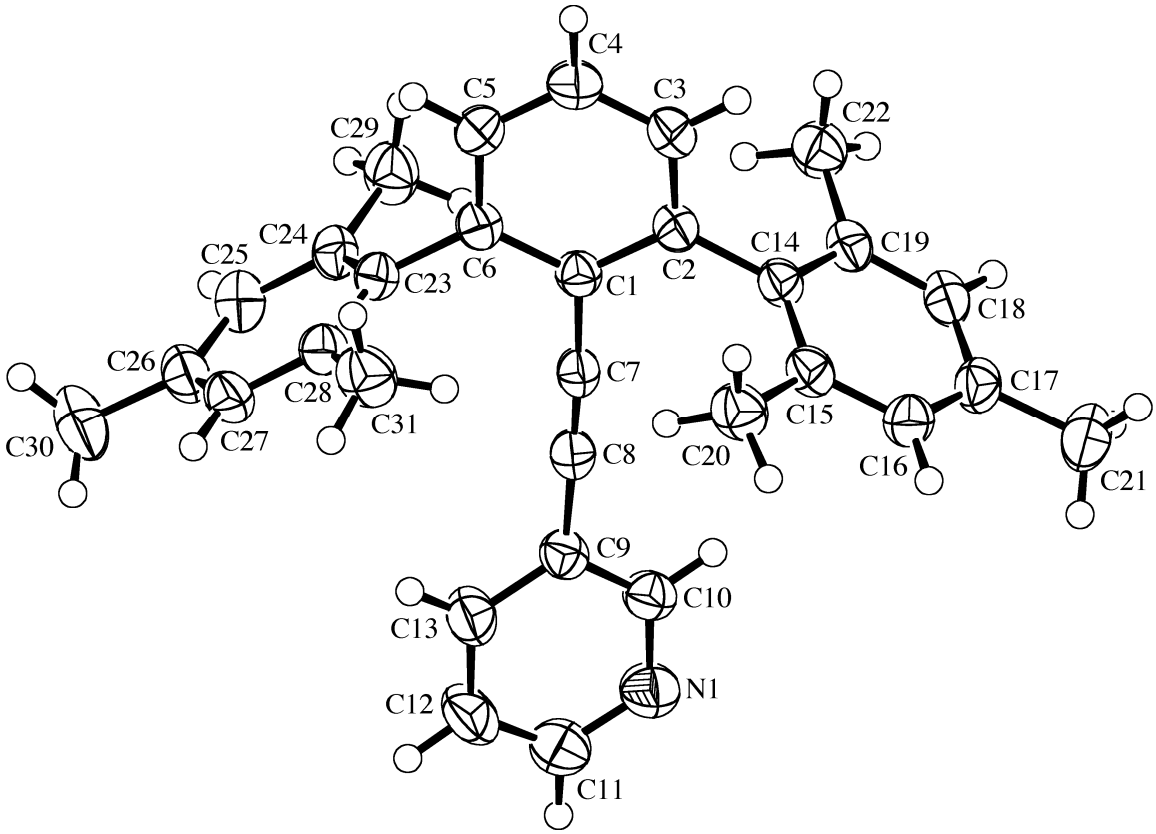
C4
C5
C3
C29
C22
C24
C25
C6
C23
C1
C2
C14
C19
C18
C26
C28
C7
C17
C30
C27
C31
C15
C20
C16
C21
C8
C9
C10
C13
N1
C12
C11

Table 3.9 *Crystallographic Data for* **5**

Crystallised from	CH_2Cl_2 / EtOH
Empirical formula	$C_{30}H_{28}N_2$
Formula weight [g mol^{-1}]	416.56
Crystal colour, habit	pale-yellow, plate
Crystal dimensions [mm]	0.05 × 0.20 × 0.25
Temperature [K]	160(1)
Crystal system	orthorhombic
Space group	*Pnna* (#52)
Z	4
Reflections for cell determination	2427
2θ range for cell determination [°]	4 – 50
Unit cell parameters a [Å]	18.9732(7)
b [Å]	14.5707(5)
c [Å]	8.6223(4)
α [°]	90
β [°]	90
γ [°]	90
V [Å^3]	2383.7(3)
F(000)	888
D_x [g cm^{-3}]	1.161
μ(Mo $K\alpha$) [mm^{-1}]	0.0674
Scan type	ω
$2\theta_{(max)}$ [°]	50
Total reflections measured	28593
Symmetry independent reflections	2112
R_{int}	0.089
Reflections with $I > 2\sigma(I)$	1506
Reflections used in refinement	2109
Parameters refined; restraints	178; 36
Final $R(F)$ [$I > 2\sigma(I)$ reflections]	0.0485
$wR(F^2)$ (all data)	0.1312
Weights: $w = [\sigma^2(F_o^2) + (0.0612P)^2 + 0.3266P]^{-1}$ where $P = (F_o^2 + 2F_c^2)/3$	
Goodness of fit	1.060
Secondary extinction coefficient	0.008(2)
Final Δ_{max}/σ	0.001
$\Delta\rho$ (max; min) [e Å^{-3}]	0.22; -0.19
$\sigma(d_{(C-C)})$ [Å]	0.002 – 0.01

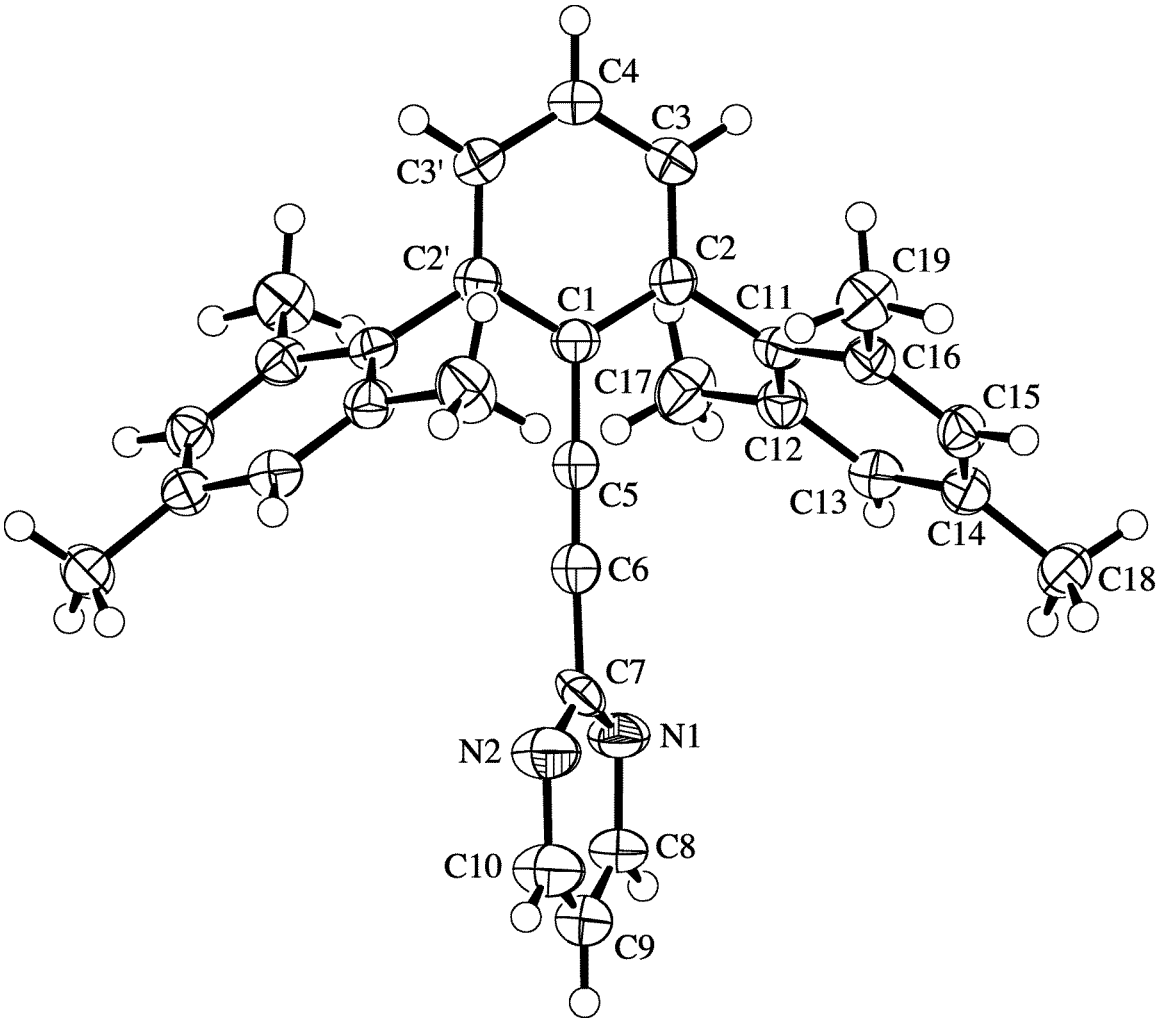
C4
C3
C3'
C2'
C2
C19
C1
C11
C16
C17
C15
C12
C5
C13
C14
C6
C18
C7
N2
N1
C10
C8
C9

Table 3.10 *Crystallographic Data for* **14**

Crystallised from	CH_2Cl_2 / hexane
Empirical formula	$C_{66}H_{72}Cl_4O_4$
Formula weight [g mol^{-1}]	1071.10
Crystal colour, habit	colourless, tablet
Crystal dimensions [mm]	0.10 × 0.17 × 0.40
Temperature [K]	160(1)
Crystal system	triclinic
Space group	$P\bar{1}$ (#2)
Z	1
Reflections for cell determination	5006
2θ range for cell determination [°]	4 – 50
Unit cell parameters a [Å]	9.5378(3)
b [Å]	11.7657(4)
c [Å]	13.6855(6)
α [°]	85.769(2)
β [°]	88.725(2)
γ [°]	71.627(2)
V [Å^3]	1453.51(9)
$F(000)$	568
D_x [g cm^{-3}]	1.224
μ(Mo $K\alpha$) [mm^{-1}]	0.251
Scan type	ω
$2\theta_{(max)}$ [°]	50
Total reflections measured	19536
Symmetry independent reflections	5099
R_{int}	0.069
Reflections with $I > 2\sigma(I)$	2948
Reflections used in refinement	5094
Parameters refined	287
Final $R(F)$ [$I > 2\sigma(I)$ reflections]	0.0661
$wR(F^2)$ (all data)	0.1903
Weights: $w = [\sigma^2(F_o^2) + (0.1087P)^2]^{-1}$ where $P = (F_o^2 + 2F_c^2)/3$	
Goodness of fit	0.965
Secondary extinction coefficient	0.030(5)
Final Δ_{max}/σ	0.001
$\Delta\rho$ (max; min) [e Å^{-3}]	0.26; -0.21
$\sigma(d_{(C-C)})$ [Å]	0.003 – 0.004

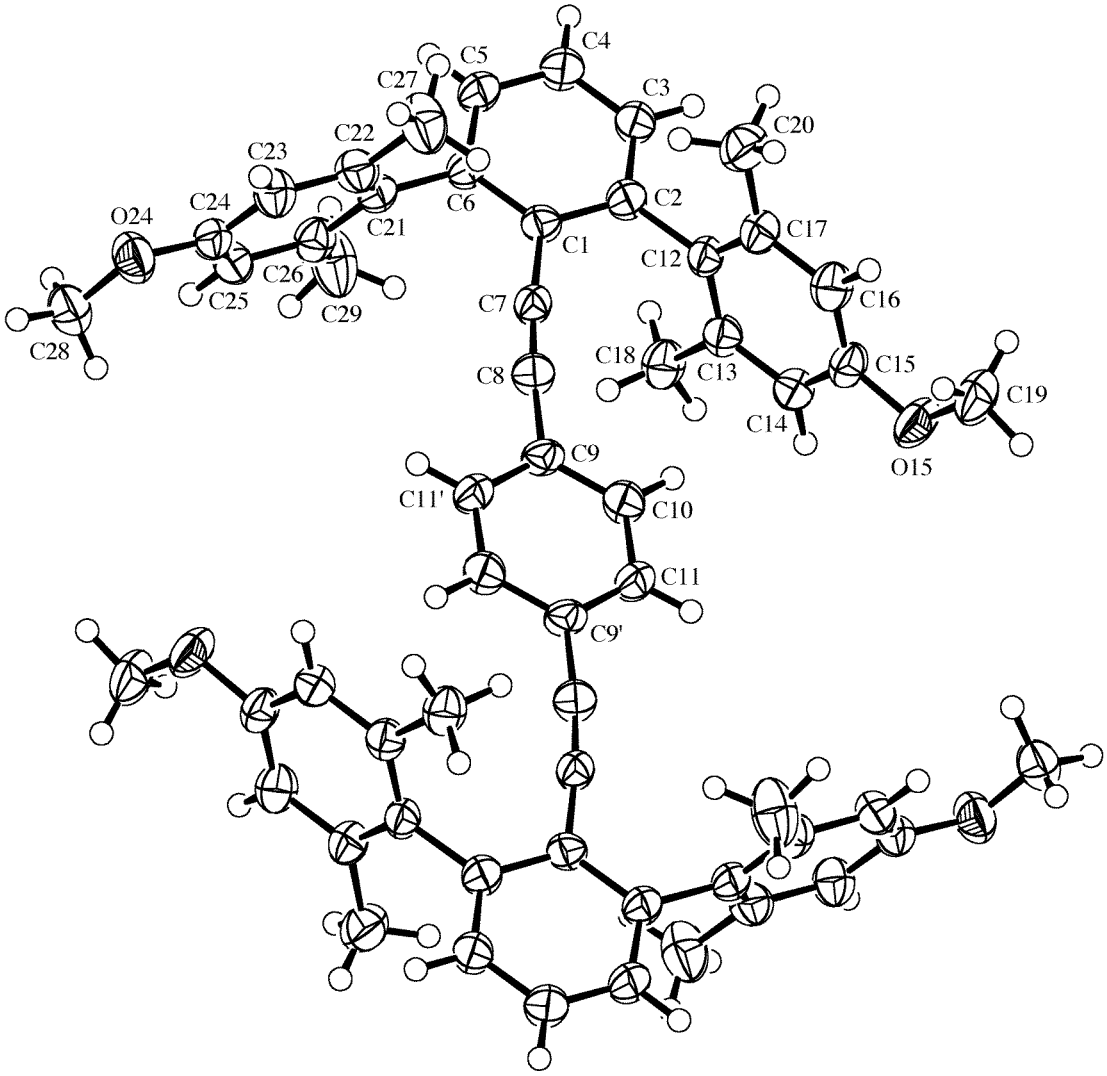
C4
C5
C27
C3
C20
C22
C23
C6
C2
O24
C24
C21
C1
C17
C12
C26
C25
C29
C7
C16
C28
C18
C13
C15
C19
C8
C14
O15
C9
C11'
C10
C11
C9'

Table 3.11 *Crystallographic Data for* **18**

Crystallised from	CH_2Cl_2 / EtOH
Empirical formula	$C_{64}H_{58}O_4$
Formula weight [g mol^{-1}]	891.16
Crystal colour, habit	colourless, tablet
Crystal dimensions [mm]	0.10 × 0.25 × 0.30
Temperature [K]	160(1)
Crystal system	monoclinic
Space group	$P2_1/c$ (#14)
Z	8
Reflections for cell determination	18356
2θ range for cell determination [°]	4 – 50
Unit cell parameters a [Å]	21.7475(7)
b [Å]	36.719(1)
c [Å]	12.9048(4)
α [°]	90
β [°]	95.539(1)
γ [°]	90
V [Å^3]	10257.0(6)
F(000)	3792
D_x [g cm^{-3}]	1.154
μ(Mo $K\alpha$) [mm^{-1}]	0.0703
Scan type	ω
$2\theta_{(max)}$ [°]	50
Total reflections measured	101722
Symmetry independent reflections	18117
R_{int}	0.100
Reflections with $I > 2\sigma(I)$	9010
Reflections used in refinement	18108
Parameters refined	1250
Final $R(F)$ [$I > 2\sigma(I)$ reflections]	0.0876
$wR(F^2)$ (all data)	0.2100
Weights: $w = [\sigma^2(F_o^2) + (0.0359P)^2 + 7.7552P]^{-1}$ where $P = (F_o^2 + 2F_c^2)/3$	
Goodness of fit	1.104
Secondary extinction coefficient	0.0008(2)
Final Δ_{max}/σ	0.001
$\Delta\rho$ (max; min) [e Å^{-3}]	0.41; -0.20
$\sigma(d_{(C-C)})$ [Å]	0.005 – 0.006

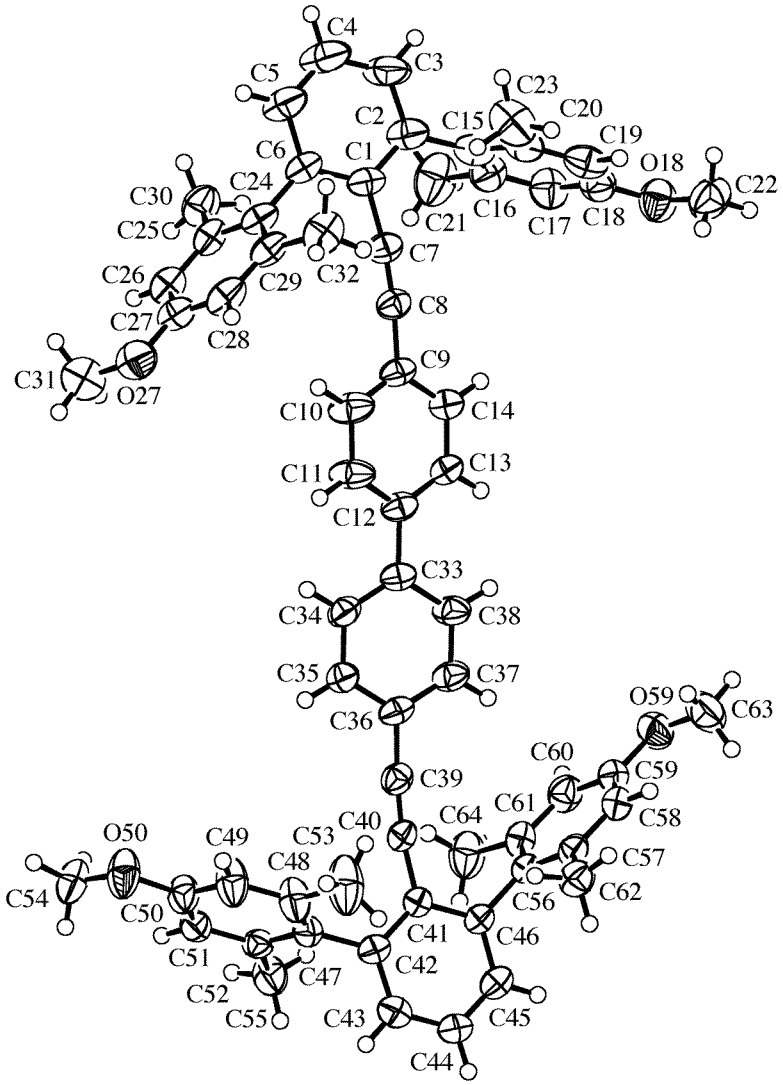
C4
C3
C5
C23
C20
C2
C15
C19
C6
C1
O18
C22
C24
C30
C16
C21
C17
C18
C25
C7
C26
C29
C32
C8
C27
C28
C9
C31
O27
C10
C14
C11
C13
C12
C33
C34
C38
C35
C37
C36
O59
C63
C60
C59
C39
C61
C58
C40
C64
O50
C49
C53
C48
C57
C54
C56
C62
C50
C41
C46
C51
C42
C47
C52
C55
C43
C45
C44

Table 3.12 *Crystallographic Data for* **16**

Crystallised from	CH_2Cl_2 / EtOH
Empirical formula	$C_{61}H_{61}Cl_8NO_4$
Formula weight [g mol^{-1}]	1155.78
Crystal colour, habit	colourless, prism
Crystal dimensions [mm]	0.15 × 0.20 × 0.25
Temperature [K]	160(1)
Crystal system	triclinic
Space group	$P\bar{1}$ (#2)
Z	1
Reflections for cell determination	52011
2θ range for cell determination [°]	4 – 50
Unit cell parameters a [Å]	9.5501(2)
b [Å]	11.9607(3)
c [Å]	13.4618(3)
α [°]	85.759(2)
β [°]	88.837(1)
γ [°]	71.180(1)
V [Å^3]	1451.48(6)
$F(000)$	602
D_x [g cm^{-3}]	1.322
μ(Mo $K\alpha$) [mm^{-1}]	0.434
Scan type	ω
$2\theta_{(max)}$ [°]	50
Transmission factors (min; max)	0.889; 0.967
Total reflections measured	19022
Symmetry independent reflections	5070
R_{int}	0.067
Reflections with $I > 2\sigma(I)$	3558
Reflections used in refinement	5069
Parameters refined	287
Final $R(F)$ [$I > 2\sigma(I)$ reflections]	0.0786
$wR(F^2)$ (all data)	0.2454
Weights:	$w = [\sigma^2(F_o^2) + (0.1749P)^2]^{-1}$ where $P = (F_o^2 + 2F_c^2)/3$
Goodness of fit	1.018
Secondary extinction coefficient	0.06(1)
Final Δ_{max}/σ	0.001
$\Delta\rho$ (max; min) [e Å^{-3}]	0.27; -0.29
$\sigma(d_{(C-C)})$ [Å]	0.003 – 0.004

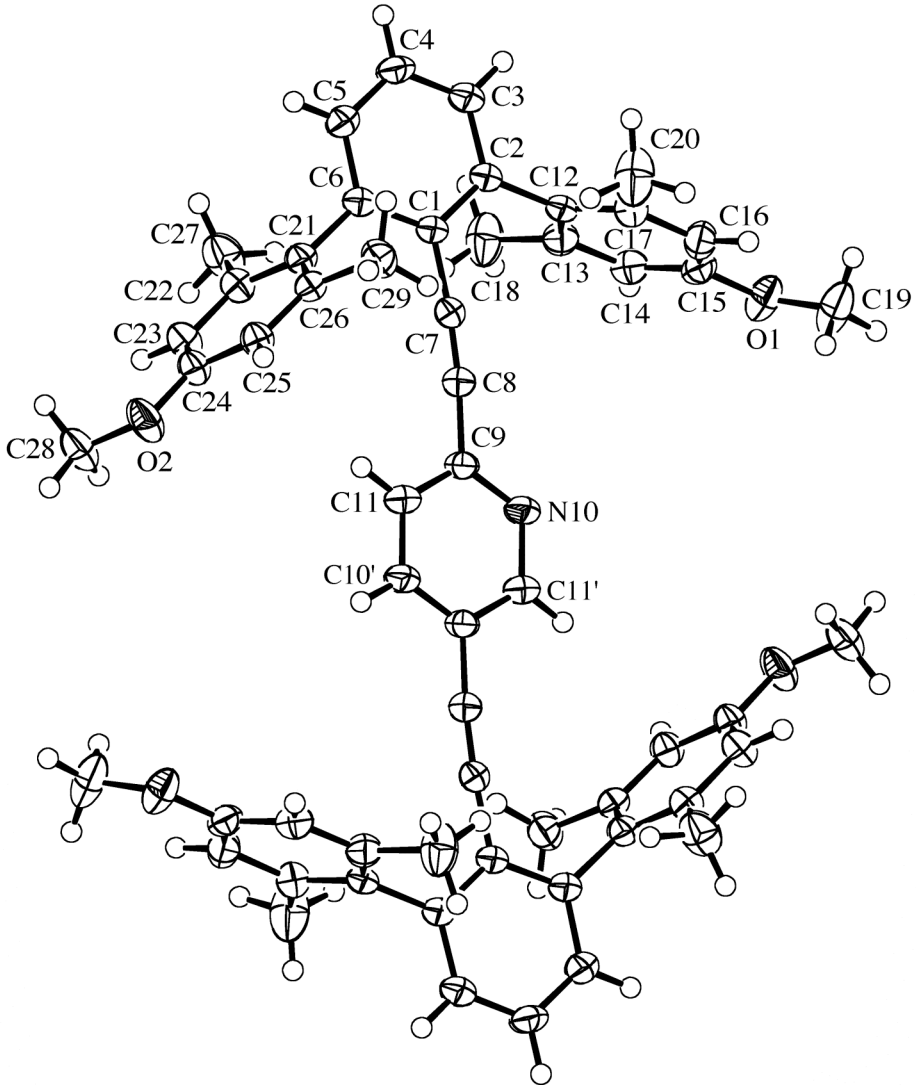
C4
C5
C3
C2
C20
C6
C12
C1
C16
C27
C21
C17
C22
C26
C29
C18
C13
C14
C15
C19
C23
C7
O1
C24
C25
C8
C28
O2
C9
C11
N10
C10'
C11'

Table 3.13 *Crystallographic Data for* **19**

Crystallised from	CH_2Cl_2 / EtOH
Empirical formula	$C_{52}H_{50}O_4$
Formula weight [g mol^{-1}]	738.96
Crystal colour, habit	colourless, plate
Crystal dimensions [mm]	0.03 × 0.17 × 0.28
Temperature [K]	160(1)
Crystal system	monoclinic
Space group	*Pc* (#7)
Z	4
Reflections for cell determination	7705
2θ range for cell determination [°]	4 – 50
Unit cell parameters *a* [Å]	12.9195(3)
b [Å]	26.1804(7)
c [Å]	13.8321(3)
α [°]	90
β [°]	114.575(1)
γ [°]	90
V [Å^3]	4254.7(2)
F(000)	1576
D_x [g cm^{-3}]	1.154
μ(Mo *K*α) [mm^{-1}]	0.0713
Scan type	ϕ and ω
$2\theta_{(max)}$ [°]	50
Total reflections measured	65817
Symmetry independent reflections	7536
R_{int}	0.084
Reflections with $I > 2\sigma(I)$	5363
Reflections used in refinement	7532
Parameters refined; restraints	1034; 2
Final *R*(*F*) [$I > 2\sigma(I)$ reflections]	0.0526
wR(F^2) (all data)	0.1166
Weights: $w = [\sigma^2(F_o^2) + (0.0555P)^2 + 0.0332P]^{-1}$ where $P = (F_o^2 + 2F_c^2)/3$	
Goodness of fit	1.091
Secondary extinction coefficient	0.0215(9)
Final Δ_{max}/σ	0.050
$\Delta\rho$ (max; min) [e Å^{-3}]	0.19; -0.19
$\sigma(d_{(C-C)})$ [Å]	0.005 – 0.006

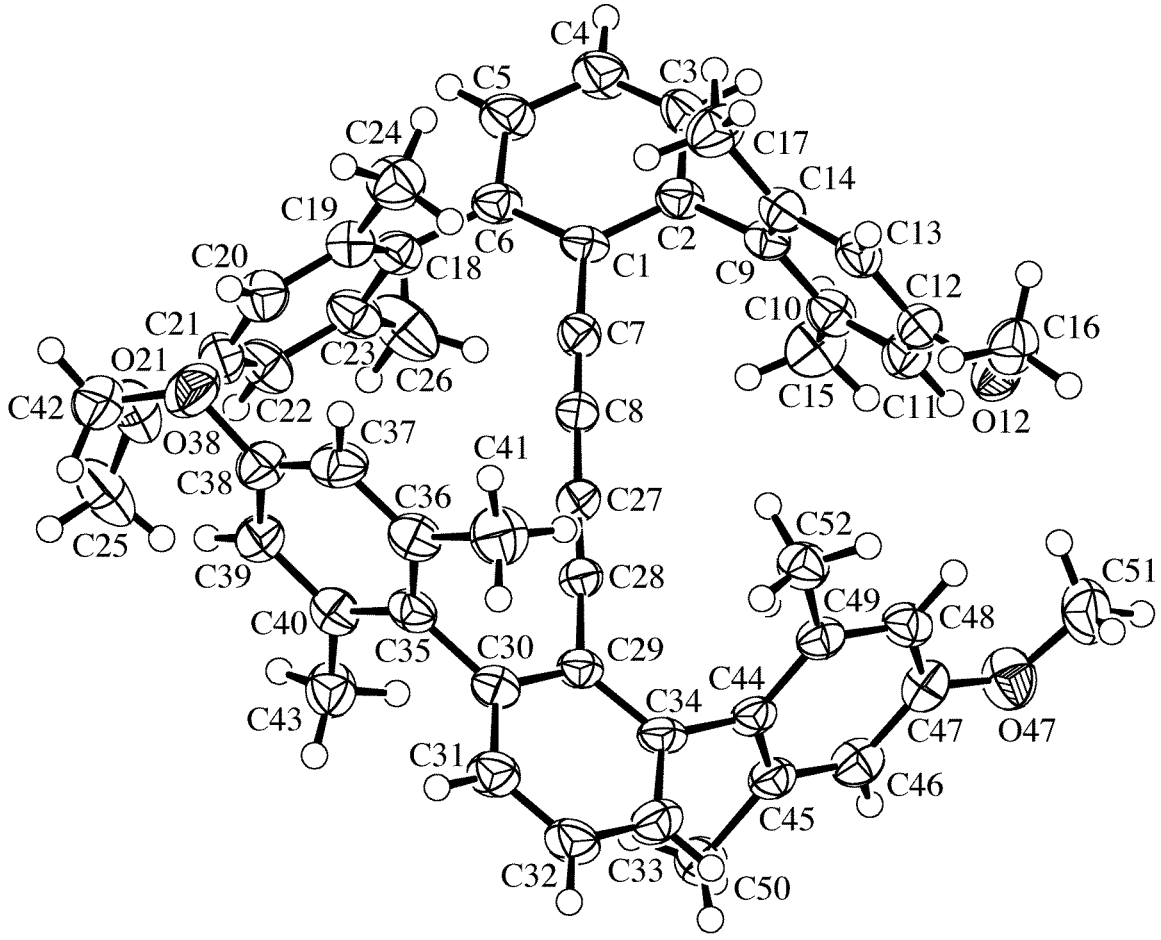
C4
C5
C3
C24
C17
C14
C19
C6
C2
C13
C20
C18
C1
C9
C12
C10
C21
C7
C16
O21
C23
C26
C15
C11
O12
C42
C22
C8
O38
C37
C41
C38
C36
C27
C25
C52
C39
C28
C51
C49
C48
C40
C35
C30
C29
C44
C43
C34
C47
O47
C31
C46
C45
C32
C33
C50

Table 3.14 *Crystallographic Data for* **26**

Crystallised from	CH_2Cl_2 / EtOH
Empirical formula	$C_{82}H_{70}O_4$
Formula weight [g mol^{-1}]	1119.45
Crystal colour, habit	colourless, prism
Crystal dimensions [mm]	0.20 × 0.20 × 0.30
Temperature [K]	160(1)
Crystal system	monoclinic
Space group	$P2_1/c$ (#14)
Z	4
Reflections for cell determination	13211
2θ range for cell determination [°]	4 – 52
Unit cell parameters a [Å]	29.4698(4)
b [Å]	13.9924(2)
c [Å]	16.0684(2)
α [°]	90
β [°]	102.4965(8)
γ [°]	90
V [Å^3]	6468.9(2)
$F(000)$	2376
D_x [g cm^{-3}]	1.149
μ(Mo $K\alpha$) [mm^{-1}]	0.0690
Scan type	ϕ and ω
$2\theta_{(max)}$ [°]	52
Total reflections measured	99005
Symmetry independent reflections	95938
R_{int}	0.088
Reflections with $I > 2\sigma(I)$	67864
Reflections used in refinement	95938
Parameters refined	789
Final $R(F)$ [$I > 2\sigma(I)$ reflections]	0.0868
$wR(F^2)$ (all data)	0.2708
Weights: $w = [\sigma^2(F_o^2) + (0.1085P)^2 + 11.9P]^{-1}$ where $P = (F_o^2 + 2F_c^2)/3$	
Goodness of fit	1.153
Secondary extinction coefficient	0.0110(3)
Final Δ_{max}/σ	0.001
$\Delta\rho$ (max; min) [e Å^{-3}]	0.67; -0.64
$\sigma(d_{(C-C)})$ [Å]	0.002 – 0.003

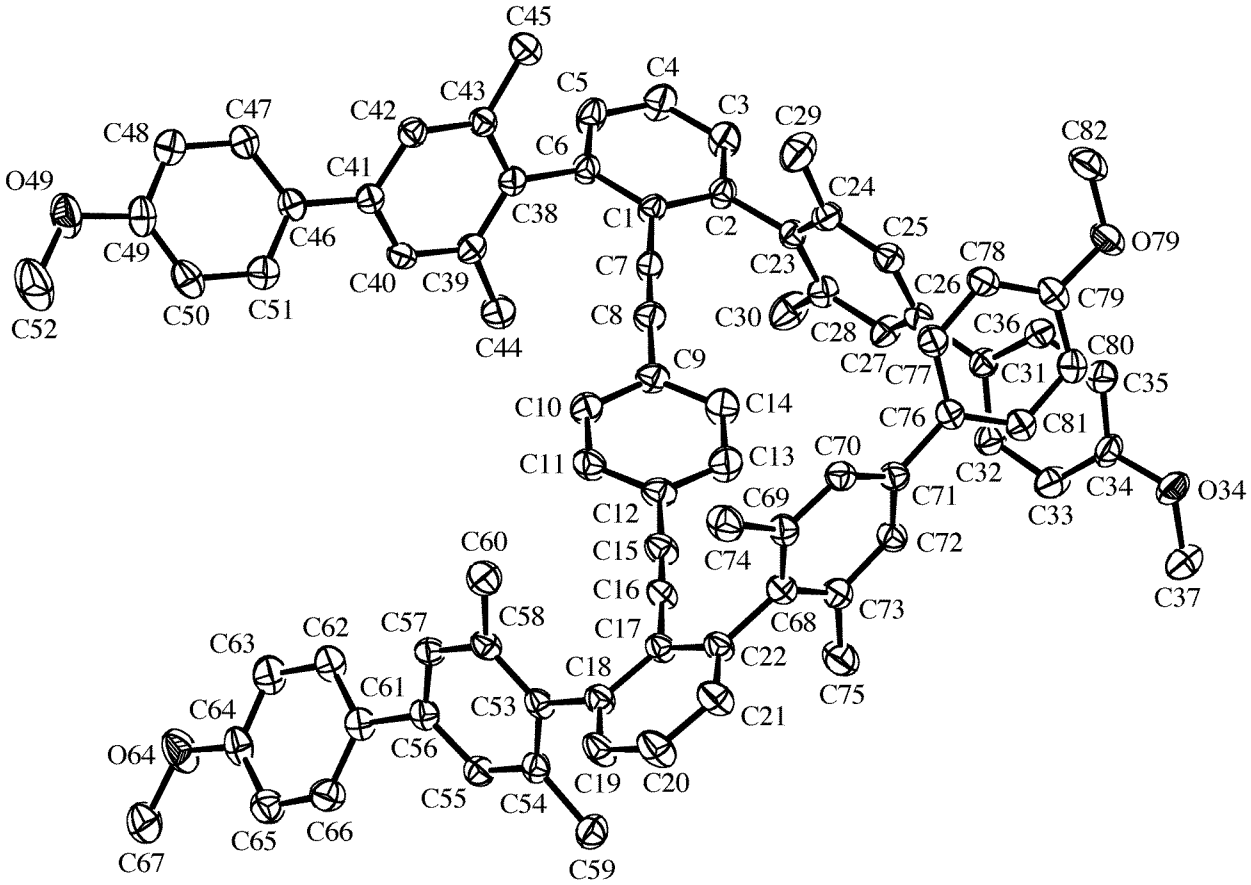
C45
C43
C5
C4
C3
C29
C82
C48
C47
C42
C6
C24
O49
C41
C38
C1
C2
C25
O79
C46
C49
C40
C39
C7
C23
C78
C26
C79
C50
C51
C8
C30
C28
C36
C52
C44
C27
C77
C31
C80
C9
C35
C10
C14
C76
C81
C11
C13
C70
C32
C34
O34
C12
C69
C71
C33
C60
C15
C74
C72
C37
C16
C73
C57
C58
C17
C68
C62
C63
C22
C18
C75
C61
C53
C21
C64
C56
O64
C55
C54
C19
C20
C65
C66
C67
C59

Table 3.15 *Crystallographic Data for* **27**

Crystallised from	CH_2Cl_2 / hexane
Empirical formula	$C_{79}H_{73}O_4$
Formula weight [g mol^{-1}]	1086.44
Crystal colour, habit	colourless, prism
Crystal dimensions [mm]	0.22 × 0.28 × 0.30
Temperature [K]	160(1)
Crystal system	triclinic
Space group	$P\bar{1}$ (#2)
Z	2
Reflections for cell determination	11295
2θ range for cell determination [°]	4 – 50
Unit cell parameters a [Å]	12.5833(5)
b [Å]	16.3905(5)
c [Å]	17.0723(7)
α [°]	73.728(2)
β [°]	74.378(2)
γ [°]	85.030(2)
V [Å^3]	3255.0(2)
$F(000)$	1158
D_x [g cm^{-3}]	1.108
μ(Mo $K\alpha$) [mm^{-1}]	0.0665
Scan type	ω
$2\theta_{(max)}$ [°]	50
Total reflections measured	54808
Symmetry independent reflections	11417
R_{int}	0.100
Reflections with $I > 2\sigma(I)$	7054
Reflections used in refinement	11415
Parameters refined; restraints	882; 678
Final $R(F)$ [$I > 2\sigma(I)$ reflections]	0.0804
$wR(F^2)$ (all data)	0.2422
Weights:	$w = [\sigma^2(F_o^2) + (0.1466P)^2]^{-1}$ where $P = (F_o^2 + 2F_c^2)/3$
Goodness of fit	1.046
Secondary extinction coefficient	0.142(8)
Final Δ_{max}/σ	0.004
$\Delta\rho$ (max; min) [e Å^{-3}]	0.38; -0.29
$\sigma(d_{(C-C)})$ [Å]	0.003 – 0.005

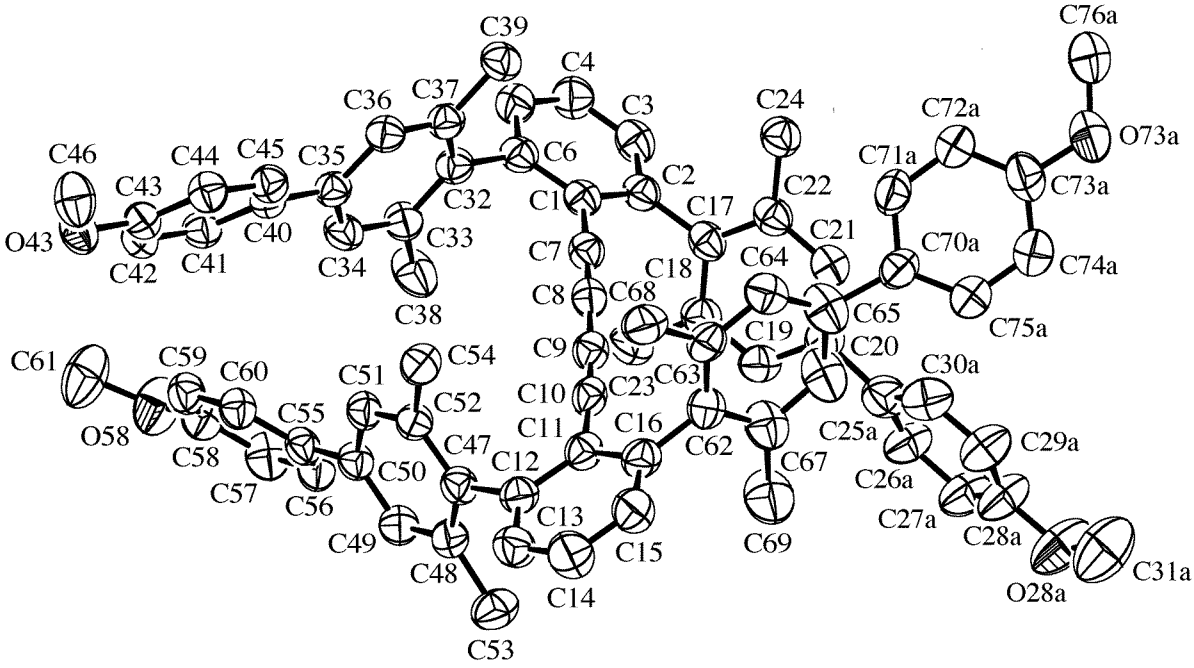
C39
C4
C36
C37
C3
C24
C76a
C72a
O73a
C46
C44
C45
C35
C6
C2
C71a
C43
C32
C1
C17
C22
C73a
O43
C40
C33
C7
C21
C70a
C42
C41
C34
C18
C64
C74a
C8
C68
C38
C65
C75a
C61
C59
C60
C54
C9
C19
C20
C51
C63
C30a
C10
C23
C52
C25a
O58
C55
C11
C16
C62
C29a
C58
C47
C12
C67
C26a
C57
C56
C50
C27a
C28a
C13
C69
C49
C15
C48
C14
O28a
C31a
C53

Table 3.16 *Crystallographic Data for* **28**

Crystallised from	CH_2Cl_2
Empirical formula	$C_{66}H_{50}O_4$
Formula weight [g mol^{-1}]	907.12
Crystal colour, habit	colourless, prism
Crystal dimensions [mm]	0.13 × 0.18 × 0.23
Temperature [K]	160(1)
Crystal system	monoclinic
Space group	*Cc* (#9)
Z	4
Reflections for cell determination	4677
2θ range for cell determination [°]	4 – 50
Unit cell parameters *a* [Å]	35.618(1)
b [Å]	9.3960(3)
c [Å]	14.9250(4)
α [°]	90
β [°]	92.473(2)
γ [°]	90
V [Å^3]	4990.2(3)
F(000)	1912
D_x [g cm^{-3}]	1.207
μ(Mo *K*α) [mm^{-1}]	0.0737
Scan type	ω
$2\theta_{(max)}$ [°]	50
Total reflections measured	36176
Symmetry independent reflections	4402
R_{int}	0.090
Reflections with $I > 2\sigma(I)$	3928
Reflections used in refinement	4402
Parameters refined; restraints	639; 2
Final *R*(*F*) [$I > 2\sigma(I)$ reflections]	0.0724
wR(F^2) (all data)	0.1890
Weights: $w = [\sigma^2(F_o^2) + (0.1465P)^2 + 0.7217P]^{-1}$ where $P = (F_o^2 + 2F_c^2)/3$	
Goodness of fit	1.073
Final Δ_{max}/σ	0.001
$\Delta\rho$ (max; min) [e Å^{-3}]	0.40; -0.28
$\sigma(d_{(C-C)})$ [Å]	0.006 – 0.008

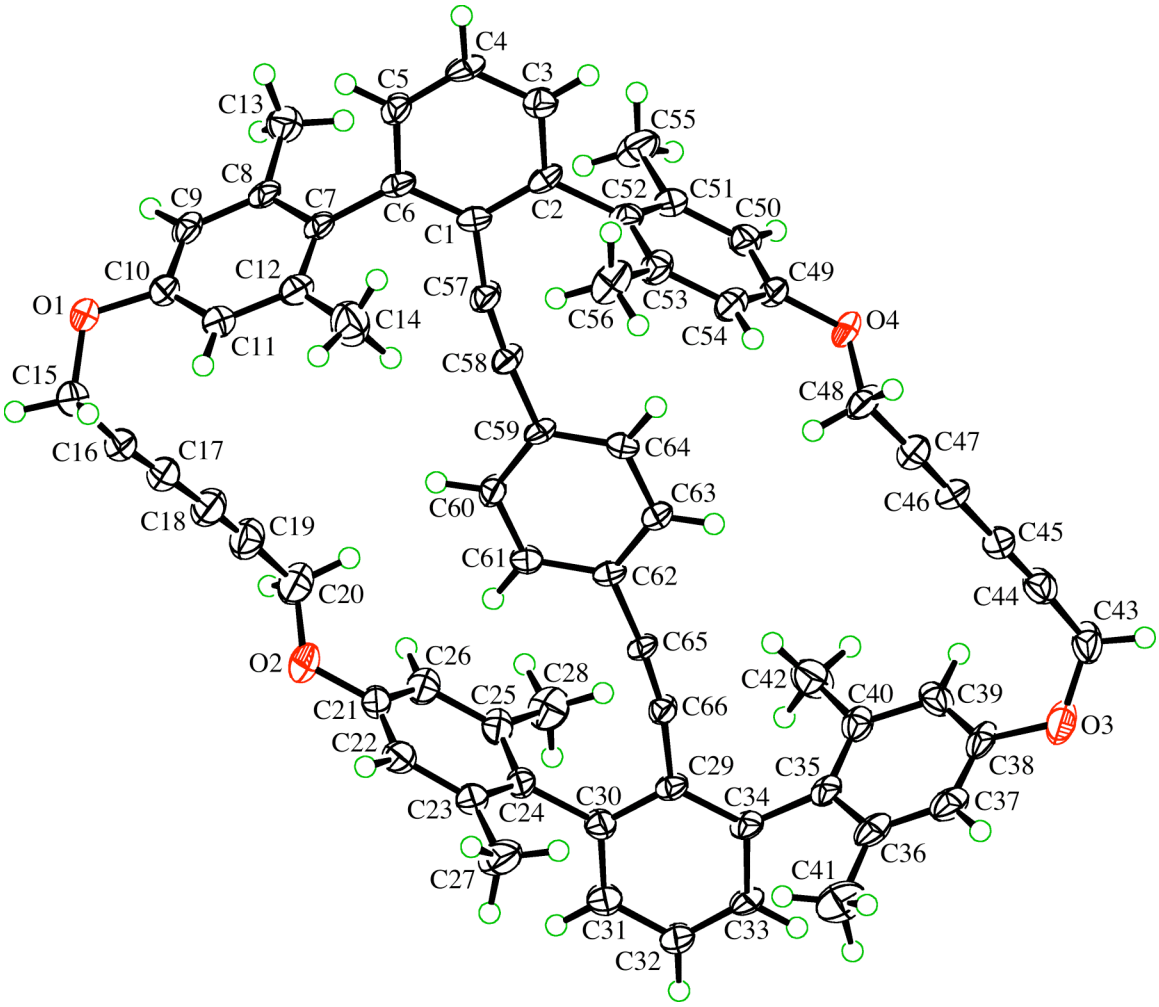
C4
C5
C3
C13
C55
C8
C9
C7
C6
C2
C52
C51
C50
C1
C10
C12
C57
C53
C49
O1
C14
C56
C54
O4
C11
C58
C15
C48
C59
C64
C16
C17
C47
C60
C63
C18
C19
C46
C45
C61
C62
C20
C44
C43
C65
O2
C26
C42
C40
C39
C28
C25
C66
O3
C21
C22
C29
C35
C38
C23
C24
C30
C34
C37
C36
C27
C41
C31
C33
C32

Table 3.17 *Crystallographic Data for* **41**

Crystallised from	acetone
Empirical formula	$C_{84}H_{74}O_6$
Formula weight [g mol^{-1}]	1179.50
Crystal colour, habit	colourless, prism
Crystal dimensions [mm]	0.20 × 0.25 × 0.25
Temperature [K]	160(1)
Crystal system	monoclinic
Space group	$P2_1/c$ (#14)
Z	4
Reflections for cell determination	12010
2θ range for cell determination [°]	4 – 50
Unit cell parameters a [Å]	14.2606(3)
b [Å]	26.2614(7)
c [Å]	18.1305(5)
α [°]	90
β [°]	97.969(1)
γ [°]	90
V [Å^3]	6724.4(3)
F(000)	2504
D_x [g cm^{-3}]	1.165
μ(Mo $K\alpha$) [mm^{-1}]	0.0717
Scan type	ϕ and ω
$2\theta_{(max)}$ [°]	50
Total reflections measured	92407
Symmetry independent reflections	11846
R_{int}	0.090
Reflections with $I > 2\sigma(I)$	6497
Reflections used in refinement	11846
Parameters refined	824
Final $R(F)$ [$I > 2\sigma(I)$ reflections]	0.0845
$wR(F^2)$ (all data)	0.2440
Weights: $w = [\sigma^2(F_o^2) + (0.0959P)^2 + 7.485P]^{-1}$ where $P = (F_o^2 + 2F_c^2)/3$	
Goodness of fit	1.016
Secondary extinction coefficient	0.0036(5)
Final Δ_{max}/σ	0.001
$\Delta\rho$ (max; min) [e Å^{-3}]	0.55; -0.46
$\sigma(d_{(C-C)})$ [Å]	0.005 – 0.01

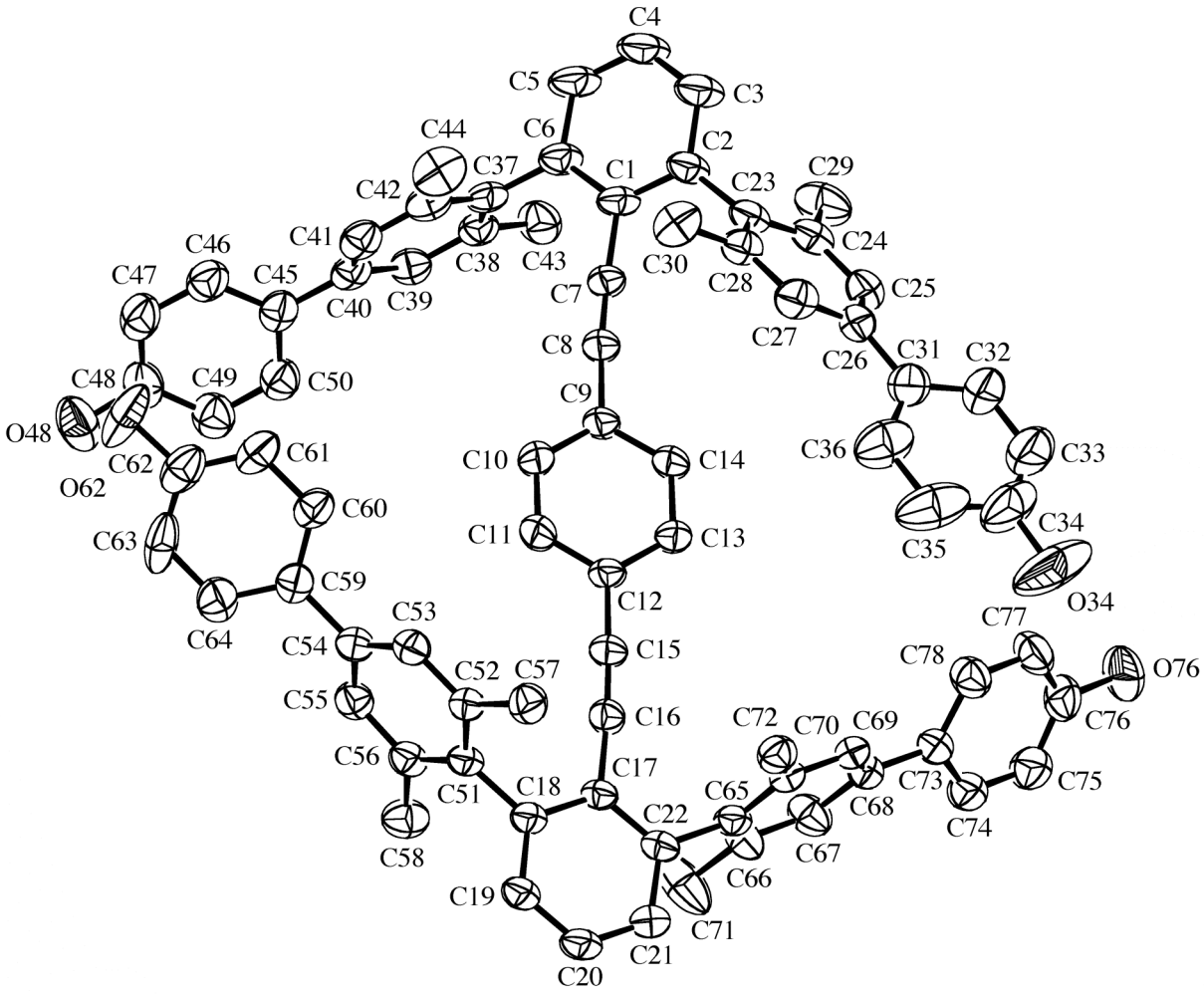
C4
C5
C3
C44
C6
C2
C37
C1
C29
C42
C23
C41
C24
C46
C38
C43
C30
C47
C45
C40
C39
C7
C28
C25
C8
C27
C26
C31
C32
C48
C49
C50
C9
O48
C62
C61
C10
C14
C36
C33
O62
C60
C11
C13
C34
C63
C35
C59
C12
O34
C53
C77
C64
C54
C15
C78
O76
C52
C57
C55
C16
C72
C70
C69
C76
C56
C17
C73
C75
C51
C18
C65
C68
C22
C74
C58
C67
C66
C19
C71
C21
C20

4 ELECTROSTATIC MODELING OF POTASSIUM ION CHANNELS

4.1 Overview of Potassium Ion Channels

4.1.1 Function and Structure

Potassium ion channels are transmembrane proteins that are used to stabilize membrane potentials in our bodies by facilitating rapid diffusion of K+ ions across the cell membrane.[1] These ion channels are critical to proper cell function, particularly in controlling membrane potentials and carrying out intracellular signaling processes. The channels are often thought of as catalysts for the passage of ions through membranes. The crystal structure of the bacterial potassium ion channel KcsA in the presence of K+ ions has already been determined, however, its mechanism of action is still unclear.[2] One of the most remarkable properties of the potassium ion channel is its selectivity for a single cation. Initially, the channel is a wide cavity in which the K+ ions are solvated by water. As the ions travel further into the channel, they reach a more confined region called the selectivity filter. Understanding the structural and energetic interactions of K+ ions as they travel through the selectivity filter is key in determining the overall mechanism of the ion channel.

4.1.2 The Selectivity Filter

The selectivity filter of the K+ channel is a narrow passage, defined by four alpha helices, that enables the channel to exclusively facilitate the flow of K+ ions through the cell membrane. According to the crystal structure in the presence of K+ ions, this filter is 12 Å long and 2.5 Å wide. Anything larger than the K+ cation is not small enough to fit through the filter. Even the K+ ion must give up its solvation shell to enter the filter. This property further contributes to the selectivity of the channel. The filter is lined by the backbone carbonyls of the four alpha helices that define the actual channel. The oxygen atoms from these backbone carbonyls can act as surrogate

water molecules to make it energetically favorable for the K+ ion to enter the filter. As previously stated, larger ions cannot enter due to size exclusion. In addition, in the case of smaller cations, such as Na+, the energy of interaction between the cation and the oxygen atoms does not outweigh the solvation energy of the cation. It is particularly noteworthy that the selectivity filter is able to avoid complexation with smaller cations, such as Na+. It has been postulated that the selectivity filter must be conformationally rigid in order to exclude the smaller Na+ ions. Whereas a dehydrated K+ ion has a radius of 1.3 Å, a dehydrated Na+ ion has a radius of 0.9 Å. Therefore, the cavity defined by the four alpha helices must be conformationally rigid in order to prevent the selectivity filter from shrinking to a smaller size that would enable complexation with sodium ions. A sufficiently rigid filter would then preclude the flow of Na+ ions.

4.2 An Electrostatic Model of K+ Channel

4.2.1 Cation-Pi Interactions

The selectivity filter relies on favorable electrostatic interactions between the backbone carbonyls of the alpha helices and the K+ ion to exclusively enable the transport of potassium ions across the cell membrane. In order for entry into the filter to be favorable, the energy of the electrostatic interaction must be sufficient enough to promote entry into the filter. The interactions between alkali metal cations and pi systems have been investigated both computationally and experimentally.

In the computational work of Ma and Dougherty, the interaction energies between alkali metal cations and benzene were calculated.[3] In each case, the interaction was found to be stabilizing and the optimized geometry showed the cation to be situated on the C_6 axis in the center of benzene. In the case of potassium, the

interaction energy was found to range from 15.0 to 19.2 kcal/mol, depending on the method used. For sodium, the energy ranged from 24.4 to 29.5 kcal/mol. These calculations are in reasonable agreement with experimental values determined in the gas phase.[4] Calculations were conducted on other alkali metals, and it was determined that a larger ionic radius resulted in a decrease in the binding energy as well as an increase in the metal-arene distance. In the case of sodium, the metal-arene distance was calculated to be 2.79 Å, compared to 3.20 Å for potassium.

Kebarle and coworkers investigated the behavior of potassium ion–benzene complexes in the gas phase experimentally.[4] They determined the association constant for the complex in an ion source reaction chamber, using magnetic mass analysis. The binding energy in this case was found to be 11.9 kcal/mol. The same measurement carried out on sodium gave a binding energy of 18.7 kcal/mol. The study also indicated that a potassium ion was capable of interacting with up to four benzenes at once. In subsequent work, Kebarle and coworkers investigated the binding of alkali metals with water.[5] The interaction energy between one potassium ion and one water molecule was found to be 11.5 kcal/mol, as compared to 17.6 kcal/mol for sodium ion. Whereas steric interactions prevent the interaction of more than four benzene molecules with a potassium ion, up to six water molecules can interact with the cation at once. The similar energy magnitudes for arene complexation and water solvation suggest the possibility of competitive binding.

Based on the above results, a sufficiently rigid selectivity filter should be able to overcome the solvation energy of a potassium ion and promote its entry into the filter. Conversely, the driving force for entry into the filter by sodium ions would not be large enough to offset its solvation energy because the carbonyl oxygens are too far apart to form a complex with the smaller cation. The primary interaction between

the potassium ion and the water molecules is a cation-dipole attraction that is inversely proportional to the square of the distance. The interaction between the cation and benzene is a cation-quadrupole interaction, which has approximately the same magnitude as the solvation energy in water. In the case of the selectivity filter, the attraction between the backbone oxygens and the K+ cation is sufficient enough to activate the process of K+ flow. The ability of noncovalent interactions of this type to overcome the solvation energy of potassium is thought to be the basis for selectivity in the potassium ion channel.

4.2.2 Designing the Model

In light of the significance of charge-charge interactions in the K+ channel, we postulated that a simple electrostatic model could provide critical information on its mode of action. As its name suggests, the selectivity filter provides the basis for exclusive flow of potassium ions. The selectivity filter can be thought of as a narrow cavity with negative point charges lining the exterior at regular intervals. A reasonable crude model of this system is four rods arranged to define a rectangular prism (Figure 4.1).

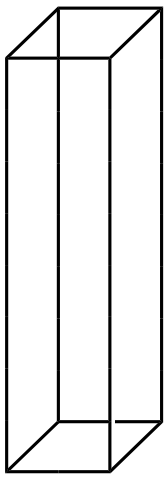

Figure 4.1 In the electrostatic model, the selectivity filter is a rectangular prism defined by four rods meant to represent the four alpha helices.

Point charges can then be placed at regular intervals along each rod to mimic the oxygens of the backbone carbonyls. K+ ions could be modeled to travel through the cavity defined by the four rods. If one considers two consecutive point charges on each of the four rods, these eight points make up the vertices for a smaller rectangular prism. In this way, the cavity is subdivided into a series of boxes (Figure 4.2).

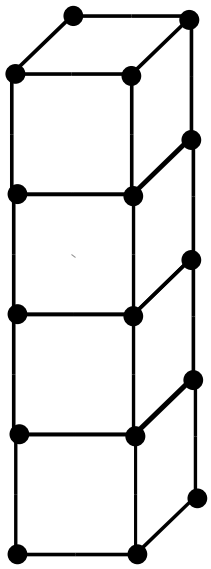

Figure 4.2 The regular placement of point charges along the rods can be thought to subdivide the prism into a series of smaller boxes.

A computer program was developed to implement this simple model. The program allows the user to input the dimensions of the box as well as the total number of boxes that will make up the cavity. This is equivalent to defining the length of the selectivity filter as well as the spacing of the backbone carbonyl oxygens. The charges at the vertices of each box can also be assigned a value, and the program then calculates the electrostatic energy between point charges associated with any particular configuration of the cavity. In this initial stage of designing the model, only the anion cavity has been considered.

4.2.3 Preliminary Calculations

The initial goal was not to mimic the structure of the actual filter, but to gain an understanding of the general behavior of the model system. The first calculations done with this model focused on determining an optimal number of 1 x 1 x 1 Å boxes based on convergence of the electrostatic interaction energy. Clearly, adding another box to the system will increase the overall energy, but the ΔE will gradually level off and the ΔΔE will approach zero (Figure 4.3).

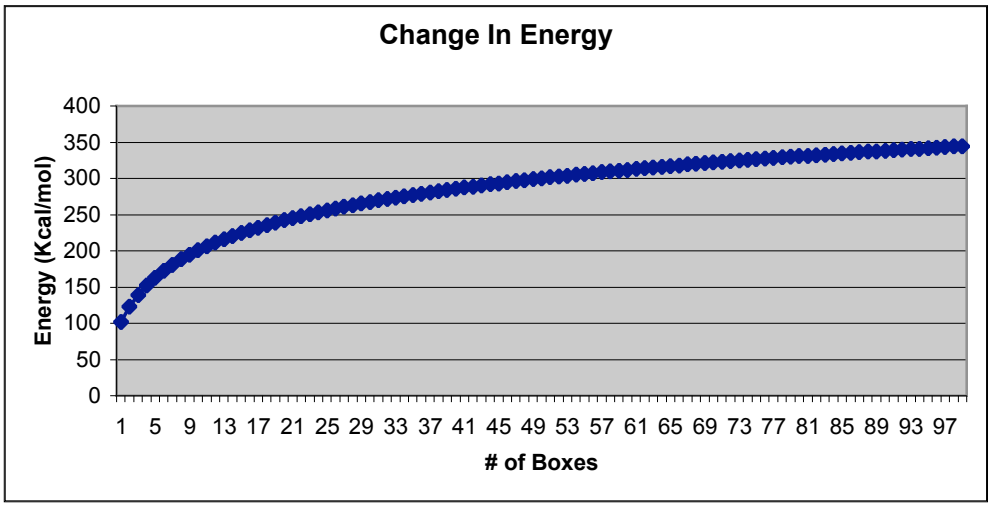

Figure 4.3 The change in energy associated with adding more anion boxes to the system. The relative significance of adding another box gradually becomes negligible.

The second graph shows that the energy effect begins to level off near 30 boxes. Beyond that point, the ΔΔE values are less than 10% of the initial value of 22 kcal/mol.

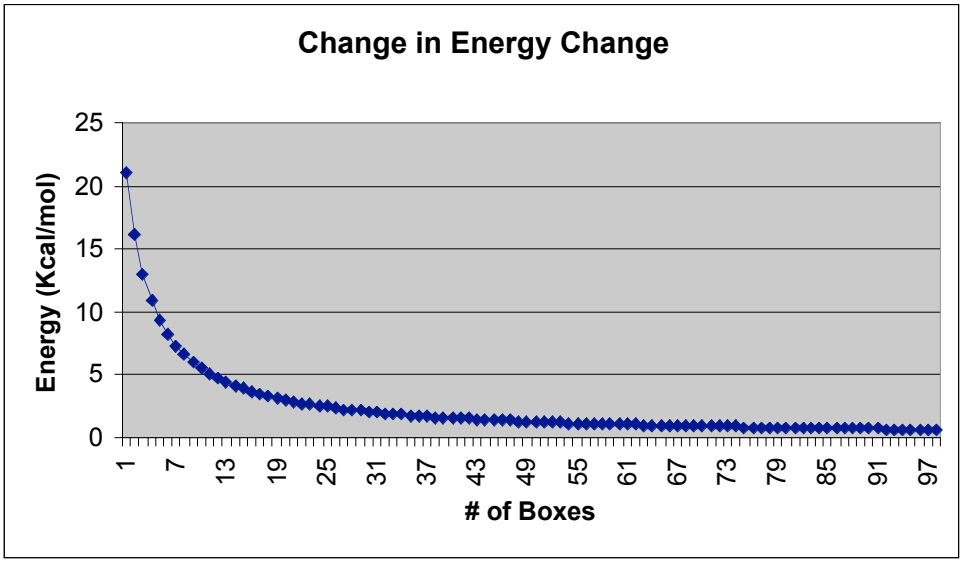

Figure 4.4 The ΔΔE for adding more boxes to the system. The energy value approaches zero as the number of boxes increases.

4.2.4 A Naming Scheme

In order to conveniently refer to different points and distances in this model, it is useful to create a naming system. If, as described earlier, the larger cavity is subdivided into smaller boxes, the first box will have vertices A1, B1, C1, D1 (Figure 4.5). These points will make up the bottom face of the box. Above this are the vertices A2, B2, C2, and D2. The A1-A2 distance will be referred to as the height of a box (H). The A1-B1 distance is the box length (L), and the A1-D1 distance is the width of the box (W).

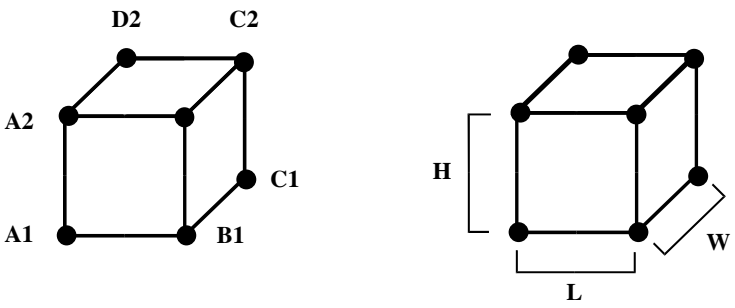

Figure 4.5 The naming scheme developed for the model system. The vertices are labeled as shown on the left and the length, width, and height are defined as shown to the right.

The characteristics of a particular system will be defined in the following way: [N,q,(L,W,H)] where N is the number of boxes and q is the charge on the anion.

4.3 Basic Ion Channel Simulations

4.3.1 Anion Energy and Box Size

Initially the convergence of the electrostaic energy of the system was only investigated for the case where each box is a cube with edge length of one Å. The graph in figure 4.6 shows the effect of varying this edge length.

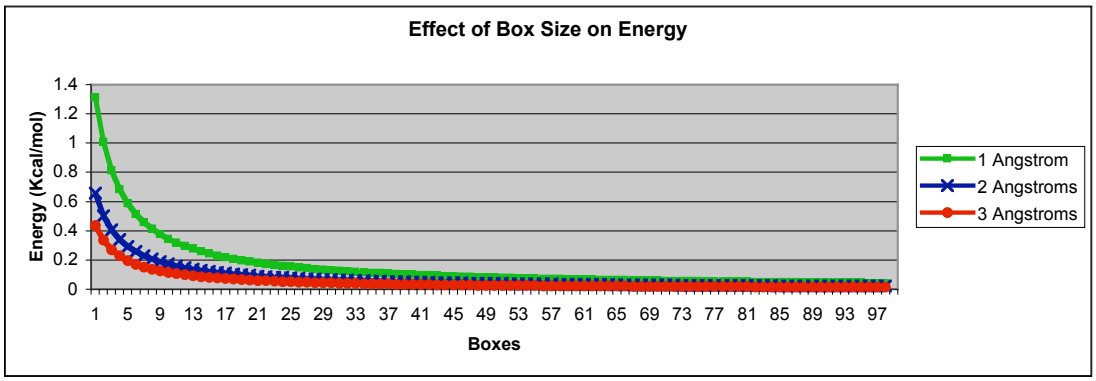

Figure 4.6 The ΔΔE approaches zero more rapidly as the edge length increases. The magnitude of the charge-charge interaction is smaller because the charges are further apart.

As would be expected, increasing the edge length of the cube caused the ΔΔE to approach zero more rapidly. This is logical since the interaction energy is inversely related to the charge-charge distance.

4.3.2 Adding in the Cation

Up to this point, there has been no consideration of the K+ cation. Here, the model is expanded to follow the movement of a single cation charge through the anion cavity defined by the four rods. The anion cavity has the parameters [10,0.25,(1,1,1)] and there is a single cation of charge +1 that starts 1 Å outside of the first box and moves down the center of the cavity until it is 1 Å beyond the last box. The cation moves through the cavity in 0.25 Å increments and the energy of the overall system is determined at each point. Next, the energy difference between consecutive points is found (Figure 4.7).

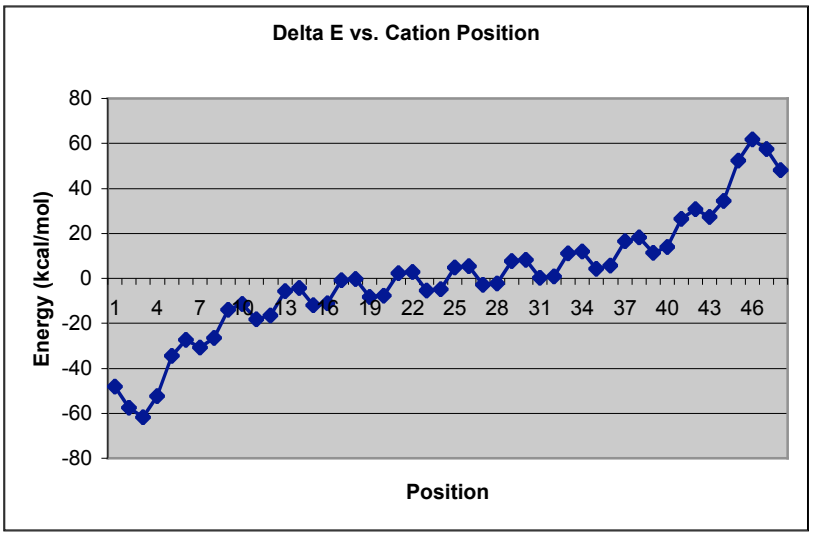

Figure 4.7 Movement of a single cation through the system [10,0.25, (1,1,1)]. The cation begins one Å outside of the first box and stops one Å beyond the last box.

The dielectric constant in this example is 2, which is consistent with a protein environment. This is a reasonable value to use because the channel is a transmembrane protein that passes through the lipid bilayer. As expected, the graph is symmetrical and the local minima occur when the cation is aligned with a box face. These minima gradually decrease in magnitude as the charge moves through the anion cavity. Once the cation goes beyond the center of the anion cavity, the movements

become less favorable because the majority of the anion-cation distances are increasing. It is reasonable that there is an energy well in the center of the anion cavity and that energy must be added in to push the cation through to the other side.

4.3.3 Anion-Cation Energy and Box Dimensions

In the following three examples, the cation starts 1 Å outside of the first box and moves until it is 1 Å outside of the last box. The dimensions are varied in each case to observe the effect on the energy profile. The first system to be studied has the parameters [10,0.25,(5,1,1)]. In this case, the graph is nearly linear and doesn't have the obvious peaks and valleys that were seen the previous graph (Figure 4.7). This result is logical because the cavity length has increased to five and the opposing charges are further apart. Another consequence of the increased charge spacing is that the minimum overall energy is smaller in magnitude.

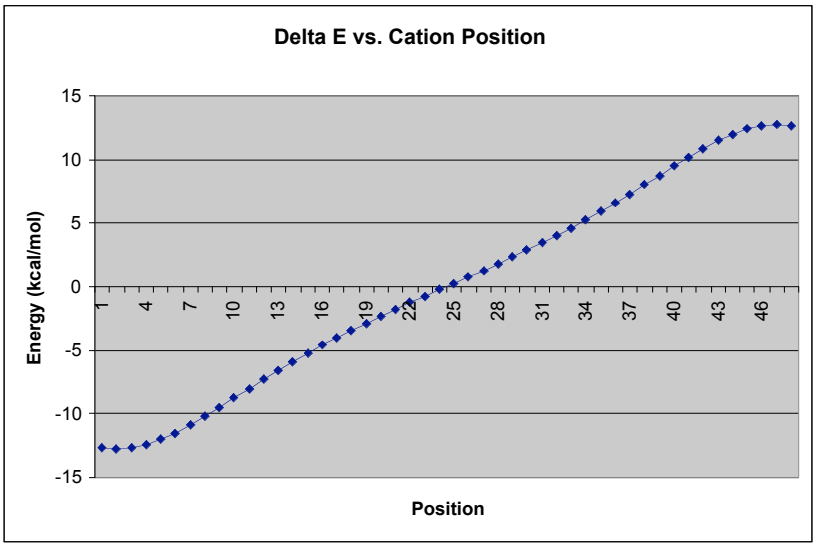

Figure 4.8 The box length has been increased from 1 angstom to 5 Å. The graph appears nearly linear in this case and the fine structure is lost.

The graph in figure 4.9 is for the parameters [10,0.25,(5,5,1)]. The above observations are also true in this case. In fact, the effect is shown even more clearly here. A similar argument can be used to explain the result.

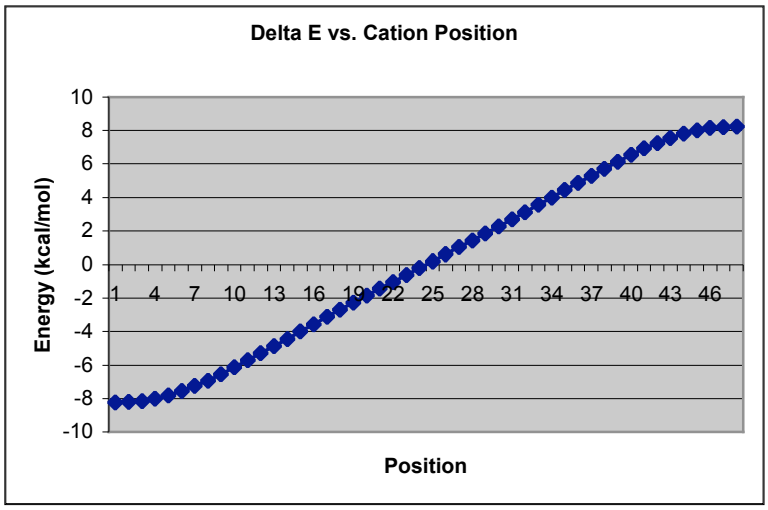

Figure 4.9 The box length and width have both been increased from 1 Å to 5 Å. The graph is very similar to the one in figure 4.8.

The results are significantly different in the case where only the box height is changed. In the graphs below, the parameters are [10,0.25,(1,1,5)]. The first graph depicts the total energy of the system (Figure 4.10). There is a clear periodicity to the graph here, which suggests that there may be some features in the previous graphs that could not be seen due to the step size. Here, the step size remains 0.25 Å, but the vertical spacing (A1-A2) between sets of anion charges has increased fivefold. The local minima are seen when the cation is aligned with one of the box faces and the maxima are seen near the center of each box. This can be seen more easily in the delta energy graph (Figure 4.11).

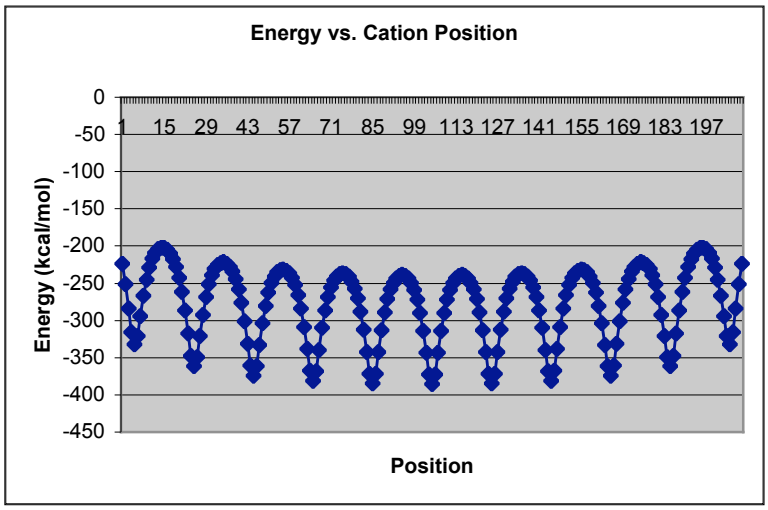

Figure 4.10 The box height has been changed from 1 Å to 5 Å. In this case, the dimension change is along the direction of motion of the cation. The valleys correspond to alignment of the cation with a box face while the peaks correspond to a cation position in the center of a box.

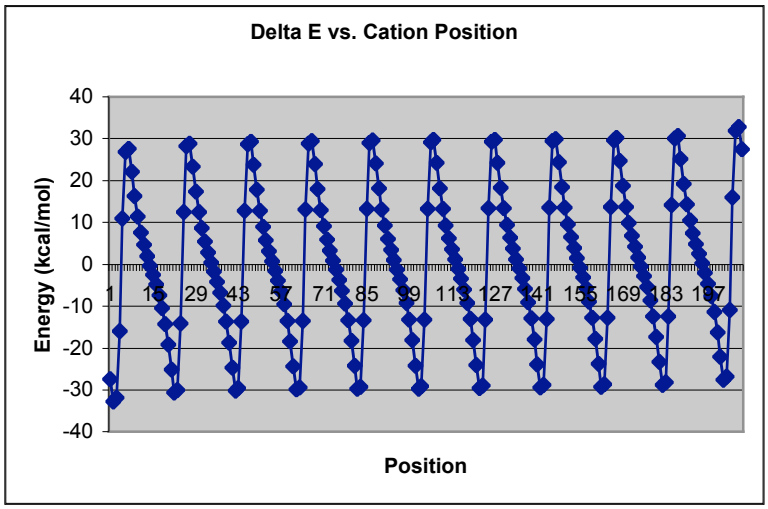

Figure 4.11 The delta energy graph that corresponds to the energy graph in figure 4.10.

The first movement that costs energy is when the cation is moved out of alignment with the first box face. This energy cost increases in the next few steps but begins to decrease again as the cation approaches the next set of anion charges. This pattern continues throughout the graph.

To investigate further, the box height was increased from 5 to 10 Å. The system depicted in figures 4.12 and 4.13 below has the parameters [10,0.25,(1,1,10)].

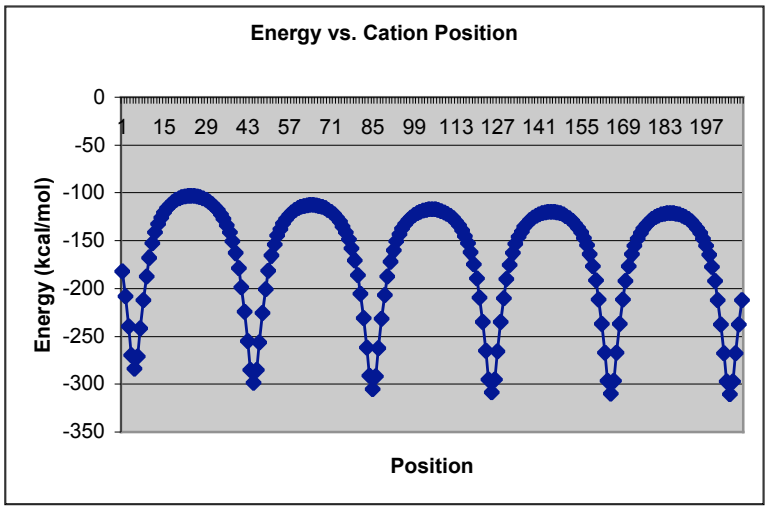

Figure 4.12 In this case, the box height has been increased to 10 Å. The graph is identical in structure to the one in figure 4.10, but the effect is magnified by doubling the box height.

The same trend is seen here with local minima in line with the box faces and maxima near the centers. The delta energy graph in figure 4.13 also illustrates this effect.

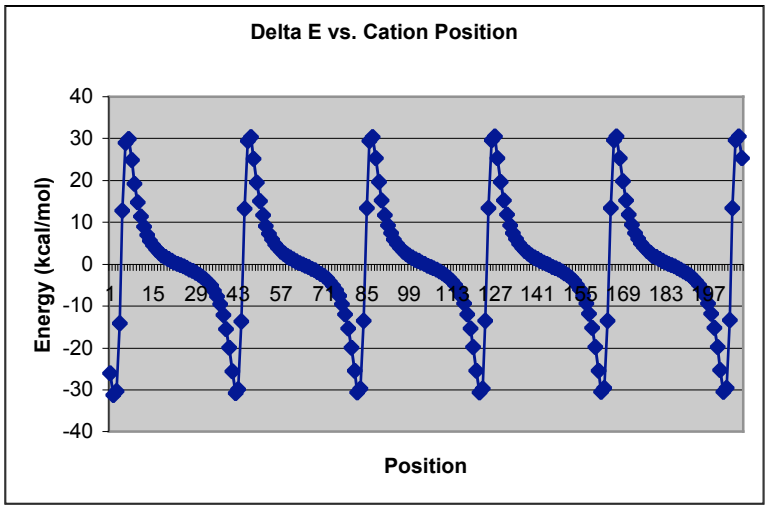

Figure 4.13 The delta energy graph that corresponds to the energy graph in figure 4.12.

4.3.4 Anion Charge Magnitude and the Dielectric Constant

In all of the examples discussed so far, the magnitude of the anion charge remained constant, as the charge was always –0.25. The original delta energy vs. charge position graph is shown below (Figure 4.14), and another graph follows, in which the anion charge is –0.5 (Figure 4.15). The carbon-oxygen bond is certainly very polarized, and it is reasonable that a point charge representation of the oxygen atom would have a charge somewhere between these two values. The charge assigned to the anion basically acts as a scalar and there is no change to the shape of the graph. The delta energy values are doubled in magnitude due to the increase in the anion charge magnitude from –0.25 to –0.5.

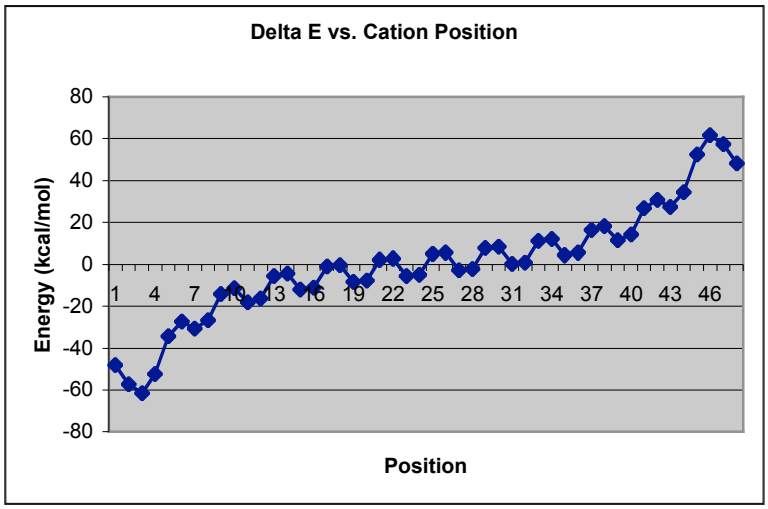

Figure 4.14 This graph is identical to the graph in figure 4.7. in which the anion charge is –0.25.

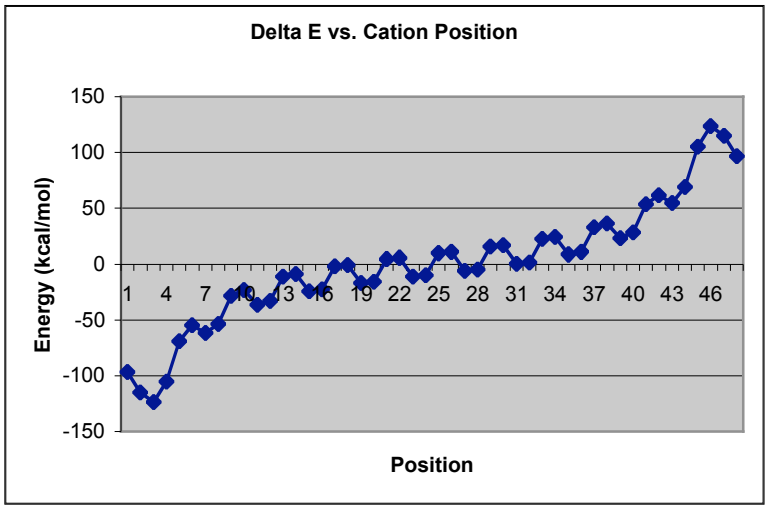

Figure 4.15 The movement of a single charge through the system [10,-0.5, (1,1,1)]. Changing the anion charge merely acts as a scalar and the shape of the graph is identical to the one in figure 4.14.

The dielectric constant also acts like a scalar. It is a significant factor in the calculation of the energy values because it is part of the expression for Coulomb's Law: $E = \frac{q_1 q_2}{4\pi\varepsilon_0 \varepsilon r}$ where ε_0 is the permittivity constant and ε is the dielectric constant.

The dielectric constant for water is 80 and the value commonly used for the protein

environment is 2. The selectivity filter passes through the lipid bilayer, which is clearly a highly nonpolar environment. However, in the small area to be considered, there are several oxygen atoms present, which may make the effective dielectric more than 2. The graphs that have been shown up to this point were done with a dielectric of 2. However, in order to move forward in the development of an accurate model, modulation of the dielectric constant must be investigated. The graph shown in figure 4.16 is the original data set for movement of a single cation through the cavity defined by the parameters [10,-0.25,(1,1,1)]. Figure 4.17 shows a graph of the same movement with a dielectric of 80. The order of magnitude changes considerably since there is a 40 fold increase in the dielectric constant, which appears in the denominator of Coulomb's Law. The energy difference with a dielectric of 2 is over 400 kcal/mol, compared to 11 kcal/mol with a dielectric of 80. The large energy value with a dielectric of 2 is not a feasible number biologically, but there are still several more features that must be added to the model system before it can be compared to realistic values. Up to this point, data has only been collected with a dielectric constant of 2.

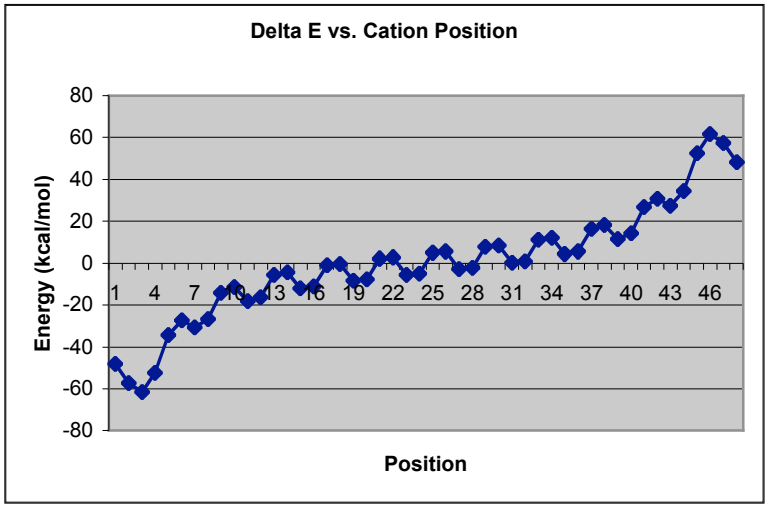

Figure 4.16 Movement of a single cation charge through the system [10,-0.25, (1,1,1)] with a dielectric constant of 2, consistent with a protein environment.

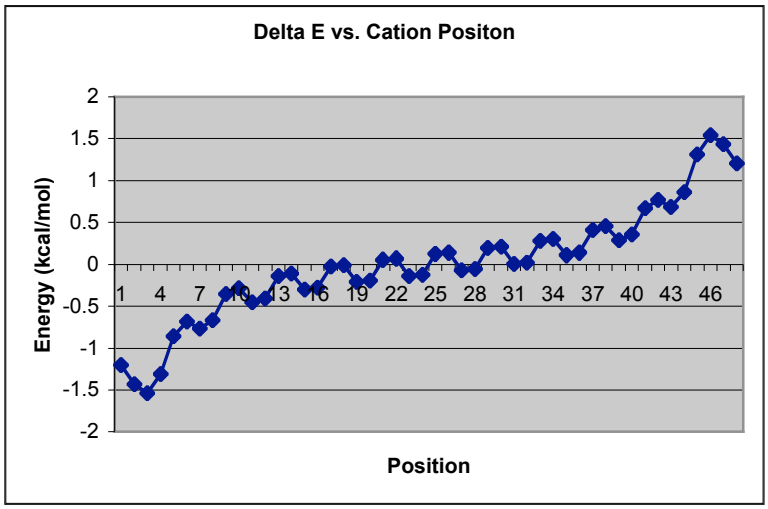

Figure 4.17 Movement of a single cation through the system [10,-0.25, (1,1,1)] with a dielectric constant of 80, consistent with an aqueous environment. The graph shape remains the same, but the energy values are dramatically shifted by the scalar.

4.3.5 Adding More Cations to the Rod

Until this point, the model has only allowed for one cation to travel through the channel at a time. However, there is experimental evidence to suggest that this is not the case. The addition of more cations will make the system more complicated, and, at this point, it will be necessary to further develop the naming scheme for the model. The anion cavity is completely described with [N,q,(L,W,H)]. Rather than a single cation point charge, there is now a rod to describe the series of cation charges. The cation rod will be described with [N,q,x,(Z0,dz)] where N is the number of cation charges and q is the magnitude of the charge. The x term gives the spacing between charges. The value Z0 is the initial distance between the entrance to the anion cavity and the first cation charge and dz is the total distance the first cation charge travels through the course of the experiment.

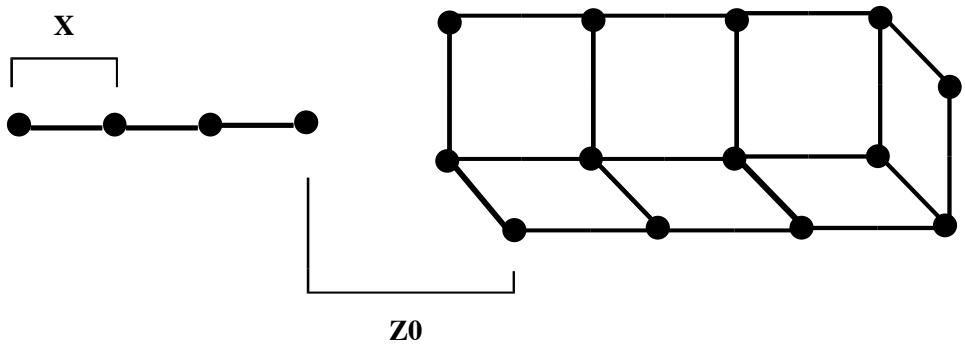

Figure 4.18 Schematic of the model system, including the cation rod. X defines the distance between adjacent cation charges and Z0 is the initial distance between the first cation charge and the entrance to the anion cavity.

The overall system can be described by: {[N,q,(L,W,H), [N,q,x,(z0,dz)]} and the first system has the parameters: {[10,-0.25,(1,1,1)],[10,1,1,(1,21)]} (Figure 4.19).

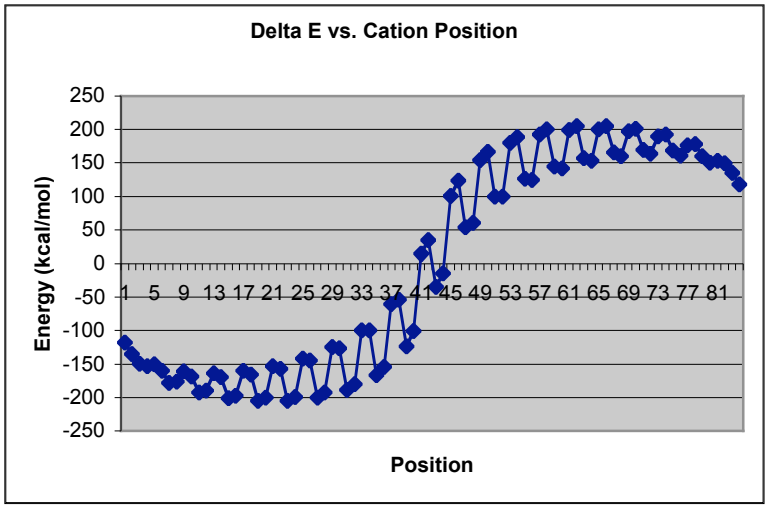

Figure 4.19 Movement of a cation rod containing 10 charges through an anion cavity that consists of 10 boxes. Approach of the cation is increasingly favorable until it reaches the center. Movement out of the cavity requires energy as favorable anion-cation interactions are lost.

There are now 10 cation charges on the rod, and, as a result, the energy magnitudes are significantly larger. The first charge begins one Å away from the entrance to the filter and the cation rod travels through until the last charge is one Å

beyond the exit. The overall energy of the system drops very rapidly until the cation rod reaches the center of the cavity. This rapid decrease is attributed to the addition of more charges. As the cation rod begins to enter the anion cavity, favorable cation-anion interactions rapidly increase in magnitude as the charge-charge distances decrease. But, once the rod is completely enclosed in the anion cavity, these distances are not changing dramatically. Slight movements in the rod do not result in a significant change in the cost of movement, which explains the small variations in energy near the middle of the cavity. Once again, there are local minima corresponding to alignment with box faces. The numerical values obtained here are not reasonable for a biological system, but the overall impact of significantly increasing the number of cation charges has been demonstrated.

4.3.6 Cation Charge Spacing

The number of charges on the cation rod has been increased from 1 to 10. As there are now multiple charges on the rod, another parameter to consider is the spacing between cation charges. The next two systems to be evaluated will also have 10 charges but the cation spacing in each trial will be different. The data shown previously was for a cation spacing of 1 Å. In the graph in figure 4.20, the cation spacing is 2 Å. The system has the parameters: {[10,-0.25,(1,1,1,)],[10,1,2,(1,30)]}

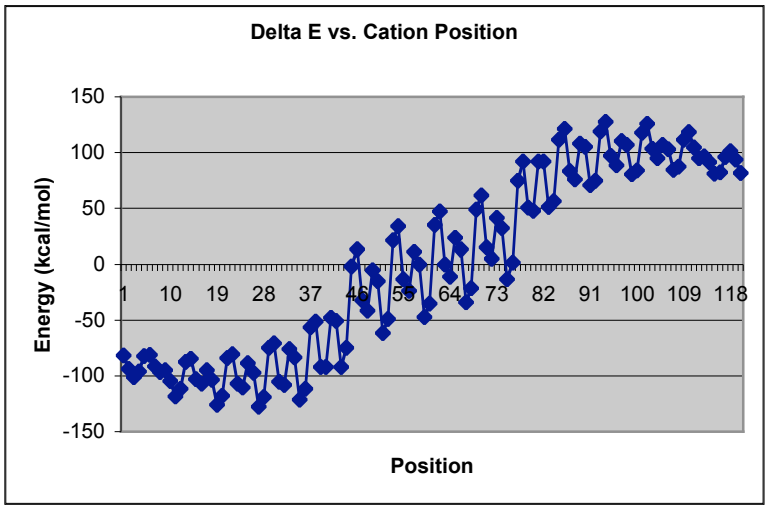

Figure 4.20 The cation charge spacing, X, has been increased from 1 Å to 2 Å. The shape of the graph remains almost the same, but the magnitude of the interaction energy is not as large because of the greater cation charge spacing.

This graph still follows the general trend of the previous one, but there is a great deal more variation from one point to the next, which can be attributed to the increased spacing between cations. The larger cation spacing prevents all of the cations from fitting in the anion cavity at once. Therefore, the cation-anion distance is greater and the magnitude of the interaction energy is smaller. As a result of the increased cation spacing, the cost of movement is less and the curve has a more gentle slope. The magnitude of the minimum energy is also smaller because the interaction distances are larger.

The next example has the properties: {[10,-0.25,(1,1,1)],[10,1,0.5,(1,16.5)]}. The cation spacing has now been reduced to 0.5 Å while all the other properties remain the same.

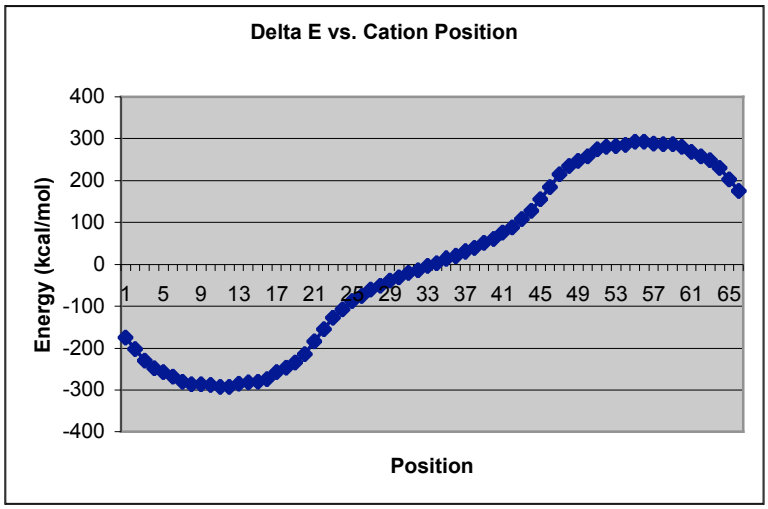

Figure 4.21 The cation spacing has been reduced to 0.5 Å in this case. The graph appears to be smoother but this is primarily a consequence of the step size relative to the cation spacing.

In this case, the graph is much smoother than in either of the previous examples. In addition, the flattening out of the graph in the middle is not as drastic. This is a logical consequence of decreasing the cation spacing. In addition, a step size of 0.25 Å when the charges are only 0.5 Å apart will lead to a more significant change in energy between consecutive positions. Also, moving the rod into the anion cavity will be more energetically favorable because the smaller cation spacing will cause the interaction energy to increase rapidly. But, some of the periodicity of the graph is lost because the charge spacing is not much larger than the step size. In this graph, there are certain positions where half of the charges are aligned with box faces and others where none of them are aligned. Since there are more positions in which charges are aligned with box faces, the energy cost varies less from point to point.

4.3.7 Cation Charge Magnitude

There is no reason to change the cation charge to any value other than 1 because the K+ cation cannot have any other charge magnitude. This is different from

the backbone carbonyl oxygen, where there is certainly room for discussion with regard to the value assigned to the anion point charges.

4.3.8 Summary of Basic Tests

All of the factors of interest have been varied in order to evaluate their individual contributions to the anion-cation interaction energy. Some of these factors act as scalars, changing every value by the same amount. The factors that are scalars are charge magnitude and the dielectric constant. On the other hand, changing other properties results in a drastic change to the entire graph. The properties that cause major changes are the anion cavity dimensions and the cation charge spacing. These basic tests have created a foundation for making an accurate electrostatic model of the potassium ion channel. This versatile model system will hopefully be able to provide some insight into the mechanism of action of the ion channel. At this point, the model must be refined to more closely reflect the specific properties of the system it is intended to simulate.

4.4 Developing the Model System

4.4.1 The Crystal Structure

In order for the model system to provide information that can be applied to the real K+ channel, the actual dimensions from the crystal structure were used. This model system is intended to simulate flow of potassium ions through the selectivity filter. In the presence of potassium, the selectivity filter was found to have a relatively rigid structure. The entire filter spans a length of 12 Å and is 2.5 Å wide. At the entrance to the filter, the backbone carbonyl oxygens of the four alpha helices are nearly coplanar and approximately form a square, with each oxygen at a vertex. This

pattern of oxygens is repeated at a regular interval of 4 Å through the length of the selectivity filter, meaning that each set of oxygens is 3 Å apart (Figure 4.22).

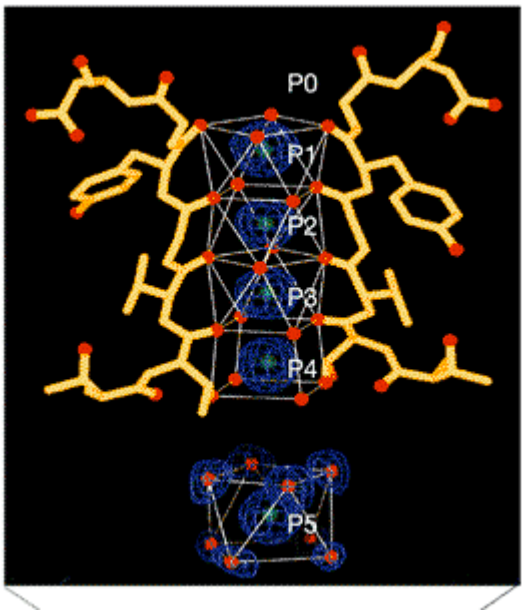

Figure 4.22. A depiction of the selectivity filter based on the crystal structure determined in the presence of K+ ions.[1]

In terms of the model, the selectivity filter corresponds to an anion cavity made up of four boxes with dimensions (2.5,2.5,3.0). Experiment has shown that there are six different preferred binding sites for potassium ions in the vicinity of the selectivity filter.[6] Four of these binding sites occur in the interior of the selectivity filter while the other two are near the entrance and exit of the filter. These experimental studies also indicated that, at most, two of the internal binding sites could be occupied simultaneously, either the first and third sites or the second and fourth. Transition between these two occupational states is facilitated by the addition of a new K+ cation into either the first or last binding site. The distance between the binding sites can be translated into the charge spacing along the cation rod. It is logical that the observed binding sites are the result of K+ ions preferentially occupying local minima in the selectivity filter. In previous simulations, minima

occurred when at least one of the cation charges was aligned with a box face. The exterior binding sites are presumably near the point where the solvation shell gives way to the electrostatic interaction with oxygen. The local minima can also be established by passing a single cation through an anion cavity corresponding to the selectivity filter. The graph in figure 4.23 shows the movement of a single cation through an anion cavity with the dimensions of the actual selectivity filter.

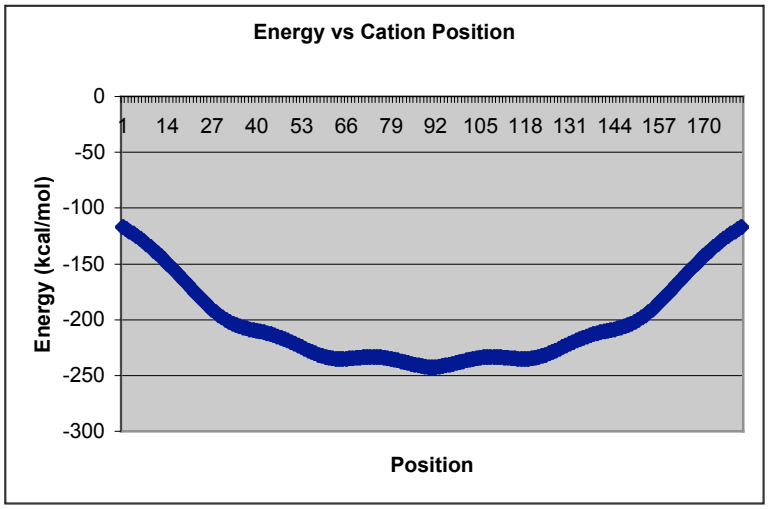

Figure 4.23. The anion cavity has been modified to mimic the dimensions of the selectivity filter. The motion of a single cation through the cavity is observed to determine the preferred occupation sites for the cation.

There is a subtle pattern of peaks and valleys in this graph. The charge begins 3 Å away from the entrance and ends up 3 Å beyond the exit of the filter. The small peaks in the two middle portions of the graph correspond to movement through boxes 2 and 3. The magnitude of the total energy is slightly less in the center of these boxes because the cation is not aligned with any box faces. Therefore, there are fewer stabilizing charge interactions. The anion cavity is symmetrical so the minimum occurs at the very center of the cavity.

The original purpose for investigating the movement of a single cation was to identify the preferential binding sites. This can be more easily determined from the delta energy graph (Figure 4.24).

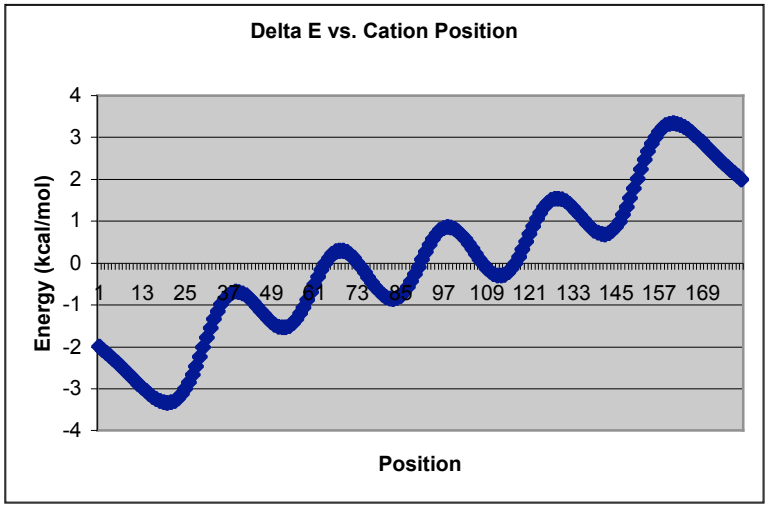

Figure 4.24 The ΔE graph that corresponds to the energy graph in figure 4.23. The peaks represent preferred binding sites for the K+ ion.

The lowest values in this graph correspond to positions where the movement cost is very small, and in some cases negative. Conversely, the highest values correspond to positions where the movement cost is large. The peaks therefore correspond to positions of preferred occupation for K+ cations. As the cation moves beyond the center of the channel, energy is required to push the charge the rest of the way through.

The binding sites need to be investigated further when there is more than one cation charge moving through the selectivity filter. The peaks in the graph are spaced about 30 data points, which corresponds to a distance of 3 Å. This distance can now be used as the cation spacing. Also, experiment indicated that only two of the sites were simultaneously occupied, and the transition was caused by a new cation entering the filter. The graphs in figure 1.25 and 1.26 depict a simulation using the filter

dimensions from the crystal with 3 cation charges spaced 3 Å apart. The dielectric is the same and the charge magnitudes remain constant.

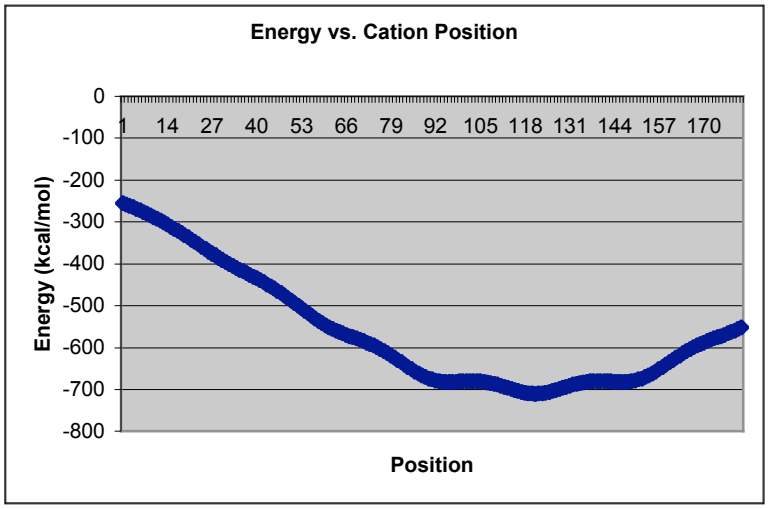

Figure 4.25 The movement of 3 cation charges through an anion cavity meant to mimic the selectivity filter. The cation spacing is 3 Å, which corresponds to the distance between the observed binding sites.

The cation charge nearest the entrance to the cavity begins at a distance of 3 Å from the first set of anion charges. The three cation charges then move together through the cavity until the first charge is 3 Å beyond the exit of the channel. The system is described by {[4,-0.25,(2.5,2.5,3.0)],[3,1,3,(3,18)]}. The first 120 steps are energetically favorable, at which point it begins to cost energy to move the remaining distance through the channel. This energy difference is approximately 150 kcal/mol. The next graph follows the movement cost as the rod proceeds through the anion cavity (Figure 4.26).

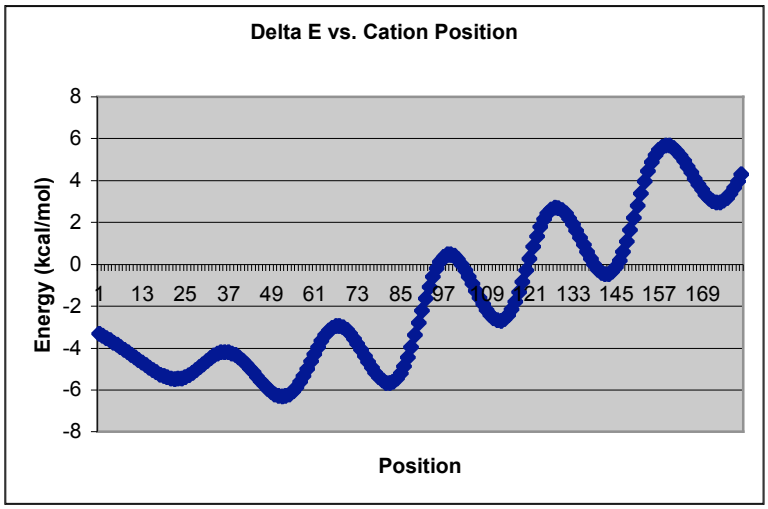

Figure 4.26 The ΔE graph that corresponds to the energy graph in figure 4.25. The graph is very similar to the one in figure 4.24, despite the fact that there are now 3 cations.

This graph looks very similar to the delta energy graph for the movement of one charge and, once again, there is a periodic variation to the movement cost.

At this point, the dimensions of the anion cavity and the cation rod have been adapted as closely as possible to the dimensions indicated by the crystal structure of the ion channel. However, the energy values for movement of the charges are too high to reasonably correspond to a biological system. But, the potassium ion channel is not constantly causing the flux of K+ ions, which suggests that there must be a way to turn on and off the channel's ability to transport potassium ions.

4.5 Energy and Conformational Change

As in other proteins, it may be possible that a conformational change serves to activate or deactivate the channel. This section will examine a particular conformational change within the selectivity filter and evaluate its energetic implications.

In this model system, it is possible to manipulate the relative positioning of the anion rods. Specifically, the two diagonally opposite rods can be shifted together. It

was established earlier in some of the simpler systems that there is preferred binding when the cation is in line with one of the box faces. This corresponds to a square planar complex (C_4 symmetry) between the carbonyl oxygens and the K+ cation. If two diagonally opposite anion charges are shifted up slightly, this breaks the square planar geometry. In fact, it now becomes possible for the K+ ion to make a pseudo-tetrahedral complex (S_4 symmetry) with the adjacent oxygen atoms. It is reasonable to believe that this will impact the energetics of cation flow. This idea will first be investigated on a one cation system.

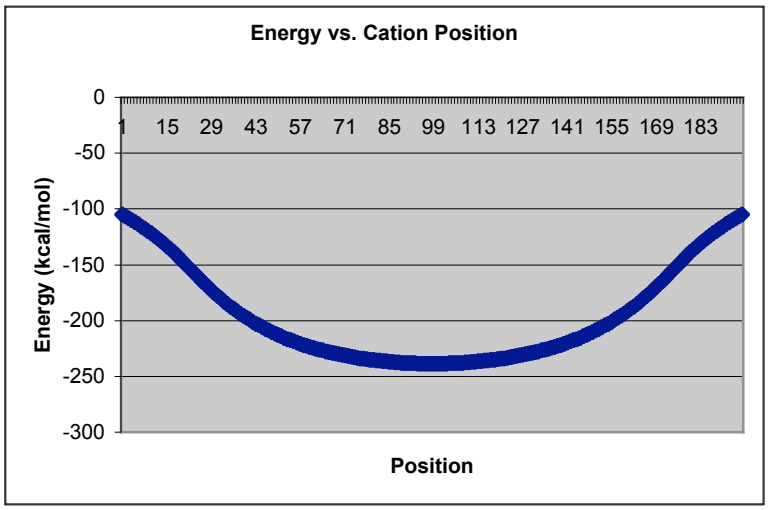

Figure 4.27 Two of the diagonally opposite anion rods have been shifted by 1.5 Å. The other parameters are still intended to mimic the dimensions of the selectivity filter. This graph represents the motion of a single cation through the shifted anion cavity.

The dimensions of the selectivity filter remain the same for this simulation. But, in this case, two of the diagonally opposite rods are shifted vertically by 1.5 Å. The cation begins 3 Å away from the entrance and travels until it is 3 Å beyond the exit. There are no peaks and valleys in this graph, instead it is a smooth curve. The magnitude of the minimum energy in this graph is about 4 kcal/mol less than in the unshifted graph. However, it can be seen that the conformational change has had an impact on the shape of the graph. It is likely that there are fewer peaks and valleys

because the conformational change made the adjacent cation positions more similar. This can be seen more clearly in the ΔE graph (Figure 4.28).

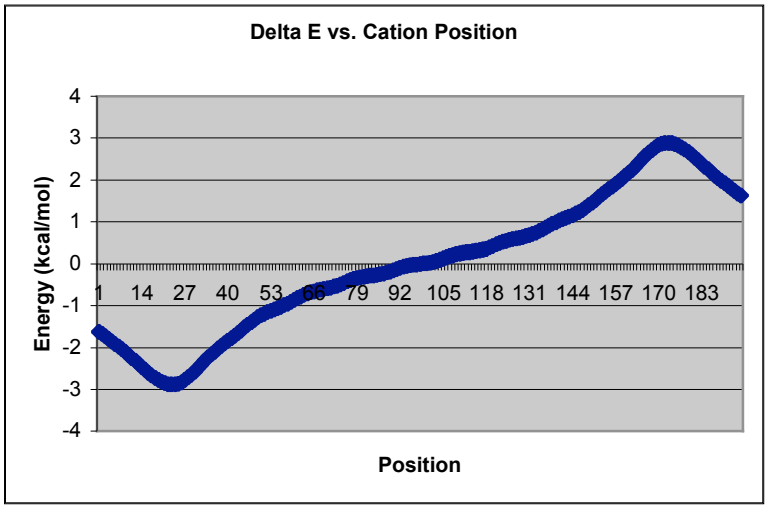

Figure 4.28 The ΔE graph that corresponds to the energy graph in figure 4.27. Approach of the cation is energetically favorable, but energy is required to move the cation beyond the center of the cavity.

Initially, movement of the cation towards the anions is increasingly favorable. Then, the cost of movement gradually increases as the cation proceeds through the filter. Removal of the cation becomes increasingly difficult until the distance is such that the energy terms begin to approach zero. There is no complicated pattern in this graph; the energy change is nearly linear inside the selectivity filter.

The conformational change can now be investigated when there are 3 cation charges traveling through the filter. The first charge begins 3 Å from the entrance and travels until it is 3 Å beyond the exit. The anion rods are again shifted by 1.5 Å (Figure 4.29).

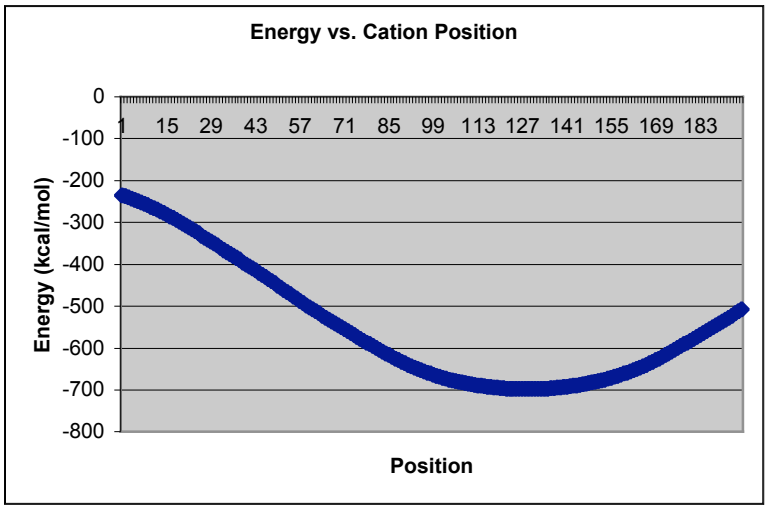

Figure 4.29 The motion of 3 cations through the shifted anion cavity. The first cation begins 3 Å from the entrance to the cavity and continues until it is 3 Å beyond the exit.

The graph is a smooth curve, lacking the small peaks and valleys that were found in the unshifted anion cavity. In this case, there is a 200 kcal/mol difference between the minimum and the point at which the first cation has passed through the filter. The ΔE graph is shown in figure 4.30.

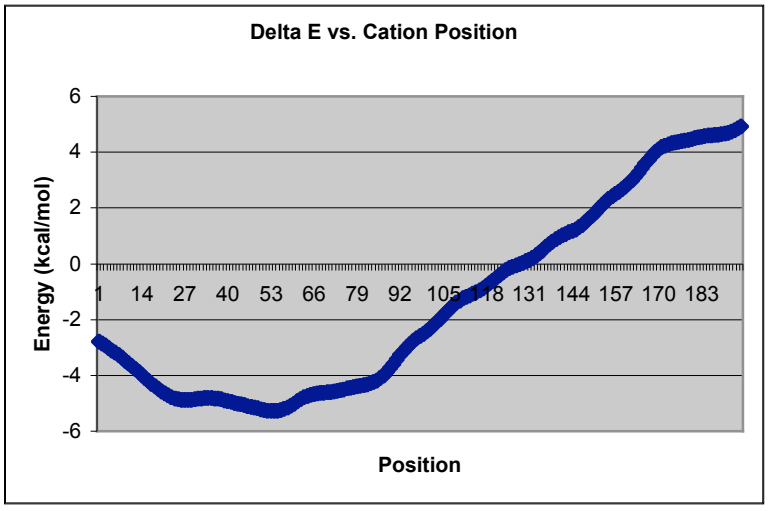

Figure 4.30 The ΔE graph corresponding to the total energy graph in figure 4.29. The approach is energetically favorable and the graph is nearly linear within the cavity.

This graph indicates that there are some peaks and valleys as the cation rod initially enters the cavity. Then, as the rod begins to approach the exit, there is a nearly linear increase in movement cost. As the charges move further away and favorable interactions dissipate, the energy rapidly increases.

This conformational modification did not provide a favorable change to the energy of potassium flux. The changes in the graph seen here were similar to the change caused by modifying the anion box dimensions in other ways. When the length and width of the boxes were changed, adjacent positions either became more or less alike. When the positions were more alike, there was less variation in the energy graph. In this case, where two of the anion rods were shifted, adjacent positions were made more similar. This resulted in the smooth graphs seen in the previous simulations.

4.6 The Knock-on Mechanism

Some studies suggest that several cations permanently occupy the selectivity filter of the K+ channel at once and the Coulombic repulsion between cations causes one of them to exit.[7] This model can best be described with a billiard ball analogy, in which the arrival of one cation in the filter forces the other one out. This mechanism differs significantly from the model system discussed above, because the cation charges are able to move independently rather than collectively on a rod. A modified version of the original program has been written in order to compare the two mechanisms.

This model uses the same anion cavity, as defined by the crystal structure. There are 3 cations in the vicinity of the filter. The starting point is the same as in the previous studies. The 3 cation charges are spaced 3 Å apart, with the first one

positioned 3 Å from the entrance to the cavity. Initially, the two charges nearest the cavity travel into the filter until they reach its center. The third cation charge is stationary during this time. This first phase of cation movement is depicted in the energy graph shown in figure 4.31.

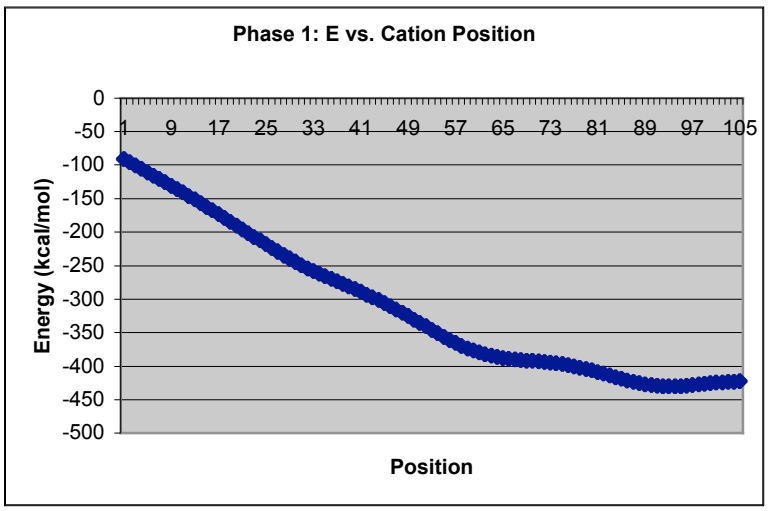

Figure 4.31 The first phase of cation motion in the knock-on mechanism. The first two cation charges move into the selectivity filter until they are in the center of the cavity. This process is downhill in energy.

Initially, this is a very favorable process because the charge charge distances are rapidly decreasing. The energy drop begins to level off as the charges reach the center of the anion cavity (Figure 4.32).

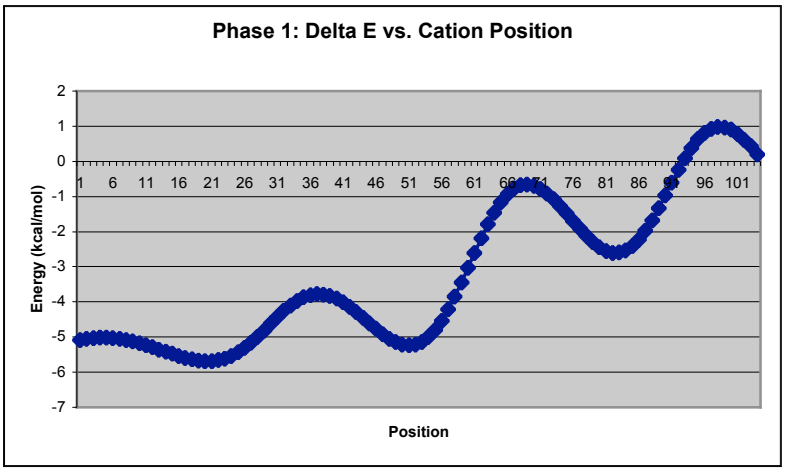

Figure 4.32 The ΔE graph corresponding to the total energy graph in figure 4.31. Peaks correspond to alignment of the charges with the box faces.

There is not significant variation as the two charges initially enter the cavity. There are peaks and valleys, which correspond to the charges being in and out of alignment with the box faces. In the next phase, the third charge, which had remained outside of the cavity, begins to approach the other two cation charges. The third charge travels into the cavity until the cation spacing is again 3 Å. The energy graph for this process is shown in figure 4.33.

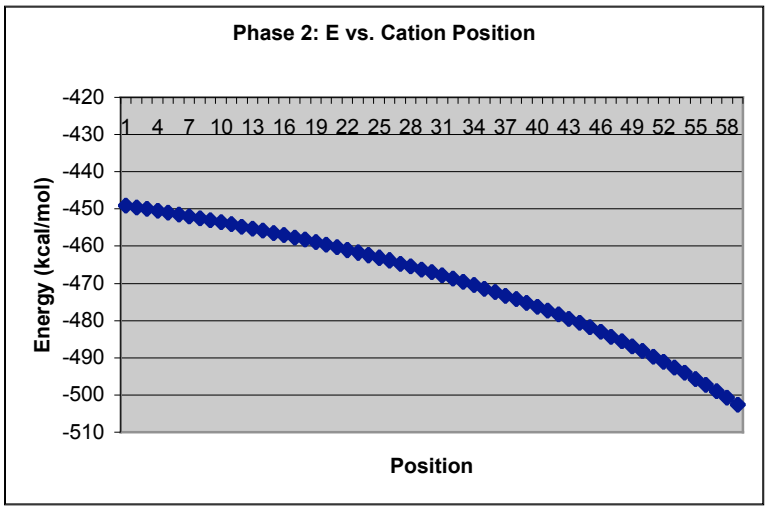

Figure 4.33 In the second phase of motion in the knock-on mechanism, the third cation entes the cavity and travels until it is 3 Å away from the other 2 cations. The favorable cation-anion interactions outweigh the cation-cation repulsion.

The entry of the third charge into the cavity is also a favorable process, but the slope is not as steep as it was for the approach of charges 1 and 2. This is a very reasonable result because the cation-cation repulsion is increasing as the third charge travels towards the first two. Also, the gain in energy is only due to the approach of one charge as opposed to two. The minimum energy is now a little less that –500 kcal/mol. The ΔE graph for this phase of motion is shown in figure 4.34.

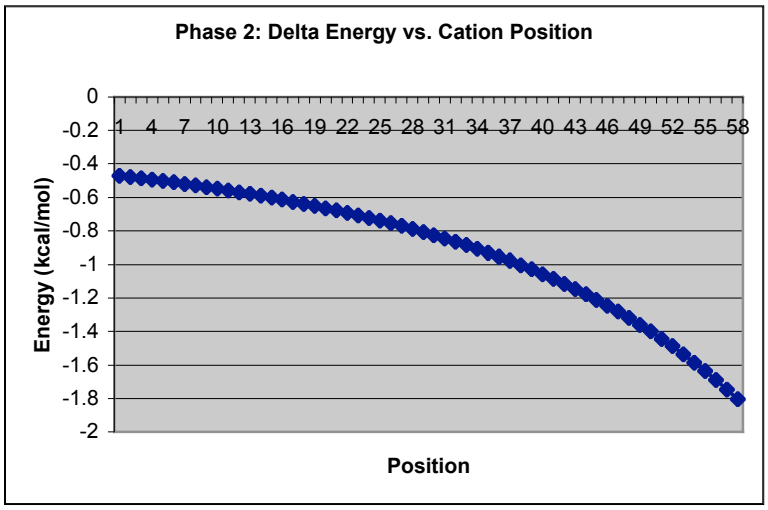

Figure 4.34 The ΔE graph corresponding to the total energy graph in figure 1.33. The shape in nearly identical to the total energy graph as the cation approach is increasingly favorable energetically.

This graph is a logical result because it simply follows the shape of the energy graph. The third and final phase of the cation movement involves the exit of the first cation while the other two remain in the cavity. The first cation travels until it is 3 Å beyond the cavity exit. This movement is shown in the graph in figure 4.35.

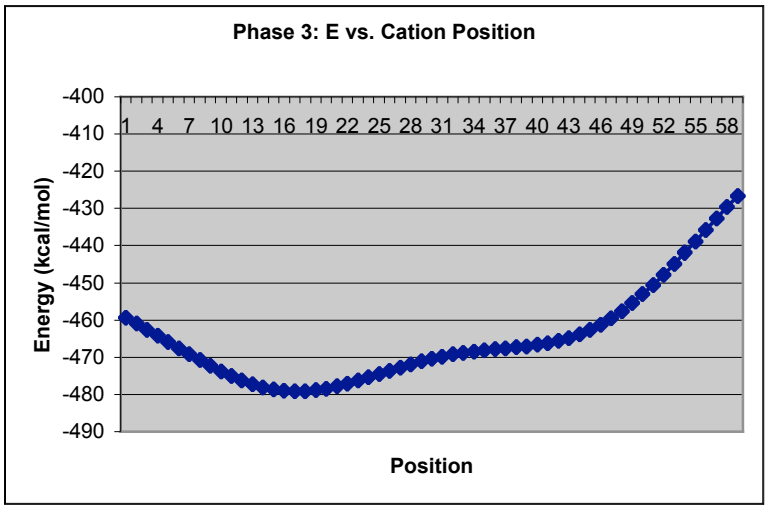

Figure 4.35 In the third phase of motion, the first cation travels out of the selectivity filter. The process is initially favorable but in the end energy is required to move the charge out of the anion cavity.

Initially, this is also a favorable process because the first cation still has other anions to interact with and cation-cation repulsion is decreasing. Gradually, the first cation nears the exit to the channel, which is no longer energetically favorable. In this graph, there is a 50 kcal/mol difference between the minimum and the point at which the first cation is 3 Å beyond the exit. Overall, the minimum in these 3 steps occurs at a little less than –500 kcal/mol, which gives a total difference of approximately 80 kcal/mol.

4.7 Conclusions and Future Work

Both the conformational change and knock-on mechanism were investigated to determine if either of these mechanisms could provide sufficient energy for potassium ion flux. However, the energy gradients in both cases were not significant enough to explain the observed transport of potassium ions. The results suggest that further development of the model system will be necessary in order to elucidate the mechanism of ion flux. One possibility is that a combination of conformational

change and decoupled motion of the cations will provide the appropriate energy differential to rationalize ion flux. In addition, the ability to precisely control the properties of the model system should allow for a more accurate depiction of the actual ion channel. For example, the modification of the dimensions of individual boxes would allow the cavity to be defined specifically. Also, the ability to modulate the dielectric constant over different regions of the selectivity filter should also provide a means to finely tune the properties of the cavity, particularly since ion channels are transmembrane proteins. In a broader sense, the model designed for this study should be applicable to the investigation of other related biological systems. Although the work presented here did not definitively establish a mechanism for ion transport, this fundamental approach based exclusively on electrostatics provides significant insight into the energetics of ion channels.

REFERENCES:

1. Choe, S. *Nature Reviews* **2002,** *3,* 115.

2. Doyle, D. *et al. Science* **1998,** *280,* 69.

3. Ma, J.; Dougherty, D.A. *Chem. Rev*. **1997,** *97,* 1303.

4. Sunner, J.; Nishizawa, K.; Kebarle, P. *J. Phys. Chem.* **1981,** *85,* 1814.

5. Searles, S.K.; Kebarle, P. *Can. J. Chem*. **1969,** *47,* 2619.

6. Morais-Cabral, J.H.; Zhou, Y.; MacKinnon, R. *Nature* **2001,** *414,* 37.

7. Berneche, S.; Roux, B. *Nature* **2001,** *414,* 73.

4.8 Fortran Code for Electrostatic Modeling

```
          program akrods
C
C         Define the variables
          implicit double precision(A-H, L-Z)
          integer boxes, rod_charges
C
C  (5)
C         Read in values for the lengths of the sides of the box
          Print *,'What are the values for L1,L2, and L3 in angstroms'
C
C         Read in the number of charges on the cation rod
          Print *,'How many charges on the cation rod?'
          Read *, rod_charges
C
C         Skip cation-cation distance if there is only one charge
          If (rod_charges > 1) then
C
C         Otherwise read in the distance L4(cation-cation distance)
          Print *,'What is the cation-cation distance in angstroms?"
          Read *, L4
C
          End if
C
C   (25 )
C         Read in the value of q1 (anion charge)
          Print *,'Input the charge for the anions'
          Read *, q1
C
C         Read in the value of q2 (cation charge)
```

```
            Print *,'Input the charge for the cations'
            Read *, q2
C
C       Convert charges to coulombs
            q1 = q1*1.602e-19
            q2 = q2*1.602e-19
C
C  (35)
C       Read in the number of boxes
            Print *,'Input the number of boxes'
            Read *, boxes
C
C       Read in the initial height of the cation rod (z1) which is distance from first box
face to first rod charge
            Print *,' What is the initial cation rod height in angstroms?'
            Read *, z1
C
C       Read in the step size for moving the cation rod (dz1)
            Print *,' What is the step size for moving the cation rod?'
            Read *, dz1
C
C  (50)
C       Read in the number of steps the cation rod will move
            Print *,'How many steps will the rod move?'
            Read *, rsteps
C
C       Read in vertical displacement of anion rods 1 and 3
            Print *,'What is the shift for rods 1 and 3?'
            Read *, z2
C
C       Read in the value for the dielectric constant
            Print *,'What is the value of the dielectric constant?'
            read *, eps
C
C       Convert the dielectric into permittivity constant
            eps=eps*(8.85419e-12)
C
C       Define the constant pi
            pi=3.14159
C
C       Open the output file
            Open(unit = 9, file = 'output1')
C
C       Convert all of the angstrom distances to meters
            L1=L1*1e-10
            L2=L2*1e-10
            L3=L3*1e-10
            L4=L4*1e-10
            z1=z1*1e-10
            dz1=dz1*1e-10
```

```
          z2=z2*1e-10
C
C       Set the sum of the cation energy to zero
          Sumcat = 0.0D+00
C
C  (75)
C       Do the cation loop for each cation-cation interaction
          do i0=1,rod_charges
C
C       Calculate the energy in joules for charge interactions on rod
          Ecat1 = (rod_charges-i0)*(q2*q2)/((4*pi*eps)*(i0*L4))
C
C       Convert from joules to kcals/mol
          Ecat = Ecat1*1.44e20
C
C       Add together all the Ecat terms
          Sumcat = Sumcat + Ecat
C
C       End the cation-cation loop
          end do
C
C  (90)
C       Define Segment AC as the facial diagonal of L1 X L2
          AC = sqrt((L1**2.0)+(L2**2.0))
C
C       Set the sum of the anion-cation interaction energy to zero
          SumEint=0.0D+00
C
C       Outer loop for moving the rod through the cavity with step dz1
C       rsteps was input by the user as the number of steps to move the rod
          do i1=0,rsteps
C
C  (100)
C       Define the vertical location of the rod as zrod
C       The initial rod position is z1, it moves down in increments of dz1
          zrod = z1-(i1*dz1)
C
C       Output the energy of a single rod position to file output1
          Write(9,*) SumEint
C
C       Second loop for every cation interaction with four anions at a time
          do i2=1, rod_charges
C
C       Inner loop to move through each set of four anions
          do i3=0,boxes
C
C       Define the distance between any charge on rod and the charges on box
C       r1 is half the facial diagonal
          r1=AC/2.0
C
```

```
C       r2 is the vertical distance between a face on the box and a rod charge
        r2=(i3*L3)+((i2-1)*L4)+zrod
C
C       r3 is the distance between the cation charges and unshifted anion rods
        r3=sqrt((r1**2.0)+(r2**2.0))
C
C       r4 is the distance between the cation charges and shifted anion rods
C       z2 is the vertical shift of rods 1 and 3 input by the user
        r4=sqrt((r1**2.0)+((r2+z2)**2.0))
C
C  (120)
C       Eint1 is the cation anion interaction energy for unshifted anions
        Eint1=2*(q1*q2)/((4*pi*eps)*(r3))
C
C       Eint2 is the cation-anion interaction energy for shifted anions
        Eint2=2*(q1*q2)/((4*pi*eps)*(r4))
C
C       Add together Eint1 and Eint2
        Eint = Eint1+Eint2
C
C       Convert Eint from joules to Kcal/mol
        Eint = Eint*1.44e20
C
C       Add together all the Eint terms
        SumEint = SumEint + Eint
        SumEint = SumEInt
C
C       Print out the values of SumEint
        Write(6,*) 'SumEint =                              ' , SumEint
        Write(6,*) 'Eint'  , i1  ,  '=',  Eint
C
C  (135)
C       End the inner loop
        end do
C
C       End the second loop
        end do
C
C       End the outer loop
        end do
C
C       Output the final value of SumEint to file
        Write(9,*) SumEint
C
C       Print out the total interaction energy
        Write(6,*)'The cation-anion interaction energy is ',  SumEint
C
C  (145)
C       Start the outer loop for anion-anion interaction
        do j=1,boxes
```

```
C
C       Set etot1 and efinal to zero
          etot1=0.0
          efinal=0.0
C
C       Calculate the first order terms (Anion-Anion)
C
C       e1 is the first order energy from L1 and L2 interactions
          e11 = (q1*q1)*(2.0*j+2.0)/((4*pi*eps*L1))
          e12 = (q1*q1)*(2.0*j+2.0)/((4*pi*eps*L2))
          e13 = (q1*q1)*(2.0*j+2.0)/((4*pi*eps*AC))
          e1 = e11 + e12 + e13
C
C       Convert joules to kcal/mol
          e1 = e1*1.44e20
          write(6,*)'e1= ' , e1
C
C       segment AE=L3, AF is facial diagonal of L1 X L3
C       segment AH is facial diagonal of L2 X L3
C       segment AG is diagonal of L1 X L2 X L3 box
          AF = sqrt((L1**2.0)+(L3**2.0))
          AH = sqrt((L2**2.0)+(L3**2.0))
          AG = sqrt((L1**2.0)+(L2**2.0)+(L3**2.0))
C
C  (170)
C       e2 has all first order energy containing L3 terms
          e21 =(q1*q1)*(4*j)/((4*pi*eps*L3))
          e22 =(q1*q1)*(4*j)/((4*pi*eps*AF))
          e23 =(q1*q1)*(4*j)/((4*pi*eps*AG))
          e24 =(q1*q1)*(4*j)/(4*pi*eps*AH))
          e2 = e21 + e22 +e23 + e24
C
C       Convert joules to Kcal/mol
          e2=e2*1.44e20
          write(6,*)'e2 = ' , e2
C       etot1 is the sum of e1 and e2
          etot1 = e1+e2
C
C       Print out the values for etot1
          Write(6,*)'etot1 ', j , ' is ' , etot1
C
C       FIND TERMS FOR N CUBES
C
C  (185)
C       Set etot2 to zero
          etot2=0.0D+00
C
C       Do the loop for all other anion-anion interaction for i boxes
                    do k=2,j
C
```

```
C       seg1 is of length k*L3
                                seg1=(k)*L3
C       seg2 is a facial diagonal of L1 and i*L3
                                seg2=sqrt((L1**2)+((k)*L3)**2)
C       seg3 is facial diagonal of L2 and i*L3
                                seg3=sqrt((L2**2)+((k)*L3)**2)
C       seg4 is diagonal across box L1 X L2 x k*L3
                                seg4=sqrt((L1**2)+(L2**2)+((k)*L3)**2)
C
C  (195)
C       Calculate energy terms for segs 1-4
                                Ek1=(q1*q1)*(4.0*(j-(k-1)))/(4*pi*eps*seg1)
                                Ek2=(q1*q1)*(4.0*(j-(k-1)))/(4*pi*eps*seg2)
                                Ek3=(q1*q1)*(4.0*(j-(k-1)))/(4*pi*eps*seg3)
                                Ek4=(q1*q1)*(4.0*(j-(k-1)))/(4*pi*eps*seg4)
                                Ek=Ek1+Ek2+Ek3+Ek4
                                Ek=Ek*1.44e20
C
C       Add together all the Ek terms
                                etot2=etot2+Ek
C
C       End the loop for all other anion-anion interactions
                        end do
C
C  (210)
C       Print out the values for etot2
          Write(6,*) 'etot2 ' , j , ' = ' ,etot2
C
C       Calculate Efinal as etot1 + etot2 and print the values
          Efinal = etot1+etot2
          Write(6,*) 'Total anion-anion energy ' ,j, ' is ' ,Efinal
C
C       Repeat the calculations after adding an additional cube
C
C  (220)
C       End the outer do loop which adds more boxes to the system
          End do
C
C       Print out the total cation-cation energy
          Print *,' The cation-cation energy is ' , Sumcat
C
C       Print out the total anion-anion energy
          Print *, ' The anion-anion energy is ' , Efinal
C
C       Determine and print the final energy
          Energy = Efinal + SumEint + Sumcat
C
C  (235)
C       End of program
          End
```